LABORATOIRE DE PHYSIQUE DES LASERS

UNIVERSITÉ PARIS-NORD
INSTITUT GALILÉE

DOCTORAL THESIS OF THE UNIVERSITÉ PARIS-NORD
presented by

Radu CHICIREANU

for the degree of: Doctor of Philosophy
specialty : physics

STUDIES OF COLD CHROMIUM ATOMS IN MAGNETIC AND OPTICAL TRAPS:
steps towards Bose-Einstein Condensation

–

ATOMES FROIDS DE CHROME PIEGÉS MAGNÉTIQUEMENT ET OPTIQUEMENT:
premières étapes vers la condensation

Defended the 25$^{\text{th}}$ October 2007, in front of the commission consisting of:

M.	Tilman PFAU	Président
M.	Jean DALIBARD	Rapporteur
M.	Christoph WESTBROOK	Rapporteur
M.	Christian CHARDONNET	Examinateur
M.	Bruno LABURTHE-TOLRA	Examinateur
M.	Olivier GORCEIX	Directeur de thèse

Familiei mele

Contents

Acknowledgements

The experimental work described in this thesis is the product of a collaboration of many people to whom I am deeply grateful. I want to thank them for all their support and encouragement through out my Ph.D. years.

I thank my supervisor, Olivier Gorceix, who made possible the realization of this project by creating this new experiment and finding resources to sustain its development. He managed to create a wonderful environment to work in, and I can say I have learned a lot during the three years I spent in his group.

By joining the Chromium project from its very beginning and helping to build the experiment piece by piece I have discovered also the importance of working as part of a team. I thus learned that building a team is not only putting together a bunch of people with different backgrounds – it takes time and a lot of work together to create synergies among them. For showing me the delights of experimental physics, I am deeply grateful to all the members of this team: Bruno, especially for his availability and for his ideas that always made us advance in times of despair; Laurent, especially for insisting in his determination that every odd experimental observation must have a logical answer; Etienne, specially for his optimism and patient explanations, and last, but not least, Arnaud, my co-Ph.D. student, for his continuous hard work and commitment. Of course, I want to thank the two older members of the group, Rene and Jean-Claude, whom I have had the pleasure to know and cherish, who have inspired me and from whom I have learned a great deal.

However, our experiment would not have been possible without the support of the technical and administrative services. Thus, I would like to thank the technical staff of the laboratory (Julien, Fabrice, Olivier, Michel, Gerard, Albert, Thierry) who provided a great deal of help, with tons of electronic, mechanical or optical components, and the administration center (Sabine, Nathalie and Martine) for their efficiency and diligence in solving all the tedious administrative problems.

Finally, I want to express my deepest gratitude to my family: my parents, Rodica and Radu, for their love and encouragement throughout my whole life, and my wife, Ramona, for standing by my side during my graduate career, for her love and constant support.

i

Introduction

Seventy years passed from Einstein's predictions, in 1925, (based on the photon statistics invented by Bose) to the outstanding first experimental realization, in 1995, of a 'pure' Bose-Einstein condensate (BEC) [1, 2], in a dilute atomic gas.

This collective behavior of a many-particle bosonic ensemble has a purely quantum-statistical nature. At sufficient low temperatures, the 'size' of a particle, given by the deBroglie wavelength Λ_{dB}, begins to be comparable, or even larger, than the interparticle separation (distance) and the particles, indistinguishable from one another, can no longer be treated as independent objects. They all sit then in the same quantum state, forming a single macroscopic 'super-particle', with exciting properties such as superfluidity (like that of ^{4}He) or long-range coherence (similar to that of a laser, but this time between massive particles).

More recently, effects of a different quantum statistics were investigated at ultra-low temperatures, using fermions. Unlike the bosons, they cannot be in the same quantum state, and pile up on top of each other to form a non-interacting Fermi sea [3].

Interesting features of BECs emerged from the interplay of the quantum-statistical effects and the interactions between particles. From a practical point of view, it was shown for example that, when the interactions are *attractive*, the condensate becomes less stable, and can collapse when a critical number of atoms is exceeded [4]. When interactions are *repulsive*, BEC is possible with large number of atoms; in this case, a deviation from the critical temperature T_c was observed [5], and the size of the BEC is greatly increased due to interactions [6, 7].

In most cases, interactions in a BEC are dominated by Van-der Waals interaction, which is short-ranged and isotropic, and can be modeled by a contact-interaction potential. At sufficiently low temperatures, it leads to an s-wave scattering, characterized by a single parameter which is the scattering length a.

In the first years of BECs, the experiments were conducted in the regime where the interaction energy $(U = \frac{4\pi\hbar^2 a}{m}n)$ was small compared to the quantum kinetic energy $(J = \frac{\hbar^2}{2md^2})$ of the particles $(U/J \propto n^{1/3}a \ll 1)$. In this regime, the coherence properties of BECs are not modified by interactions, and the mean-field theories are sufficient for describing their effects. The interference between two condensates [8], the realization of atom-lasers [9, 10] and the formation of vortices [11, 12] were thus achieved.

More recently-developed experimental tools – such as Feshbach resonances (which allow to tune the contact interaction, and thus increase the scattering length), and optical lattices (periodic arrays created by the AC Stark shift of a standing light wave, which tightly-confine the atoms and reduce their mobility) – allowed reaching the 'strongly-correlated regimes', by either increasing U or decreasing J. Due to this, new phenomena arose, such as the Mott transition between a superfluid and an insulating phase [13, 14], or the 'fermionization' of a 1D Bose gas [15]. For fermions, reaching the strong-interaction regime led to the creation of a BEC of molecules, formed by pairing between two fermionic atoms [16, 17, 18], and the study of the BEC-BCS crossover [19, 20, 21].

We see that interactions greatly enrich the physics of BECs, by opening a bond with other domains of physics, such as the condensed matter physics, or quantum information. From this point of view, degenerate systems with other types of interaction may increase even more the perspectives for the study of interactions in the quantum regimes. This is why several theoretical and experimental teams turned towards the dipole-dipole interaction, which is long-ranged $(\propto 1/r^3)$ and anisotropic (attractive in one direction and repulsive in the other two).

The long-range character makes the dipole-dipole interaction quite different from the contact interaction: even at low temperatures, many partial waves contribute to collisions between atoms. Another consequence is that, if a dipolar BEC is loaded in an optical lattice, the sites cannot be treated as independent and will interact with each other.

The anisotropic character on the other hand greatly influences the stability diagram of a dipolar BEC [22, 23], and also can lead to new quantum phases, such as the supersolid phase or the insulating checkerboard phase [24]. In a 2D geometry of pancake-shaped traps the occurrence of a roton-maxon excitation spectrum [25] is expected.

Although there are several candidates for studying the quantum-degenerate regimes with dipole-dipole interactions (such as heteronuclear molecules or Rydberg atoms, with large electric dipoles), chromium is the only system which has been already condensed [26], in the group of T. Pfau in Stuttgart. It has a large magnetic dipole moment $\mu = 6\mu_B$; the dipole-dipole interaction energy U_{dd} (scaling with the square of μ) is thus 36 times stronger than for an alkali atom. Soon after condensation of Cr, the same

group showed that dipolar effects affect the expansion of a BEC when released from its trap [27].

To characterize how important dipole-dipole interactions are compared to contact interaction, it is useful to introduce the parameter $\epsilon_{dd} = \frac{\mu_0 \mu^2 m}{12\pi\hbar^2 a} \propto \frac{U_{dd}}{U}$. Although strongly enhanced by the large magnetic dipole moment, the dipole-dipole interactions in Cr are however dominated by the contact interaction: for ^{52}Cr, $\epsilon_{dd} = 0.159$. Reducing the scattering length using a Feshbach resonance allowed to reach the regime of a quantum ferrofluid [28], where the dipole-dipole interaction is comparable to the contact interaction ($\epsilon_{dd} \sim 1$). In this case, the stability diagram of a BEC is completely modified. One enters a fascinating regime where dipole-dipole interactions dominate...

Another interest of Chromium is the existence of a fermionic isotope (^{53}Cr) with a relatively high natural abundance; it is a good candidate for experimentally studying, for the first time, dipole-dipole interaction in a Fermi Sea. We note that, usually a non-interacting at low temperatures, a gas of spin-polarized dipolar fermions can still interact through dipole-dipole interaction (which does not vanish when $T \to 0$).

This thesis

I began my Ph.D. just as a new experiment, concerning the study of dipolar interactions in ultracold, degenerate Bose and Fermi gases of Cr started, in the group of O. Gorceix. My work has been performed in *Laboratoire de Physique des Lasers*, at *Université Paris Nord* in Villetaneuse, France.

This thesis consists of seven chapters. The first chapter is an introduction which summarizes some of the important properties of Cr (such as the atomic levels of interest for laser cooling, etc.).

Before our experiment, there were only two groups in the world which had obtained magneto-optical traps with the ^{52}Cr isotope [29, 30]. To obtain a MOT with Cr atoms is a technical challenge, due to the necessity of a high-temperature oven, and to the need to generate a high power of 425 nm laser light. Our solutions to these problems are described in *Chapter 2*, as well as the rest of the experimental apparatus. As in many cold atom experiments, it consists of ultra-high vacuum chambers, a Zeeman slower which is used to load atoms in a magneto-optical trap, repumper and optical pumping laser systems, an absorption imaging system and computer-control and data-analysis systems.

Cr magneto-optical traps are different from alkali atom MOTs: they are dominated by unusually-large inelastic collision rates, which limit the number of atoms that can be accumulated, to a few 10^6 (in the case of ^{52}Cr). *Chapters 3 and 4* of this manuscript are dedicated to the experimental realization and characterization of Cr MOTs, as well as that of the main limiting factors.

In *Chapter 3* I describe our main results on magneto-optical trapping of ^{52}Cr ($\sim 4 \times 10^6$ atoms at a temperature $T = 120\ \mu$K), ^{53}Cr ($\sim 5 \times 10^5$ atoms) and on simultaneous magneto-optical trapping of both isotopes. We found that the atom numbers are limited even more in the case of the fermion – besides the inelastic collisions – by its smaller natural abundance, and by its hyperfine structure, which significantly reduce the flux of Zeeman-slowed atoms.

Chapter 4 is dedicated to the study of light-assisted inelastic collisions in Cr MOTs. For the fermionic isotope, we measured an inelastic collision parameter $\beta \sim 8 \times 10^{-9}$ cm^3/s, almost one order of magnitude larger than for the boson. We also develop, in the same chapter, a theoretical model to interpret the differences with the alkalis, for which the $\beta-$parameters are about two orders of magnitude lower than for Cr.

Because of the presence of long-lived metastable states, and of the leaks towards them from the excited MOT atoms via intercombination lines, Cr offers an interesting way of decoupling cooling and trapping. We were able to accumulate large number of atoms (up to 4×10^7 for ^{52}Cr) in these states, as they are shielded from the light-assisted collisions of the MOT.

In *Chapter 5* we study the possibility of combining the continuous accumulation of atoms in the metastable states with evaporative cooling. For that, we added an RF magnetic field which truncates the magnetic trap at different depths, depending on the RF frequency. At low frequencies, we observe an increase of the phase-space density, reaching values up to 6×10^{-6}, about six times larger that in the MOT, in less than 300 ms. In the same chapter I present a theoretical model, based on simple rate equations, which reproduces the experimental observations, and allowed to infer the inelastic loss parameter with the excited MOT atoms $\beta_{PD} = 5 \times 10^{-10}$ cm^3/s, which is the main limitation factor for the phase-space density in this experiment.

In order to diminish the effect of the collisional limitation factors, and increase thus the number of atoms accumulated in the metastable states, we investigated the possibility of creating large, W-shaped magnetic traps; a limitation in this case was found to be the presence of RF second harmonics.

In *Chapter 5*, I also describe two experiments to measure the inelastic and elastic collisional properties of the metastable ^{5}D$_4$ state (i.e. the elastic collision cross section $\sigma_{el.} = 7 \times 10^{-10}$ cm^2 and the inelastic collision parameter between metastable atoms $\beta_{DD} = 3.3 \times 10^{-11}$ cm^3/s).

The high inelastic collision loss parameter β_{DD} shows that evaporative cooling in the metastable states cannot lead to condensation. On the other hand, condensation of ground-state Cr atoms in a magnetic trap is not likely, because of strong dipolar relaxation processes. A solution (which successfully led to condensation in T.Pfau's group) is to transfer the atoms in the lowest energy state, which is not magnetically trappable; they can however be trapped in optical dipole traps (ODT).

In our quadrupole magnetic trap, spin-changing collisions and Majorana losses limit the evaporative cooling stage before transferring the atoms in an ODT. In *Chapter 6* we demonstrate a way of directly loading a mixed, magnetic+single-beam optical dipole trap with metastable atoms; after switching off the magnetic trap, up to 1.2×10^6 atoms, at 100 μK, remain trapped in the ODT. This very efficient accumulation process is nevertheless equally limited by inelastic collisions between metastable atoms, and by Majorana spin-flips.

I also describe in *Chapter 6* two procedures to limit these effects: one is to shift the position of the ODT beam away from the zero magnetic field position; the other is to use RF magnetic fields, which allow to trap both high- and low-field seeking atoms. Finally, I describe the parametric excitation spectroscopy in the ODT, which allows to characterize our trapping potential, and to measure for the first time the AC Stark shift of the $^5D_4$ metastable state.

In the last chapter of this thesis I present recent works that were performed towards the condensation of Cr. I tested in particular the effect of optical pumping to the lowest energy states, by demonstrating a strong reduction of inelastic losses, in a crossed ODT configuration. The modification of the shape of the ODT, from a single-beam to a two-crossed-beam configuration led to a 20-fold increase of the phase-space density. Finally, I present some preliminary optimization procedures of evaporative cooling in the crossed optical trap.

Chapter 1

Chromium

In this chapter I summarize some of the general physical properties of Chromium, which are relevant for the experiments presented in this dissertation.

Chromium (Cr) is a transition element with an atomic number $Z = 24$, belonging to the 6th group of the periodic table of the elements. It is a steel-gray, lustrous, hard metal which has high melting (1850°C) and boiling (2690°C) points, at atmospheric pressure.

Naturally-occurring chromium is composed of four stable isotopes: ^{50}Cr, ^{52}Cr and ^{54}Cr, which are bosons, and ^{53}Cr, which is a fermion. Some properties of these isotopes are summarized in Table(1.1).

Isotope	^{50}Cr	^{52}**Cr**	^{53}**Cr**	^{54}Cr
Abundance	4.35%	83.79%	9.50%	2.37%
Nuclear spin	$I = 0$	$I = 0$	$I = 3/2$	$I = 0$
Statistics	boson	boson	fermion	boson

Table 1.1: Properties of the Cr natural isotopes.

The work presented in this dissertation uses the two most abundant isotopes, ^{52}Cr and ^{53}Cr, which are interesting from an experimental point of view because they obey to different quantum-mechanical statistics. They are good candidates for creating and studying degenerate mixtures of bosons and fermions.

Spectroscopic properties of ^{52}Cr

All the bosonic isotopes of Cr have a zero nuclear spin, resulting in the absence of any hyperfine structure. The relevant part of the ^{52}Cr atomic level structure is shown in fig.(1.1). This isotope has an ('almost closed') strong electronic transition, between the ground ^{7}S$_3$ state and the excited ^{7}P$_4$ state, which is used in our experiment for Zeeman-slowing and magneto-optical trapping the ^{52}Cr atoms. Some important properties of this transition are summarized in Table(1.2).

Besides the cooling transition, Cr also has a non-cycling transition ^{7}S$_3$ →^{7}P$_3$, at a wavelength of 427.60 nm, which is appropriate for optically pumping the atoms to the lowest-in-energy stretched state (see Chapter(7)).
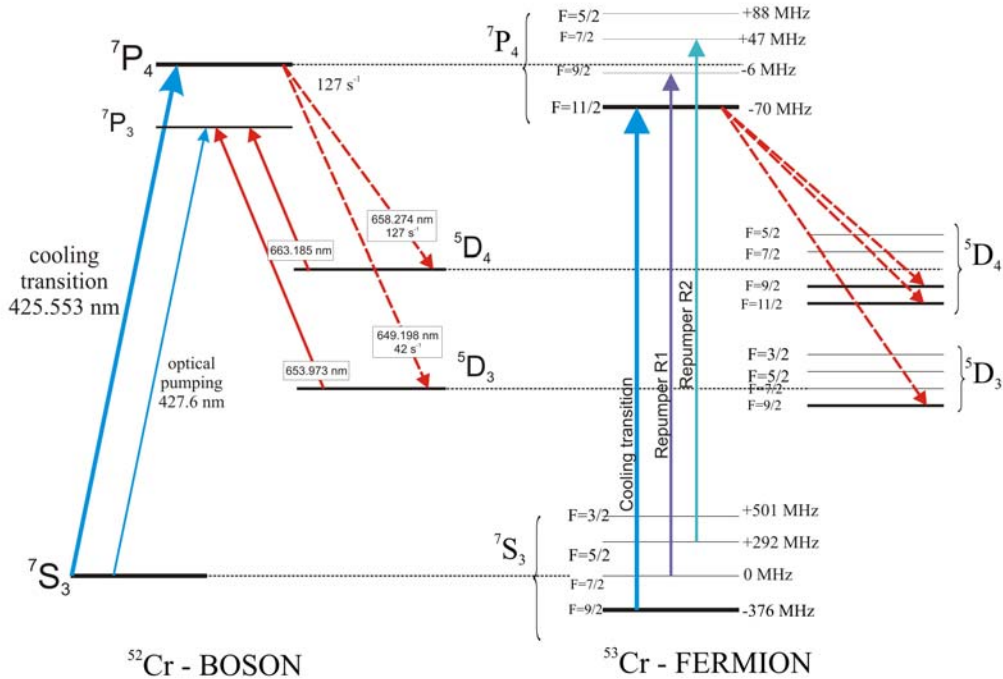
Figure 1.1: Simplified level structure of ^{52}Cr and ^{53}Cr; only transitions relevant to our laser cooling experiments are shown.

The Table (1.3) shows some properties of the levels of Cr which are important for our experiment. Another interesting property of Cr is thus the value of $6\mu_B$ of

magnetic moment in the ground state $^7S_3$. The reason for this is the presence of six valence electrons ($[Ar]3d^54s^1$ configuration), which leads to a total spin S=3. This high value makes the dipole-dipole interaction between two Cr atoms (which scales with the square of the magnetic moment) to be 36 times higher than of the alkali atoms. Cr is thus a good candidate for studying effects of the magnetic dipole-dipole interaction in quantum gases.

Vacuum wavelength	$\lambda = \frac{2\pi}{k} = 425.553$ nm
Transition energy	$\frac{hc}{\lambda} = 2{,}62$ eV
Linewidth	$\Gamma = \frac{1}{\tau} = 31.8 \times 10^6$ s^{-1}
Saturation intensity	$I_{sat} = \frac{\pi hc\Gamma}{3\lambda} = 8.52$ mW/cm^{-2}
Doppler temperature	$T_D = \frac{\hbar\Gamma}{2k_B} = 124$ μK
Recoil temperature	$T_{rec} = \frac{(\hbar k)^2}{mk_B} = 1.02$ μK
Recoil velocity	$v_{rec} = \frac{\hbar k}{m} = 1.8$ cm/s

Table 1.2: Properties of the $^7S_3 \rightarrow {}^7P_4$ transition of ^{52}Cr.

The ^{52}Cr atoms in the excited $^7P_4$ state can radiatively decay, via intercombination lines, towards two metastable states ($^5D_4$ and $^5D_3$), which have a long lifetime, of more than 50 s [32]. The corresponding decay rates ($\gamma_{^5D_4} = 127$ s^{-1} and $\gamma_{^5D_3} = 42$ s^{-1} [31]) are considerably smaller than the cycling rate of the cooling transition, and do not prevent laser cooling in a MOT.

The metastable $^5D_{3,4}$ states have also large magnetic moments – respectively $4.5\mu_B$ and $6\mu_B$ –, which makes possible the accumulation of the atoms (decaying to these states from the MOT), even in the magnetic trap formed by the relatively-low gradients of the MOT (~ 9 G/cm). These atoms can be repumped back in the ground state via the $^7P_3$ state (transitions at respectively 653.973 nm and 663.185 nm).

Level	J	Energy [cm^{-1}]	g_J	$|\overrightarrow{\mu}|$
^{7}S	3	0	2.00	$6\mu_B$
$z\ ^7$P	4	23498.84	1.75	$7\mu_B$
$z\ ^7$P	3	23386.35	1.92	$5.8\mu_B$
$a\ ^5$D	4	8307.57	1.50	$6\mu_B$
$a\ ^5$D	3	8095.21	1.50	$4.5\mu_B$

Table 1.3: Properties of the relevant levels of the ^{52}Cr isotope: Energy, Landé g-factor, magnetic moment.

Properties of the fermionic ^{53}Cr isotope

Unlike the bosonic isotopes, the fermionic ^{53}Cr has a nuclear spin $I = 3/2$. The coupling between the nuclear spin $\mathbf{I}$ with the electronic total momentum $\mathbf{J}$ (see Appendix(A)) leads to the splitting of each atomic level into four hyperfine sublevels, as it can be seen in fig.(1.1). The values of the hyperfine coupling constants A and B are given in Table(1.4); we note that these values are negative, leading to a so-called 'inverted' hyperfine structure.

The relatively small values of the hyperfine constants leads to a hyperfine splitting of less than 1 GHz in the ground state, and less than 200 MHz in the excited state. Experimentally this is very convenient, because the laser cooling frequencies of the fermion are sufficiently close to the ones of the boson to be obtained by means of acousto-optical modulators (AOMs).

Level	A [MHz]	B [MHz]
$^7S_3$	-83.599 ± 0.002	0
$^7P_4$	-11.8 ± 0.4	-0.6 ± 0.6
$^7P_3$	-1.5 ± 2.0	-2.0
$^5D_4$	-48.755 ± 0.005	63.021 ± 0.010
$^5D_3$	-35.683 ± 0.005	15.565 ± 0.005

Table 1.4:   The dipolar (A) and quadrupolar (B) hyperfine constants of ^{53}Cr.

Chapter 2

Experimental setup

In this Chapter I present the experimental setup which was built during my thesis.

2.1   The atomic source

The saturated vapor pressure of Cr is expected to be very low at room temperature, because of the high melting point, of 1857°C (at atmospheric pressure). To create a Cr vapor source, required for laser cooling experiments, one needs to heat up Cr, as close as possible to its melting point. In our experiment, this is done using a high-temperature Cr oven.

The choice of the oven temperature is very important as it sets the atomic flux. The available data on the saturated vapor pressure temperature dependence, as well as prior experiments in other groups, show that Cr atomic fluxes suitable for our applications can be obtained using ovens operated at about 1500°C.

The temperature dependence of the saturated vapor pressure for Cr, in the 300 K to 2000 K range, can be estimated using [33]:

$$P_{sat}(T) = \exp\left(a - \frac{b}{T} + c\ln(T) - \frac{d}{T^3}\right) \tag{2.1}$$

where P_{sat} is in Pa, T is in K and $a = 27.2$, $b = 47740$ K, $c = 0.44$, $d = 0.94$ K^3 are constants. This formula can be used to obtain a rough estimate of the dependence of the atom flux as a function of the oven temperature. In the effusive regime (i.e. when the diameter $\phi_{em.}$ of the emission hole is much smaller than the mean free path of atoms inside the oven) the longitudinal velocity distribution of atoms emitted inside a

small solid angle of azimuth $\theta_{em.}$, is given by:

$$f_{em.}(v,T) = \left(\frac{\pi\phi_{em.}}{2}\right)^2 \frac{P_{sat}(T)}{k_B T} \left(\frac{m}{2\pi k_B T}\right)^{3/2} v^3 \exp\left(-\frac{mv^2}{2k_B T}\right) \sin^2(\theta_{em.}), \qquad (2.2)$$

where v is the longitudinal velocity of the beam, k_B is the Boltzmann constant and m is the Cr mass. $f_{em.}(v,t)$ is plotted in fig.(2.1.A) for three different temperatures.
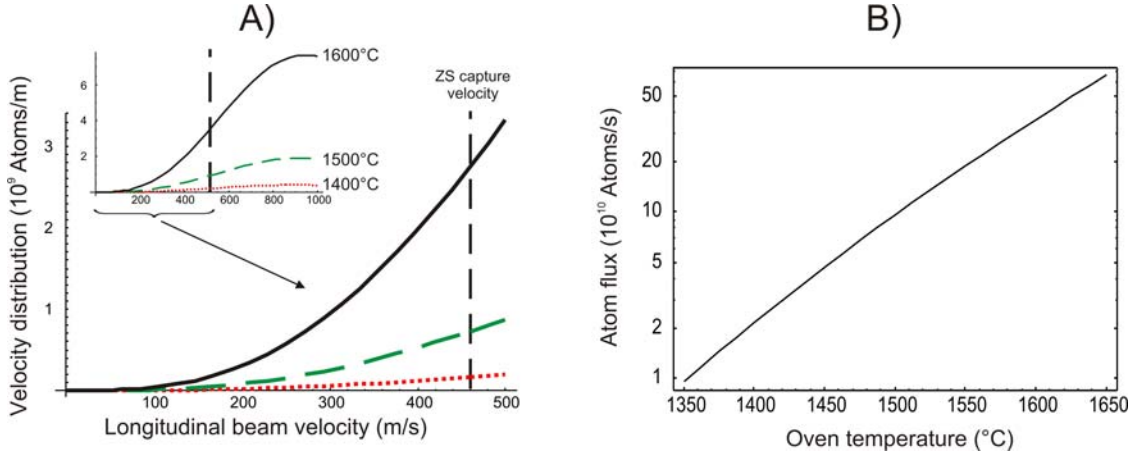
Figure 2.1: A) Velocity distribution $f(v,T)$ for 3 different temperatures: T=1400°C (dotted line), T=1500°C (dashed line) and T=1600°C (full line). The vertical dashed line indicates the Zeeman slower capture velocity. B) The total flux temperature dependence (integration up to $v_c \sim 460$ m/s), shown in a semi-log scale.

At a temperature ~ 1500°C, $f_{em.}(v,T)$ has a maximum at $v_{max} = \sqrt{\frac{3k_B T}{m}} \sim 900$ m/s. The fraction of atoms having a velocity smaller than 40 m/s (typical MOT capture velocity) is very small ($\sim 10^{-5}$) and the use of a Zeeman slower is mandatory. In this case, the 'useful' flux of atoms $\Phi(T)$ can be estimated by integration of eq.(2.2) up to the Zeeman slower capture velocity v_c (~ 460 m/s, as shown later): $\Phi(T) = \int_0^{v_c} f_{em.}(v,T)dv \propto \frac{P_{sat}(T)}{\sqrt{T}}$.

An indication on the temperature dependence of $\Phi(T)$ is shown in fig.(2.1.B).

Oven design

To build a chromium source is a technical challenge. The main reason is that Cr tends to react with most of the materials used for making high-temperature ovens. For example, direct contact between tantalum (Ta) or tungsten (W) must be avoided, because they form alloys with Cr, with melting point temperature lower than that of each individual component (eutectic).

Fairly long 'lifetimes' (set by the evaporation of the Cr bar), of at least several months, are required, because of ultra-high vacuum constraints. Because of the need

of a Zeeman slower, the Cr source has to be placed fairly far from the experimental chamber. Another difficulty comes from the fact that a beam with relatively small angular apertures, aiming to the MOT, is required.

Our chromium oven is a commercial high-temperature effusion cell fabricated by *Addon*. A schematic description of the oven is given in fig.(2.2). Two different combinations of materials were used in different stages of the experiment, as explained below. For practical (and security) reasons – such as having the experimental chamber and the laser beams well below the height of the eyes – we chose to operate the oven in the horizontal plane[1].
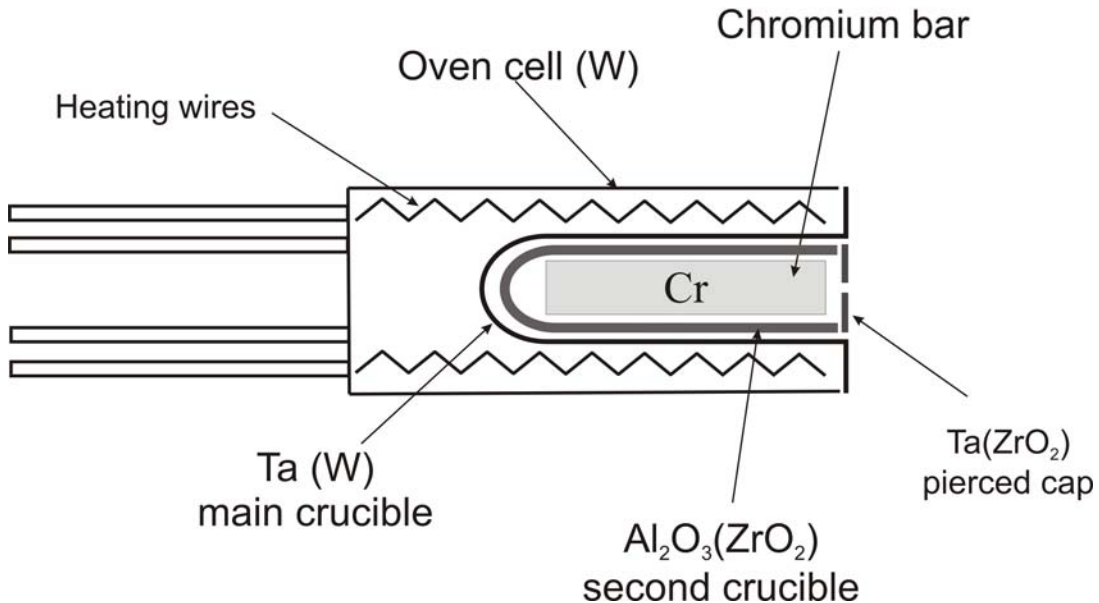
Figure 2.2: The Cr oven. Different choices for the crucibles are given, as explained in the text.

The oven consists of a main crucible initially made of Ta[2] which is heated by the radiation emitted by two current-carrying, self-sustained W filaments. The main crucible and the filaments are enclosed inside an oven cell also made of W. A water-cooled thermal shield, surrounding the oven cell, maintains the oven vacuum chamber at a moderate temperature (below $\sim 70°$C everywhere).

Due to the low temperature eutectic formed by Cr and Ta, Cr cannot be directly

---

[1] This was not an obvious choice, because of the possibility of deformation of the heating filaments (under gravity and at high temperatures), which may have led to short-circuits.

[2] This was a first choice, because *Addon* did not provide W crucibles and no other supplier could initially be found.

inserted inside the main crucible; it must be isolated using an internal crucible, with a low high-temperature reactivity with both Ta and Cr. A Cr bar (20 g, 6.5 cm long, 8 mm of diameter) of purity 99.7% is enclosed inside the internal crucible by a pierced cap, having a diameter $\phi_{em.} = 2$ mm, which is thus the 'emission source'. A second, 4-mm-diameter aperture (not shown in fig.(2.2)), set at a distance of 5 cm from the emission source, defines the direction of the effusion beam.

The oven is connected to the vacuum chamber through a CF40 directional flange. This provides the necessary fine tuning for the orientation of the atomic beam along the 1-meter-long Zeeman slower tube. The beam can be switched on and off within 200 ms with a computer-controlled mechanical shutter, placed at 1 cm after the 'emission source'.

The temperature of the oven is measured with a W/Re thermocouple. The DC source which feeds the heating wires is controlled by a programable controller through a PID loop. The oven temperature is always lowered to 1000°C during nighttime, to increase the lifetime of the Cr bar. We always use relatively long temperature-ramps, in order to avoid possible damages caused by fast temperature variations ; for instance, heating or cooling the oven between 1000°C and 1500°C is usually done using 2.5 to 3 hour ramps. A security system, using rechargeable batteries, was prepared for automatically lowering the oven temperature down to room temperature in case of power outages.

Choice of the crucible materials

For the internal crucible we tested two different materials: ZrO_2 (zirconia – a orange-colored ceramic) and Al_2O_3 (alumina – a white ceramic).

We first performed preliminary tests, without Cr, in order to test the compatibility between the materials of the two crucibles. We observed that the combination ZrO_2-Ta was not suitable, because, after heating up to 1600°C, the ZrO_2 crucible changed its color to black and became extremely fragile (it had even broken inside the oven). On the other hand the test with a second crucible, made of Al_2O_3, gave good results, both to the empty crucible test (heating up to 1600°C) and to the Cr-filled crucible test (heating up to 1500°C). The cap which seals the Cr bar was made of Ta.

This first combination of materials allowed us to obtain our first Cr MOTs and worked fine for about one year of operation at 1500°C. After this period, a sudden change of the value of the heating wires resistance was noticed. Analyzing the oven showed that the alumina crucible had significantly shrunk, while the Ta main crucible was severely flexed downwards, under the action of gravity, probably as it softened during the high-temperature operation. The Cr bar was consumed to about 2g while the alumina crucible was filled with a very light, pink powder (probably ruby). The change of the filament resistance was probably due to a short-circuit. We however could

not check what was the exact cause of this short-circuit (bent Ta crucible touching the filaments, or bent filaments touching the oven cell), as it was impossible to extract the deformed Ta crucible out of the oven cell without breaking it.

A second choice of materials was then tested (along with a new oven cell). We used a main oven crucible made of W along with an internal crucible made of ZrO_2. Due to the bad reaction observed between Ta and ZrO_2, the Ta cap was replaced by another, made of ZrO_2 and glued to the crucible (with high-temperature – up to 2200°C – resistant glue). The second oven has been operated for more than 12 month (and is still working), at temperatures up to 1550°C.

2.2 The vacuum system

Our ultra-high vacuum (UHV) system consists of two horizontally-arranged vacuum chambers. The first one (the oven chamber) is used for isolating the hot Cr source from the second one (the experimental chamber), where the vacuum requirements are more severe. The two are connected by the Zeeman slower (ZS) tube.
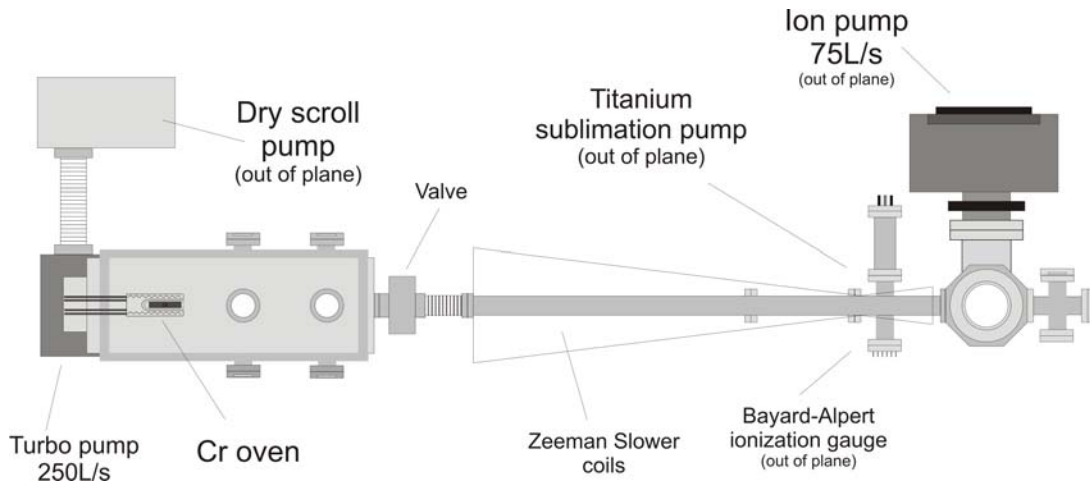
Figure 2.3: Vacuum system.

The oven is placed inside a cylindrical (0.5m long and 30cm diameter) vacuum chamber, which is pumped by a Turbo pump (with a pumping speed of 250 L/s), pre-pumped by a dry scroll pump (110 L/min) through a 1 m long flexible hose. The scroll pump is kept in a ventilated, acoustically-isolated box. Pressure inside the oven chamber is measured by a thermocouple gauge and a Bayard-Alpert ionization gauge. The pressure is typically equal to 6×10^{-11} mbar when the oven is at $T = 1000$°C and raises to 2×10^{-10} mbar when the oven is heated to $T = 1500$°C. The pressure in the oven chamber is significantly improved by the getter properties of Cr. Indeed we

observe that, after opening this chamber, the vacuum gradually improves, throughout a few days, when operating the oven.

A pneumatic valve is used to isolate the oven chamber from the Turbo pump. A security circuit automatically closes this valve if the pressure becomes to high.

The oven chamber has eight 425 nm-AR-coated CF40 viewports (four in the horizontal and four in the vertical plane), which are used to diagnose the Cr beam and to perform a 2D atomic beam collimation, as explained in the next chapter.
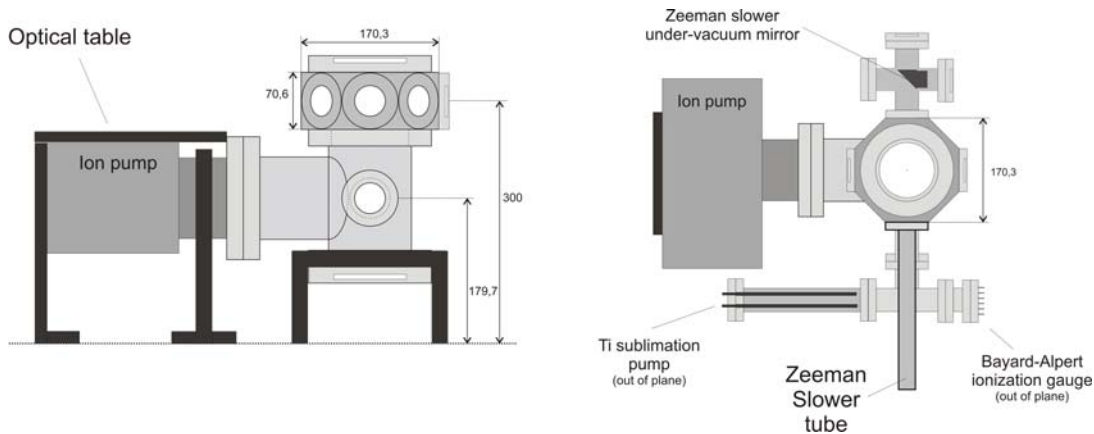
Figure 2.4: Experimental chamber, seen along the direction of the Zeeman Slower tube (left) and from above (right).

The experimental chamber (fig.(2.4)) is a compact octagonal chamber with eight CF40 viewports in the horizontal plane and two CF100 viewports for the coupling of vertical laser beams. A 150 L/s ion pump and a Ti-sublimation pump maintain the pressure at about 5×10^{-11} mbar. This value is measured with a Bayard-Alpert ionization gauge; the pressure might be lower at the position of the MOT, which is closer to the ion pump than the gauge. Magnetic trap lifetime measurements (described later) show, in the low atomic density regime, a $1/e$ time constant of 30 s. An additional pneumatic valve separates the two ultra-vacuum chambers. It is controlled by a security circuit, and closes if the pressure in the oven chamber passes above a certain threshold (a few 10^{-9} mbar).

Four of the CF40 viewports are wide range AR-coated, between 400 nm and 700 nm and used for coupling the horizontal MOT beams and the 'red' repumpers. The other viewports of the chamber (two CF40 and two CF100, coated for 425 nm, 530 nm and 1075 nm) are used also for coupling the optical dipole trap laser and possible optical lattice lasers (not used in this thesis).

A direct coupling of the ZS beam through a viewport must be avoided in our exper-

iment because the atomic Cr beam would rapidly coat it[3]. We use an undervacuum metallic Al mirror – made at our lab's optics shop – to reflect the ZS beam and direct it along the ZS axis (although this mirror also becomes coated with Cr, the changes of its reflectivity properties are moderate, compared to those of a Cr-coated viewport, whose transmissivity would rapidly fall).
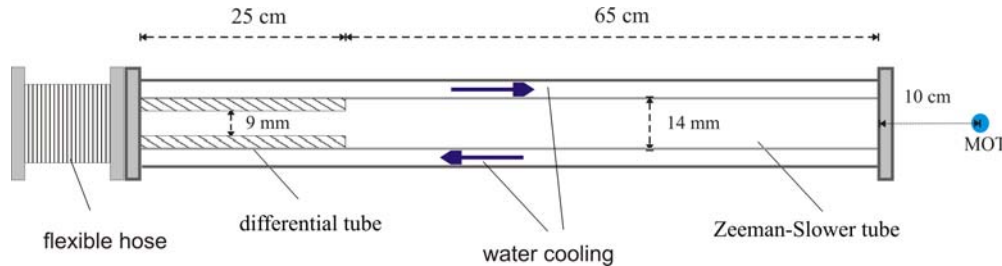
Figure 2.5: Zeeman shower tube and the differential tube.

The 90 cm-long, 14 mm inner diameter Zeeman Slower tube connects the two vacuum chambers. During the baking of the vacuum system, we observed the apparition of leaks at the connection with the experiment chamber, induced probably by the thermal dilatation of the ZS tube; we therefore added a 10 cm-long flexible hose at the entrance of the ZS tube, shown in fig.(2.5), which finally prevents the thermal dilatation effects on the ZS connections.

An additional differential tube (25 cm long and 9 mm of diameter) is placed at the entrance of the ZS. It can ensure a pressure reduction factor of ~ 400, in order not to alter the pressure in the experimental chamber, in the case where the pressure in the oven chamber accidentally increases to the 10^{-8} mbar range. We note that usually this high reduction factor is not required, as the oven chamber pressure is much lower than 10^{-8} mBar; it is however useful, after the oven chamber chamber is opened, for example after the replacement of the oven cell.

2.3 The laser sources

Several laser sources are necessary to cool and manipulate Cr atoms. These sources can be grouped in four components: the optical cooling laser-chain, the 'red' repumpers, the optical pumping system and the optical dipole trapping laser.

The magneto-optical cooling light is obtained by frequency-doubling a Ti:saphire laser. The Ti:saphire is frequency-locked to an external reference Fabry-Perot cavity, itself locked to a Cr atomic transition. The 'red' repumpers are provided by extended-cavity laser diodes, frequency-stabilized on the same Fabry-Perot cavity. The optical

---

[3] J.J. McClelland and T. Pfau, private communications.

pumping system is a frequency-doubled laser diode, stabilized independently on an atomic reference. Each of these components will be described in the following pages. The laser system used for optical trapping will be presented later, in Chapter(6).

2.3.1 The cooling lasers

Chromium has a strong 'blue' optical transition at 425.553 nm. No commercial laser diode system, providing both the required wavelength and a reasonable power (a few 100 mW for a cold atom experiment), is currently available. The solution we use in the experiment is based on the external cavity frequency doubling of a Ti:saphire laser.

The Ti:saphire laser

The Ti:saphire is a commercial *Tekhnoscan* laser, model TIS–SF–07. At the beginning of the experiment it was pumped by a *Coherent* Ar^+ laser, already available in our lab. After about 1.5 years, the pump laser was replaced by a Coherent Verdi laser, providing 18 W of single mode green light, at a wavelength of 532 nm. From a practical point of view, the better pointing stability and mode quality of the Verdi laser improved the stability our Ti:saphire laser (and, consequently, of the whole laser cooling system).

About 10.5 W of the Verdi laser are used for pumping the Ti:saphire; the extra 7.5 W available, single mode, laser power will be used in future optical lattice experiments with degenerate Cr gases. The Ti:saphire efficiency also improved with the new pump laser. In normal operating conditions we get 1.45 W, single mode laser at 851.105 nm from 10.5 W of pump laser. This yields an efficiency of almost 14% (compared to $\sim 11\%$ obtained with the Ar^+ laser). The frequency jitter of the Ti:saphire, specified by the manufacturer, is < 5 MHz rms at a one second scale.

Our Ti:saphire has a typical warming-up time of about two hours (after turning on the pump laser), during which the power reaches the maximum value and the frequency mode-hops stop. We observed that, for optimal operating conditions, a good thermal stability of the experiment room is required (typically of $\pm 1°C$), as well as the use of a flow box. Some occasional problems occur (typically two to three times a year) when the thin etalon of the laser gets misaligned; this requires a realignment of the etalon, as well as of the laser cavity.

We also observed that the performances of our Ti:saphire become poorer (power decreasing of $\sim 10\%$) during summertime, when the cooling water is warmer. To solve this problem, we adapted the cooling circuit to a water chiller, which keeps the crystal temperature constant to $12.5°C$.

The doubling cavity

The Ti:saphire laser light is frequency-doubled in an external four-mirror ring commercial cavity (model FD–SF–07), also produced by *Tekhnoscan*. The second harmonic is generated in a 15-mm-long lithium triborate (LBO) crystal. The doubling cavity can be continuously scanned, with a 3 GHz span, using the piezos supporting two of the cavity mirrors.

A Hänsch-Couillaud [35] scheme locks the doubling cavity length to the Ti:saphire laser frequency. The Ti:saphire beam needs to be injected in the doubling cavity through an optical isolator, which has a 93% transmission. Indeed, in absence of the optical isolator, we observed back-reflection effects on the lock of the Ti:saphire when the doubling cavity is locked on resonance with the IR light; this is attributed to the fact that the front of the LBO crystal is cut perpendicularly to the IR beam direction.

We also observed thermal effects in the doubling crystal: after the cavity was locked on resonance with the Ti:Saphire laser, the output power progressively dropped down (because of thermal dilatation of the crystal, the optical length of the cavity is modified and the resonance condition is no longer fulfilled). In order to reduce these effects, we set up a temperature stabilization device, which heats up the crystal, at a temperature of about 30°C, and the heating from the IR laser becomes negligible.

We finally obtain an output power of $\sim$ 340 mW of 425.553 nm blue laser light, with a doubling efficiency of 20%. We note however that the intensity noise is relatively high (about 10% of amplitude), and the cavity is quite sensitive to acoustic noise.

The output beam of the doubling cavity presents a strong astigmatism, which is mainly due to the crystal[4], and needs to be corrected for. We measured with a beam analyzer the position and size of the beam waists along the horizontal (OX) and vertical (OY) axis. In the horizontal direction we found a waist of $w_{x,0} = 26$ μm situated at $X_0 = -189$ mm (with respect to the output mirror of the cavity), while in the vertical direction the waist is $w_{y,0} = 99.3$ μm situated at $Y_0 = -215$ mm. We correct for the astigmatism using two lenses: a first $f = 150$ mm spherical lens followed by a second, cylindrical, $f = 150$ mm lens [34].

The reference cavity

The frequency of the Ti:saphire is stabilized using a high-stability Fabry-Perot (FP) reference cavity. Its mirrors are mounted on a tube made of *Invar* (which has a very low thermal dilatation coefficient $\sim 10^{-6}$ K^{-1}), which ensures a good mechanical and thermal stability. The cavity is placed in a vacuum chamber ($\sim$ 10 mbar) in order to protect it from air-pressure variations and to lower acoustic perturbations.

We use a $L = 0.5$ m long confocal cavity, for which all the modes of the same

---

[4] Ordinary-ordinary-extraordinary (OOE) type.

parity are degenerate. The free spectral range is $\Delta_{cav.} = c/2L = 300$ MHz and the reflectivity of the cavity mirrors is $R = 98.5\%$, yielding a theoretical finesse $\Im_{th.} = 107$. We measured a width of the transmission peaks of the cavity $\Delta f_0 = 5$ MHz, which corresponds to an experimental finesse value $\Im_{exp.} = 60$ [5].

The laser frequency is stabilized on the side of a Fabry-Perot reference cavity transmission peak. The error signal is generated by a differential photodiode, which records the difference between the transmitted FP signal intensity and the intensity of an additional (offset) optical signal[6]; a feedback is sent to the piezos of the laser-cavity mirrors (a fast and a slow loop – according to the band-width of the corresponding piezos – are required for correcting both the high and low frequency drifts). We are able to stabilize the frequency jitter of the Ti:saphire down to a few 10 kHz, with respect to the length of the FP cavity.

Figure 2.6: Scheme of the laser system for magneto-optically trapping and cooling Cr atoms.

---

[5] This is consistent with the measured cavity transmission $T = 15$ %, yielding additional intracavity losses of 3.5%. These losses are probably due to a misalignment of the two mirrors of the FP cavity, which makes the output beam slightly 'clipped' by the final cavity mirror.

[6] This differential scheme minimizes the sensitivity to laser intensity fluctuations.

The reference cavity stabilization

Once locked, the wavelength λ_{IR} of the Ti:saphire (and of the blue light) is set by the length L_0 of the FP reference cavity:

$$L_0 = N\frac{\lambda_{IR}}{2} = N\frac{c}{2f_{IR}} \qquad (2.3)$$

where N is an integer (we will call it 'the FP order') and f_{IR} is the Ti:saphire frequency. We can tune λ_{IR} by changing the length of the cavity, using the piezo supporting one of its mirrors.

An atomic reference is used to set the frequency of the blue light at a precise value, close to the Cr transition frequency. To do that we use the saturated absorption technique. A Cr vapor is obtained (by a krypton discharge) inside a commercial hollow cathode lamp.
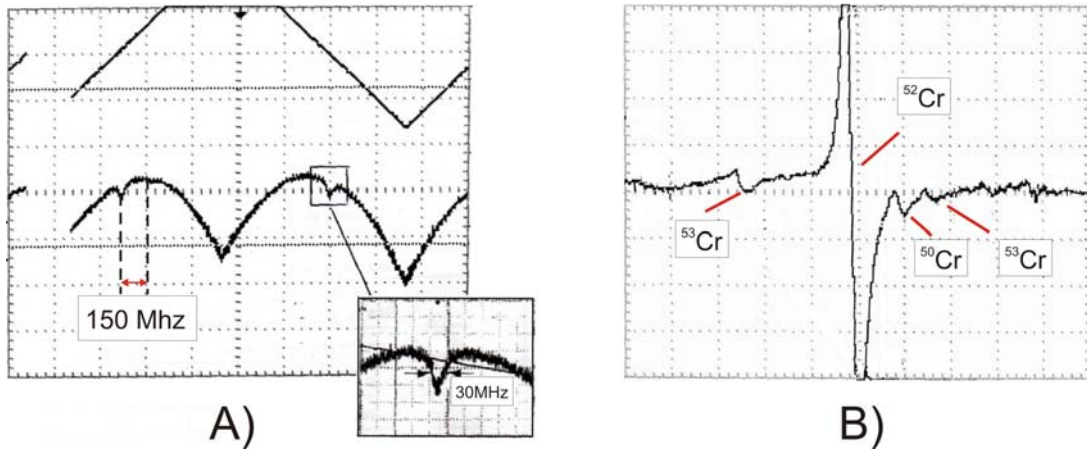
Figure 2.7: A) Saturated absorption signal, shifted by -150 MHz from the ^{52}Cr atomic resonance (center of the Doppler distribution). B) Lock-in amplifier signal. We observe additional atomic signals, that can be identified with transitions of other Cr isotopes.

A sinusoidal modulation at 100 kHz is applied to the frequency of a saturating pump beam passing through the hollow cathode via a double-pass acousto-optical modulator (AOM). The pump frequency is thus shifted by 300 MHz with respect to a counter-propagating low intensity probe beam. Both the pump and the probe beams are obtained from the residual transmission of one of the doubling cavity mirrors (see fig.(2.6)).

The two beams can be simultaneously resonant with the same velocity-class atoms only when the probe beam frequency is shifted by 150 MHz below atomic resonance. This can be observed in the saturated absorption signal shown in fig.(2.7.A). We also measured, using a calibrated sweep of the length of the cavity, a width (FWHM) of 30

MHz of the saturated absorption signal. This is about six times the natural width of the ^{52}Cr ^{7}S$_3$ →^{7}P$_4$ transition, and we explain this difference by collisional effects in the hollow cathode lamp. Demodulation at 100 kHz of the probe, using a lock-in amplifier, provides the dispersive error signal shown in fig.(2.7.A). This signal is used to lock the length of the FP cavity, via a PID loop, whose output is sent to the piezo-mount of one of the FP cavity mirrors.

The output of the doubling cavity, which has the same frequency as the probe, is therefore frequency-locked 150 MHz below the resonance of the ^{52}Cr ^{7}S$_3$ →^{7}P$_4$ transition. Finally, we estimate that the frequency of the cooling laser is stabilized to ~ 2.5 MHz[7]. This value is probably limited by the bandwidth of the piezo used to lock the reference cavity.

The ^{52}Cr and ^{53}Cr trapping frequencies

Five different laser frequencies are needed for the simultaneous magneto-optical trapping of ^{52}Cr and ^{53}Cr, as explained in the next chapter. One of them coincides directly with the output of the doubling cavity, while the other four are obtained using acousto-optical modulators (AOM).
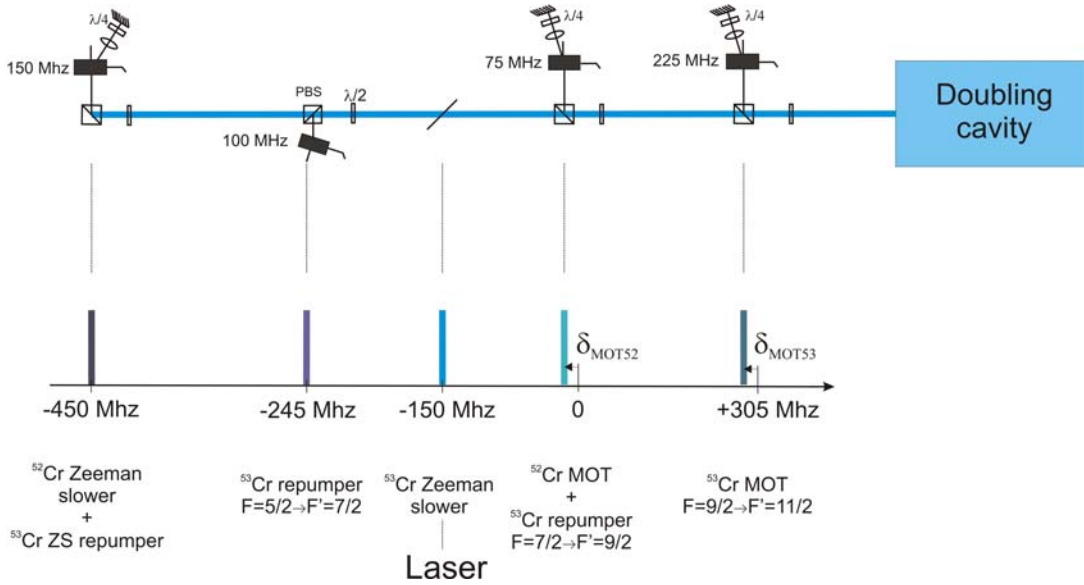
Figure 2.8: Frequency diagram for magneto-optical trapping of ^{52}Cr and ^{53}Cr isotopes. All frequencies are given with respect to the ^{52}Cr MOT transition. The output of the doubling cavity, detuned by -150 MHz, gives directly the ^{53}Cr Zeeman slower frequency.

These different frequencies are schematically shown in fig.(2.8). The AOMs we

---

[7] This value is deduced by comparing the amplitude of the error signal when the laser is locked to the widths of the saturated absorption signal – see fig.(2.7)

use have limited overall efficiencies, which is mainly due to a very high absorption, of about 10% at 425nm. The AOM overall efficiencies, after double-pass, are between 26% and 45%. This is an additional limitation for the power available for magneto-optical cooling in our experiment.

2.3.2   The 'red' diodes

The cooling transition of Cr is not perfectly closed, due to leaks to the metastable ^5D states (see the level scheme in fig.(1.1)). In our experiment, we use two extended-cavity laser diodes, operating at 663 and 654 nm in order to repump the $^5D_4$ and $^5D_3$ states back into the cooling cycle via the $^7P_3$ state. These laser diodes, fabricated by Toptica (model DL100), provide a power of typically 10-20 mW and have a spectral width of ~ 1 MHz.
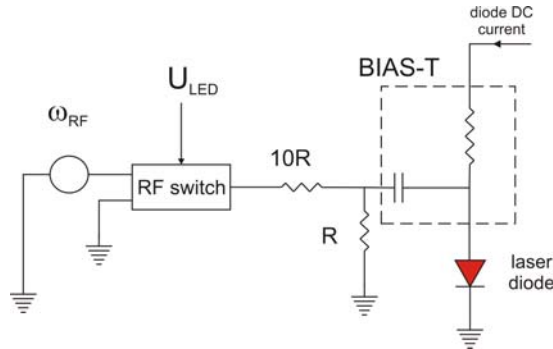
Figure 2.9: Modulation circuit for the laser diodes. The modulation is applied through the 'Bias-T' circuit before passing through a security switch.

The diodes are frequency-stabilized, using a Pound-Drever-Hall (PDH) scheme [36], on the same external Fabry-Perot cavity used to stabilize the Ti:saphire laser.

A modulation is applied directly to the current of each diode via the 'bias-T' circuit shown in fig.(2.9). We added extra security circuits, which stop the AC modulation if the DC current applied to the diode is accidentally stopped (which may damage the diode, if the AC modulation is still present).

The optical setup is shown in fig.(2.10). We use optical isolators (90% transmission) to protect the diodes from back-reflections, and their beams transverse modes are circularized with anamorphic prisms pairs (not shown in fig.(2.10)).

Small fractions (~ 1 mW) of the light emitted by each diode are combined on a non-polarizing plate before being injected into the reference cavity. The light reflected by the cavity is detected on a photodiode. We use different modulation frequencies (f_{RF1} and f_{RF2}) for each diode, which allows for the electric signal to be demodulated
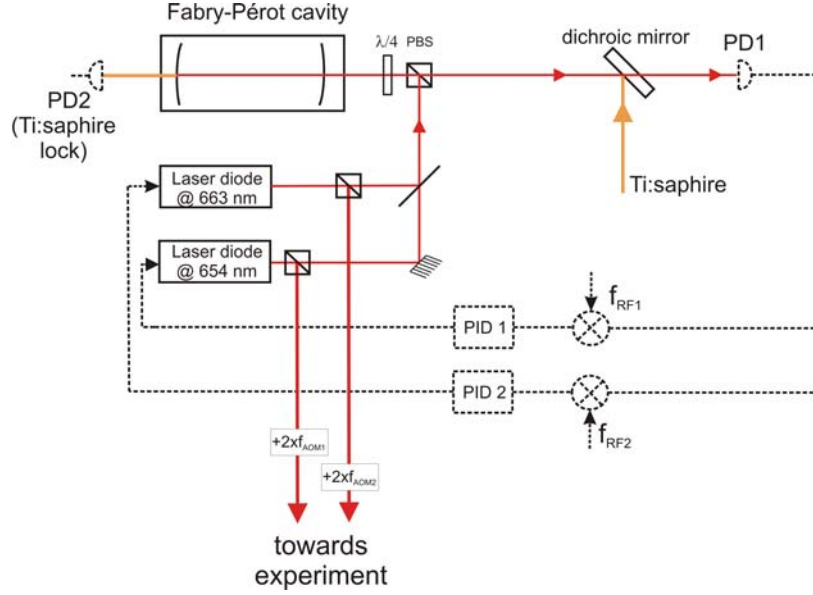
Figure 2.10: Optical setup for locking the two 'red' repumper diodes. Small fractions of the laser light are combined before injection into the FP cavity. The dichroic mirror both allows simultaneous injection of the Ti:saphire light and filtering of the IR from the red light reflected by the FP cavity.

separately. This allows to independently obtain the dispersive error signals required for locking each diode. We use the values $f_{RF1} = 6.5$ MHz and $f_{RF2} = 11$ MHz, which were experimentally chosen such that each one of the locks does not affect the other.

Finally, the error signal is sent to a PID correction loop. The correction signal obtained is sent to the laser diode via two channels: fast corrections are applied directly to the current of the diode, whereas slow corrections are sent both to the diode current and diffraction grating (via the *'Scan-Control'* module provided by the constructor), in order to prevent mode-hops.

Once stabilized on the FP cavity, it is possible to simultaneously tune the frequencies of both diodes on resonance with the $^5D_i \rightarrow {}^7P_3$ ($i = 3, 4$) atomic transitions, using two double-passed AOMs. Indeed, the required AOM frequency $f_{AOM,i}$ for each diode is set by the condition:

$$\frac{N}{f_{IR}} = \frac{N'}{f_{red,i} - 2f_{AOM,i}}, \tag{2.4}$$

where f_{IR} is the Ti:saphire laser frequency when the FP cavity is locked on the Cr atomic signal, and $f_{red,i}$ is the $^5D_i \rightarrow {}^7P_3$ transition frequency; N is the FP cavity order, set by eq.(2.3). The AOM frequency $f_{AOM,i}$ must thus be set to a value which yields an integer value for N', and which 'falls' inside the AOM band-width. In our case, this represents 2×70 MHz (for a double passed AOM), which is close to about half the free spectral range of the cavity.

Temperature lock of the FP cavity

The choice of locking three lasers on the same reference cavity is very convenient for the simplicity of implementation. On the other hand it may also raise complications, linked to the thermal drifts of the FP cavity length L_0. Indeed, a small variation, on the order of 450 nm, cannot be recovered with the cavity piezo and leads to a change of one for the cavity order. This will consequently change the two AOM frequencies which fulfill the resonance condition for both 'red' transition.

These considerations translate into a temperature stability criterion, since we require a thermal variation of the cavity order N of less than $\pm 1/4$ (meaning L_0 variations $\leq \lambda_{IR}/8$):

$$|\Delta T| \leq \frac{1}{4} \frac{\lambda_{IR}}{2\alpha L_0} \qquad (2.5)$$

where α is the *Invar* thermal dilatation coefficient. It corresponds to a temperature variation $\Delta T \leq 0.18°C$.

We measured temperature variations of the experiment room of $\pm 0.5°C$ throughout one day, which is far from satisfactory considering our criterion. A temperature stabilization system was constructed by Arnaud Pouderous [34]. It consists of an isolating box (which reduces the room temperature variations by a factor of 3) and of an active temperature regulator.

Temperature is measured inside the isolating box, using a thermistor in a Wheatstone bridge. A correction, obtained with a common PID controller, is applied through a heating wire uniformly wrapped around the vacuum chamber of the FP cavity. To ensure a better uniformity of the heating, the cavity was additionally wrapped in aluminum foils. Results are remarkably good, since the temperature variations were lowered down to less than $0.05°C$ (which corresponds thus to an improvement of more than a factor 10).

2.3.3 The optical pumping system

An additional laser system was set up for optically-pumping the atoms to the lowest energy Zeeman state. It uses an extended-cavity laser diode (model SYS DLL100L from Toptica), providing a power of 140 mW at a 855.2 nm wavelength. The output of the diode is frequency-doubled by an LBO crystal, inside a commercial external cavity (Wavetrain from Spectra Physics). The cavity is frequency-locked on the laser diode with a Pound-Drever-Hall technique (using an electro-optic modulation of the IR light frequency). We obtain 5 mW of 427 nm light, representing a 3.6% conversion efficiency.

A small fraction ($\sim$ 1 mW) of the blue light is used to obtain a Cr saturated absorption signal, in a second hollow-cathode lamp. The scheme is similar to the one used to get the saturated absorption signal of the 425 nm transition; the frequency

of the pump is shifted by 400 MHz (with a double-passed, 200 MHz AOM) below the atomic transition. A dispersive signal, obtained with a lock-in amplifier, is used as an error signal for locking the frequency of the diode. The output of the doubling cavity is, in these conditions, 200 MHz below the atomic transition frequency, and can be shifted on-resonance with a single-passed AOM.

The optical setup presented here was installed on a separate optical table; the 427 nm light is transported to the experiment with a polarization-maintaining optical fiber, with a $\sim 50\%$ total efficiency. The output beam of the fiber is 'collimated' to a 1.6 mm $1/e^2$ radius and sent to the atoms. Finally, a 2 mW blue laser beam is available, which corresponds to an intensity of 50 mW/cm^2 ($\sim 6I_{sat}$).

2.4   The magnetic fields

This section presents the design and realization of the coils which produce the 'main' magnetic fields used in our experiment, for Zeeman-slowing and magneto-optical trapping Cr atoms.

2.4.1   The Zeeman slower

As we showed earlier, in Section(2.1), the atoms emitted by the 1500°C oven have a mean longitudinal velocity of 900 m/s, and only a negligible fraction have a velocity smaller than the typical capture velocity of a magneto-optical trap. The flux of slow atoms must be enhanced with the use of a Zeeman slower (ZS). In our experiment, the Zeeman slower works on the Cr $|^7S_3, m_J = +3\rangle \rightarrow |^7P_4, m'_J = +4\rangle$ cycling transition (see fig.(1.1)).

Principle of a Zeeman slower

The atoms of an effusive beam can be slowed down using a resonant, counter-propagating laser beam. After each absorption of a photon from the beam, an atom receives a momentum kick $\hbar k$ in the direction opposite to its velocity (k being the light wavenumber). On the other hand, the spontaneous decay which follows is isotropic, and the corresponding momentum kicks average down to zero after several fluorescence cycles.

Because of the Doppler effect, the atoms having a velocity v feel a laser frequency $f(v) = f_{L,0} + kv$, where $f_{L,0}$ is the laser frequency. In order for the light to be resonant until the atoms are decelerated down to almost zero velocity, the Doppler effect variation needs to be compensated, in the case of a ZS [38] by a space-varying magnetic field $B(z)$, which modifies the energy of the atomic levels by Zeeman effect. The position-dependent atomic transition frequency reads: $f_{at}(z) = f_{at,0} + (\mu_B/h)B(z)$, $f_{at,0}$ being

the atomic transition frequency in zero magnetic field. The effective detuning is:

$$\delta(z,v) = f(v) - f_{at}(z) = \delta_0 + \frac{v}{\lambda} - \frac{\mu_B}{h}B(z) \qquad (2.6)$$

where $\delta_0 = f_{L,0} - f_{at,0}$.

The deceleration that can be achieved by laser means is limited by the maximum photon scattering rate of an atom to a value called Doppler deceleration, given by: $a_D = v_{rec} \cdot \frac{\Gamma}{2} = 5.6 \times 10^6$ m/s^2, where $v_{rec} = \frac{\hbar k}{m} = 1.8$ cm/s is the recoil velocity for Cr atoms.

Design

In practice, we choose a constant value a_{zs} of the deceleration (smaller than a_D) as a starting point in the ZS conception. This sets the velocity dependence to: $v^2(z) = v_c^2 - 2a_{zs}z$, where the *'capture velocity'* v_c is the maximum velocity of atoms that can be slowed by the ZS. Atoms are typically slowed down to a small, positive *'extraction velocity'* $v_e = \sqrt{v_c^2 - 2a_{zs}L} \ll v_c$. The velocity dependence fixes the ZS magnetic field profile, by imposing $\delta(z,v) = 0$ in eq.(2.6):

$$B(z) = \frac{h}{\mu_B}\left(\delta_0 + \frac{1}{\lambda}\sqrt{v_c^2 - 2a_{zs}z}\right) \qquad (2.7)$$

This is a *'square-root'* profile and the magnetic field intensity varies between an initial value $B_i = \frac{h}{\mu_B}\left(\delta_0 + \frac{v_c}{\lambda}\right)$ and a final value $B_f = \frac{h}{\mu_B}\left(\delta_0 + \frac{v_e}{\lambda}\right)$.

The parameters to be chosen for a Zeeman slower design are: the capture velocity v_c, the ZS beam detuning δ_0 and the so-called *'security parameter'* $\eta = \frac{a_{zs}}{a_D}$ (which accounts for the irregularities of the 'real' magnetic field profile, as explained in the next paragraphs). v_c has to be as high as possible, in order to increase the flux of atoms that can be slowed. On the other hand, since the deceleration is limited to a_D, the length of the deceleration zone L (and of the ZS) increases proportionally to v_c^2 and there is a constraint about the compactness of the experiment. A proper extraction of atoms (i.e. the atoms slowed to v_e need to get rapidly out of resonance with the ZS beam once they exit the ZS, in order to travel 'safely' to the MOT region) imposes $|\delta_0 + v_e/\lambda| \gg \Gamma$ (or $|\frac{\mu_B}{h}B_f| \gg \Gamma$). There are also constrains for δ_0, some of them related to the overall design of the experiment[8], but also to the fact that the ZS beam has to be off-resonance with the MOT atoms.

Finally we chose a value of $v_c \simeq 550$ m/s, which gives both a sufficient ZS atom flux and a reasonable ZS length $L \simeq 0.9$ m. A detuning $\delta_0 = -450$ MHz was chosen for two reasons: first it allows a flexible frequency scheme both for the boson and fermion

---

[8] In our case to have a suitable laser frequency scheme, allowing simultaneous magneto-optical trapping of two Cr isotopes.

magneto-optical trapping[9]. Second, the corresponding magnetic field profile varies between a positive initial value to a negative final value, which reduces considerably the power dissipated by the ZS coils, and allows a better definition for the extraction velocity v_e [39].

ZS coils design and slowing simulation

Once the ideal B-field profile is known, one needs to approximate it using several layers of coils, all having different lengths. The transition between layers induces irregularities of the magnetic field compared to the ideal profile. If the irregularities are too steep, atoms may drop out of resonance before they could be sufficiently slowed in order to follow the ideal deceleration profile.
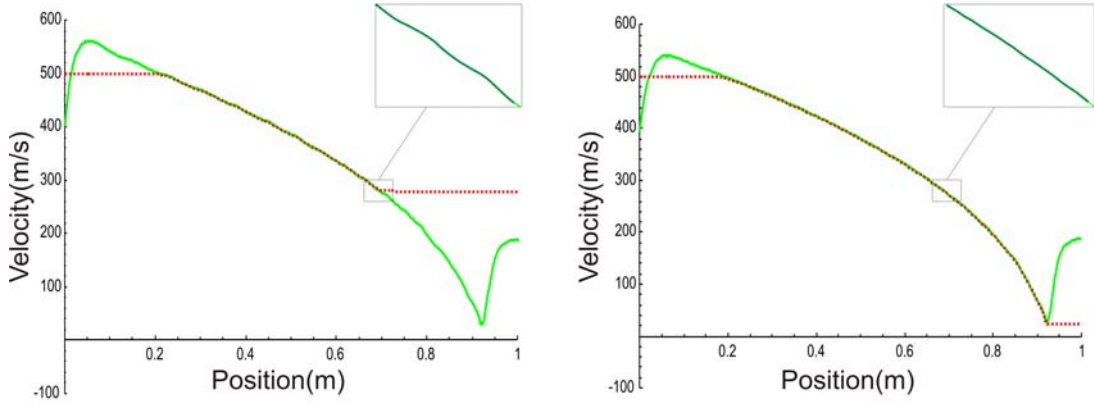
Figure 2.11: Comparison between two different ZS coil designs. The first corresponds to 15 layers and the second to 21. The magnetic field (full line) – plotted in 'velocity units', i.e. $\lambda\left(-\delta_0 + \frac{\mu_B}{h} \cdot B(z)\right)$ – corresponds to the desired velocity z-dependence. The dotted line is the result of the velocity evolution found by solving the equation of motion, for an initial velocity of 500 m/s. The difference between the two field profiles is hardly distinguishable (see insert: zoom of the magnetic field profile); it is sufficient nevertheless, in the first case, to make atoms leave the ZS slowing region well before reaching the extraction velocity v_e.

As the real profile will always be slightly different from the ideal one, one should take a certain margin in the ZS deceleration compared to the maximal value. For that we chose a value $\eta = 0.85$ for the security parameter. With a beam saturation parameter $s_0 \equiv I/I_{sat} = 2.5$, we have $a_{ZS} = \eta\frac{s_0}{1+s_0}a_D \sim 0.61 \, a_D$.

In fig.(2.11) (full lines) we show two different designs for the ZS magnetic field profile $B_{test}(z)$. They have a different number of layers, meaning different B-field modulations. We can then solve the equation of motion of an atom in the 'real' magnetic field profile. For this we use $\delta(z,v)$ given in eq.(2.6) to determine the exact acceleration:

$$a(z,v) = \frac{\Gamma}{2} \cdot \frac{I/I_{sat}}{1 + I/I_{sat} + (2\delta(z,v)/\Gamma)^2}v_{rec} \ . \tag{2.8}$$

---

[9] As mentioned earlier, the ^{53}Cr Zeeman slower frequency is directly obtained from the output of the doubling cavity, without any additional AOM.

Using the fact that $a(z, v) = dv/dt = v\, dv/dz$ we obtain a first order differential equation which can be solved numerically. Fig.(2.11) shows the result of such a calculation for the two different $B_{test}(z)$ profiles. In one case, because of the irregularities of the magnetic field, the atoms leave the resonance before the end of the ZS; in the other case, with a more regular profile, they are slowed up to the final ZS velocity.

Final characteristics

In order to achieve the desired field profile we chose to separate the ZS into 3 independent coils. The first, containing 21 layers, is producing the positive part of the field (between $z = 0$ and $z = 80$ cm). The negative part of the B-field is produced by two different coils. One is between $z = 80$ cm and $z = 95$ cm and contains 10 layers. The final coil is very narrow (1cm only) and has a small diameter which assures a steep variation of B and a proper 'extraction' of atoms, once they leave the Zeeman slowing region. It also allows us to produce the MOTs close to the exit of the tube (10 cm), which reduces losses due to transverse expansion of the slowed atomic beam at the exit of the ZS.
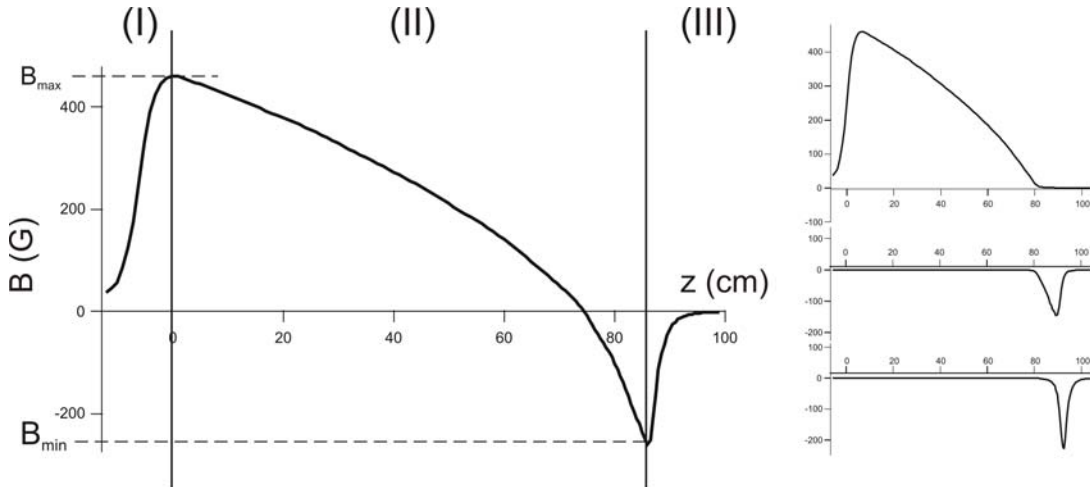
Figure 2.12: On the left: the 'final' (measured) profile of the Zeeman slower magnetic field. We highlighted the three main zones: I) the 'branching zone', II) the 'slowing zone' and III) the 'extraction zone'. On the right hand side we show each of the three magnetic fields, given by the three independent set of coils used to produce the 'final' profile.

The coils were wrapped directly onto the Zeeman slower tube, which contains a water-cooling circuit – see fig.(2.5) – in order to dissipate the heat generated by the ZS coils (respectively 100W, 6W and 22W).

The magnetic field profile was measured using a Hall-effect Gauss-meter and is shown in fig.(2.12). The final values of current for each coil was fixed experimentally, when optimizing our MOT (see chapter(3)) and are slightly different from the values predicted during the design phase. For a ZS detuning $\delta_0 = -450$ MHz we found

23

$B_{max} = 470$ G and $B_{min} = -260$ G, which correspond to a capture velocity $v_c = 460$ m/s and to an extraction velocity $v_e = 40$ m/s. This value is smaller than the one found for the design of the ZS (550 m/s): this could be explained by irregularities in the 'real' ZS B-field profile, or by the transverse broadening of the slowed atomic beam, which increases with the ZS capture velocity, as explained in the next paragraph.

Transverse broadening of the atomic beam

The number of photons that are absorbed, during the whole deceleration time $\tau_{zs} \simeq v_c/a_{zs} \sim 2.7$ ms from v_c to v_e, is: $N_{phot} = (v_c - v_e)/v_{rec} \sim 24000$. As the photons are scattered in random directions, the atoms will experience a transverse heating of $\Delta T = N_{phot} \frac{mv_{rec}^2}{k_B} \sim 50$ mK. This is much smaller than the temperature T~ 10 K corresponding to the typical MOT capture velocity, and will not affect the possibility of atoms to be captured by the MOT beams.

Photon scattering leads also to a transverse broadening of the atomic beam, whose diameter increases throughout the Zeeman deceleration. To evaluate this effect, let us consider a packet of atoms, with an initial transverse velocity $v_\perp$ and initial transverse extension Δr_0, at a time t during the propagation through the ZS. Each atom has scattered $N(t) = a_{zs}t/v_{rec}$ photons, and the velocity of the packet is broadened by $\Delta v_\perp(t) = v_{rec}\sqrt{N(t)} \sim 2.8$ m/s. The radius of the packet is:

$$\Delta r_\perp(t) = \Delta r_0 + \int_0^t \Delta v_\perp(t')dt' = \Delta r_0 + \frac{2}{3} t^{3/2} \cdot \sqrt{a_{zs}v_{rec}} \ . \tag{2.9}$$

At the end of the ZS, after the deceleration time τ_{zs}, the final size of the packet is:

$$\Delta r_\perp(\tau_{zs}) = \Delta r_0 + \frac{2}{3} \frac{v_c^{3/2}v_{rec}^{1/2}}{a_{zs}} \ . \tag{2.10}$$

With our ZS parameters, this gives an increase of the atom packet radius of 5.3 mm. This means that the MOT capture radius (mainly fixed by the size of the MOT beams) should be larger than this value[10]. On the other hand, because of the $v_c^{3/2}$ dependence in eq.(2.10), we notice that an increase of the ZS capture velocity leads to a fast increase in the beam broadening. This represents a limitation of the value of the capture velocity (and of the length) of a Zeeman Slower.

Finally, we mention that other effects come into play: for example, there is an additional transverse expansion (due to $\Delta v_\perp$) of the slowed atomic beam while traveling

---

[10] A substantial increase of the MOT beam diameter is difficult in our case, because of power limitations.

the distance between the end of the ZS and the MOT ($\sim$ 12 cm in our case). This expansion increases further the radius of the beam to about 10 mm: this value defines the 'ideal' capture volume of a MOT. In our case however, because of power limitations, the MOT beams have smaller radii (as explained in the following chapter).

2.4.2 The MOT coils

The MOT magnetic field gradient is produced by a pair of coils, in the anti-Helmtoltz configuration, symmetrically positioned on each side of the octagonal experimental cell, as shown in fig.(2.13.A). The coils are separated by $\sim$ 10 cm, and each one is made of 130 turns of $\phi = 1.5$ mm diameter copper wire, with a mean radius of $\sim$ 18 cm.

The MOT coils typically produce, in the center of the cell, a magnetic field gradient of 20 G/cm along the vertical z axis and two times smaller on the x and y axis. In these conditions, they dissipate about 200 W and a water-cooling circuit is needed. The coils were thus wrapped on a solid copper structure (made in our labs' mechanical shop) on which we attached the cooling water-pipes, also made of copper, using a thermoconducting glue.

A fast switch, shown in fig.(2.13) is used to rapidly turn off the current in the coils. We use a MOS-FET transistor which switches off the current of the supply, while the current in the coils dissipates into a resistance $R = 18\ \Omega$ which fixes the time constant to $\tau \simeq L/R$. The measured switch-off 1/e time constant is 500 μs, while the turning-on time is about 6ms, limited by the power supply. We also measured, using a small coil placed on the upper viewport of the cell, an effective switch-off time of 20ms for the magnetic fields. This time scale is fixed by the extinction of the eddy currents induced in our metal cell.

A security circuit was built for turning off the MOT coils current supply if the temperature exceeds 50°C, or in case there is no water running in the cooling circuit. Three additional pairs of coils were built for compensating the residual magnetic fields near the cell center, in all three directions. Two of these pairs, have a large diameter (0.8 m) and are placed far from the experimental chamber (for securing the beam passages); the third is wrapped together with the MOT coils and compensates along the vertical direction.

2.5 The imaging system

The imaging system allows for the acquisition of images of the atomic cloud and provides information about the shape and size of the trapped cloud and also allows a measurement of the number of atoms. In our experiment we use an imaging system
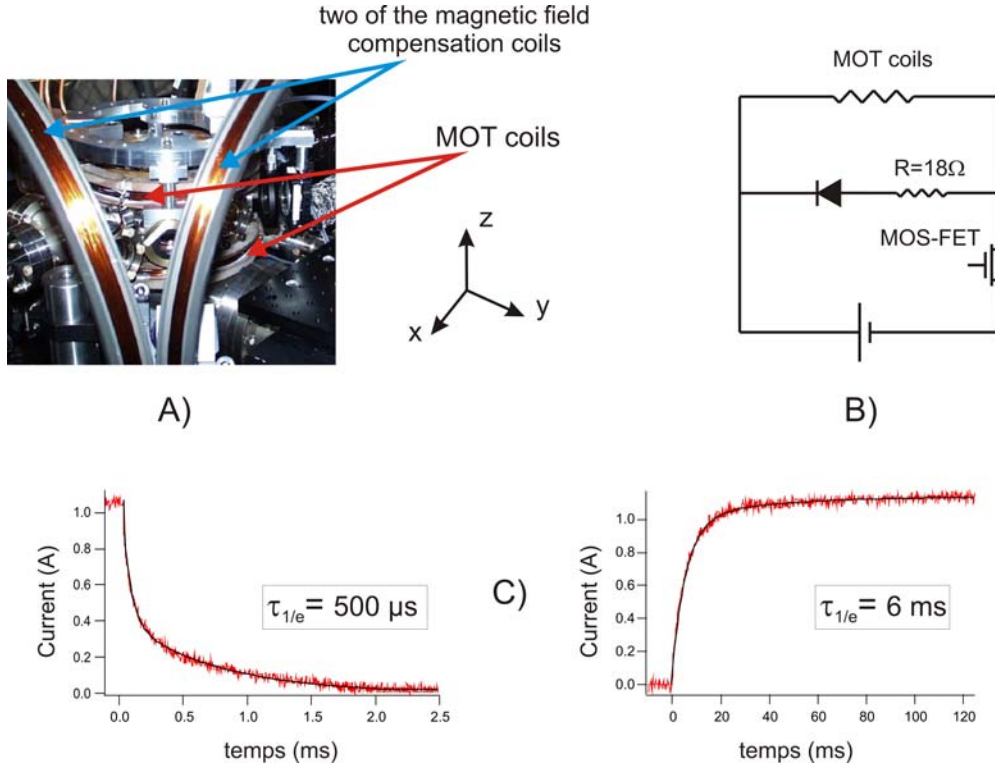
Figure 2.13: A) picture of the MOT coils B) MOT coils switch circuit C) the corresponding 'switch-off' and 'switch-on' time-sequences.

which is adapted both for fluorescence and absorption imaging[11]. It was conceived and built by Arnaud Pouderous; more details are available in [34].

Additionally, the time-resolved evolution of the fluorescence of the atomic clouds can be recorded using a photomultiplier.

We use a 12bit CCD camera, model QE from PixelFly, with a 1392×1024 resolution. It has square-shaped pixels (6.45×6.45 μm) with a quantum efficiency of 50% at 425 nm. The imaging axis is in the horizontal plane, perpendicular to the ZS axis. This provides both a good accessibility and a fairly good numerical aperture, the drawback being a fairly important (15 cm minimum) distance to the center of the experiment chamber.

The solution we adopted consists of a symmetrical, $1 \div 1$ telescope made of two identical f=20 cm achromatic doublets (model $AC508 - 200A1$ from $Thorlabs$). The on-axis imaging performance is limited by the pixel size. Problems due to off-axis abberations may appear when taking time-of-flight (TOF) images, as the expanding

---

[11] The imaging system presented here was available only for the experiments presented in the Chapters(5) to (7).
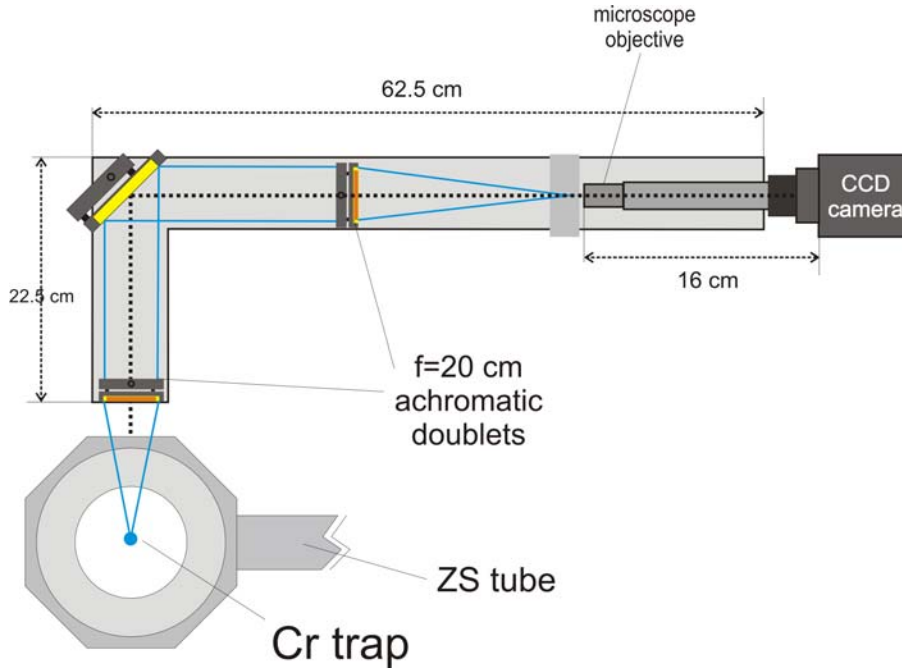
Figure 2.14: Absorption imaging system.

cloud is falling under gravity (for a 20 ms TOF for instance the cloud falls by 2 mm). In order to bypass the off-axis abberations, the whole absorption imaging system is mounted on a rigid L-shaped aluminium platform which can be translated vertically by a computer-controlled translation stage (not used in this thesis).

An additional ×4 magnification system was conceived for in-situ imaging of small (∼ few 10 μm) atomic clouds, such as a BEC. It is made of a commercial microscope objective – model $XSZ - H - OP4$ from $Nachet$, with a 0.1 numerical aperture. In this configuration the main limitation comes from the abberations introduced by the intermediate doublets of the telescope, but we estimate that they are only slightly above the diffraction limit.

The photomultiplier is placed above the experimental chamber, at 30 cm from the position of the MOT. The fluorescence of the atoms is collected with a $1 \div 1$ imaging lens (2.4 cm diameter and 7.5 cm focal length). We performed a calibration of the conversion factor of the PM (33 mV/nW in our case), which allows a quantitative evaluation of the number of trapped atoms. The PM was mostly used in the first stage of our experiment, when the absorption imaging system was not yet available – see Chapter(3-4).

2.6 The control system

The time-sequences of our experiment are computer-controlled. We use a 64-output digital card (Viewpoint Systems DIO-64) and an 8-output analogical card (National Instruments PCI 6713), both controlled by a specially-dedicated computer.

Figure 2.15: Labview control sequence.

In most cold atom and BEC experiments the cycling time is rather long (up to a few minutes), and the number of different 'events' is relatively low; on the other hand a good timing accuracy is necessary. The DIO-64 card we use is well adapted for controlling such experiments, because it requires for the user to indicate only the time instants when changes of the outputs are intended (a different and more common way of addressing would be to continuously send the data, at a constant rate, to the card, even if no change of the outputs is intended). In this way the amount of data sent to the card is significantly reduced, and can be first loaded into the buffer of the DIO-64 card before an external trigger marks the beginning of the sequence. The DIO-64 digital card can thus have a time resolution of 100 ns.

Besides providing different trigger signals for the experiment, the digital card also

serves as master for the analogical card, assuring the synchronization between the analogical and digital control data. A Labview sequence drives the two cards and provides a user-friendly interface which is shown in fig.(2.15).

For protecting the card, most of its outputs are sent to the experiment through optocouplor circuits. Their use increases the output switching time up to 1 μs; however this time still remains short enough for our applications.

2.7   Image acquisition and analysis

The control of our CCD camera, as well as the image acquisition are performed by a second Labview program, running on a separate computer; this choice was made so that the image acquisition and treatment does not affect the performances of the computer controlling the experimental time-sequences. The image treatment is performed using the IGOR-pro (v.5) analysis software.

As it is usually done in absorption-imaging technique, three pictures of the imaging beam are taken ('A' – in presence of the cloud, for having the absorption of the atoms, 'B' – without the cloud, giving the laser beam 'reference' profile, and 'C' for having an image of the 'background' light). Labview performs the $\frac{A-C}{B-C}$ operation and the result – a 1392 × 1024 matrix – is automatically transferred to a IGOR analysis routine. The data transfer is possible using *ActiveX* controls ('Automation') of communication between two Windows programs (Labview and IGOR in our case).

IGOR Pro is a well-adapted software for image analysis and for implementing data-fitting procedures, all using a programmable interface. The procedure I wrote for our experiment, shown in fig.(2.16), allows to perform a real-time analysis of the absorption images.

Each image of the cloud is automatically sent to the Igor routine (as explained above), which displays it on the main window. Different types of analysis were programmed, according to the nature of the imaged cloud (i.e. magnetically- or optically-trapped). With a click of a button, one can for example make slices through the image and fit them, using different user-defined functions (for having the size and the peak density of the cloud) or integrate the image (for having the total absorption of the cloud and the number of atoms).
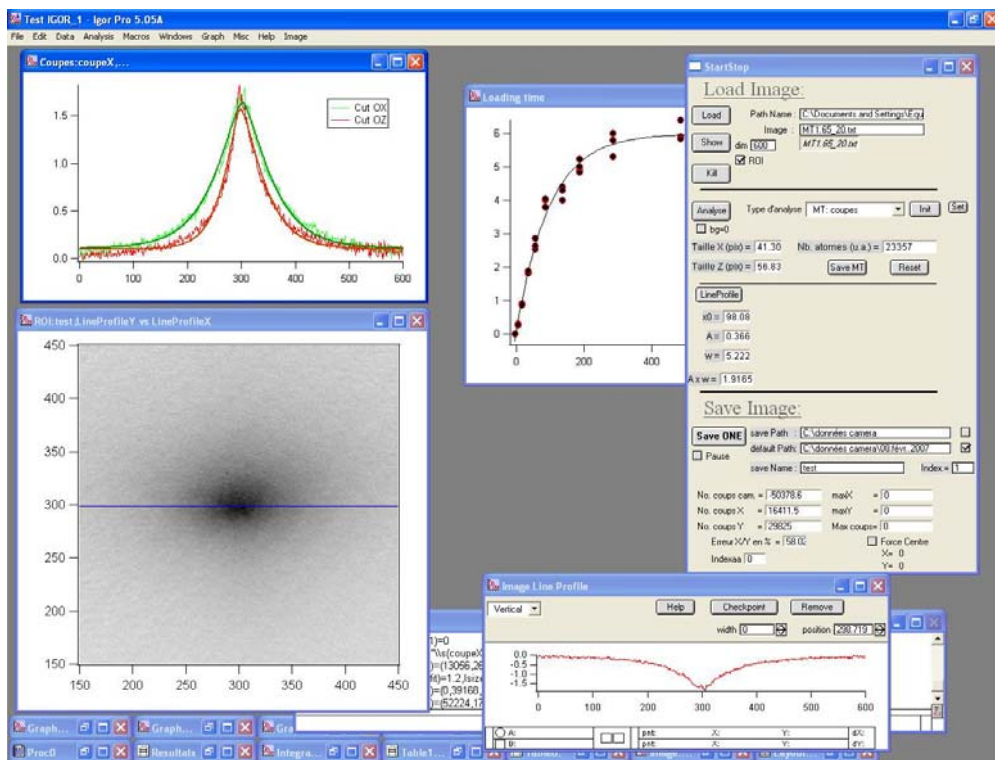
Figure 2.16: Igor interface for the real-time analysis of the images of the cloud.

Chapter 3

Magneto-optical trapping of fermionic and bosonic chromium isotopes

This chapter presents the realization and study of magneto-optical traps for the two main isotopes of chromium. We first present the results for bosonic isotope ^{52}Cr and then concentrate on the fermionic isotope ^{53}Cr. We also demonstrate the possibility of creating a double-isotope MOT.

3.1 Fluorescence imaging system

For the experiments presented in this chapter, we used two different tools to evaluate the properties of the trapped clouds, both presented in fig.(3.1). A $f = 12.5$ cm plano-convex lens is used to capture the fluorescence of the atoms and make a $2f - 2f$ (magnification -1) image of the cloud, at 50 cm. A 50/50 (experimentally 40/60) non-polarizing beam-splitter separates the fluorescence into two: one part is sent to a CCD camera, to evaluate the size of the atomic cloud, the other part is collected by a calibrated photomultiplier (PM) which records the power of the light scattered by the atoms.

The number of atoms N can be derived considering the scattering rate of one atom:

$$R_{scatt}(\Omega, \delta) = \frac{\Gamma}{2} \frac{\langle C^2 \rangle \frac{\Omega^2}{2}}{\langle C^2 \rangle \frac{\Omega^2}{2} + \frac{\Gamma^2}{4} + \delta^2}. \tag{3.1}$$

where Γ is the width of the excited state, δ is the detuning of the MOT laser beams and $\Omega = \Gamma\sqrt{I/2I_{sat}}$ is the Rabi frequency, which depends on the total intensity of the MOT beams. The $\langle C^2 \rangle$ coefficient is taken equal to the averaged squared Clebsch-Gordan coefficient over all the Zeeman sublevels of the ground state, for a given light

31
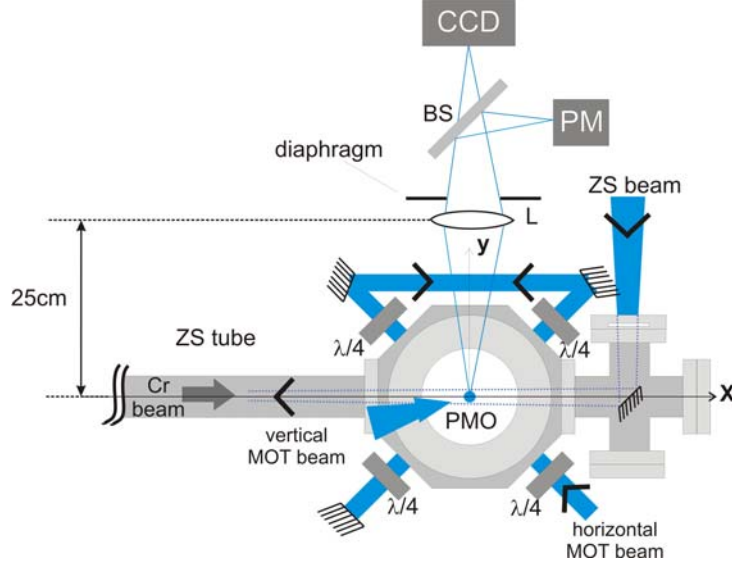
Figure 3.1: MOT fluorescence imaging system.

polarization[1]. For the boson $(J = 3) \rightarrow (J = 4)$ transition we have $\langle C^2 \rangle = 3/7$, while for the fermion $(F = 9/2) \rightarrow (F = 11/2)$ transition $\langle C^2 \rangle = 2/5$. Determining the Rabi frequency Ω requires a precise measurement of the laser intensity of all the MOT beams.

Using the measured scattering rate, the following equation relates the number of atoms in the MOT N to the light power recorded by the PM:

$$P_{PM} = T \cdot N \frac{\Phi}{4\pi} R_{scatt}(\Omega, \delta) \ \hbar\omega, \tag{3.2}$$

where ω is the photon frequency, Φ is the solid angle defined by the MOT and the aperture of the imaging lens and T is the transmission coefficient of the different optical elements (beam splitter, viewports, lens, etc.).

3.2 Magneto-optical trapping of ^{52}Cr atoms

3.2.1 Study of a ^{52}Cr MOT

A first achievement of this thesis was the magneto-optical trapping of bosonic ^{52}Cr atoms. Because ^{52}Cr has no hyperfine structure, a single frequency is sufficient to slow the atoms in the ZS and another to cool and trap atoms in the MOT.

---

[1] This formula assumes that the MOT atoms are evenly distributed in all the Zeeman sublevels; the $\langle C^2 \rangle$ values are the same for any light polarization ($\sigma^{\pm}$ or π).

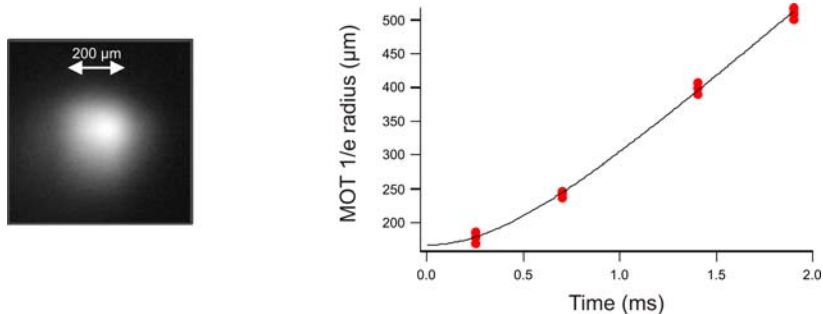Figure 3.2: Left: Fluorescence image of the ^{52}Cr MOT. Right: ballistic expansion of the cloud, when released from the MOT: 1/e radius w_{MOT} as a function of the expansion time. The fit to the data, using the function $w_{MOT}(t) = \sqrt{w_{MOT}^2(0) + \frac{k_B T_{MOT}}{m}}$, corresponds to a MOT temperature $T_{MOT} = 120 \ \mu$K.

MOT and ZS beam coupling

After the double-passed AOM (see fig.(2.6)), the horizontal and vertical MOT beams are separated, using a non-polarizing beam splitter. In order to increase the total 'useful' laser power, the four horizontal arms of the MOT are obtained using the same retro-reflected beam, as shown in fig.(3.1); the vertical beam is also retro-reflected. This procedure can be applied in our case, because of the small absorption of the light by the trapped cloud (due to the fairly small atom number possible in the Cr MOTs), which does not unbalance significantly the power in the horizontal MOT beams.

The size of the MOT beams is finally set using a pair of telescopes (one for the horizontal and the other for the vertical beams). Because of the beam trajectories, passing through a large number of optical elements (viewports, $\lambda/4$ plates, etc.), which results in non-negligible absorption, the MOT beams are made slightly convergent, such that the intensity after each passage is almost constant.

The size of the ZS beam is increased, after the double-pass through the corresponding AOM, using a 'telescope', which also focalizes it on the oven emission hole. In the case of the Zeeman slower beam we found that a convenient way to vary the beam size at the entrance of the ZS was to translate the retro-reflecting mirror of the ZS double-passed AOM.

Optimization

The optimization of the atom number in a MOT is usually a slow-converging process, because of the large number of the adjusting experimental parameters; we changed alternatively several parameters, such as the size and power of the MOT and ZS beams, the value of the magnetic field gradient, the ZS extraction velocity. Several optimization procedures were performed.

33

By varying the relative power of the MOT and ZS beams, as well as their sizes, we found that the optimal values correspond to ~ 30 mW for the MOT beams and ~ 22 mW for the ZS. The optimal mean $1/e^2$ radius of the MOT beams was about 7 mm, which corresponds to an intensity of ~ 19 mW/cm^2 per MOT beam. The $1/e^2$ radius of the converging ZS beam, when entering the ZS tube, is about 3 mm.
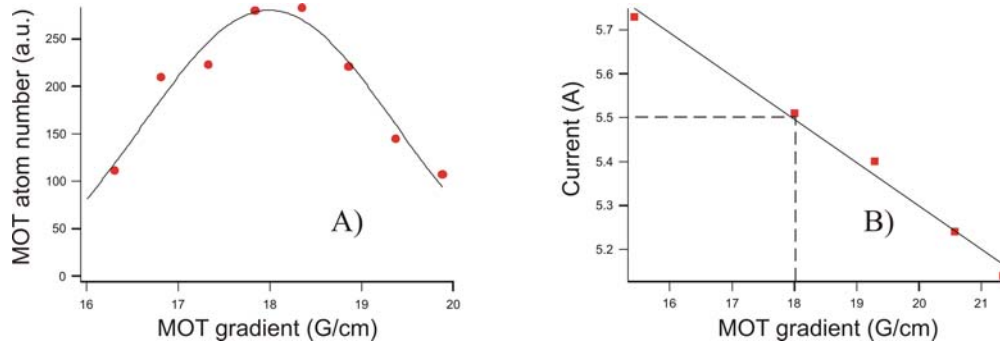

Figure 3.3: A): ^{52}Cr MOT atom number as a function of the magnetic field gradient. The optimal gradient value is 18 G/cm. B): Value of the current of the ZS extraction coil, obtained by optimizing the MOT atom number, as a function of the MOT gradient.

Additionally, we varied the final velocity of the Zeeman-slowed atoms, by changing the current in the extraction coil of the ZS. For each value of the current, we optimized the MOT number of atoms, by changing the MOT magnetic field gradient; the results are shown in fig.(3.3.A). We found that the optimum is obtained for a magnetic field gradient of 18 G/cm (along the axis of the coils), as shown in fig.(3.3), and an extraction velocity of ~ 40 m/s (corresponding to a 5.5 A current in the ZS extraction coil).

The optimal value of the MOT gradient and ZS final velocity appear almost constant, over the detuning ranges of the MOT beams that we studied[2]. We note that it is expected that the best loading rate of the MOT corresponds to a matching between the ZS final velocity and the capture velocity fixed by the size of our MOT beams.

Characteristics of the ^{52}Cr MOT

We studied the dependence of the number of atoms and of the MOT density by varying the MOT laser beams detuning. The results are shown in fig.(3.4).

We obtain a maximum number of 4×10^6 atoms for a detuning of -22 MHz and a total laser intensity of 116 mW/cm^2. The maximum central density of the cloud is 8×10^{10} atoms/cm^{-3}, and is reached for a detuning equal to -12 MHz. The loading

---

[2] Having larger laser powers available would permit to explore larger detunings. In this case, for keeping a constant MOT capture volume one would probably find that an increase in the gradient would be needed - see [37]

rate (measured in the experiments presented in the next sections) is $\Gamma_{load} = 3.7 \times 10^8$ atoms/s. Although we did not experimentally investigate what determines the dependance of the MOT atoms number on the detuning, we believe that the sudden decrease below -25 MHz may be explained by the decrease of the MOT capture velocity below the ZS extraction velocity.
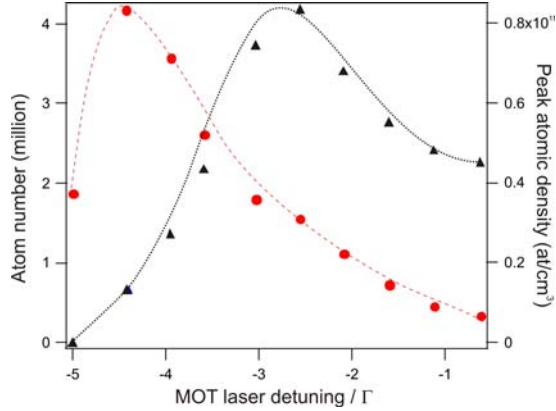
Figure 3.4: ^{52}Cr MOT atom number (circles) and peak atom density (triangles) as a function of the detuning of the MOT laser beams. The lines are guidelines for the eye.

The temperature of the MOT was measured by analyzing the free expansion of the atomic cloud released from the MOT. An evolution of the cloud radius is shown in fig.(3.2), and the results are typically around 120 ± 20 μK, close to the Doppler temperature (124 μK). The maximum phase space density obtained in the ^{52}Cr MOT is around 10^{-6}.

We mention that our results roughly reproduce those previously obtained in the groups of J.J.McClelland [30] and T.Pfau [29].

We also measured the MOT loading times, for different laser detunings, and found that they typically scale between 10 and 100ms. These are short timescales, compared for example to the alkali atoms; this point will be discussed in detail in the following section.

3.2.2 Loading dynamics of a Cr MOT

The ^{52}Cr MOT characteristics, presented in the previous section, are quite different from those of the alkali MOTs. Much smaller loading time scales are observed, and consequently the atom number which are obtained are also considerably reduced. In this subsection we will study the loading dynamics of the ^{52}Cr MOTs, in order to understand what are the main limitations.

The loading time of magneto-optical traps is known to be limited by two main factors. One is the one-body losses, which are density-independent processes, usually due to collisions with hot atoms from the background gas. The other is the two-body inelastic losses, which are density-dependent processes, due to collisions between the trapped atoms.

We will describe the loading dynamics of the MOT with the following equation[3]:

$$\frac{dN}{dt} = \Gamma_{load} - \frac{N}{\tau} - \frac{\beta}{\overline{V}}N^2 \tag{3.3}$$

where Γ_{load} is the loading term, τ is the one-body decay time constant. The last term is the two-body decay rate, characterized by the inelastic collision parameter β and the collision volume $\overline{V}$ (proportional to the MOT volume V_{MOT}; $\overline{V}$ generally depends on the shape of the density profile of the cloud, as shown later on). Analyzing the steady-state of equation (3.3), one finds:

$$N_\infty = \frac{\sqrt{1 + 4\tau^2 \Gamma_{load}\beta/\overline{V}} - 1}{2\tau\beta/\overline{V}}. \tag{3.4}$$

There are two extreme regimes for equation (3.3):

- *The exponential (low collision) loading regime*, when the last term of eq.(3.3) can be neglected. The required condition is that $\frac{N_\infty}{\tau} \gg \frac{\beta N_\infty^2}{\overline{V}}$, which can be reduced to: $2\Gamma_{load}\beta\tau^2 \ll \overline{V}$. In this case, there is a purely exponential loading of the MOT and the steady-state solution is $N_\infty = \Gamma_{load}\,\tau$. One sees that increasing by factor of 2 the loading term Γ_{load} results in an increase of 2 in N_∞. The 1/e characteristic loading time is $\tau_{1/e} = \tau$.

- *The collision regime*, when the second term in eq.(3.3) can be neglected. Then the loading is no longer exponential and the required condition for this regime reads: $2\Gamma_{load}\beta\tau^2 \gg \overline{V}$. The steady-state is $N_\infty = \sqrt{\frac{\Gamma_{load}\overline{V}}{\beta}}$. Increasing the loading term by 2 implies an increase by only a factor $\sqrt{2}$ in the steady-state MOT atom number. The 1/e characteristic loading time is $\tau_{1/e} = \alpha\frac{\overline{V}}{N_\infty\beta}$, and decreases, in this regime, with the final number of atoms (α is a numerical factor, $\simeq 0.7$).

Loading term

The loading term in eq.(3.3) is given by the fraction of the flux of Zeeman-slowed atoms having a velocity smaller than the capture velocity of the MOT and which arrive inside the MOT's capture region. A direct measurement of the loading term can be

---

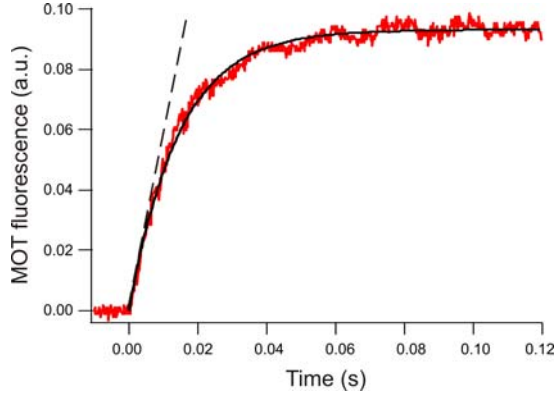[3] A justification of this expression is given in the following chapter.

Figure 3.5: Loading of the ^{52}Cr MOT. The cloud fluorescence, as recorded on the PM, is plotted as a function of time. A linear fit at short time, represented by the straight dashed line, gives the loading term $\Gamma_{load} = 3.7 \times 10^8$ atoms/s. The time-evolution can be well fitted (full line) by an exponential function (although we are in a regime where inelastic collisions cannot be neglected – see text), which gives the 1/e loading time $\tau_{1/e} = 15$ms

performed, whatever the collisional regime. It is simply given by the slope at the origin of the MOT loading curve. For the ^{52}Cr MOT we measured, under optimal conditions[4], a loading rate $\Gamma_{load} = 3.7 \times 10^8$ atoms/s at an oven temperature of $1500°$C (see fig.(3.5)).

A detailed study on the oven temperature dependence of the MOT loading rate, as well as a comparison with the fermion case will be presented below.

One body losses

The Cr MOTs are characterized by very fast loading times, scaling from a few 10 ms to ~ 100 ms. The presence of leaks towards the metastable states can partly explain these short time scales. It has been previously measured [31] that the total decay rate of atoms in $^7P_4$ state towards the ^{5}D states is $\gamma_{5_D} = (\gamma_{5_{D_4}} + \gamma_{5_{D_3}}) = 170$ s^{-1} (where $\gamma_{5_{D_{3(4)}}}$ are the decay rates towards the ^{5}D$_{3(4)}$ state). The corresponding loss term is proportional to the number of atoms which are in the excited state.

The one body decay rate in eq.(3.3) can then be expressed as:

$$\frac{1}{\tau} = \Pi_{7_{P_4}}\gamma_{5_D} + \gamma_{res} \ , \tag{3.5}$$

where $\Pi_{7_{P_4}}$ is the excited state fraction and γ_{res} is the residual loss rate, related to background gas collisions (in our case, especially with hot atoms from the Cr beam). $\Pi_{7_{P_4}}$ depends on the MOT laser intensity and detuning. Since the decay rate to the metastable states is much smaller than the one towards the ground state (3.10^7 s^{-1})

---

[4] Including a 2D transverse cooling in the oven chamber, presented in detail in the next section.

the excited fraction is[5]:

$$\Pi_{7_{P_4}} = \frac{\langle C^2 \rangle \frac{\Omega^2}{4}}{\langle C^2 \rangle \frac{\Omega^2}{2} + \frac{\Gamma^2}{4} + \delta^2} \ . \tag{3.6}$$

Two body losses

Our experimental observations show that the loading dynamics of our ^{52}Cr MOT cannot be interpreted using only the one body decay term in eq.(3.3). The MOT characteristic $1/e$ loading times (given by exponential fits – see fig.(3.5)) for different loading curves, corresponding to different detunings and intensities, are always shorter than the ones predicted by the time constant given by eq.(3.5). Moreover, the residual collision time constant $\gamma_{res}^{-1} = 8$ s (independently measured – see Chapter(5)) is much larger than the observed loading times.

On the other hand one can almost entirely block the one body loss channels towards the metastables by using two 'red' repumpers at 654 and 663 mn. They practically close the cooling transitions, by repumping the atoms 'lost' to the metastable states back into the MOT cycle. In absence of other limiting factors, this is expected to increase the MOT steady state number by a factor $1+(\gamma_{5_D}/\gamma_{res})$, which in our case corresponds to a gain of more than 10^3. In practice we observe that adding the repumpers increases N_∞ only by a factor of about two.

This indicates that inelastic processes are a second limiting factor. At our MOT densities, they appear to be on the same order of magnitude as the one body losses. We can make a rough estimate of the loss parameter β, by comparing the stationary solutions of eq.(3.3), in presence (when two-body losses totaly dominate) and in absence (when both types of losses are present) of the 'red' repumpers. For a peak density of 10^{11} at./cm^3 and for an excited state fraction of $\sim 1/2$ we find that $\beta \sim 8.10^{-10}$ cm^3 s^{-1}.

A precise measurement of inelastic collision parameters, presented in the next chapter, confirms this rough estimate. This value represents an *extremely high inelastic collision parameter* in a MOT and is about 2 orders of magnitude larger than for the alkali MOTs.

We finally present in fig.(3.6) a numerical comparison of the results of eq.(3.3), which shows the role of inelastic collision in limiting the number of atoms in a Cr MOT. The full and dashed curves reproduce the loading of a Cr MOT, using the typical measured loading and loss rates. For the full curve, we take into account both the leaks towards the metastable states and the inelastic collisions while for the dashed one we neglect the losses to the metastable states. For the dotted curve, the inelastic loss parameter is reduced by a factor of 50, which roughly reproduces the loss parameters of the alkalis.

---

[5] $\Pi_{7_{P_4}}$ is related to the mean scattering rate of the MOT atoms R_{scatt}, given in eq.(3.1), by: $R_{scatt} = \Gamma \cdot \Pi_{7_{P_4}}$.
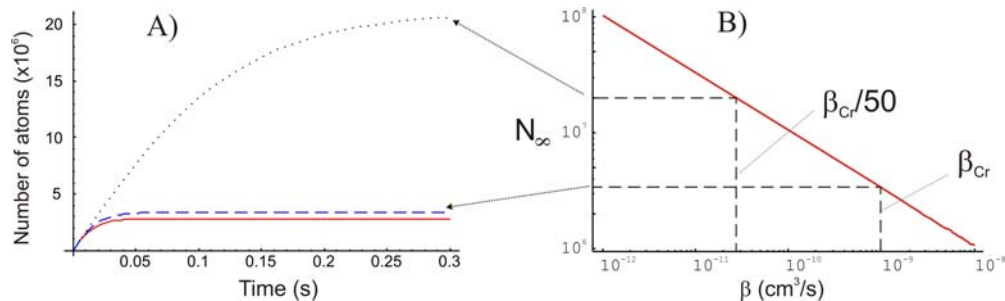
Figure 3.6: A) MOT loading in different regimes. The full-line curve is a simulation of the 'real' Cr MOT loading curve, where both the leaks to the metastable states and inelastic collisions are present. The dashed curve is the *'collision regime'* for Cr, where leaks towards the metastable states are removed. The dotted curve is a hypothetical situation, where leaks towards the metastable are suppressed and the inelastic collision parameter was reduced by a factor of fifty (which is analogous to the one measured in alkalis). B) MOT steady-state number of atoms, given by eq.(3.4), as a function of the β parameter (log-log scale), when $\gamma_{5D} = 0$. The dotted lines correspond respectively to the dashed and dotted curve in A).

These curves show that inelastic collisions not only reduce the loading time constant of a Cr MOT, but also dramatically limit the steady-state number of atoms that can be trapped.

Conclusions

The previous considerations show that, despite the necessity of using a high-temperature effusion cell, we are able to obtain reasonably good slowed atom fluxes; however the fairly small atom numbers obtained in the ^{52}Cr MOTs are severely limited by the high light-assisted inelastic collision rates.

Finally, in order to emphasize the originality of a Cr magneto-optical trap, let us compare some of the relevant characteristic timescales. One is the loading time, fixed by the one body losses to the metastable states and the inelastic collisions, and is as low as a few 10 ms. We independently measured, in experiments presented in the next chapter (fig.(4.2)) a second timescale: it is the 'trapping time' (i.e. the time needed to form a MOT from a large magnetically trapped sample) of our Cr MOTs, which is on the time scale of 2 to 20 ms. We see that these timescales are not very different, which means there is an interesting question one can raise, about how one can correctly describe the 'equilibrium' of a Cr MOT.

We finally note that the MOT cooling time, which is required for decelerating an atom from ~ 40 m/s down to the Doppler temperature, is on the order of 0.2 ms (at $a_{D,max}$). This is shorter than the two previous timescales, which means that temperatures as low as the Doppler temperature can indeed be reached, which we observe experimentally.

3.2.3 Density saturation

Our experimental observations show a saturation of the peak density of the cloud when increasing the number of atoms in the MOT.

For better understanding this phenomenon, we performed a systematic study and the results are shown in fig.(3.7). We notice a fast initial increase of the density, which begins to slow down when the atom number becomes larger than $\sim 10^6$; a full saturation is not observed and relatively high value of 1.1×10^{11} atomes/cm^3 is reached.
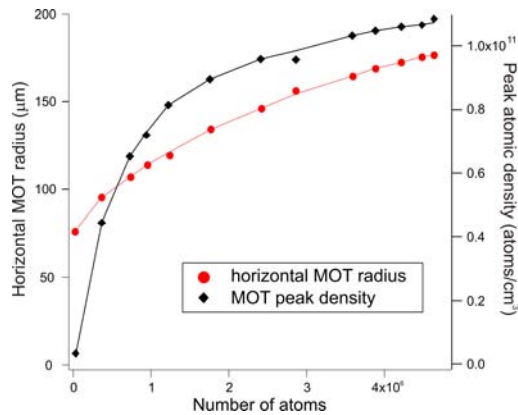
Figure 3.7: MOT radius and peak density versus the number of magneto-optically trapped atoms.

Changing the number of atoms in the MOT was achieved by varying the power of the Zeeman slower beam. Fluorescence pictures provided information about the size and number of atoms in the MOT. The cloud shape appears gaussian in both directions of the imaging plane, with an aspect ratio of ~ 2 (presumably due to a tighter confinement on the MOT coil axis). The experiment was performed for a fixed MOT beams total intensity of ~ 200 mW/cm^2 and for a detuning of -12 MHz. In order to extend the study to higher MOT atom numbers, both 'red' repumpers were permanently kept on.

We may consider two possible explanations for the MOT density saturation. One is due to multiple scattering of the light by an optically dense trapped cloud and has already been demonstrated for other atomic species (see for example [64]). The radiation spontaneously emitted by the excited trapped atoms may be reabsorbed by the neighboring atoms. This creates an overall repulsive force and consequently limits the peak density.

Another possibility we take into account, which is more specific to chromium, comes from the very high inelastic collision rate presented earlier. Indeed, the atoms which are close to the trap center, where the density is higher, have a higher probability of undergoing inelastic collisions compared to the atoms closer to the edge of the cloud.

The space-dependent density of the cloud produces a space-dependent loss rate which may change the size of the cloud and limit the density.

We will try in the following lines to evaluate the influence of inelastic collisions on the size and density of a Cr MOT. Our model uses the Fokker-Plank equation [40, 41] with two additional terms:

$$\frac{\partial n(\mathbf{r}, t)}{\partial t} = \nabla \cdot \left[\frac{1}{m\gamma_v} n(\mathbf{r}, t) \nabla U(\mathbf{r}) + D_{\mathbf{r}} \nabla n(\mathbf{r}, t) \right] + \Gamma_{load}(\mathbf{r}) - \beta n^2(\mathbf{r}, t). \qquad (3.7)$$

The additional terms are a loading term $\Gamma_{load}(\mathbf{r})$, and an inelastic collision term[6] $-\beta n^2(\mathbf{r}, t)$, depending quadratically on the density. The first term in the right-hand side is the divergence of the total current of particles. It is the sum of the drift current $-(1/m\gamma_p)n(\mathbf{r}, t)\nabla U(\mathbf{r})$, due to the MOT confining potential $U(\mathbf{r})$ – and of the diffusion current $-D_{\mathbf{r}}\nabla n(\mathbf{r}, t)$. In eq.(3.7) γ_v is the velocity-damping coefficient of the MOT and $D_{\mathbf{r}} = k_B T/m\gamma_v$ is the spatial diffusion constant.

In our simulations we consider the maximum value of the damping coefficient $\gamma_v \simeq \hbar k^2/2m = E_{rec}/\hbar$ [63], which is about $2\pi \times$ 20 kHz. The confining potential is $U(\mathbf{r}) = -\kappa r^2/2$, where κ is the MOT spring constant. We determined κ from the measured MOT temperature $T = 120~\mu$K and from the mean $1/e$ radius $\overline{w} = 60~\mu$m of the MOT at small atom number: $\kappa = 2k_B T/\overline{w}^2$. For simplicity of the numerical simulations, we consider a uniform spatial distribution, with a finite extent, of the loading term $\Gamma_{load}(\mathbf{r})$; integrating $\Gamma_{load}(\mathbf{r})$ over the whole space gives the total MOT loading rate, which is the experimental parameter we varied for obtaining fig.(3.7). In order to give an upper boundary for the effect of inelastic collisions, we consider a value $\beta = 10^{-9}$ cm^3/s.

Our simulations typically show an almost gaussian-shaped cloud, with a radius depending on the Γ_{load} parameter. Results are shown in fig.(3.8), where we compare the simulated cloud $1/e$ radius to the one determined experimentally. At small atom number, the initial size of the MOT is not affected by the inelastic collisions, and coincides (as expected) with the experimental value. When the atom number increases, the we observe that cloud radius increases; we checked that, for a β parameter one order of magnitude smaller, the cloud radius remains constant (in the values shown in fig.(3.8)). Finally, we notice that, when the atom number reaches 4.5×10^6, the inelastic collisions lead to an increase up to 40% of the cloud radius .

This value does not entirely explained the measured increase (of about 120%). We therefore think that multiple scattering is responsible for the major part of the density saturation. A simple model could take into account their role, adding a repulsive po-

---

[6] Integrating this term over $\mathbf{r}$ provides the last term in eq.(3.3) – as shown in the following chapter.
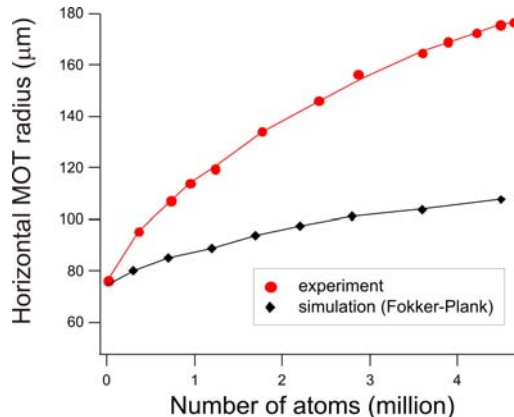
Figure 3.8: Effect of the inelastic collisions on the size of the MOT: the results of our simulations (diamonds) may explain up to 40% of the observed (circles) increase of the MOT radius.

tential (see below) to the MOT confining potential.

Very simple considerations can qualitatively give the space-dependance of the multiple scattering repulsive potential $U_{m.sc.}(r)$. Because of the presence of the trapping lasers, the atoms scatter photons, which can be subsequently reabsorbed by their neighbors. The repulsion force between two atoms, separated by a distance r, is proportional to the intensity of the scattered light, which is proportional to r^{-2}. Multiple scattering gives thus rise to a Coulomb-like, $1/r$ potential.

In the (very simplified) case of a spherical MOT, with uniform density distribution, we can thus apply the Gauss theorem[7] and find that the multiple scattering potential is proportional can be written as: $U_{m.sc.}(r) = \alpha_{sc.} r^2$ within the MOT volume. We see that $U_{m.sc.}(r)$ has the same space-dependence, but an opposite sign as the MOT confining (harmonic) potential: it leads to a reduction of the MOT spring constant, to an 'effective value': $\kappa_{eff} = \kappa - \alpha_{sc.}$.

The $\alpha_{sc.}$ coefficient is expected to depend on the density of the cloud. This means that, in reality, things are more complicated than in our simple model, for example in case of a non-uniform density distribution of a MOT. However, multiple scattering may cancel the confinement in the center of a MOT, which led to the observation, for other atoms, of 'uniform density' profiles [64, 65].

Finally, let us notice that the coefficient $\alpha_{sc.}$ is proportional to the probability of reabsorption of the scattered photons, i.e. to the absorption cross section σ_{abs}. It scales thus with the square of the wavelength: $\alpha_{sc.} \propto \lambda^2$. This scaling law qualitatively explains why, at densities comparable to those obtained for other atoms, with IR transitions (below 10^{11} atoms/cm^3 for Cs, with $\lambda = 852$ nm [65]), in our Cr MOTs

---

[7] Exactly as in the case of a uniform charge distribution

($\lambda = 425$ nm) uniform density distributions are not observed and saturation is not fully reached (see fig.(3.7)).

3.2.4 ^{52}Cr Zeeman slower

In this subsection I will address two issues: one is the possibility of having efficient optical pumping in the increasing B-field region, at the entrance of the ZS (ZS 'branching zone'), and the other is a method to enhance the flux of slowed atoms, by transverse-cooling the atomic beam.

Optical pumping in the ^{52}Cr ZS 'branching zone'

The hot ^{52}Cr atoms which leave the oven are evenly distributed in the different Zeeman sublevels of the $^7S_3$ ground state.

The Zeeman slower can only slow down the ^{52}Cr atoms which are in the $|m_J = +3\rangle$ state. This is explained in fig.(3.9), where we plotted (horizontal dotted lines) the magnetic field corresponding to the ZS resonance for the $|m_J = +3\rangle$ and the $|m_J = +2\rangle$ atoms, traveling at a given velocity – here, 300 m/s – , smaller than the ZS capture velocity.

In the 'slowing region' (II), the $m_J = +3$ atoms are resonant in the (b)-point; they start scattering photons from the ZS beam, and remain in the $|m_J = +3\rangle$ state all along the ZS profile. On the other hand, the $m_J = +2$ atoms, resonant in (b'), are optically pumped to $|m_J = +3\rangle$ state by the ZS σ^+ beam. They are however lost, despite arriving in this state, because they are not resonant any more with the ZS beam (because of the Doppler effect).
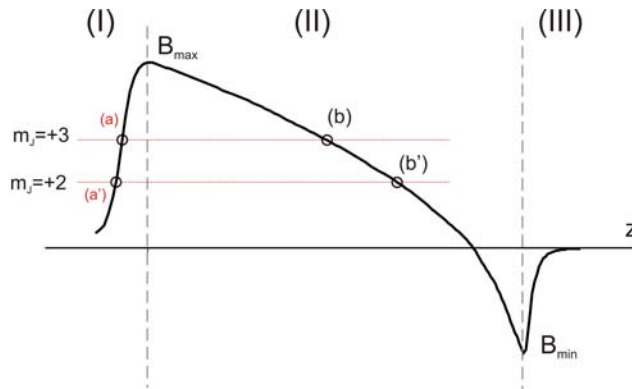

Figure 3.9: Resonances corresponding to the $m_J = +2$ and $m_J = +3$ atoms of the Cr beam, traveling at 460 m/s, in the ZS B-field profile.

In fig.(3.9) we see that there is however a first resonance for the $|m_J = +2\rangle$ atoms, in the ZS 'branching region'(I); in (a'), these atoms may be optically pumped to $|m_J =$

$+3\rangle$ by the ZS beam, and enter the 'slowing region' in the 'good' Zeeman state. We analyzed this possibility, by performing optical pumping simulations, which show that, for an estimated interaction time of $\sim 4~\mu s$ (which is realistic for our ZS B-field profile and capture velocity) all the atoms are expected to be efficiently pumped to the $|m_J = +3\rangle$ state in the ZS 'branching zone'.

We will come back to this point later, when we will address the question of optical pumping of the ^{53}Cr isotope in the 'branching zone'.

Transverse cooling of the ^{52}Cr atomic beam

To increase the flux of atoms that can be slowed down by the ZS and reach the MOT capture region, we implemented a transverse cooling scheme. The principle is schematically shown in fig.(3.10.A). One can see that the atoms that may be captured by the MOT are those traveling inside the solid angle defined by the oven aperture and the surface corresponding to the MOT capture volume. One might increase the corresponding atom flux, by cooling down the transverse velocity distribution after the oven collimation aperture. We note however that the real situation is more complicated than the one shown in fig.(3.10.A), because of the additional transverse heating during the Zeeman slowing process (discussed in Section(2.4)).
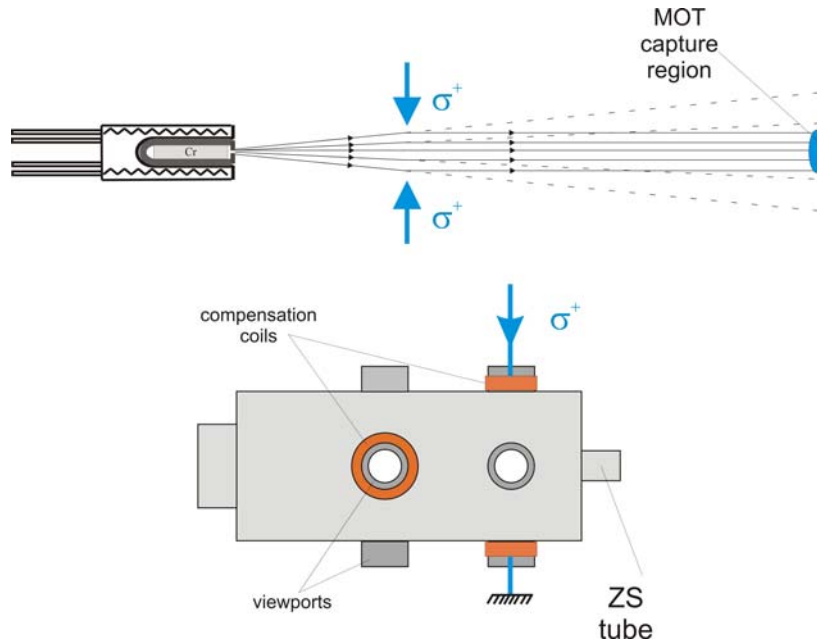

Figure 3.10: A) Principle of the beam transverse cooling. B) Experimental setup for the transverse cooling scheme.

For the transverse cooling we use a small fraction of the MOT laser light (~ 10

mW), directed towards the oven and sent perpendicularly to the atomic beam; the light is than retro-reflected, as shown in fig.(3.10). The aspect ratio of the beam was changed using a $\times 5$ cylindrical telescope, in order to better match the shape of the atomic beam, and increase thus the interaction length up to 2 cm, which corresponds to $\sim 40\mu$s interaction time for atoms traveling at the ZS capture velocity (~ 460 m/s).

We also superimposed, in the interaction zone, a magnetic field to tune the atomic levels and change the detuning of the transverse cooling light, independently of the MOT detuning. A pair of 'compensation coils' (with a diameter of 5 cm, separated by 26 cm and each having 800 turns, made of 0.5 mm diameter copper wire) can produce an adjustable magnetic field at the atomic beam location, roughly between 0 and 6G. An additional water-cooling circuit had to be used in order to limit the heating due to these coils (~ 15 W).

We performed two optimization experiments of the 1D transverse cooling and the results are shown in fig.(3.11). First we studied the influence of the transverse magnetic field. We found that the value of 5G optimizes the transverse cooling, for a MOT detuning of -2.5 Γ [8]. We also studied the evolution of the MOT fluorescence as a function of the laser power in the transverse beam, at fixed MOT intensity (which was intentionally lowered to 17mW, in order to have about 20 mW of transverse power available to perform this experiment). We observe that saturation occurs at about 10 mW, corresponding to ~ 16 mW/cm^2.

In a later stage of the experiment (April 2007) we implemented the transverse cooling in the vertical direction. The light used for the first – horizontal – cooling stage was recycled and sent through the other set of view-ports shown in fig.(3.10). An additional set of 'compensation coils' was constructed.
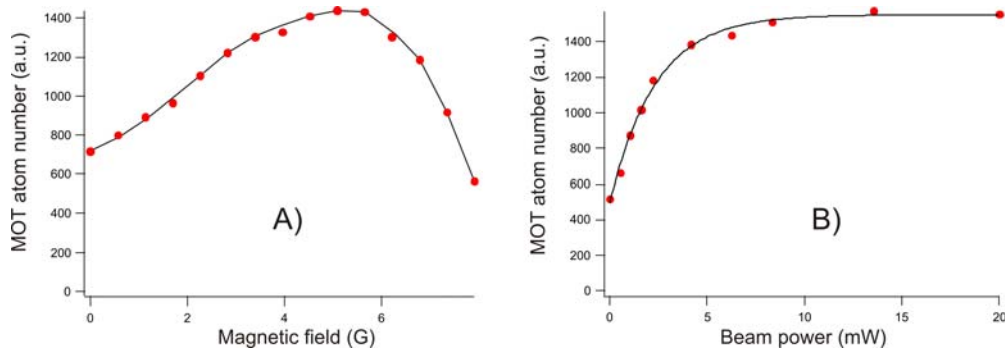
Figure 3.11: A) Number of atoms in the MOT (arbitrary units) as a function of the magnetic field used for compensating for the MOT beams detuning. The optimum is obtained for value of 5G. B) Saturation of the atom number in the MOT with the power of the transverse cooling beam.

---

[8] This value corresponds to an 'effective' detuning of the transverse cooling beams of $\sim -\Gamma$, with respect to the $|^7S_3, m_J = 3\rangle \rightarrow |^7P_4, m_J = 3\rangle$.

To evaluate the gain on the slowed atomic flux at the end of the ZS, we compared the MOT signal, with and without the transverse cooling, keeping the two red repumpers on. We thus substantially decrease the influence of one body losses (by blocking the leaks towards the metastable states) compared to the two body losses and forcing the system into the *'collision regime'* (defined earlier). The steady state atom number is: $N_\infty = \sqrt{\frac{\Gamma \overline{V}}{\beta}}$, and the slowed atom flux Γ is:

$$\Gamma \propto \beta N_\infty n_{0,\infty} \tag{3.8}$$

where $n_{0,\infty}$ is the steady-state MOT peak density. Using only the horizontal cooling stage gives a 2.7 gain in N_∞, while adding the second gives an overall 4.9 gain. By measuring the volume of the MOT, we also observed that $n_{0,\infty}$ increases less rapidly than N_∞ (by a factor 1.3, respectively 1.5, for the 1D/2D stage), which is explained by the saturation of the peak density mentioned earlier.

We finally conclude from eq.(3.8) that the 2D (1D – horizontal) transverse cooling increases the slowed atomic flux by a factor 7.4 (3.2). We then indirectly deduce a gain of 2.3 for the vertical cooling, which appears less effective than the horizontal one. This may be attributed to the fact that $\sim 65\%$ less power is available for the second (vertical) stage – due to light absorption of the atoms and of the optical elements – and to the fact that the beam shape is appreciably different, because of imperfect collimation.

In conclusion, using the two transverse cooling stages, we obtain a flux $\sim 3.7 \times 10^8$ (slowed) atoms/s which are captured in the MOT.

3.3   Magneto-optical trapping of ^{53}Cr atoms

Magneto-optical trapping of fermionic ^{53}Cr is not a straightforward extension of the work concerning ^{52}Cr. The main difference between the two isotopes is the additional, complex hyperfine structure of ^{53}Cr (see Chapter(1)), whose electronic ground and excited states have four hyperfine components. As a consequence, several repumpers are needed in a ^{53}Cr MOTs.

The fermionic ^{53}Cr isotope has already been cooled by collisions with a cold buffer gas in the group of Doyle [42]. Preliminary observations of a ^{53}Cr MOT were also made in the group of T. Pfau [31].

3.3.1 ^{53}Cr Zeeman slower

The ^{53}Cr atom flux is expected to be significantly smaller than the ^{52}Cr flux for two main reasons. First, the natural abundance is ~ 9 times smaller. Second, the hyperfine splitting of the ground state (~ 42 mK) is much smaller than the oven temperature

(1773 K). This means that the ^{53}Cr atoms in the oven are evenly distributed in all the 28 Zeeman sublevels of the ground state. In *absence of optical pumping*, only 1/28 of them are expected to be slowed down by the Zeeman slower, and the fermionic Zeeman-slowed flux will be a factor of ~ 250 smaller than the bosonic one.

In the following part we will address two issues concerning the fermionic ZS: the need of a repumper inside the ZS, and the possibility to have efficient optical pumping in the 'branching zone' of the Zeeman slower, as it was the case for the boson.

Need of a Zeeman slower repumper for ^{53}Cr

We carefully analyzed the fermionic transitions inside the Zeeman slower, looking for effects of slight polarization imperfections of the ZS beam. We found a 'bad crossing' taking place at a magnetic field B= 25.4 G. At this magnetic field value, two excited eigenstates, which are adiabatically connected to $|F' = 11/2, m_{F'} = +11/2\rangle$ and to $|F' = 9/2, m_{F'} = +7/2\rangle$ at B=0, become degenerate (see fig.(3.12).). This means that any σ^--polarized component in the ZS laser beam depumps the atoms towards the F= 7/2 ground state[9].

In our experiment we think that the ZS laser beam may not be perfectly σ^+ polarized, because the undervacuum aluminium mirror which reflects the ZS beam gets coated with chromium, and does no longer act as a perfect metallic mirror for the 425 nm light.
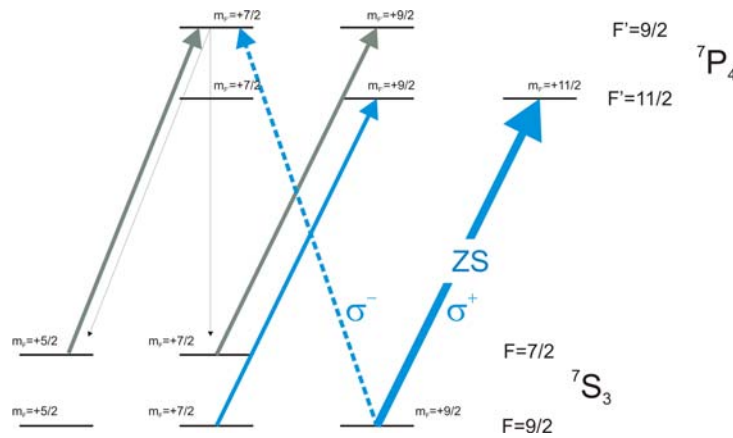
Figure 3.12: ^{53}Cr Zeeman slower repumping mechanism. The diagram corresponds to a value of 25 G of the magnetic field, where the $|F' = 11/2, m_{F'} = +11/2\rangle$ and $|F' = 9/2, m_{F'} = +7/2\rangle$ states are degenerate. A small σ^- component of the ZS (dashed arrow) can thus depump the atoms in $|F = 9/2, m_F = 9/2\rangle$ to the $|F = 7/2, m_F = 5/2\rangle$ and $|F = 7/2, m_F = 7/2\rangle$ states. The lost atoms can be repumped into the $|F = 9/2, m_F = 9/2\rangle$ state using a repumper beam (grey arrow).

---

[9] We remind the reader that only the ^{53}Cr atoms in the $|F = 9/2, m_F = +9/2\rangle$ can be slowed down by the ZS, as seen for the ^{52}Cr, in Section(3.2).

Atoms travel relatively slowly throughout the 'bad crossing' region, as B=25 G corresponds to a velocity of about 200 m/s (see eq.(2.7)). At this point the gradient of the ZS magnetic field is 11G/cm and we estimate the interaction time with the depumping light to 20 μs. Optical pumping calculations showed that about 50% of the atoms can be lost if 10% of the ZS power is σ^- polarized. This means that an additional laser, resonant at B=25 G with the transition between the states adiabatically connected to $|F = 7/2, m_F = 7/2\rangle$ – $|F' = 9/2, m_{F'} = 9/2\rangle$, needs to be used in order to pump back the atoms to $|F = 9/2, m_F = 9/2\rangle$. The frequency of the repumper needs to be about 300 MHz above the ^{53}Cr ZS frequency. In fact, this frequency nearly coincides with the ^{52}Cr ZS beam frequency, and no additional laser frequency has to be generated.

Optical pumping in the ZS 'branching zone'

In Section(3.2) we presented the bosonic Zeeman slower. We showed that only the atoms arriving in the 'slowing region' (II in fig.(2.12)) being in the right internal state $|J = 3, m_J = +3\rangle$ will eventually be slowed. Fortunately, optical pumping in the 'branching zone' is expected to efficiently bring all the ^{52}Cr beam atoms (having a velocity $\sim$ 460 m/s or less) to the $|J = 3, m_J = +3\rangle$ state. Let us focus now on the possibility of optical pumping in the 'branching zone', in the case of the fermion.

The approach is the following: we start from an initial population evenly distributed in the 28 Zeeman sublevels of the ground state. For a given velocity class (we chose here 460 m/s, which is the ZS capture velocity), we consider a series of resonances of the (σ^+−polarized) ZS beam, with the transitions connecting these levels to the 38 Zeeman sublevels of the $^7P_4$ excited state. These resonances occur in a certain order, in the increasing B-field profile of the ZS 'branching zone'. Using optical pumping calculations (based on rate equations), we estimate the populations of each of the Zeeman sublevels of the ground state, after each resonance, until reaching the maximum B-field value, which corresponds to the beginning of the ZS 'slowing zone'. Finally, we are interested by the number of atoms which are found in the $|F = 9/2, m_F = +9/2\rangle$ state, which may be slowed down by the ZS.

The situation is quite complicated, because of the non-linear Zeeman effect. Due to the small values of the hyperfine constant A and to the large g_F-factors (see Chapter(1)), the transition between the low-field and high-field-limit eigenstates takes place at relatively low values for the magnetic fields, for the $^7S_3$ state, and at even lower values for the $^7P_4$ state; the exact order of the ZS resonances is thus not straightforward to predict.

In fig.(3.13) we (try to) show the complexity of the problem, by first considering the transitions from the $^7S_3$ – F=9/2 manifold to the $^7P_4$ – F'=11/2 manifold, which
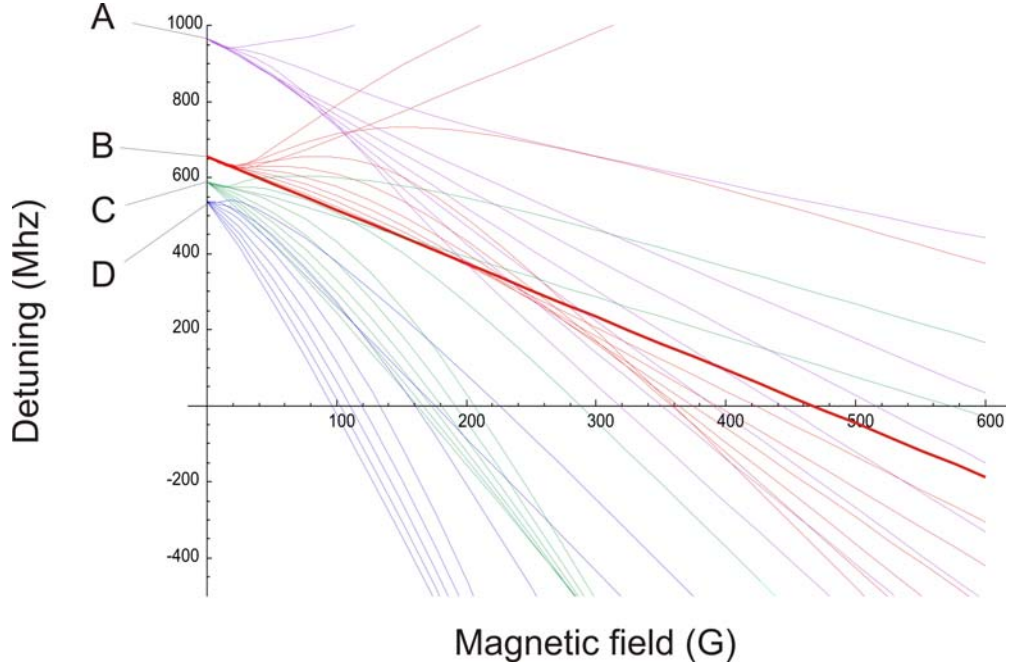
Figure 3.13: ^{53}Cr Zeeman transition diagram, for the 460 m/s velocity class: detuning vs. magnetic field in the ZS 'branching' zone. We represented the following ZS beam transitions: $|F = 7/2\rangle \rightarrow |F' = 9/2\rangle$ (A), $|F = 9/2\rangle \rightarrow |F' = 11/2\rangle$ (B), $|F = 9/2\rangle \rightarrow |F' = 9/2\rangle$ (C), $|F = 9/2\rangle \rightarrow |F' = 7/2\rangle$ (D). Intersections with the x-axis represent the magnetic field values for which different transition come in resonance. The thick line represents the ZS transition ($|F = 9/2, m_F = 9/2\rangle \rightarrow |F' = 11/2, m_{F'} = 11/2\rangle$)

may eventually increase the population of the $|F = 9/2, m_F = +9/2\rangle$ state (as they arrive in the 'good' order, i.e. for increasing m_Fs). However, there are other σ^+ transitions possible, for example from the $^7S_3$ – F=9/2 manifold to the $^7P_5$ – F'=9/2 manifold. Atoms in the $^7P_5$ – F'=9/2 manifold decay essentially to the $^7S_3$ – F=7/2 manifold (because of the stronger Clebsch-Gordan coefficients); these are rather 'bad' transitions, which empty the $^7S_3$ – F=9/2 manifold; we see that they occur for smaller B-field values, i.e. before the $^7S_3$ – F=9/2 to $^7P_4$ – F'=11/2 transitions.

One should also consider a small σ^- polarization component of the ZS beam, and additional transitions due to the ZS repumper (we recall that it has a σ^+ polarization, as the ZS beam, and it is detuned by 300 MHz).

One can see now that the problem of performing optical pumping calculations, taking into account 28 ground-state sublevels (evenly populated with $1/28 = 3.57\%$ of the total population at $t = 0$) connected to 38 excited-state levels is quite complex. The calculations are based on several assumptions, like the exact amount of σ^- component in the ZS beam and the interaction time for a certain longitudinal velocity class considered. Moreover, the use of rate equations is not valid in our case, where a narrow-frequency laser is used, and the adiabatic elimination of coherences is not justi-

fied. For all these reasons, we think that the results are rather qualitative; we however estimate that they give at least some hints about the optical pumping dynamics in the ZS 'branching zone'.
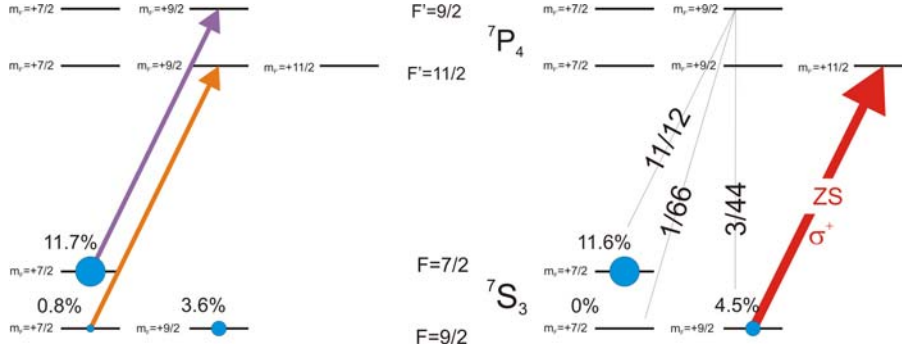
Figure 3.14: Population enhancement of the $|F = 9/2, m_F = 9/2\rangle$ level at the end of the 'branching' zone: only the small fraction in $|F = 9/2, m_F = 7/2\rangle$ is efficiently transferred by the laser beam to the desired state. The color code is the same as in fig.(3.13): violet is the ZS (σ^+) beam on the $F = 7/2 \rightarrow F' = 9/2$ transition and orange is also the ZS beam on the $F = 9/2 \rightarrow F' = 11/2$ transition.

We counted a total of 25 successive resonances[10] (some of them taking place at about the same value of the magnetic field). Most of these resonances do not affect the population of atoms in the $|F = 9/2, m_F = 9/2\rangle$ state. Only the last ones, occurring around $B = 445$ G, are likely to increase significantly its population. The situation before this resonance is shown in fig.(3.14). We observe that a relatively significant amount of atoms (about 12%) has been accumulated in the $|F = 7/2, m_F = 7/2\rangle$ state. Unfortunately, because of the small Clebsch-Gordan coefficients involved (see fig.(3.14.B)), these atoms are not efficient transferred into the desired state; we efficiently 'recuperate' only the atoms in the $|F = 9/2, m_F = 7/2\rangle$ state (which unfortunately are very few).

Our estimations show a final enhancement of only 25% of the $|F = 9/2, m_F = 9/2\rangle$ state (from 3.6% to 4.5%). This means that, unfortunately, the optical pumping in the ^{53}Cr ZS 'branching zone' is not expected to increase significantly the initial flux of atoms exiting the oven in the 'good' Zeeman state.

---

[10] For simplicity, we considered only transitions which affect the atoms in F=7/2 and F=9/2 hyperfine levels; it is less likely for the F=3/2 and F=5/2 to be pumped to the $|F = 9/2, m_F = 9/2\rangle$ state.

3.3.2 The ^{53}Cr MOT

The necessity of using MOT repumpers

Another consequence of the hyperfine structure is the necessity to use repumpers for the MOT.

The trapped atoms are cycling, due to the MOT lasers, between the $|^7S_3, F = 9/2\rangle$ and the $|^7P_4, F' = 11/2\rangle$ hyperfine states. This is a closed transition: once excited, atoms can only decay back to the $|^7S_3, F = 9/2\rangle$ state. On the other hand, due to the hyperfine structure of the excited state, every once in a while ground state atoms can be also excited, off-resonance, to $|^7P_4, F' = 9/2\rangle$ which is 66 MHz away from the $|^7P_4, F' = 11/2\rangle$ state. We estimate this excitation rate to be about 10000 s^{-1} for our typical MOT beam detunings and intensities. Once in $|^7P_4, F' = 9/2\rangle$ state, atoms will mainly decay to $|^7S_3, F = 7/2\rangle$. In this state the MOT laser detuning will be on the order of 300 MHz and the atoms, that no longer see the trapping light, are lost.

A similar process is possible for the off-resonance excitations to $|^7P_4, F' = 7/2\rangle$ followed by decays mainly to $|^7S_3, F = 5/2\rangle$. The corresponding loss rate is estimated to ~ 100 s^{-1}, much smaller, due to a larger detuning and smaller Clebsch-Gordan coefficients (mean squared value of 1/1260, compared to 1/36 for the transition to $|^7P_4, F' = 9/2\rangle$). Other losses may occur to the $|^7S_3, F = 3/2\rangle$, but with a probability expected to be much smaller (as such a process would imply at least two photons).

As in the case of other magneto-optically trapped atoms having a hyperfine structure (Rb, Cs,...) the solution is the use of MOT repumpers: the 'depumped' atoms are put back into the cycling transition, being re-captured by the MOT. Since there are three possible loss channels (excitation to F'=9/2, 7/2 and 5/2 and decay to F=7/2, 5/2 and 3/2) a total of three repumpers is needed.

We first decided to test the effect of first two MOT repumpers, one being detuned by -310 MHz ($R1$) and the other by -550 MHz ($R2$) with respect to the ^{53}Cr MOT transition. Here we take profit (once more, as in the case of the ZS repumper) of the quasi-coincidence of $R1$'s frequency with the ^{52}Cr MOT transition frequency and we consequently use the same laser beam. $R2$ is obtained with an additional AOM.

Realization of the ^{53}Cr MOT

The setup for obtaining the frequencies needed for the ^{53}Cr MOT and ZS beams and repumpers, using several AOMs, was presented in Section(2.3). For coupling the ^{53}Cr MOT beams, we chose to superimpose them on the ^{52}Cr MOT beams (which play the role of the R1 repumpers), by combining them on a non-polarizing beam splitter. The ^{53}Cr ZS beam was coupled into the ZS tube simultaneously with the ^{52}Cr ZS beam (i.e. ^{53}Cr ZS repumper) with a small angle between them.
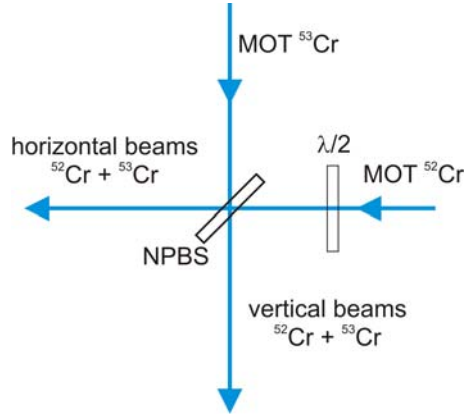
Figure 3.15: Coupling of the ^{53}Cr MOT and repumper (i.e. ^{52}Cr MOT) beams.

Experimentally we found that detection of a first ^{53}Cr MOT signal was somewhat complicated by the fact that the repumpers could still form by themselves a (small) ^{52}Cr MOT. The solution for isolating the ^{53}Cr MOT signal was to change the polarization of the ^{52}Cr MOT beams, using a $\lambda/2$ wave plate placed before the non-polarizing beam splitter which combined the MOT beams for the two species (see fig.(3.15)). This changes the ^{52}Cr MOT beam polarization to a 'anti-trapping' configuration, where the ^{52}Cr are expelled from the trap.

This procedure allowed us to isolate the ^{53}Cr MOT, and clearly demonstrate its realization.

Characteristics of the ^{53}Cr MOT

The optimization procedure of the ^{53}Cr MOT atom number, although slightly complicated by the need for using several repumpers, was similar to the one used for the ^{52}Cr MOT, presented in Section(2.3). We found roughly the same optimal values for the ZS final velocity and MOT gradient.

We performed systematic studies to measure the total number of atoms in the MOT, as a function of the cooling laser intensity and detuning, and the results are shown in fig.(3.16). The information about the number of atoms and the cloud size was obtained by fluorescence-imaging, using the analysis technique presented in Section(3.1).

The data were obtained for an average $1/e^2$ size of the MOT beams of 4.5 mm and for a total power of 24 mW; this corresponds to a total (six-beam) MOT intensity of 225 mW/cm^2. The ZS beam has a total power of 30 mW; it has a $1/e^2$ radius of 3.6 mm, when entering the ZS tube, and is focalized on the oven aperture.

The maximum number of atoms we obtained in a ^{53}Cr MOT was $(5\pm0.25\pm1)\times10^5$, for a detuning of -22 MHz (see fig.(3.16.A)). In fig.(3.16.B) we see that that the number of atoms saturates with the intensity, while the peak density does not saturate for the
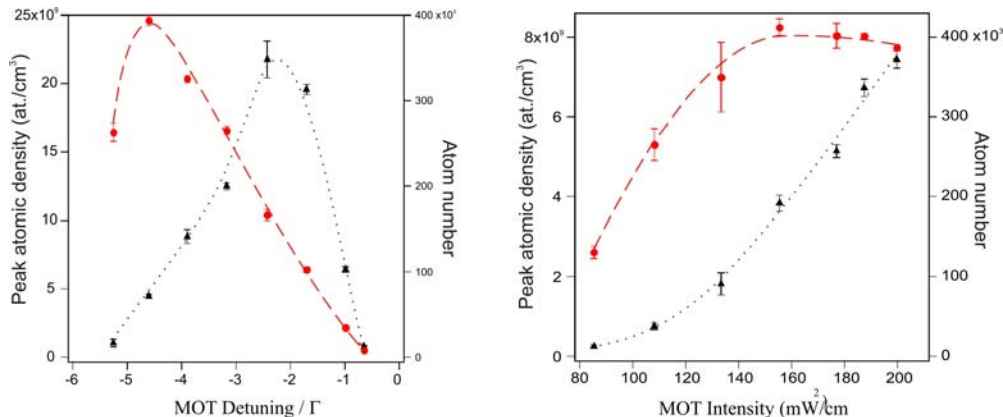
Figure 3.16: A) ^{53}Cr MOTatom number (dots) and peak atom density (triangles) as a function of the normalized detuning of the MOT beams, for a total laser intensity of 200 mW/cm^2 B)Atom number (dots) and peak atom density (triangles) as a function of the total power in the MOT cooling beams, for a detuning of -21.5 MHz.

laser power available. The highest peak atomic density obtained was up to 2.5×10^{10} atoms/cm^{-3} (with a systematic uncertainty of 30%, mostly due to the MOT beams intensity measurement).

Influence of the different repumpers

We studied the influence of the first two MOT repumpers on the trapped ^{53}Cr atom number. We found that the effect of the first repumper is crucial: no MOT could be obtained without $R1$. When the second repumper is removed the number of atoms in the MOT is only reduced by 30%. We inferred from this observation that repumping on the transition $|^7S_3, F = 3/2\rangle$ to $|^7P_4, F' = 5/2\rangle$ would not significantly increase the number of atoms in the MOT.

We also checked that the repumping effect of $R1$ and $R2$ saturates, at an intensity respectively of 13 mW/cm^2 and 7 mW/cm^2. This corresponds to a total power respectively of 10 mW ($1/e^2$ beam radius of 7 mm) for R1 and 3 mW ($1/e^2$ radius of 5.2 mm) for R2.

3.3.3 Oven temperature-dependence of the MOT loading rates

One of the questions which rose at the beginning of our experiment was related to the possibility of obtaining a sufficiently high flux of laser-slowed ^{53}Cr atoms. As shown previously, due to the smaller natural abundance and to the presence of hyperfine structure, the initial (i.e. at the beginning of the Zeeman slowing region) flux of fermions is expected to be about two orders of magnitude smaller than the bosonic one. The experimental realization of magneto-optical traps, for the bosons and for the fermions, allowed us to measure the corresponding MOT loading constants, as well as
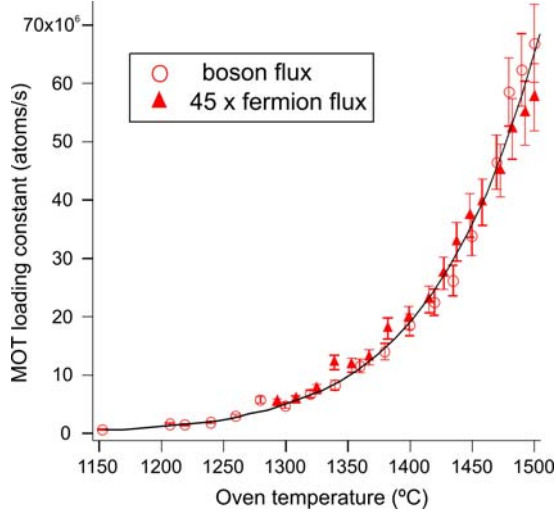
their dependence on the oven temperature (T_{oven}).

Figure 3.17: Dependence of ^{52}Cr and ^{53}Cr MOT loading constants on the oven temperature, deduced from the initial slopes of the MOT loading curves. The experiment series was performed in absence of any transverse cooling, in order to have a more appropriate comparison with the theoretical fluxes. The full line represents the theoretical flux, considering a 'real' temperature which is 150 K lower then the one indicated by the ovens' thermocouple.

For that, we recorded with a photomultiplier several MOT loading sequences, for different values of temperature measured by the oven's thermocouple $T_{th.}$. Fitting their initial slopes provides a direct measurement of the loading constant Γ_{load}. Fig.(3.17) shows the experimental results; we find a ratio of 45 between the boson and fermion loading constants (we remind that the initial theoretical ratio between the 'useful' oven fluxes was ~ 250, as explained above).

Even though the measurements were performed in absence of any transverse cooling, it is still difficult to interpret this difference. The MOT and Zeeman Slower beams have different sizes and the total laser power available in each case is different[11]. This is expected to change both the MOT capture velocities and the Zeeman Slowing performances. On the other hand the theoretical ratio is obtained using optical pumping calculations in the branching zone of the Zeeman Slower, which are particularly complicated in the case of the fermion.

Finally, we compared our experimental data with the 'theoretical' prediction of the oven flux $\Phi(T)$, obtained using the saturated vapor pressure given by the formula (2.1) – see Section(2.1). We observe that a reasonable agreement is obtained by considering a difference $\Delta T \sim 150 \pm 50$ K between the temperature measured by the thermocouple and the temperature T_{oven} of the 'emission source'.

_____

[11] For ^{53}Cr we have more laser power available, because no AOM is needed for obtaining the beam frequency.

A possible explanation may come from the fact that the temperature at the position of the thermocouple (i.e. at the bottom end of the W 'main crucible' – see fig.(2.2)) is somewhat higher than the temperature of the 'emission source' of the oven[12].

3.4 Accumulation of metastable Cr atoms in a magnetic trap

In the previous sections we showed that relatively small atom numbers can be obtained in Cr MOTs. Chromium nevertheless offers a nice way to decouple cooling an trapping. Indeed, atoms in Cr MOTs are slowly optically pumped into the long-lived metastable ^5D states, decoupled from the MOT light, and hence from light assisted collisions. Furthermore, the magnetic moment in the metastable states is large enough (up to $6\mu_B$) for the atoms to be trapped in the MOT magnetic field gradient, provided they are produced in a low-field-seeking state. This procedure was already demonstrated for ^{52}Cr [43] and allowed to raise the number of cold atoms by one order of magnitude, compared to the number of atoms in magneto-optical traps.

After giving some experimental results obtained for ^{53}Cr, we will demonstrate the possibility of extending the same continuous accumulation method to the case of the fermionic ^{53}Cr isotope.

3.4.1 Magnetic trapping of ^{52}Cr

The experimental procedure is the following: we start by forming a MOT during a few seconds, in absence of any repumping light, which leads to accumulation of atoms in the metastable states. At the end of the accumulation, the MOT beams are switched off. In order to be observed, the atoms accumulated in the ^5D states must first be repumped in the ground state, where their fluorescence can be recorded, either on the CCD camera or the PM, by briefly shining the MOT beams, tuned on resonance. The duration of this 'imaging' pulse is typically a few 100 μs (much smaller than the MOT formation time, of a few ms), in order to affect as little as possible the atoms and to obtain accurate information about the cloud size[13].

We observe that in the case of ^{52}Cr, the number of accumulated metastable atoms saturates in a time scale which is fixed mostly by the inelastic collisions, between the metastable atoms and with the MOT atoms in the excited state $^7P_4$ (as described in detail in Chapter(5). The typical time scale for this accumulation varies between 1.5 s and 8 s, depending on the MOT parameters. The upper time scale boundary (reached at large MOT detunings, when both the MT and MOT are not optimal) is fixed by

---

[12] However, we mention that the formula (2.1) could not be confirmed from several sources, other sources than [33].

[13] Since these first results, we implemented an absorption imaging system, described in Section(2.5).

collisions with hot atoms from the Cr oven beam (as discussed in the next section). As many as 4×10^7 ^{52}Cr atoms could be accumulated, at a temperature of roughly 100 μK.

3.4.2 Magnetic trapping of ^{53}Cr

The techniques we applied for ^{52}Cr were found to be also suitable in the case of ^{53}Cr.

The loading times we measured for the continuous accumulation of fermions in the metastable states are about 8 s when the oven is operated at 1500°C. This is longer than what was measured (in best operating conditions) in the case of ^{52}Cr. On the other hand, this timescale is equal to the measured lifetime of the metastable fermions in the magnetic trap when the atom shutter is not closed (when it is closed, the lifetime increases to 30 s). We conclude that in the case of ^{53}Cr the number of accumulated atoms is mainly limited by the collisions with fast atoms coming from the oven.

After the accumulation in the $^5D_4$ metastable state and a 10 ms repumping sequence, we measured up to $8.5 \ 10^5$ atoms remaining magnetically trapped in the $^7S_3$ state. This number was obtained for a detuning of the MOT beams equal to 12.5 MHz and a total intensity in the MOT beams equal to 200 mW/cm^2. This corresponds to an increase of almost a factor of 6.5 compared to the steady-state MOT atom number for these parameters.

This measurement was achieved close to resonance, and should probably not correspond to the optimal ^{53}Cr atom number accumulated in the metastable state. For technical reasons (related to the oven), we could not perform an elaborate optimization of the accumulation. In addition, such a number was measured using only one red repumper ($^5D_4 \rightarrow {}^7P_3$), and the use of another red repumper for the $^5D_3$ state should give us a reasonable starting point for further experiments.

3.5 Resonance frequency measurements and isotopic shift determination

The magnetic trapping of both Cr isotopes in the same apparatus made possible to make an accurate experimental determination of the resonance frequency of ^{52}Cr and ^{53}Cr MOT transitions, and of the isotopic shift.

Collisional shift in the hollow cathode

We first performed the spectroscopy of a magnetically trapped ^{52}Cr atom cloud. After accumulating the atoms in the metastable states and repumping them in the ground state, we briefly turned on the MOT lasers and recorded the atomic fluorescence, for

different values of the MOT AOM frequencies. A lorentzian fit of this spectrum permitted the precise determination of the resonance frequency of the ^{52}Cr MOT transition, which was found 146.5 MHz above the laser frequency.

The frequency of the laser is locked 150 MHz below the atomic resonance in the hollow cathode (see Section(2.3)). We observe thus that there is a 4.5 MHz difference between the two frequencies, which may be attributed to a collisional shift of the atomic resonance in the hollow cathode lamp.

'Isotopic shift'

A similar technique was used for finding the ^{53}Cr transition resonance frequency, and the results are shown in fig.(3.18). The slight dissymmetry of the lineshape comes from the fact that the Bragg angle of the ^{53}Cr MOT beam AOM depends on the RF frequency (it was optimized for a MOT detuning of -3Γ and the diffraction efficiency drops down as we approach the resonance). The fit shown in fig.(3.18) takes into account this frequency-dependence of the beam intensity. The zero value of the frequency axis (not shown) represents the ^{52}Cr MOT transition frequency.
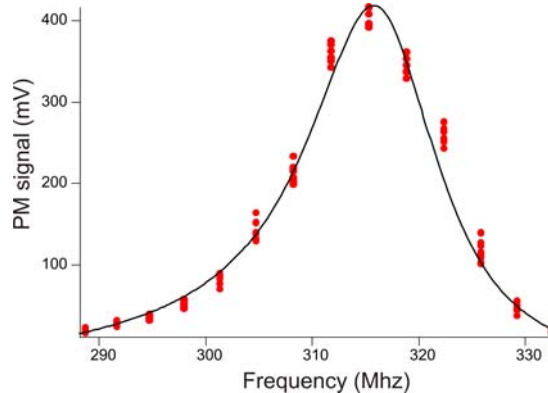
Figure 3.18: Measurement of the resonance of the ^{53}Cr MOT transition. The origin of the frequency axis corresponds to the ^{52}Cr MOT transition resonance. The solid line is a modified Lorenzian fit, which takes into account the dependence of the beam intensity on the AOM frequency.

From these measurements we can infer the value of the 'isotopic shift' – defined here as the frequency difference between the bosonic $(J = 3) \to (J = 4)$ and the fermionic $(F = 9/2) \to (F = 11/2)$ transitions; we obtain 316.5 ± 1 MHz.

The same (modified) Lorenzian fit indicates a FWHM of 15 MHz of the spectra. In order to interpret this value, we consider three broadening factors for the fluorescence spectrum. One is the power-broadening, on the scale of 8 MHz for a 200 mW/cm^2 total MOT beam intensity. The second comes from the linewidth of our 425 nm laser, of 2.5 MHz. The last one comes from the fact that the fluorescence of the cloud was recorded

57

in presence of the trapping magnetic field gradient. This leads to an additional Zeeman broadening of the transition, which we estimate on the order of 7 MHz (this value was obtained using the experimentally-determined shape of the cloud and the magnetic field profile).

These three factors are thus expected to lead to a *symmetrical* broadening of the fluorescence spectrum to a FWHM of 12 MHz, which seems in reasonable agreement to the observed 15 MHz widths, and should not affect significantly the results of our determination of the isotopic shift.

3.6 Magneto-optical trapping of a cold mixture of ^{52}Cr and ^{53}Cr atoms

In many experiments which study degenerate mixtures of two different atomic species [66, 67], or of two different isotopes [68, 69], the starting point is to create a MOT which traps simultaneously both species.

Because of the considerably smaller atom numbers available in the ^{53}Cr MOTs and magnetic traps, compared to ^{52}Cr, creating a cold mixture of the two isotopes seems an important point in reaching the degenerate regime for the fermion. Our experiment was indeed designed for cooling and trapping the two most abundant isotopes of Cr.

Double-isotope MOT for ^{52}Cr and ^{53}Cr atoms

We also realized the simultaneous magneto-optical trapping of ^{52}Cr and ^{53}Cr atoms. This experiment requires to generate many different frequencies simultaneously. However it is made simple by the fortuitous quasi-coincidence between two transitions: the cooling transition for ^{52}Cr and the 'R1' transition for ^{53}Cr (see Section(2.3)). As a consequence, the cooling beam for ^{52}Cr is used in the ^{53}Cr MOT as R1. Another consequence is that the ^{52}Cr ZS beam also plays the role of a repumper for the ^{53}Cr ZS.

Fig.(3.19) demonstrates the successive loading of a magneto-optical trap, first with ^{52}Cr atoms and then with ^{53}Cr atoms. The experiment consists in turning on first the ^{52}Cr MOT beams and, once the steady-state atom number for ^{52}Cr is reached, the ^{53}Cr MOT beams.

Despite our efforts of optimization, the atom numbers we are able to obtain in a two-isotope trap is severely reduced (up to a few 10^5), compared to the case of single-species MOTs. In fig.(3.19) we can also see that the number of ^{52}Cr atoms is the same, before and after the creation of the ^{53}Cr MOT; this proves that the reduction is not related to any bad influence of the ^{53}Cr MOT beams on the ^{52}Cr cloud. This point is discussed in the following paragraph.
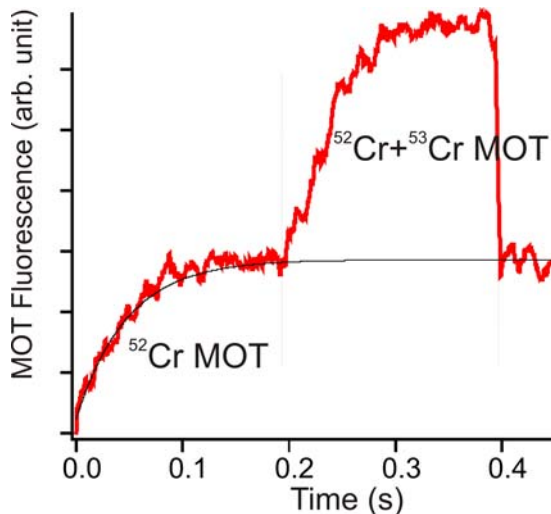
Figure 3.19: Loading of a double-isotope magneto-optical trap for ^{52}Cr and ^{53}Cr atoms; the steady-state atom numbers are $\sim 10^5$. The full line represents an exponential fit of the loading of the ^{52}Cr MOT; it shows that the steady-state number of ^{52}Cr atoms is not influenced by the presence of the ^{53}Cr MOT beams.

Influence of ^{53}Cr Zeeman slower beam on ^{52}Cr slowed atoms

There are several limitations to producing a magneto-optically trapped mixture of the two Cr isotopes with large number of atoms. One is related to the limited laser power available, which must be split between the two MOT and ZS beams. Having less power for the ZS means that saturation of the atomic transition throughout the slowing region will be less efficiently accomplished than in the single species case, which diminishes the slowed atom flux. On the other hand, lowering the power for the MOT results in a decrease of its capture velocity.

We encountered a second, more subtle problem. We observed that the simple presence of the ^{53}Cr Zeeman slower beam was sufficient to diminish the number of atoms in the ^{52}Cr MOT. This can be understood considering the resonance condition of the ^{53}Cr ZS beam, in the 'extraction region' of the ZS (see fig.(2.12)), with respect to the ^{52}Cr transition:

$$\delta_{ZS,53} = \frac{\mu_B B(z)}{h} + \frac{v_f}{\lambda} \, , \tag{3.9}$$

where $\delta_{ZS,53}$ is the detuning of the ^{53}Cr ZS beam with respect to the ^{52}Cr atomic resonance ($\delta_{ZS,53} = -150$ MHz).

The magnetic field $B(z)$ varies between $B_f = -260$ G and 0 G throughout the ZS 'extraction region', and v_f is the final velocity of the ^{52}Cr ZS, given by $\delta_{ZS,52} = \frac{\mu_B B_f}{h} + \frac{v_f}{\lambda}$. We observe that the ZS resonance condition (given by eq.(2.6)) is fulfilled

59

in z_0, where the magnetic field is:

$$B(z_0) = B_f + \frac{h}{\mu_B}(\delta_{ZS,53} - \delta_{ZS,52}) = -45.7 \text{ G.} \qquad (3.10)$$

This means that the slowed ^{52}Cr atoms will pass, with a small velocity (i.e. ZS final velocity v_f) of 40 m/s, on resonance with the ^{53}Cr ZS beam in the final part of the ZS and will partly be pushed back towards the oven before reaching the MOT trapping region.

Perspectives

This unwanted resonance limits the number of ^{52}Cr atoms in the double-species MOT, as well as the one in the metastable states (as they are loaded due to the spontaneous decay of the excited MOT atoms).

A perspective for increasing the ^{52}Cr number of atoms in the double-species MOT would be to bypass the influence of the ^{53}Cr ZS on the slowed ^{52}Cr atoms. This could be achieved by using an RF magnetic field, to flip the spin of the slowed ^{52}Cr atoms from $m_J = +3$ to $m_J = -3$ (for details, see Section(5.6)). This changes the sign of the first term in the right-hand-side of eq.(3.9), and the resonance condition is fulfilled for a positive value of the magnetic field (+45.7 G). This resonance would in fact never occur, considering the ZS profile shown in fig.(2.12).

A second possibility for avoiding the unwanted ZS resonance is to operate separately the two magneto-optical traps. This allows to sequentially accumulate large number of atoms, form both isotopes, in the metastable states. Preliminary observations of this method were made, and led to the measurement of the inter-isotope light-assisted collision parameter; the procedure is explained in the following chapter.

Conclusions and perspectives

In this chapter I presented the realization of magneto-optical traps conceived for trapping independently, or simultaneously, the two most abundant isotopes of Cr.

The results for ^{52}Cr – 4×10^6 ground-state atoms at $\sim 100 \ \mu$K in the MOT, and 4×10^7 atoms at roughly the same temperature, in metastable states, are the starting point for most experiments presented in the rest of this dissertation (Chapters(5-7)).

In the case of fermionic ^{53}Cr we found that the atom numbers are reduced (5×10^5 at $\sim 100 \ \mu$K) with respect to ^{52}Cr, mostly due to the smaller natural abundance and existence of a hyperfine structure.

We demonstrated the accumulation of ^{53}Cr in the metastable ^{5}D$_4$ as a possibility to increase the number of trapped atoms. This allowed to develop a method for studying

light-assisted inelastic collisions of ^{53}Cr, which will make the subject of the following chapter.

The achievement of a double-isotope MOT opens the way to many future studies: determination of the two-isotope collisional properties, both in the ground and metastable states, the search for inter-isotope Feshbach resonances and obtaining sympathetic cooling are some of the perspectives. Most importantly, it also opens the way to the potential realization of a quantum degenerate Bose-Fermi mixture involving dipolar species.

Chapter 4

Light-assisted inelastic collisions in Chromium MOTs

As mentioned in the previous chapter, the main factors limiting the number of atoms that can be obtained in Cr MOTs are the one body losses, related mainly to the leak towards the metastable states (which can be prevented by 'closing' the cooling transition with 'red' repumpers), and the two body losses. Usually, the two body losses in MOTs come from the light-assisted inelastic collisions, which involve one atom in the ground- and the other in the excited-state

The light-assisted collision parameters in Chromium are unusually large compared to those measured for other atomic species. They are also about two orders of magnitude larger than the corresponding inelastic collision parameters between two ground-state Cr atoms [59, 60, 61, 62, 58].

In this chapter I will first present in detail the experimental methods we used to measure the two body loss rate parameter in the fermionic ^{53}Cr MOTs. I will try to interpret the very large values we measured by making a qualitative comparison with other atomic species, for which the collision mechanisms are well understood. Finally I will present some theoretical considerations concerning our results, based on the 'Julienne-Vigué' model for light-assisted collisions in magneto-optical traps.

My hope is that these considerations will trigger further, more elaborate theoretical and experimental investigations of Cr MOT loss mechanisms.

4.1 Measurement of inelastic collision parameters of Cr

4.1.1 Inelastic collision parameters in a single-species Cr MOT

In the case of bosonic ^{52}Cr, the inelastic collision parameter β has already been measured, first in the NIST group [30] and then in Konstanz [31]. Their method consists in analyzing the non-exponential decay of the number of atoms from the MOT when the source (Zeeman slower) is suddenly switched off.

In our experiment we have a different and slightly more complicated approach in measuring the β coefficient. Our motivation stands from the fact that we are interested especially in investigating the characteristics of the fermionic ^{53}Cr isotope. This appears as a more difficult task because, as shown in the previous chapter, the number of MOT atoms and their density are smaller than those of ^{52}Cr. The idea is to benefit from the fact that higher atom numbers are available in the metastable states. By repumping them into the ground state (in absence of any blue light) and then turning back on the MOT lasers one can enhance the effect of light-assisted collisions on the atom number evolution.

The time evolution of the MOT fluorescence is recorded with a calibrated photomultiplier (PM) on an oscilloscope. In parallel, we also take fluorescence pictures on a CCD camera, via a $f = 12.5$cm lens, in order to obtain the time evolution of atomic cloud radius $w_x(t)$ and $w_z(t)$. The procedure is repeated for different MOT laser detunings, at an almost constant total intensity of 160 mW cm^{-2}. Fig.(4.1) shows a typical decay of the MOT fluorescence and fig.(4.2) presents time evolutions of the cloud volume.

The standard definition of the inelastic collision parameter β is via the equation:

$$\frac{dN(t)}{dt} = -\frac{N(t)}{\tau} - \beta \int n^2(\overrightarrow{r}, t) d^3 r \tag{4.1}$$

where N(t) is the number of atoms in the MOT, τ is the one body decay time constant (related to the decay towards metastable states, collisions with the hot atoms coming from the oven or from the background gas, etc.) and $n(\overrightarrow{r}, t)$ is the time-dependent MOT spatial density:

$$n(\overrightarrow{r}, t) = n_0(t) \exp\left[-\frac{2(x^2 + y^2)}{w_x^2(t)} - \frac{2z^2}{w_z^2(t)}\right] \tag{4.2}$$

Here we assume that the cloud has a 3D gaussian shape with rotational symmetry along the axis of the two MOT coils. Integrating $n(\overrightarrow{r}, t)$ in eq.(4.2) over $\overrightarrow{r}$ gives N(t):

$$N(t) \equiv n_0(t) \, V_{MOT}(t) = n_0(t) \, \left(\frac{\pi}{2}\right)^{3/2} \, w_x^2(t) \, w_z(t) \tag{4.3}$$
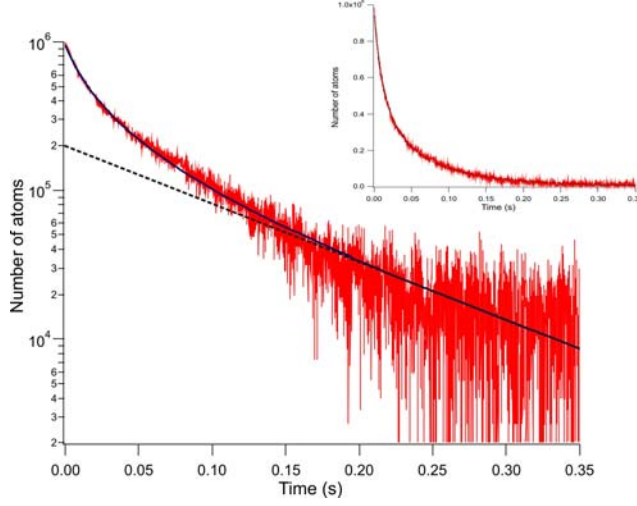
Figure 4.1: ^{53}Cr atom number decay in the experiment permitting to measure the light-assisted collision parameter β. The non-exponential character of the decay is easily seen in a semi-logarithmic scale. The continuous line is a fit of the data while the dotted line is a exponential fit of the final part of the curve, containing less than 3.10^4 atoms. The experimental curve is taken at a detuning of -6.5 MHz and at a total laser intensity of 160 mW cm^{-3}. *Insert*: normal linear scale, as seen on the screen of the oscilloscope.

From equation (4.2) we calculate the collision integral $\int n^2(\overrightarrow{r}, t)d^3r$:

$$\int n^2(\overrightarrow{r}, t)d^3r = n_0^2(t) \left(\frac{\pi}{4}\right)^{3/2} w_x^2(t) \; w_z(t) = \frac{N^2(t)}{2^{3/2}V_{MOT}(t)} \tag{4.4}$$

and equation (4.1) becomes:

$$\frac{dN(t)}{dt} = -\frac{N(t)}{\tau} - \beta \; \frac{N^2(t)}{V_{coll}(t)} \tag{4.5}$$

where $V_{coll} \equiv 2^{3/2} \; V_{MOT}$. The solution of eq.(4.5) can be written as:

$$N(t) = \frac{N_0 \cdot \exp(-t/\tau)}{1 + N_0\beta \int\limits_0^t \frac{\exp(-t'/\tau)}{V_{coll}(t')}dt'} \tag{4.6}$$

In the NIST experiment [30], the authors verify the fact that the volume of the MOT remains almost constant and the time dependence of n($\overrightarrow{r}$,t) comes only from N(t)[1]. In our experiment, the initial size of the cloud – that of the MT – is larger than the typical size of a MOT (the MOT confinement being stronger than that of the magnetic potential). We observe a relatively fast reduction in size, in a timescale between $\sim$ 10 ms and up to 100 ms for larger laser detunings.

---

[1]In this case the integration of (4.6) becomes straightforward and one obtains:

$N(t) = \frac{N_0 e^{-t/\tau}}{1 + \beta\tau\frac{N_0}{V_{coll}}(1 - e^{-t/\tau})}$
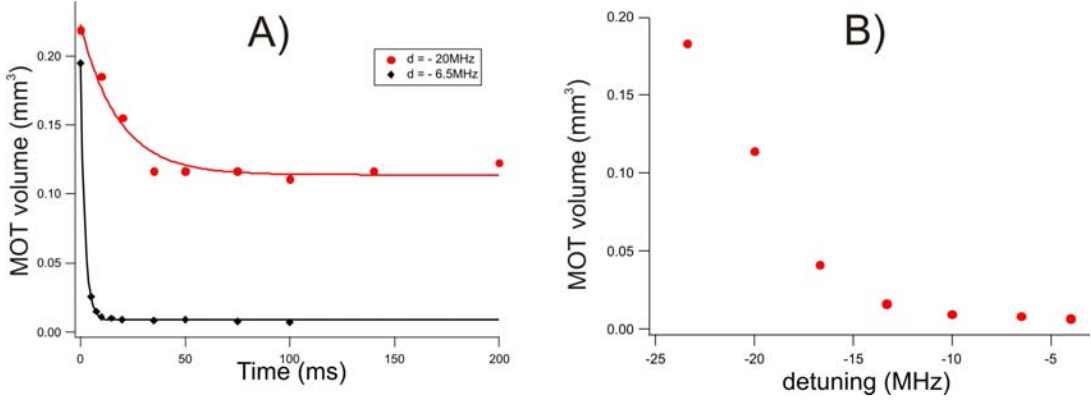
Figure 4.2: A) Evolution of the volume of the atomic sample during the compression of the magnetic trap into a MOT, at two different laser detunings. The solid lines are fits using $V_0 (1 + a \exp(-\gamma t))$; the time constants τ are 20 ms for $\delta = -20$ MHz and 3ms for $\delta = -6.5$MHz B) MOT final volume as a function of the detuning.

The integral in (4.6) depends on the exact time evolution found for $V_{coll}(t)$. Even though an interpolation of $V_{coll}(t)$ followed by numerical integration is always possible, this is quite complicated for fitting $N(t)$. In practice, we can fit $V_{coll}(t)$ by the empirical function $V_0 (1 + a \exp(-\gamma t))$ which agrees reasonably well with the data in Fig (4.2). Under these conditions the result of (4.6) is analytical and can be further used to fit the experimental data.

To study the inelastic losses, we fit the observed decay of $N(t)$ using τ and β as free parameters. We start either only at a time long enough for the cloud to have reached its final size or include the complete recorded time evolution of the volume. The second approach gives more significant corrections on the fitting parameter β at large laser detunings, for which the volume evolution is slower.

Figure 4.3: One-body decay rate $\gamma = 1/\tau$ as a function of the fraction of atoms in the excited state.

Figure (4.3) shows the inverse of the first fit parameter – the one body decay rate $(\tau)^{-1}$ – as a function of the fraction of atoms which are in the excited state Π_{ee}, deduced from eq.(3.5). Between the possible one body loss mechanisms mentioned earlier, only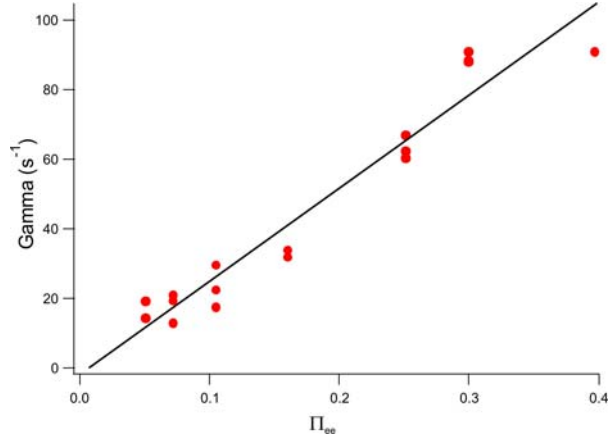 the spontaneous decay towards the metastable states depends on the excited fraction of MOT atoms: $\gamma = \sigma_{ee} \cdot \gamma_{PD}$. The linear fit in fig.(4.3) shows that this indeed the dominant mechanism and allows us to infer the value $\gamma_{PD} = 280$ s^{-1}, which is, to our knowledge, the first determination of the *total* loss rate of the ^{53}Cr towards the metastastable states. We estimate that this value has a 30% relative uncertainty, mainly of statistical origin.

The dependence of the other fit parameter β as a function of the MOT laser detuning is shown in fig.(4.4). This study shows that, in the case of fermionic ^{53}Cr the two body loss rate coefficient is, as in the case of ^{52}Cr, unusually large, and scales typically in the $(2 \pm 0.2 \pm 0.3) \times 10^{-9}$ to $(7 \pm 0.8 \pm 2.5) \times 10^{-9}$ cm^3 s^{-1} range.
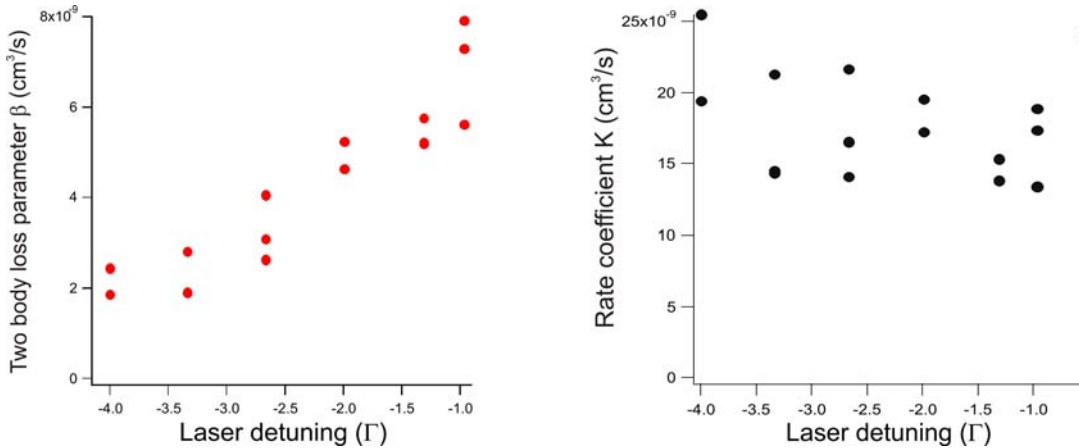
Figure 4.4: Two body loss rate coefficient β (A) and rate coefficient K (B) as a function of the laser detuning (normalized to the transition natural linewidth Γ).

As a validation of our method, we also measured the inelastic loss parameter of ^{52}Cr. We find a value of $(6.25 \pm 0.9 \pm 1.9) \times 10^{-10}$ cm^3 s^{-1} at a detuning of -10 MHz and a total laser intensity of 116 mW cm^{-2}, in good agreement with the values found in previous ^{52}Cr experiments [30, 31]. Our results thus indicate that the inelastic losses in ^{53}Cr MOTs are typically 10 times larger than in ^{52}Cr MOTs.

We also plot in fig.(4.4-B) the rate coefficient $K = \beta/(\Pi_{ee}\Pi_{gg})$. To a good approximation, K is constant over the range of detunings we studied. This indicates that the loss mechanism involves indeed one atom in the excited state and one atom in the ground state: in Cr MOTs, as in other atom MOTs, the two body loss term comes from light-assisted collisions.

4.1.2   Inelastic collision parameters in a double-species MOT

As we have shown previously, our experiment enables us to simultaneously magneto-optically trap the two main isotopes of Cr. This gives also the opportunity to investigate the interspecies light-assisted collisions. The experimental problem is, here again, the limited number of atoms and the low densities – both for ^{52}Cr and ^{53}Cr – available in the steady-state mixed MOT.

The strategy we chose is again to accumulate (in $\sim 10\,\text{s}$) a large number of metastable ^{53}Cr atoms in the quadrupole magnetic trap formed by the MOT coils. We then form a MOT of ^{52}Cr and, once the steady-state with 4×10^4 atoms is reached, we suddenly repump all the $^5D_4$ ^{53}Cr atoms in the ground state while turning on the ^{53}Cr MOT lasers for 20 ms. We thus superimpose a fairly large MOT of 7×10^5 atoms on the bosonic MOT. The estimated peak density upon the fermionic cloud is about 4×10^{10} cm^{-3}.

The evolution of the fluorescence is recorded by a photomultiplier on an oscilloscope, the result being shown in fig.(4.5). We observe a substantial loss of ^{52}Cr atoms after the ^{53}Cr MOT is superimposed, at time t_1 on the bosonic MOT. This, along with the fact that the ^{53}Cr MOT light does not influence the ^{52}Cr MOT (as demonstrated earlier, in fig.(3.19)), is a proof that fermionic atoms provide a new loss channel for the bosonic MOT. After turning off the ^{53}Cr MOT lasers (at the time t_2) we observe that the number of ^{52}Cr MOT atoms increases back to the same steady-state value.

Additional information concerning the clouds sizes and positions, for quantitatively characterizing the collision parameter, is obtained through imaging the MOTs on a CCD camera (as discussed in the Section(2.2)).

In analogy with the eq.(4.1), we define the interisotope loss coefficient β_{BF} through the following rate equation:

$$\frac{dN_{52}}{dt} = \Gamma - \frac{N_{52}}{\tau} - \beta_{BF} \int n_{52}(\overrightarrow{r})n_{53}(\overrightarrow{r})d^3r, \qquad (4.7)$$

where Γ is the loading rate of the ^{52}Cr MOT, τ is the depumping time constant towards the metastable states, and $n_{52}(\overrightarrow{r})$ and $n_{53}(\overrightarrow{r})$ are the densities of the two clouds. In eq.(4.7) we neglected any light-assisted collisions of the bosons amongst them, because of their reduced density.

We can rewrite these densities as $n_i(\overrightarrow{r}) = n_{i,0}\, f_i(\overrightarrow{r})$, where i is either 52 or 53, $n_{i,0}$ are the peak densities and $f_i(\overrightarrow{r})$ are Gaussians describing the measured cloud shapes. In these case, the overlap integral in eq.(4.7) can be expressed in function of N_{52} and a certain average fermionic density at the bosonic MOT position $\overline{n}_{53} = N_{53}/\overline{V}_{52-53}$. This
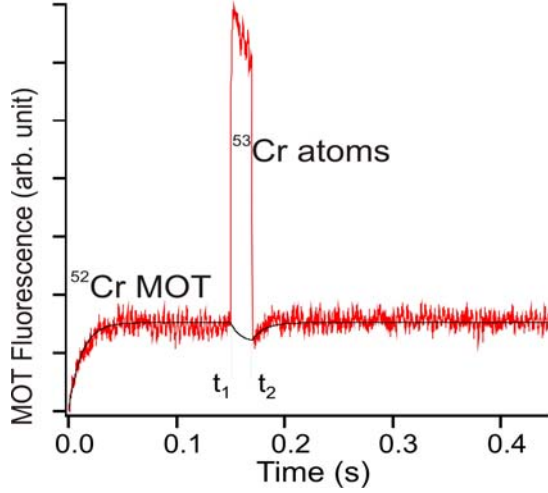
Figure 4.5: Evolution of the fluorescence recorded by the PM. For times $t < 0$ (not shown): a large number of ^{53}Cr atoms were loaded in the metastable states. At $t = 0$ the ^{53}Cr MOT lasers are turned off, while turning on the ^{52}Cr MOT. At $t = t_1$ the ^{53}Cr atoms are repumped in the ground state and the ^{53}Cr MOT lasers are turned back on, until $t = t_2$. We observe then a loss of ^{52}Cr atoms with respect to the steady-state, which we interpret as light-assisted collisions between atoms of the two isotopes. Since the Zeeman slower for ^{52}Cr has been kept on all along, starting from t_2 we observe a second loading of the ^{52}Cr MOT to the same steady-state as for $t < t_1$. The black line represents the corresponding fit of the ^{52}Cr fluorescence evolution (see text).

average density is obtained dividing N_{53} by the interisotopic collision volume defined as: $\overline{V}_{52-53} = \frac{\int f_{52}(r)d^3r \int f_{53}(r)d^3r}{\int f_{52}(r)f_{53}(r)d^3r}$.

With the previous notations, eq.(4.7) can be presented in the form:

$$\frac{dN_{52}}{dt} = \Gamma - \left(\frac{1}{\tau} + \beta_{BF}\overline{n}_{53}\right) N_{52}. \qquad (4.8)$$

which clearly shows that, from the bosonic atoms perspective, the presence of fermions corresponds to an additional linear loss rate, equal to $\beta_{BF}\overline{n}_{53}$.

Experimentally we found that the MOT density distributions $f_i(\overrightarrow{r})$ are well fitted by Gaussians. We measured the $1/e$ horizontal and vertical radii of the two MOTs ($w_{H52} = 110\ \mu$m, $w_{H53} = 150\ \mu$m, $w_{V52} = 110\ \mu$m, $w_{V53} = 150\ \mu$m) and a small cloud center separation ($\Delta z = 60\ \mu$m, along the vertical axis), which allows us to evaluate $\overline{V}_{52-53}$. We also checked that the $\Delta t = t_2 - t_1 = 20$ ms time is sufficient for the ^{53}Cr MOT to reach its steady-state volume (which takes ~ 6 ms).

For analyzing the evolution of the ^{52}Cr atom number, shown in fig.(4.5), we proceed as follows. We first fit the time evolution for $t < t_1$, where there is no influence of the light-assisted collisions with the fermions and, deduce the parameters Γ and τ. We then adjusted β_{BF} to reproduce the reduction of ^{52}Cr atoms when the ^{53}Cr MOT is removed at $t = t_2$. From this analysis (similar to the one performed for a K-Rb MOT in [53]), we estimated the light assisted inelastic loss coefficient between ^{52}Cr and ^{53}Cr

to be $\beta_{BF} = (1.8 \pm 0.45 \pm 0.65) \times 10^{-9}$ cm^3 s^{-1}. For this determination, the ^{52}Cr (^{53}Cr) MOT beams had a total intensity of 70(200) mW cm^{-2} and were red-detuned from resonance by 10(12.5) MHz respectively.

4.2 General considerations

4.2.1 Loss mechanisms in light assisted collisions

As mentioned before, the two body losses in MOTs are usually dominated by light assisted collisions. This is the case of our Cr MOTs, and I will give here some physical insight about the mechanism of these kind of collisions.

Molecular potentials of two colliding atoms The physics of the light-assisted collisions between two neutral atoms is governed by the molecular potentials which adiabatically connect to the dissociation limit of the two separated atoms, one being in the ground and the other in an excited state. At large internuclear separations, the interaction between the two neutral atoms is dominated by the electrostatic dipole-dipole interaction:

$$V(\overrightarrow{R_A}, \overrightarrow{R_B}) = \frac{e^2}{4\pi\varepsilon_0} \cdot \frac{\left(\overrightarrow{R_A} \cdot \overrightarrow{R_B} - 3(\overrightarrow{R_A} \cdot \overrightarrow{n})(\overrightarrow{R_B} \cdot \overrightarrow{n})\right)}{\left|\overrightarrow{R_A} - \overrightarrow{R_B}\right|^3}, \tag{4.9}$$

$\overrightarrow{R_A}$ and $\overrightarrow{R_A}$ being the center of mass positions of the two atoms and $\overrightarrow{n}$ – the unitary vector along the direction defined by the two atoms. This interaction potential can be treated as a perturbation of the two-separated atom hamiltonian and I will only consider the leading term C_n/R^n of its development in R.

- *Two atoms of the same species in the ground state*: $|A: {}^7S_3; B: {}^7S_3\rangle$

  In this case both atoms have no dipole moment and the interaction diagonal matrix element equals zero at first order in perturbation theory. At second order, there is interaction between the fluctuations of the dipole of the atom A (or B) and the dipole it induces in B (or A). This gives rise to a Van der Waals potential which varies as C_6/R^6 (dipole- induced dipole interaction). Furthermore, since the two atoms are both in their ground state, the C_6 coefficient is negative and the interaction is always attractive.

- *One atom in the ground–, the other in an excited state*: $|A: {}^7S_3; B: {}^7P_4\rangle$

  The un-perturbed state $|A: {}^7S_3; B: {}^7P_4\rangle$ is degenerated with the $|A: {}^7P_4; B: {}^7S_3\rangle$ state, while a P-state atom possesses a non-zero dipole moment. The dipolar energy is non-zero at first order perturbation theory and the interaction energy

varies as C_3/R^3 (resonant dipole-induced dipole interaction). The value of the C_3 coefficient is state-dependent and proportional to the square of the atomic dipole [54, 55, 56, 57]: $C_3 \propto \frac{|d|^2}{4\pi\varepsilon_0} = \frac{3}{4}\hbar\Gamma(\frac{\lambda}{2\pi})^3$. The maximum absolute value is $|C_{3,max}| = 2 \cdot \frac{|d|^2}{4\pi\varepsilon_0}$.

- *Two atoms of different species (^{52}Cr and ^{53}Cr)*

  Let's consider one atom in the ground- and the other in the excited state. In this case the interaction is non-resonant, because the $|^{52}Cr,\ ^7S_3;\ ^{53}Cr,\ ^7P_4\rangle$ and $|^{52}Cr,\ ^7P_4;\ ^{53}Cr,\ ^7S_3\rangle$ non-perturbed states are not degenerate. The second order perturbation theory indicates that the interaction varies once more as C_6/R^6. The sign of the C_6 coefficient depends on the energy difference between the considered free-atom asymptotes[2]. This proves that the $|^{52}Cr\ ^7S_3;\ ^{53}Cr\ ^7P_4\rangle$ state gives rise to a repulsive potential (positive C_6), while the $|^{52}Cr\ ^7P_4;\ ^{53}Cr\ ^7S_3\rangle$ state corresponds to a attractive potential (negative C_6).

In the following sections I will only focus on the case of light assisted collisions of a single-species MOT.

Scenario

The reference [58] – 'Julienne et Vigué (JV) model' – presents the suitable way to describe the cold collisions between ground- and excited-state atoms in a MOT. The authors present the mechanism of such collisions by considering three characteristic zones with different physical implications: the *outer*, *intermediate* and *inner* zones.

An atom pair is excited to an attractive excited molecular potential at large interatomic distances, in the *outer zone*. The atoms are thus 'prepared' for the collision by optical pumping due to the MOT laser light. The excitation is more or less localized, depending on the MOT detuning (see fig.(4.6)-B)), because of the $1/R^3$ space-dependence of the excited state energy.

The *intermediate zone* corresponds to the acceleration of the two atoms towards each other, due to the attractive character of the excited potential. This zone extends typically from a characteristic distance $R_\nu \sim \lambda/2\pi$ of separation with the first zone[3] to the short-range distances (a few Bohr radii a_0). Finally, the arrival of the excited pair to the *third zone* may lead to the loss of the pair, through various molecular mechanisms.

---

[2] I am assuming that the sign is fixed by the leading term of the sum over all molecular states - i.e. the coupling to the state the closest in energy. In our case the large-distance energy difference between $|^{52}Cr,\ ^7S_3;\ ^{53}Cr,\ ^7P_4\rangle$ and $|^{52}Cr,\ ^7P_4;\ ^{52}Cr,\ ^7S_3\rangle$ is only 300MHz.

[3] The authors note that the boundary between the first two zones is by no means a sharp one, because of the relatively slow variation of the potential at large interatomic separations.
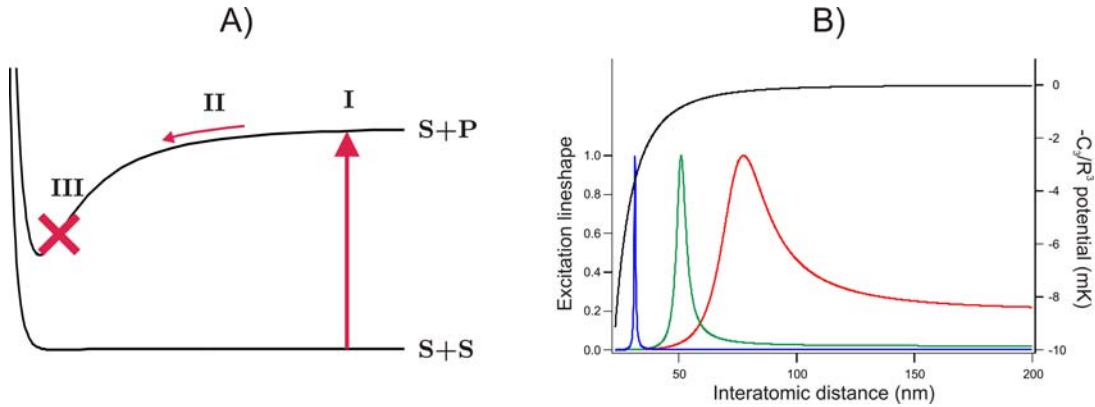
Figure 4.6: A) Light assisted collision mechanism. The long-distance excitation of the S+P attractive potential (outer zone I) is followed by the acceleration (intermediate zone II) and the short-range loss (inner zone III). B) Localization of the excitation for three different laser detunings: -1Γ (red), -4Γ (green), -15Γ (blue). The excitation probabilities are peaked at the Condon point $R_C = \left(\frac{C_3}{\hbar\delta}\right)^{1/3}$.

The approach introduced by Julienne and Vigué consists in taking into account the probability P_{exc} for a pair to be excited at long distance R by the MOT lasers, convoluted to the survival probability of the pair, in the excited state, up to a certain (small) distance R_0 and to the probability $P_{loss}(R_0)$ for the inelastic process to actually occur at R_0.

Different possible loss mechanisms

The previously-described model was initially applied to the alkalis, in the case of two possible loss mechanisms: fine structure changing collisions (FS) and radiative escape (RE), but it can be extended basically to any other loss process, like for example the Penning ionization in the case of metastable He [72].

In the case of FS, the two atoms are accelerated towards each-other until they reach the crossing region with a repulsive molecular potential of another fine-structure manifold. A non-adiabatic crossing can occur, resulting, at the end of the collision, in an extra kinetic energy, equal to the fine structure energy splitting. This kinetic energy is large enough ($\sim$ a few 100 K, for Cr) to expel both atoms from the MOT. The crossing usually occurs at very small interatomic distances $R_{FS} \sim (2C_3/\Delta E_{FS})^{1/3}$(a few a_0).

In the case of RE the atoms are accelerated on the attractive C_3/R^3 excited potential and may gain a velocity larger than the MOT escape velocity v_E (before spontaneous decaying to the ground state)[4]. Losses occur at interatomic distances $R_{RE} \sim (2C_3/mv_E^2)^{1/3}$ (few a_0).

---

[4] The escape velocity of a MOT is expected to be somewhat smaller than the capture velocity, since the escaping atoms have to travel only half the diameter of the beams.

The mechanism of the Penning ionization is the following: an electron, occupying the metastable state of one atom, 'jumps' and fills the hole in the core of the collision partner. The metastable electron of the latter becomes then unbound, while the first atom is ionized. This exchange process is a very efficient loss mechanism, as it occurs with a probability almost equal to 1, once the colliding atoms have reached a distance R_0 of $7a_0$ or less [72, 73].

Non-polarized collisions in a MOT

In the case of a MOT there are many excited molecular potentials populated by the laser beams. Optical pumping is generally very hard to be taken into account and the usual answer to the problem is to consider that the collisions are entirely non-polarized. This means that, in the case where a fairly large number of molecular potentials are involved, one considers that they all have the same excitation probability[5].

In order to interpret the experimental results of inelastic collision parameter measurements one considers then a statistical average over all the possible collision channels. For example, Julienne et Vigué showed that for alkalis there is only a small number of channels that actually lead to trap losses. The loss rate for these channels must then be weighted by the degeneracy factor (number of collision channels) of the excited state molecular potential. The 'effective' trap losses, which are measured experimentally, will thus be considerably reduced.

4.2.2   Temperature dependence

A) High-temperature limit

At high temperature a semiclassical treatment is used for finding the loss rate [58]. The thermal (kinetic) energies of the colliding atoms are large enough in this case so that spontaneous emission does not play an important role in the survival probability to small distances. The calculation takes into account a cutoff of the classical impact parameter due to the centrifugal repulsion in the excited state.

Finally the loss rate parameter is proportional to the Langevin capture rate coefficient:

$$\beta_L = 3\pi \frac{C_3^{2/3}}{\mu^{1/2}(2E)^{1/6}}. \tag{4.10}$$

times the probability P_{loss} for the loss to actually take place at short internuclear distances. In (4.10), $\mu = m/2$ is the reduced mass and $E = \hbar^2 k^2/2\mu$ is the kinetic collision energy (k is the de Broglie wavenumber). In a thermal average, the loss rate is obtained

---

[5] except when symmetry selection rules need to be taken into account, since they can null this excitation channel.

by replacing E by the thermal energy $k_B T$.

If we simply apply this formula in the case of a MOT, the temperature, in the low saturation limit and at large detunings ($\delta \gg \Gamma$), is mainly fixed by the laser detuning: $E \sim k_B T \sim \hbar \delta$ [6]. Under these circumstances, the Langevin capture rate becomes equal to the flux of particles through a sphere of radius equal to the Condon radius $R_C = (C_3/\hbar\delta)^{1/3}$ (i.e. the typical distance where resonance with the MOT lasers occurs[7]).

B) Low-temperature limit

The previous expressions are not expected to give the correct description of the light-assisted losses in the cold collision regime, i.e. for the low temperatures of a MOT. The difference comes from the fact that spontaneous emission starts to play an important role and may lead to a severe reduction of the inelastic collision rates with respect to the high temperature behavior (Langevin rate).

Indeed in this regime the thermal velocities are as low as 0.1 m/s= 1 Å/ns, (typical Doppler velocity) and the colliding atoms should only approach each other by a few Å within one atomic excited state lifetime. Spontaneous emission then reduces significantly the probability for the excited pair to reach short interatomic distances where losses are expected to take place.

4.3 Considerations about Chromium

4.3.1 The case of Chromium

At this point I would like to stress out two striking differences between light-assisted collisions in Cr and in other atomic species.

- The first is the fact that in the case of the magneto-optically trapped alkali atoms the measured inelastic loss parameters are two to three orders of magnitude smaller than in the case of Cr.

- The second is the fact that the inelastic loss parameters that we measured (see fig.(4.4) are only slightly different from the high-temperature (Langevin) capture

---

[6] $T = T_D(1 + 2I/I_{sat} + (2\delta/\Gamma)^2)(\Gamma/2\delta)$, where T_D is the Doppler temperature: see, for example [63]

[7] The meaning of the R_C distance is rather qualitative for the small detunings of a MOT; because of the smooth variation of the C_3/R^3 potential, the excitation is (de)localized over a fairly large zone.

rate, which corresponds to the maximal theoretical light-assisted loss rate. Indeed, applying equation (4.10) in the case of chromium at $\sim 100~\mu$K (as in our MOTs), we obtain[8] the value $\beta_L = 1.57 \times 10^{-8}$ cm^3 s^{-1}. This value is remarkably close to the values of the inelastic loss parameter β and rate coefficient K we measured for Cr (see fig.(4.4)).

We note that, in the case of the alkalis, this is not the case: JV showed that the low-temperature loss rates are expected to be about two orders of magnitude smaller than the corresponding high-temperature (Langevin) rate.

4.3.2 Qualitative comparison with other atoms

In the case of the alkalis, for which the main inelastic loss parameters are related to FS and RE, the measured loss parameters are about two orders of magnitude smaller than those of chromium. This is explained mainly by their simple electronic structure. JV shows that the FS mechanism is dominant (except for Li, where it is forbidden) and can only occur through one channel: either the 0_u^+ or 2_u (and both in the case of Rb). Finally the strong reduction comes from the *relatively low excitation probability* of these channels.

A special case where a high inelastic loss parameter $\beta \sim 4.5 \times 10^{-10}$ cm^3 s^{-1} has been measured [71] is strontium. The explanation is the following: *there are only four excited molecular potentials* for Sr that connect to the $|^1S_0,^1P_1\rangle$ dissociation limit. Only two of them are attractive at long range, and one of them becomes metastable (for symmetry reasons) at short distance. This *enhances the survival probability to short distances*, where efficient losses occur due to state-changing collisions.

The situation is rather different in chromium, where there is a total of 294 molecular potentials which are connected to the $|^7S_3,^7P_4\rangle$ asymptote. Only one of them being metastable[9], the probability of exciting it in our MOT is expected to be much smaller compared to the case of Sr.

Another interesting example is that of metastable He MOTs. Several experimental groups [44, 45, 46, 47] have reported large inelastic losses, on the order of 10^{-8} cm^3 s^{-1}. He* is a very light atom and the MOT cooling transition width ($\Gamma_{^4He^*} = 1.4$ MHz) is about three times smaller than in Cr. This means that the typical distance traveled, at a MOT thermal velocity of $\sim 2m/s$, within an atomic excited state lifetime $\tau_{at} \simeq 100$ ns is on the order of 2.10^{-7}m, almost two order of magnitude bigger than for other atoms. *The probability of reaching small interatomic distances becomes*

---

[8] The given value takes into account the maximum possible value $\frac{3}{2}\hbar\Gamma(\frac{\lambda}{2\pi})^3 \simeq 2.4$ *a.u.* for the C_3 coefficient. More rigorously, one should consider the average over all the possible collisions channels.

[9] We have investigated different possibilities during stimulating discussions with O. Dulieu at *Laboratoire Aimé Cotton* (Orsay).

significant. Furthermore, as mentioned earlier, He* has a very efficient short-range loss mechanism. The Penning collisions, which take place at distances around $7a_0$, lead to loss with probability *close to 1 for every attractive collision channel.*

I want to point out that for He* it has been shown [47] that a way to circumvent light assisted inelastic losses was to detune the MOT lasers very far away from resonance (up to 40 natural linewidths). This decreases considerably the fraction of excited state atoms and the density. Up to 10^9 atoms were loaded in He* MOTs, despite the huge value of the β parameter. Even though a high detuning is expected to dramatically lower the capture velocity of a MOT, the available laser power was sufficient to increase it back (^{4}He* saturation intensity being of only 0.17 mW/cm^2 for the 1083 nm transition used). This could not be achieved in our case, mainly because of the limited amount of laser power available (Cr having a much higher saturation intensity, of 8.5 mW/cm^2).

From this comparison to alkalis, Sr and He* we can deduce that there are probably two important factors that together lead to a high light assisted collision parameter in the case of Cr MOTs:

1. *Once a molecular excited state is excited in the outer zone, the survival probability to short distances must be ~ 1 in the case of Cr*

2. *Most of the attractive excited potentials in Cr must lead to losses.*

4.4   Chromium temperature dependence

The purpose of the following part is to see if the relevant Cr physical parameters of the light-assisted collision problem could qualitatively explain the fact that the measured loss parameters are so close to the high-temperature Langevin limit, even in the 100 μK temperature range.

I want to point out that a complete treatment, giving quantitative results to compare to our experimental results, must be performed using the exact molecular excited potentials, which are unfortunately unknown for Cr (for the moment). I expect that the calculation presented here should nevertheless give some correct qualitative idea on collisions in Cr MOTs.

My approach is the following: based on the JV model and on their results concerning the Cs 0_u^+ potential[10] I will consider a 'model potential' for Cr, by rescaling the C_3 coefficient with the Cr atomic dipole moment in the $^7P_4$ state. The 'model potential' has then a C_3 coefficient 8 times smaller than the Cs potential. The calculations will also take into account the Cr mass, which is about 2.5 smaller than the Cs mass.

---

[10] The attractive Cs 0_u^+ potential which correlates to the $^2P_{3/2}+^2S_{1/2}$ separated atom asymptote has a coefficient $C_3 = \frac{5}{3}\frac{d^2}{4\pi\varepsilon_0}$ and a lifetime $\tau_{0_u^+} = \frac{3}{4}\tau$

4.4.1   Julienne – Vigué model

• The effective potential

We will consider the center-of-mass frame of the two colliding atoms and write the effective molecular interaction potential for a given partial wave l:

$$V(R) = -\frac{C_3}{R^3} + \frac{\hbar^2 l(l+1)}{2\mu R^2}. \tag{4.11}$$

where μ is the reduced mass. The first term is the attractive molecular interaction potential ($C_3 > 0$) and the second is the rotational (centrifugal) barrier for a given l. This effective potential presents a maximum at the distance:

$$R_0 = \frac{3\mu C_3}{\hbar^2 l(l+1)} \tag{4.12}$$

and the height of the barrier is $V(R_0) = C_3/2R_0^3$. The existence of such a barrier introduces a natural cutoff in the number of partial waves that can play a role in the light-assisted collisions:

$$l_{max} = \frac{\sqrt{3\mu}}{\hbar} C_3^{1/3} (2E)^{1/6} \tag{4.13}$$

This cutoff is fixed thus by the competition of the attractive interaction potential and the rotation barrier: for any partial wave with $l > l_{max}$ the energy E is less than the height $V(R_0)$ of the barrier and the atoms will be reflected before they can reach the 'inner zone', where losses occur.

This feature marks a difference with the collisions between two ground-state atoms, which at our MOT temperatures essentially are only s-wave ($l = 0$) collisions. For the light-assisted collisions, there is a significant number of partial waves involved. For Cr we obtain $l_{max} \simeq 15$ at $T_{MOT} \sim 120~\mu K$.

• The atom-pair distribution

For a given partial wave l, one has to consider the distribution of ground-state atom pairs, i.e. the number of atoms pairs, having a relative separation between R and $R+dR$ and an energy between E and $E + dE$. At thermal equilibrium, this distribution reads [58]:

$$dN = \frac{N^2}{2} \frac{(2l+1)\exp(-E/k_B T)}{hv(R,E,l)(2\pi\mu k_B T/h^2)^{3/2}} dRdE. \tag{4.14}$$

where $v(R, E, l)$ represents[11] the relative velocity of the atom pair, with a collision energy E, when it reaches a distance R:

$$v(R, E, l) = \sqrt{\frac{2}{\mu}\left(E - \frac{\hbar^2 l(l+1)}{2\mu R^2}\right)}. \tag{4.15}$$

Eq.(4.14) shows the importance of the ground-state rotational barriers in the light-assisted collision process. It prevents two ground-state atoms (for a certain l and a certain collision energy E) from coming closer than a distance given by:

$$R_{E,l} = \sqrt{\frac{\hbar^2 l(l+1)}{2\mu E}}. \tag{4.16}$$

No pair can thus be excited at a distance $R < R_{E,l}$.

- The excitation rate

Julienne and Vigué consider the following expression of the excitation rate by the MOT lasers, valid in the low intensity limit:

$$\Omega_{exc}(R) = \frac{\lambda^2}{2\pi}\frac{(\Gamma/2)^2}{(\Gamma/2)^2 + (\delta_0 - C_3/R^3)^2}I_0. \tag{4.17}$$

where I_0 is the laser intensity. The spatial dependence of $\Omega_{exc}(R)$ comes from the fact that the excited state energy, and thus the light detuning depends on R: $\delta(R) = \delta_0 - C_3/R^3$, where δ_0 is the MOT detuning (i.e. at $R \to \infty$).

Eq.(4.17) illustrates the fact that the excitation is localized at long interatomic distances; at small R the MOT light comes rapidly out of resonance, as it can be seen in fig.(4.6.B). We also observe that $\Omega_{exc}(R)$ presents a well-defined maximum, located at the Condon distance $R_C = (C_3/\delta_0)^{1/3}$.

- The survival probability

Once the pair is excited at R, we consider its survival probability to a relative distance R':

$$S(R, R') = \exp\left(-\int_{t(R)}^{t(R')} 2\pi\Gamma_M(t')dt'\right) \tag{4.18}$$

and then the probability $P_{loss}(R')$ – for the loss to occur at R'. Here $t(R)$ is the time when the excitation occurred and $t(R')$ is the time when the pair reaches the relative

---

[11] this expression neglects the $-C_6/R^6$ molecular ground-state potential, which has a much shorter range than the excited $-C_3/R^3$ potential

separation R'; Γ_M is the decay rate of the pair.

- The loss probability

The final ingredient is the probability $P_{loss}(R')$ for a loss to occur, once the pair has reached the relative distance R'.

We note that in some cases (FS collisions and Penning ionization) the loss mechanism is relatively well localized, at a distance R_0, and the probability can be replaced with the constant $P_{loss}(R_0)$. This is not true for RE collisions (this case is not considered here).

- The one-channel loss rate

Under these conditions the loss rate K_{loss} for a given collision channel α is obtained by taking the product of all these different probabilities, integrate it over R and E and sum over all the partial waves:

$$K_{loss} = \sum_{l=0}^{l_{max}} \int_{R=R_{E,l}}^{\infty} \int_{E=0}^{\infty} P_{loss}(R_0) \times S(R, R_0) \times \Omega(R) \times dN. \qquad (4.19)$$

We note that in this expression the sum over l was limited to $l \leq l_{max}$, because of the partial wave cutoff. The integral over R is also taken only between $R_{E,l}$ and ∞, because of the rotational barrier in the ground state, discussed earlier.

4.4.2 Results for Cr

I first performed the calculation for the J-V model in the case of the 0_u^+ Cs molecular potential, for different temperatures, and the results are shown in fig.(4.7). The calculation was performed using a saturation parameter $s_0 = I/I_{sat} = 10$ and a detuning $\delta = -10$ MHz, which corresponds to two atomic linewidths. These results reproduce the temperature-dependance reported in [58].

Temperature dependence

In the case of Cr, using the 'model potential' (i.e. using the rescaled C_3 coefficient), we observe a different behavior. At high temperature we find the expected $T^{-1/6}$ dependence, and the loss parameters connects to the corresponding Langevin limits eq.(4.10).

For Cs the loss rate starts deviating from the Langevin rate at about 100 mK and at $T = 100~\mu$K there is a 12.5 reduction factor. In Cr the decrease occurs considerably
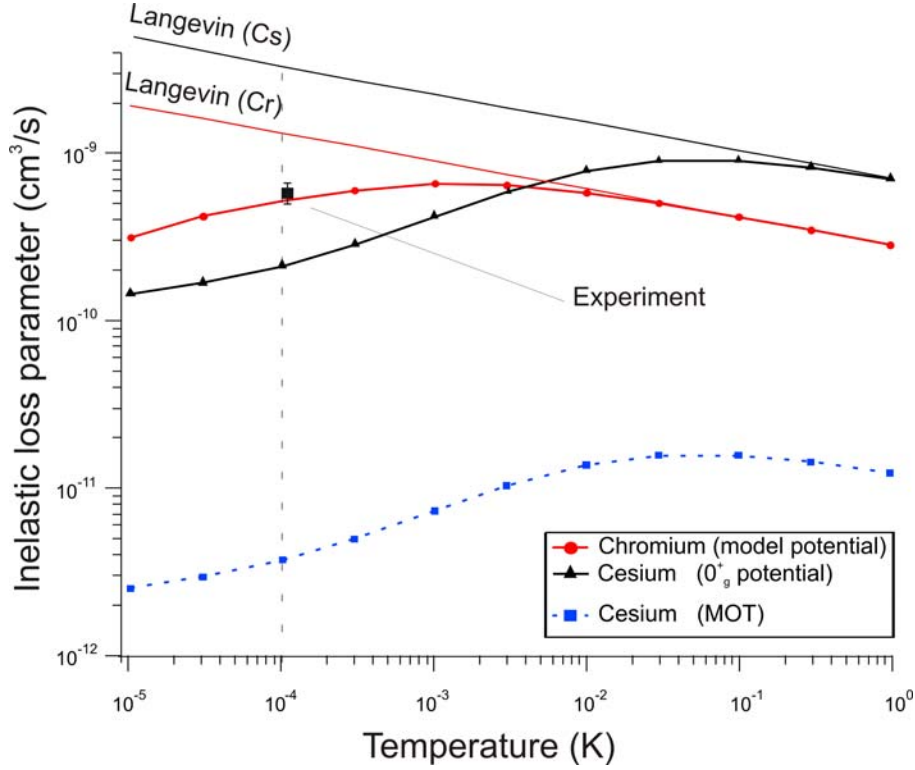
79

Figure 4.7: Comparison of the temperature dependence of the inelastic loss parameter associated to a single loss channel: for Cs (triangles) we used the 0_u^+ potential, while for Cr (dots) we used a rescaled potential. We also show (squares) the case of non-polarized collisions in a Cs MOT, where the rates are significantly reduced (as losses are important for only one channel (0_u^+) out of 16 and happen with a probability of 0.28 [58]). The curves correspond to a detuning of 10 MHz and an intensity of $10I_{sat}$. The straight lines are the corresponding Langevin rates, for Cr and Cs.

later, at a few mK. At $T = 100 \ \mu$K the inelastic loss parameter is only a factor 2.5 smaller than the high-temperature asymptote.

This different temperature-dependence can be attributed to the fact that the partial wave cutoff l_{max}, given by eq.(4.13), is different for the two atoms. Indeed, as Cr has as a smaller mass and C_3 coefficient, there are about 3 times less partial waves contributing to the collision process than in the case of Cs.

Saturation effects

JV model applies in the low laser intensity limit, where the excitation probability, and thus the inelastic collision parameter depend linearly on the laser power.

In my simulations I tried to take into account saturation effects (see Appendix(B)), by considering a different expression for the excitation probability of a pair. The results for this simulation, for Cr (at 100 μK and a detuning of $\delta = 2\Gamma$), are shown in fig.(4.8). We observe that the inelastic collision parameter increases with the laser power, and

the beginning of the saturation is observed. At very high laser powers, we expect for β to approach the high-temperature asymptote β_L (~ 1.3 cm^3/s). This should however happen for intensities much larger than what is experimentally achievable.
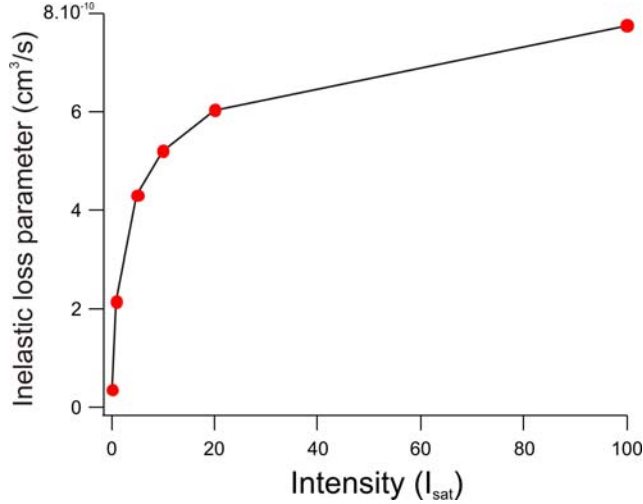

Figure 4.8: Simulation results, showing the dependence of the light-assisted collision parameter on the intensity.

Finally I would like to note that there are other possible physical mechanisms, occurring at high laser intensities, which may increase the value of the inelastic loss parameter; it can thus come even closer to the high-temperature asymptote (or even exceed it!!!). For example there are 'population recycling' [48] effects, which means that at high laser intensities the atoms decaying from the excited molecular potential further than the Condon point R_C may be re-excited by the MOT lasers and continue their evolution to short interatomic distances. Usually this scenario is theoretically explored by performing quantum Monte-Carlo simulations [49, 50].

Detuning dependence

Another comparison between Cs and Cr is shown in fig.(4.9), where I present the dependence of the loss parameter β on the MOT laser detuning. The behavior seems again qualitatively different, as for Cr we observe a decrease occurring quite rapidly for detunings larger than 2Γ.

The detuning-dependence of β, for Cr, does not reproduce exactly the experimental data shown in fig.(4.4.A). Although in our measurements we observe that the inelastic collision parameter decreases with the detuning, we however do not observe any increase at small detunings (see fig.(4.9), for $\delta < 2\Gamma$).
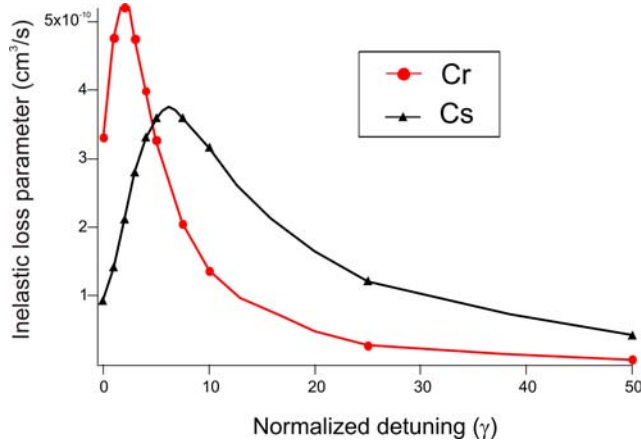
Figure 4.9: Simulation results, showing the dependence of the light-assisted collision parameter on the detuning.

This difference between simulation and experiments may come from the difficulty to have a precise treatment of the saturation effects, which are expected to be more important at small detunings. Indeed, 'population recycling' tends to increase the collision parameters when the excitation takes place at large distances (i.e. at small detunings).

Conclusions

Our simple model proves qualitatively that for Cr the low-temperature collision behavior is expected to be different than the one described by [58] for Cs. At a temperature of 100 μK, the expected deviation from the high-temperature limit is reduced for Cr by about one order of magnitude.

On the other hand, for alkalis the measured loss parameter in a MOT is much smaller than the one-channel maximum rate, due to the fact that there is only a small number (one or two) of excited potentials which lead to trap losses. For non-polarized collisions in a MOT, the probability of excitation to that particular channel is reduced by a factor on the order of the degeneracy of the excited molecular state, due to selection rules in the excitation process.

In chromium we have both a high degeneracy and a high measured loss parameter. This may be explained by the existence of a large number among the excited potentials which have high short-range loss probabilities, and which actually contribute to the light assisted losses in a Cr magneto-optical trap.

These considerations still need a rigorous confirmation. A major difficulty is that calculations for Cr_2 molecular potentials are known to be extremely complicated, due

to the large number of electrons involved. Such molecular physics considerations are far beyond the goal of this thesis.

Finally, our measurements also show that the loss parameters for the ^{53}Cr are higher than in the case of ^{52}Cr. We measured a difference of almost one order of magnitude (for a detuning of -2Γ and with a laser intensity of $13 I_{sat}$ for ^{52}Cr and $20 I_{sat}$ for ^{53}Cr). This indicates that the hyperfine structure of ^{53}Cr, even though relatively small in the excited state (160 MHz), enhances the loss mechanism.

The very large light assisted collision parameters of Cr limits the maximum number of atoms in our MOTs. This sets a strategy towards reaching Bose-Einstein with Cr, which will be described in the rest of the manuscript.

In perspective, optical shielding [74] – involving the use of a blue-detuned laser to prevent pairs form approaching one another – may be a way to increase the number of atoms in Cr MOTs. Because of the lack of the suitable laser (until recently) we were not able to test this possibility.

Chapter 5

Continuous loading of a finite-depth magnetic trap with ^{52}Cr metastable atoms

The road to Bose-Einstein condensation in magnetic traps usually consists in (at least) three steps, separated in time: first comes the accumulation of large (up to 10^{10}) atom numbers in magneto-optical traps, followed by a second step, which is the transfer in a magnetic trap. The third step consists in applying RF-evaporative cooling techniques, i.e. continuously removing the hottest atoms, and reducing thus the mean energy per trapped atom. In presence of 'enough' elastic collisions, the energy of the remaining atoms is redistributed, and one tends towards a new (quasi-)equilibrium situation, where the temperature is reduced.

In the case of Cr, the first two steps can be favorably performed together [81, 43]. In the previous chapters I presented a study of the light-assisted collisions in Cr MOTs. The large values of the corresponding inelastic loss parameters β show that, in presence of the quasi-resonant cooling light, the atom numbers in MOTs are severely reduced, compared to the alkali atoms. On the other hand, the electronic structure and the high magnetic moment of chromium provide an interesting way of loading large 'reservoirs' – represented by the metastable ^5D states – which are shielded from the MOT light. This increases by more than one order of magnitude the number of atoms available in the MOT.

This chapter is dedicated to the study of the magnetically trapped metastable ^{52}Cr atoms. After presenting some measurements of the collisional (elastic and inelastic) properties of the metastable states, I will present a new trapping scheme, which combines together all three steps: continuous loading and evaporation in a RF-truncated magnetic trap. This scheme allowed in our case to obtain, in less than 1 s, phase-space densities up to 7×10^{-6}. I will also present a simple theoretical model which describes the physics of continuous loading and evaporation, and provides a better understanding

*of the limiting factors. In the final part of the chapter I will discuss some prelimi-
nary results in the attempt of reducing the limiting factors, by accumulating atoms in
a large-volume, RF-dressed magnetic trap.*

5.1   Magnetic trapping

In this section I present some issues related to magnetic trapping inside a quadrupole
trap and to the measuring procedures which we use for analyzing absorption images,
in order to estimate the number of atoms and the density of the cloud.

Magnetic trapping potential

The classical interaction potential between an atom, having a magnetic dipole mo-
ment $\vec{\mu}$, and an external magnetic field $\vec{B}$ reads: $V(\vec{r}) = -\vec{\mu} \cdot \vec{B}(\vec{r})$. If the magnetic
field is 'strong enough', the direction of $\vec{\mu}$ adiabatically follows that of the magnetic
field and the potential simply becomes: $V(\vec{r}) = -|\vec{\mu}||\vec{B}(\vec{r})|$.

In the quantum picture, the projection of the magnetic moment on a given axis (in
our case the axis defined by the local direction of $\vec{B}$) is quantized, and the magnetic
trapping potential reads:

$$V(x, y, z) = m_J g_J \mu_B |\vec{B}(x, y, z)| \tag{5.1}$$

where m_J is the magnetic quantum number (going from $-J$ to $+J$), g_J is the Landé
factor, and μ_B is the Bohr magneton. This expression can be used for any magnetic
field profile; in our case, the atoms are trapped in the quadrupole magnetic field created
by the MOT coils, given by:

$$\vec{B}(x, y, z) = b'(x\hat{\mathbf{x}} + y\hat{\mathbf{y}} - 2z\hat{\mathbf{z}}) \tag{5.2}$$

where b' is the field gradient along the $\hat{\mathbf{x}}$ and $\hat{\mathbf{y}}$ axis and half the one along $\hat{\mathbf{z}}$ (because of
Gauss theorem and for symmetry reasons). The expression of the magnetic potential
becomes thus:

$$V_{MT}(x, y, z) = m_J g_J \mu_B b' \sqrt{x^2 + y^2 + 4z^2}. \tag{5.3}$$

Typically, we have $b' = 9$ G/cm.

Depending on the sign of m_J, the atoms can have three different behaviors. If
$m_J > 0$ (low field seeker state) the atoms are trapped, as they are attracted towards
the $|\vec{B}|$ minima ($|\vec{B}| = 0$ in our case); on the contrary, atoms with $m_J < 0$ (high field
seekers) are expelled from $|\vec{B}|$ minima, while $m_J = 0$ atoms do not interact with the
field and eventually fall under gravity.

The experiments described in the present chapter will only concern the ^{52}Cr atoms, magnetically trapped in the $^5D_4$ state. For this state the Landé factor is $g_J = 3/2$, and m_J can take integer values between from -4 to +4. We mention that for the ^{52}Cr $^5D_3$ state (not studied here) m_J is between -3 to +3 and $g_J = 3/2$. An expression similar to eq.(5.3) can be also applied for ^{53}Cr magnetic potential, by replacing m_J and g_J by m_F and g_F.

Density profile at thermal equilibrium

In our experiment we deal with magnetically-trapped atom clouds that are not spin-polarized in a single m_J state. The reason is that they are initially accumulated into the metastable ^5D states through spontaneous emission from magneto-optically trapped excited atoms, whose m_J−distribution is random. Furthermore, polarization by optical pumping means inside our magnetic trap is not possible (not even after repumping in the $^7S_3$ state), because the quantization axis given by the local direction of the quadrupole magnetic field varies in space throughout the atomic sample.

Eq.(5.3) shows that atoms in different m_J−states feel different trapping potentials. The density profile of the entire cloud is thus a sum over all $m_J > 0$ density distributions (3 for $^7S_3$ and $^5D_3$, 4 for $^5D_4$), each of them being given, at thermal equilibrium, by the Boltzmann distribution:

$$n(x,y,z) = \sum_{m_J>0} n_{0,m_J} \exp\left(-\frac{m_J g_J \mu_B b' \sqrt{x^2 + y^2 + 4z^2}}{k_B T}\right), \qquad (5.4)$$

where n_{0,m_J} is the peak density for each m_J−component and T is the temperature.

In principle, eq.(5.4) could be used for determining the temperature of the trapped cloud, provided that one has a precise knowledge of the relative populations of different m_J states, using for example a Stern-Gerlach-like experiment. This is however not possible, in our current experiment, because we cannot produce high-enough magnetic field gradients in order to spatially separate the different m_J components, for the typical temperatures ($\sim 100\ \mu$K) of our trapped clouds.

Since the atom cloud is not polarized, the exact analysis of the absorption images is complicated. We find it useful, for sake of simplicity, to assume that all atoms experience an average magnetic potential given by:

$$V(x,y,z) = \overline{V_0}\sqrt{x^2 + y^2 + 4z^2} \qquad (5.5)$$

where $\overline{V_0} = \overline{m_J} g_J \mu_B b'$ and $\overline{m_J}$ is an 'average' magnetic quantum number. The density profile at thermal equilibrium is then approximately given by the simplified expression:

$$n_{MT}(x,y,z) = n_0 \exp\left(-\frac{\overline{V_0}}{k_B T}\sqrt{x^2 + y^2 + 4z^2}\right). \qquad (5.6)$$

Using this expression we can define the $1/e$ size $\bar{a}$ of the atomic cloud in the x and y directions:

$$\bar{a} = \frac{k_B T}{V_0}. \tag{5.7}$$

Integrating eq.(5.6), we can relate the peak atomic density n_0 and $\bar{a}$ to the total number of atoms in the MT: $N_{MT} = 4\pi n_0 \bar{a}^3$. We also define the volume of the magnetic trap by: $V_{MT} \equiv N_{MT}/n_0 = 4\pi\bar{a}^3$

Analysis of the absorption images

The absorption imaging technique has been used for the experiments presented in the remaining part of this manuscript. Like the fluorescence imaging technique, it provides information on the properties of an atomic sample (number of atoms, density and cloud size). The main advantage of absorption imaging is that it does not require a precise measurement of the laser beam power, which is a main error source in fluorescence imaging.

The absorption of the laser imaging beam passing through the atomic sample can be expressed, in the low-saturation limit, using the Beer-Lambert law:

$$\frac{dI(x,y,z)}{I(x,y,z)} = -o.d.(x,y,z)dy. \tag{5.8}$$

where $o.d.(x,y,z)$ is the optical density of the cloud and $I(x,y,z)$ is the intensity profile of the laser which propagates along the y (CCD camera) axis.

The optical depth $O.D.(x,z)$ of the cloud, measured in the plane of the camera – see fig.(5.1), can be obtained by integration of eq.(5.8) along the y axis:

$$O.D.(x,z) \equiv -\ln\left[\frac{I_\infty(x,z)}{I_{-\infty}(x,z)}\right] = +\int_{-\infty}^{+\infty} o.d.(x,y,z)dy. \tag{5.9}$$

where $I_{-\infty}(x,z) \equiv I(x,y=-\infty,z)$ and $I_\infty(x,z) \equiv I(x,y=+\infty,z)$ are the beam intensity profiles before and after passing through the atomic cloud.

The optical density can be related to the atomic density via the absorption cross section σ_{abs}: $o.d.(x,y,z) = \sigma_{abs} \cdot n(x,y,z)$. Replacing this expression in (5.9) gives:

$$O.D.(x,z) = \sigma_{abs}\int_{-\infty}^{+\infty} n(x,y,z)dy \tag{5.10}$$

Eq.(5.10) relates thus the optical depth of the cloud to the 'column density' of the atomic cloud, defined as: $n(x,z) \equiv \int_{-\infty}^{+\infty} n(x,y,z)dy$.

88

Analysis of the in-situ magnetic trap profile

The number of atoms in the cloud can be found by integration of eq.(5.10):

$$N = \frac{1}{\sigma_{abs}} \int\limits_{-\infty}^{+\infty} O.D.(x,z) \; dxdz \tag{5.11}$$

Since the atomic sample is not spin-polarized and the magnetic field is inhomogeneous, we assume (as we also did in the case of the fluorescence imaging of the MOT) an average Clebsch-Gordan coefficient of $3/7$. This yields a mean value for the resonant photon absorption cross section $\sigma_{abs} = \frac{3}{7}\sigma_0$, where $\sigma_0 = \frac{3\lambda^2}{2\pi}$ is the resonant photon scattering cross section in the low-intensity regime (our imaging beam has a peak intensity of ~ 0.2 mW/cm^2, well below $I_{sat} = 8.5$ mW/cm^2).
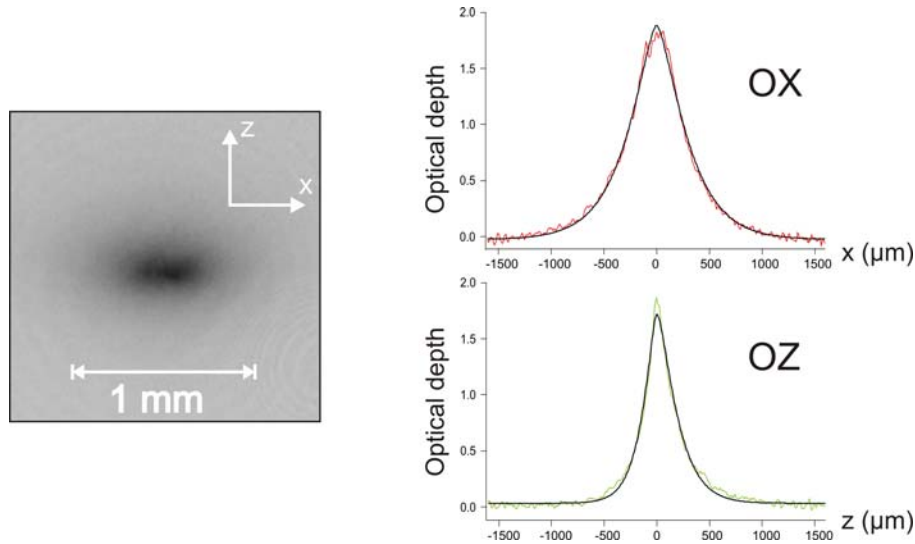

Figure 5.1: In-situ absorption image of a magnetically trapped cloud of ^{52}Cr. To the right: two slices of the image, passing through the center of the cloud, in the horizontal (above) and vertical (below) plane. The fit of the horizontal cut is done using the function $n_{MT}(x,0)$ given by eq.(5.12). For the vertical slice, the fitting function $n_{MT}(0,z)$ was modified for taking into account the slight dissymmetry due to the gravity (not mentioned in the text). In principle, this dissymmetry could provide an independent measure of $\overline{m_J}$ [31], but in our case this is not possible, as the vertical $\widehat{\mathbf{z}}$ axis is the strong-confining axis of the trap and the dissymmetry is too small, yielding large systematic fitting uncertainties.

The column density profile of a magnetically trapped cloud is obtained by integration of eq.(5.6) along the imaging direction y:

$$n_{MT}(x,z) = 2n_0\sqrt{x^2 + 4z^2} \; \text{BesselK}\left(1, \frac{\sqrt{x^2 + 4z^2}}{\overline{a}}\right), \tag{5.12}$$

where BesselK is the modified Bessel function of the second kind. Fig.(5.1) shows that this expression provides a good approximation for the observed shape of the atomic cloud.

Fitting a cut of the absorption image which passes through the center of the cloud provides the $1/e$ radius $\bar{a}$ and the peak optical depth $O.D._{max}$, from which we can calculate the value of the peak density n_0. The peak atom density is then simply given by: $n_0 = \dfrac{O.D._{max}}{2\bar{a}\ \sigma_{abs}}$.

Absorption imaging can be used for the atoms in the ground state, via the $^7S_3 \rightarrow ^7P_4$ strong transition. This technique is not applicable directly to the metastable ^5D trapped cloud; it is nevertheless possible to 'map' its density distribution onto the $^7S_3$ state, by repumping the atoms with the 'red' diodes and immediately absorption-imaging them. The information about the shape of the cloud is correct, provided that the repumping time is short enough compared to the typical oscillation period in the MT.

In the case of an anharmonic trap, the oscillation period depends on the energy; we can however define a typical (mean) oscillation period $\langle T_{osc} \rangle$, by taking the thermal average of the oscillation frequencies of all atoms:

$$\langle T_{osc} \rangle = \frac{4m\overline{v_{th}}}{m_J g_J \mu_B b'} \tag{5.13}$$

where $\overline{v_{th}}$ is the mean thermal velocity. For $m_J = 4$ and a MT temperature $T = 100\ \mu K$, we see that the typical oscillation period is ~ 12 ms.

We found that pulsing the repumping light for 1 ms is sufficient to repump most of the metastable atoms in the ground state, for a 'red' repumper intensity of about 15 mW/cm^2. Since this time is about $1/10$ of the typical oscillation period of the atoms at the MT temperature ($100\ \mu K$), we can rely on our method of 'mapping' the metastable atoms density distribution.

Temperature and mean magnetic moment

In addition to the density measurements, we perform direct temperature measurements by analyzing the free-fall expansion of the atoms after suddenly switching off the magnetic trap. As we mentioned in Chapter(2), the eddy currents generate a non-negligible residual magnetic field at the atom location, which dies away in about 20 ms. We estimate however that this field does not affect the ballistic expansion of the atoms and consequently does not alter the results of the temperature measurements. Indeed, we checked that the center of mass of the cloud falls vertically, and is accelerated only by gravity. The residual field introduces however some additional Zeeman shift and broadening of the imaging-laser resonance, but does not influence the temperature determination.

On the other hand the MOT coils current, and thus the trapping magnetic field gradient, are switched off in 500 μs ($1/e$ time), and we therefore include in our analysis

only the time of flights longer than 500 μs.

Finally, the value of the mean magnetic quantum number $\overline{m_J}$ can be deduced using the temperature and the measured in-situ $1/e$ radius of the cloud $\overline{a}$:

$$\overline{m_J} = \frac{k_B T}{\overline{a} g_J \mu_B b'}. \tag{5.14}$$

5.2 Collisional properties of metastable ^{52}Cr atoms

After introducing, in the previous section, some general aspects of magnetic traps and the related measuring procedures, we will now turn to an investigation of some of the properties of metastable ^{52}Cr. In this section, we will measure the elastic and inelastic collision parameters, which are very important for all experiments presented in the rest of this dissertation, because our strategy towards condensation consists in first accumulating atoms in these states.

5.2.1 Inelastic D-D collisions

To investigate the inelastic collisions between metastable Cr atoms, we performed a lifetime measurement of the magnetic trap in the ^{5}D$_4$ state. For this experiment, the atoms are first accumulated for 5 s in the magnetic trap. The MOT beams are then switched off and, after an adjustable delay t, the atoms are repumped into the ground state. The number of atoms is measured and plotted as a function of t, as it is shown in fig.(5.2) in a semi-log scale. We observe a clear non-exponential initial decay, which indicates the influence of the two-body inelastic collisions on the lifetime of the trapped cloud.

We fitted the data, assuming that the decay is characterized by the following equation:

$$\frac{dN}{dt} = -\Gamma_0 N - \frac{\beta_{DD}}{V_{coll}(t)} N^2, \tag{5.15}$$

where, in addition to a one-body loss rate Γ_0, we consider a temperature-independent two-body loss parameter β_{DD}. This equation and the corresponding fitting procedure are very similar to the ones used for the light-assisted collisions (see eq.(4.5-4.6) in Chapter(4)). From the MT density distribution (5.6) we calculate[1] the collisional volume $V_{coll} = 32\pi \overline{a}^3 = 8V_{MT}$. During the decay, the cloud volume V_{MT} increases approximately linearly, and we include this dependence in the equation describing the decay.

---

[1] The collisional volume is defined, in a similar way as for the light-assisted collisions (see Section(4.1)), by: $V_{coll} = \frac{\left(\int n_{MT}(\overrightarrow{r}) d^3 r\right)^2}{\int \left(n_{MT}(\overrightarrow{r})\right)^2 d^3 r}$
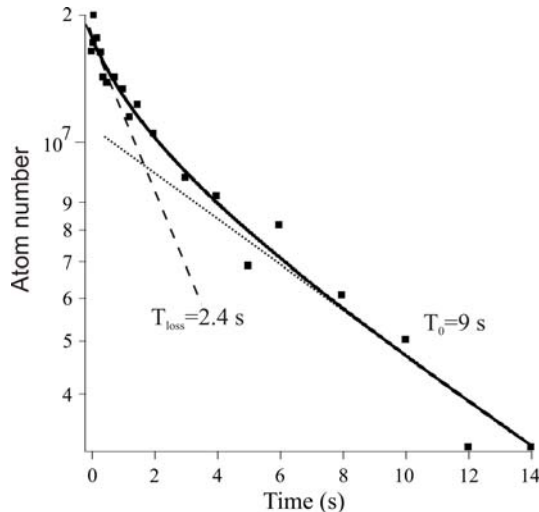
Figure 5.2: Decay of the magnetically-trapped metastable atoms. Solid line: result of the fit (see text) which gives the inelastic collision parameter β_{DD}. The dotted line is a result of a purely exponential fit for t>5 s, providing the lifetime due to background gas collisions (mostly with hot atoms from the Cr beam). The dashed line is a result of an exponential fit for t<1 s.

We find the inelastic loss parameter to be $\beta_{DD} = (3.3 \pm 0.5 \pm 0.5) \times 10^{-11}$ cm^3/s (in reasonable agreement with [43]). The respective error bars are the statistic error bar of the fit, and the systematic error bar, mostly coming from the uncertainty on the total number of atoms.

We note that this inelastic loss parameter is much larger than the expected dipolar relaxation inelastic parameter $\beta_{d.r.} \simeq 3 \times 10^{-12}$, for low magnetic fields (see [76]), which rules out dipolar relaxation as the main inelastic loss channel. In our quadrupole magnetic trap there are however other collisional mechanisms which may explain the high value of β_{DD}: for example spin-exchange collisions, which were observed to have larger $\beta-$parameters [76].

From the same fit we also deduce the one-body decay time constant $T_0 = 1/\Gamma_0 = 9$ s. We repeated the same experiment without the Cr beam (by blocking it immediately after the accumulation, together with the MOT beams) and found a longer one-body loss time constant, of 30 s, which we interpret as being fixed by the collisions with the vacuum background gas. We interpret this difference as the influence of the collisions with the hot Cr atoms of the beam.

We additionally analyzed the temperature evolution during the decay. We observe a strong heating at short times, which is shown in fig.(5.3) (squares). We interpret this heating as the effect of inelastic collisions, which mostly expel the low-energy atoms (as explained later, in Section(5.4)).

5.2.2 Elastic collision cross-section of the $^5D_4$ state

Evaporative cooling is based on preferential removal of atoms with an energy higher than the average. Knowing the elastic collision properties is important, because they are responsible for the energy redistribution among the remaining atoms and for reaching a new quasi-thermal equilibrium, at a lower temperature. In this section I present experiments which led to a measurement of the elastic cross-section of atoms in the metastable $^5D_4$ state. This is, to our knowledge, the first measurement of an elastic cross section for a transition element in a metastable state.

In order to study the evaporation in the magnetic trap, we use a RF magnetic field, which truncates the MT trap to a finite depth. The RF magnetic field, with a frequency ω, induces spin-flip transitions of the atoms to non-trapped ($m_J < 0$) states, which are expelled from the trap. These transitions take place at the position of the RF resonance, where the energy difference between two adjacent m_J states is equal to the energy of a RF photon: $g_J \mu_B B(\overrightarrow{r}) = \hbar\omega$. In the case of our quadrupole magnetic field, this resonance condition is fulfilled on a 'iso-B' ellipsoid, defined by the equation:

$$x^2 + y^2 + 4z^2 = \left(\frac{\hbar\omega}{g_J \mu_B b'} \right)^2 . \tag{5.16}$$

We assume that all the atoms that reach this surface are efficiently removed from the trap.

RF 'shock-cooling'

We repeated the lifetime experiments presented in the previous subsection, by suddenly applying a $\omega = 2\pi \times 3$ MHz RF field ('shock cooling' [75]), at $t = 0$, just after the 5 s accumulation time in the $^5D_4$ state. We observe that the decay of the cloud is modified by evaporation, which changes both the total loss rate, and the evolution of the temperature, as shown in fig.(5.3) (triangles). We will use these observations to estimate the evaporation rate and infer the elastic collision rate.

For that, one must first evaluate the modification of the lifetime of the cloud linked to spilling of atoms out of the trapping volume set by the RF frequency: the experimentally observed heating 'produces' atoms whose energy is larger than the trap depth. They then leave the trap, without undergoing any elastic collision, assuming that the mean free path of the atoms is larger than the size of the sample. Heating without RF translates into spilling when RF is applied, and the rate at which spilling occurs is therefore linked to the heating rate without RF. We measure the time evolution of the $1/e$ radius of the cloud $\overline{a}$, without RF, to estimate $\Gamma_{spill} \approx 0.1$ s^{-1}. Γ_{spill} corresponds
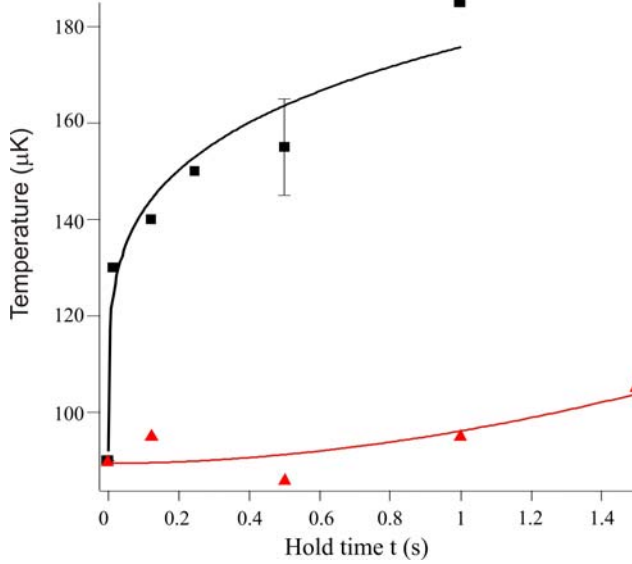
Figure 5.3: Time-dependence of the temperature of the atoms magnetically-trapped in the $^5D_4$ state. In absence of the RF (squares) we observe a strong heating of the cloud at short times, which we interpret as an effect of inelastic collisions. In presence of a 3 MHz RF field (triangles), evaporation and 'spilling' of hot atoms compensate for the heating (see Section(5.2.2)). The full lines are guides for the eyes.

to the rate of atoms leaving the trapping volume set by the RF frequency, i.e. the rate of atoms spilled out of the trap volume.

From the atom number decay at short times, we deduce the experimental values of the atom loss rates without RF (see fig.(5.2)), $\Gamma_{loss} = 1/T_{loss} = 1/2.4$ s^{-1}, and with RF, $\Gamma_{loss,RF} = 1/1.35$ s^{-1}. We can therefore estimate the value of $\Gamma_{ev} + \Gamma_{spill} = \Gamma_{loss,RF} - \Gamma_{loss} = 0.32$ s^{-1}. We therefore obtain an estimate for the evaporation rate from the modification in the lifetime of the cloud in presence of the RF: $\Gamma_{ev} \approx 0.22$ s^{-1}. In general, Γ_{ev} is temperature dependent, but, in presence of RF, we performed this measurement in a situation where the temperature is almost constant (see fig.(5.3)).

The determination of the evaporation rate Γ_{ev} allows us to infer the value of the elastic collision rate. For a given RF frequency, Γ_{ev} can be directly related to the elastic collision rate, defined as $\Gamma_{el} = n_0 \sigma_{el} \bar{v}$, where σ_{el} is the elastic cross section and $\bar{v} = \sqrt{\frac{8k_BT}{\pi m}}$ is the mean thermal velocity. Using eq.(5.36) – which will be explained in the theoretical model presented in Section(5.4) – we find $\Gamma_{el} = (20 \pm 4 \pm 11)$ s^{-1}. The experimentally measured temperature, at t=0, is 100 μK, and the peak density is 10^{11} cm^{-3}. We therefore infer an average elastic cross section of $\sigma_{el} = (7.0 \pm 1.4 \pm 3.5) \times 10^{-16}$ m^2.

94

5.3 Continuous accumulation in a RF-truncated magnetic trap

After determining the collisional properties of ^{52}Cr atoms in the ^{5}D$_4$ state, I will present now the main result of this chapter, which is the study of the continuous loading of metastable Cr atoms in a RF-truncated quadrupole magnetic trap.

From the experimental point of view, the accumulation procedure, presented in fig.(5.4), is the same as in the absence of the RF: atoms are continuously loaded in the MT from the MOT, using the 'leaks' due to spontaneous decay of the atoms in the ^{7}P$_4$ state towards the ^{5}D$_4$ state. Interesting features arise from the presence of the RF field: not only the loading, but also the evaporation are continuous, and they both take place simultaneously. In the next paragraphs I will analyze the dependance of the characteristics of the could on the value of the RF frequency.
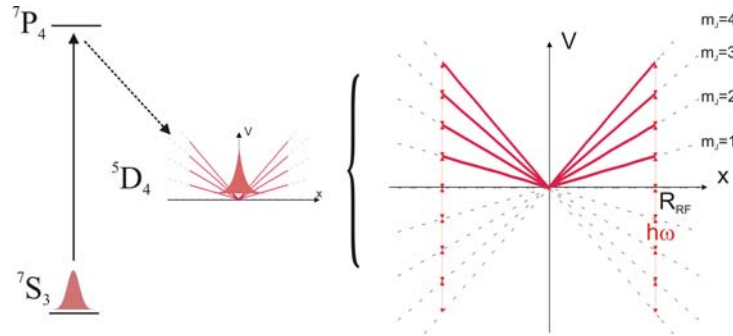

Figure 5.4: *Right:* scheme of accumulation of ^{5}D$_4$ metastable ^{52}Cr atoms in RF-truncated quadrupole magnetic trap formed by the MOT gradient. *Left:* zoom of the truncated magnetic potentials, for different m_J Zeeman substates.

Atom number and density measurements

We analyzed the in-situ absorption images of the cloud, after a 5 s accumulation time in the metastable states, for different values of the frequency of the RF field.

An interesting feature of the experimental data is the RF frequency dependence of the cloud peak density in the steady state, also shown in fig.(5.5): although the atom number decreases dramatically when lowering ν, we observe that the peak density remains almost at the constant value of $\sim 0.8 \times 10^{11}$ atoms/cm^3 for a large range of RF frequencies; it only starts decreasing when ν is set to values smaller than 1.5 MHz.

Additionally, we measure the number of atoms accumulated in the truncated MT, as a function of time τ, for different RF frequencies ν. At any frequency, we observe that the loading of the trap can be well fitted by an exponential, and we plot in fig.(5.6) the
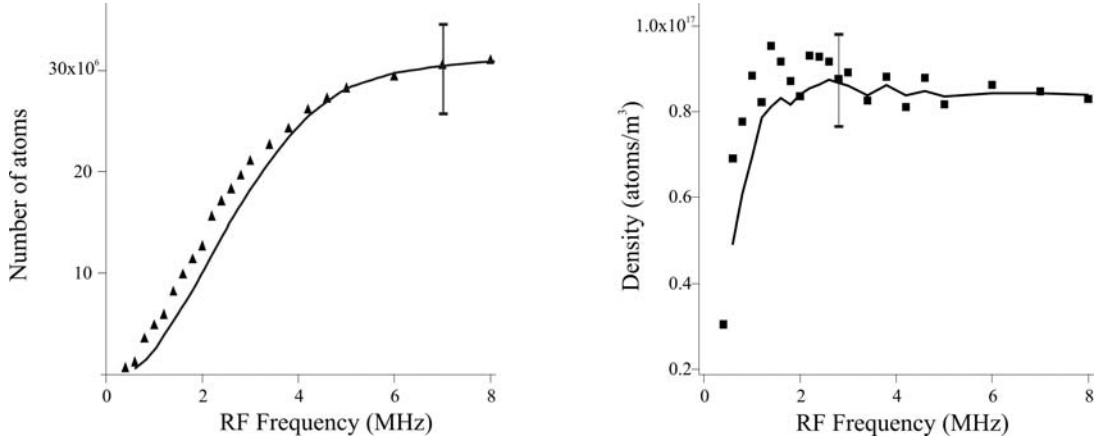
Figure 5.5: Metastable atom number (left) and peak atom density (right), after 5 s of accumulation in the MT, as a function of the RF frequency. The error bars correspond to the uncertainty in determining the total number of atoms by absorption imaging. The solid lines represent the results of the rate-equation theoretical model, presented in Section(5.4).

corresponding $1/e$ accumulation time, T_{load}, as a function of the RF frequency. The accumulation time increases approximately linearly from 0.3 s for $\nu = 1$ MHz to 1.4 s for $\nu \geq 6$ MHz. For higher frequencies the accumulation time saturates to an almost constant value, which is equal to the accumulation time without RF. This proves that, after 5 s of accumulation the steady-state atom number in fig.(5.5) was indeed fully reached.

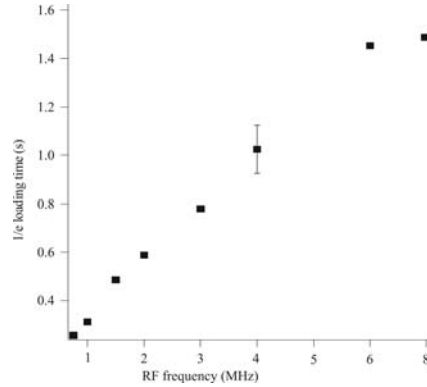Figure 5.6: Accumulation time T_{load} in the truncated MT, as a function of the RF frequency. The error bar is the typical statistical error in an exponential fit of the number of accumulated atoms as a function of τ.

Temperature measurements

The ballistic expansion of the cloud is used for measuring the temperature of the cloud, for different values of the RF frequency. The results are shown in fig.(5.7.A)

96

The cloud analysis is made by gaussian fits, which is a good approximation in the limit where the cloud size after expansion becomes large compared to the initial size. Some systematic errors are nevertheless expected at short times, because of the non-gaussian initial shape of the cloud (see fig.(5.1)). We checked that the systematic error bar of this procedure is less than 10%, when fitting the vertical direction, along which the initial extension of the cloud is the smallest.
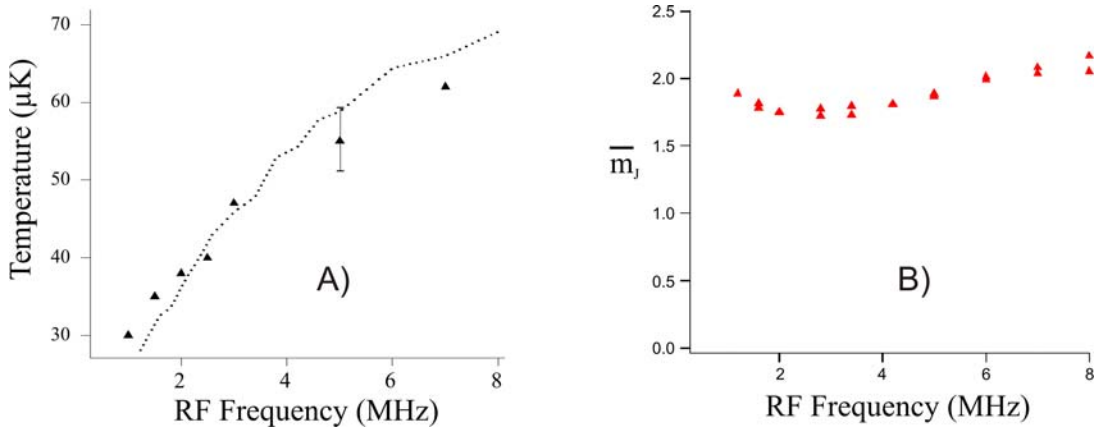
Figure 5.7: A) Temperature of the atoms after 5 s of accumulation, as a function of the RF frequency. The error bar corresponds to the estimated 10% systematic error in temperature determination. Dotted line: results, using the rate-equation theoretical model (see Section(5.4)). B) Mean magnetic quantum number $\overline{m_J}$ as a function of the RF frequency.

Using this temperature and the measured $1/e$ in-situ radius of the cloud $\overline{a}$, we can deduce the mean magnetic quantum number $\overline{m_J}$, using eq.(5.14). The results are shown in fig.(5.7.B), and we interestingly observe that $\overline{m_J}$ does not change much with the RF frequency, staying close to 2. This indicates that the presence of the RF does not change much the m_J-distribution of the cloud, which may seem surprising, as the trap depth depends on the value of m_J, as illustrated in fig.(5.4) (the atoms with lower m_J may evaporate faster than those with higher m_J).

Phase space density

From the previous measurements of the peak atom density and temperature we can infer the values of the peak phase space density $D_{ph.}$:

$$D_{ph.} = n_0 \Lambda_{dB}^3 = n_0 \left(\frac{h^2}{2\pi m k_B T} \right)^{3/2} . \tag{5.17}$$

In fig.(5.8) we show the steady-state phase space density (i.e. after $\tau = 5$ s of accumulation) in the magnetic trap as a function of the RF frequency. Because the

97
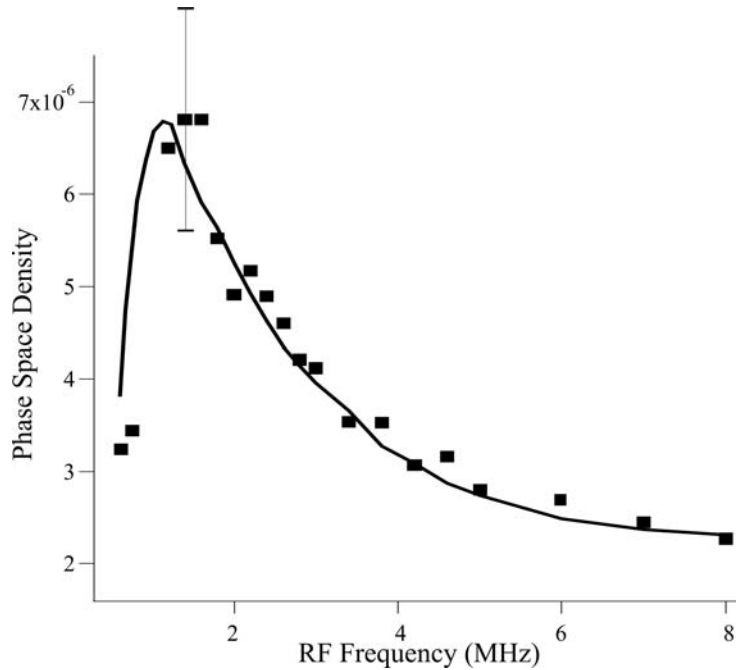
Figure 5.8: Phase-space density as a function of the RF frequency. The solid line represents the result of the theoretical rate-equation model, presented in the Section(5.4).

measured temperature of the atoms decreases with decreasing RF frequency (as shown in the same figure), and because the measured peak atom density remains almost constant (fig.(5.5)), we observe that the phase space density increases at lower RF frequencies, to reach a maximum value of $(7\pm1.5)\times10^{-6}$ at ν=1.5 MHz. The error bar is due to the systematic errors on the density and on the temperature measurements. We notice that this maximum phase-space density value is significantly higher than typical phase-space densities achieved in a standard MOT, involving a strong resonance line.

At frequencies smaller than 1.5 MHz, the trend inverts: when lowering the RF frequency, the density of the atoms decreases (see fig.(5.5)), which yields a decrease of the phase-space density. For such low frequencies, the depth of the magnetic trap becomes lower than the MOT temperature, and most of the atoms arriving in the $^5D_4$ state are immediately spilled out of the trap.

5.4 Theoretical model

In this section I present a theoretical model which is used to interpret our experimental results, concerning the accumulation of the atoms in the RF-truncated magnetic trap. The model is based on refs. [77] and [78] and consists of two rate equations, for

the total number of atoms N and the total energy E of the system:

$$\frac{dN}{dt} = \Gamma - \left(\sum_i \Gamma_i\right) N \qquad (5.18)$$

$$\frac{dE}{dt} = \Gamma E' - \left(\sum_i f_i \Gamma_i\right) N k_B T. \qquad (5.19)$$

Eq.(5.18) includes a loading term Γ and a loss rate, having several contributions, each describing a different loss process (labeled i) with a rate Γ_i. The f_i coefficients in (5.19) account for the average energy lost per particle, in units of $k_B T$, for each of the loss mechanism considered and E' is the mean energy per loaded atom.

In the following pages I will first detail the model in the case of continuous accumulation of Cr metastable atoms in a finite-depth quadrupole magnetic trap, and then I will present some numerical results, which are compared to the previously-presented experimental observations.

I also point out that the model described by the rate equations (5.18)-(5.19) can have a fairly large degree of generality, as one may include, besides different loading terms, many various physical loss mechanisms, such as one-, two- and three-body losses, Majorana losses, evaporation, etc. It can also, in principle, be applied to any arbitrary trapping potentials $U(\vec{r})$.

Trap depth

A complete description of the accumulation process, taking into account all four low-field-seeking magnetic sublevels of the $^5D_4$ state is quite complicated and hard to interpret in our experimental case (as the exact m_J−distribution is unknown). In order to describe the accumulation in the metastable finite-depth magnetic traps, we will again consider the simplified model of a cloud with an average (measured) magnetic quantum number $\overline{m_J}$.

In the case of our quadrupole magnetic trap, the RF resonances shown in fig.(5.4) lead to m_J−dependent trap depths; we will nevertheless define an average depth, corresponding to $\overline{m_J}$:

$$U_0 = \overline{m_J} h\nu_{RF}, \qquad (5.20)$$

and the situation we consider is schematically shown in fig.(5.9). As usually done in evaporative cooling description, we also define the dimensionless evaporation parameter η, which is the ratio between the trap depth to the temperature: $\eta \equiv U_0/k_B T$. It is interesting to notice that the measurement of the $1/e$ radius of the cloud $\overline{a}$ allows one to have an experimental estimate of η. Indeed, using (5.7) and (5.20), we find:

$$\eta = \frac{h\nu_{RF}}{g_J \mu_B b' \overline{a}} \qquad (5.21)$$
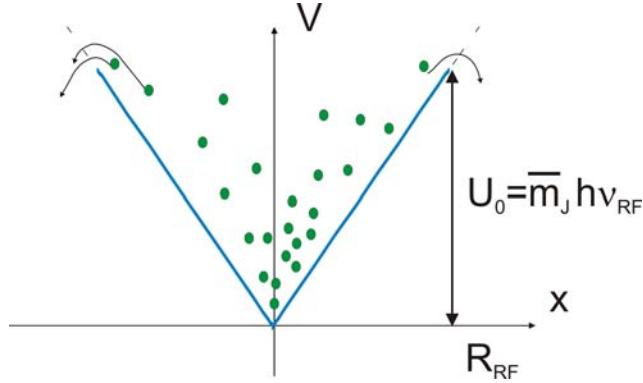
99

Figure 5.9: The simplified situation we consider for describing the continuous accumulation of metastable atoms in a finite depth quadrupole magnetic trap: we characterize the cloud by its mean magnetic quantum number $\overline{m_J}$, and the trapping potential is given by eq.(5.3). The trap is truncated at R_{RF} (position of the RF resonance) and has a depth $U_0 = \overline{m_J} h \nu_{RF}$.

which does not depend on $\overline{m_J}$.

5.4.1 Theoretical model for Cr

I will now detail the model in the case which was presented in the previous section. Throughout this section I will assume that the phase-space distribution of metastable atoms in the magnetic trap is that of an ideal classical gas at thermal equilibrium. This is equivalent to saying that: a) the elastic collisions are sufficiently fast to define a temperature T, b) the ratio η of the total trap depth U_0 to the temperature is sufficiently large that we can ignore the truncations of the Boltzmann distribution [79] and c) the atoms are non-interacting, so the single particle statistics are sufficient to calculate thermal averages of the relevant parameters. The validity of these assumptions will be investigated in detail in the next sections.

The RF frequency-dependence that we want to interpret will be taken into account by two terms in eq(5.18). One is the evaporation term, which depends on the trap depth, fixed by the RF frequency. The other ones are the loading rate Γ and the average energy per atom loaded in the MT, E', and we will show that both depend on the RF frequency.

The loss terms relevant to our problem (which we include in the model) are the collisions with the background gas, the collisions between the metastable and the MOT atoms, and the two-body losses. Other loss mechanisms, such as Majorana spin-flips and three-body recombination are negligible under the conditions (temperature and density) of our experiments.

Average energy per magnetically-trapped atom

In the case of a linear magnetic trap, the magnetic potential energy of a trapped atom, $V_{MT}(x, y, z)$, is given by eq.(5.3). At thermal equilibrium in the trap, the local mean energy of atoms in the MT is $\langle E_{MT}\rangle(\overrightarrow{r}) = \frac{3}{2}k_B T + V_{MT}(\overrightarrow{r})$; this expression assumes that the average kinetic energy per trapped atom is $\frac{3}{2}k_B T$, whatever the position of the atoms (which implies no correlation between position and velocity). The average total energy per trapped atom is then:

$$\langle E_{MT}\rangle = \frac{\int n_{MT}(x, y, z)\left(\frac{3}{2}k_B T + V_{MT}(x, y, z)\right)d^3r}{\int n_{MT}(x, y, z)d^3r} = \frac{9}{2}k_B T. \qquad (5.22)$$

The integral was evaluated using (5.5) and (5.6) for the MT potential $V_{MT}(x, y, z)$ and density distribution $n_{MT}(x, y, z)$.

An important remark can now be made, concerning the f_i coefficients defined in the energy rate equation (5.19). A given loss mechanism i leads to the heating of the cloud if the mean energy per lost particle is smaller than the mean trap energy; in our case, according to eq.(5.22), this condition reads: $f_i < 9/2$. If, on the contrary, $f_i > 9/2$, the mean energy per lost particle is larger than the mean trap energy, and the mechanism leads to the cooling of the cloud[2].

The loading terms

As mentioned in the previous chapter, the loading of the MT is due to the radiative leaks of the excited MOT atoms into the metastable $^5D_4$ state. We experimentally checked that the MOT atom number is not modified by the presence of the RF field (which indicates that the optical pumping rate due to the MOT lasers is much faster than spin-redistributions induced by the RF field). As a consequence we can assume in our model that the *total* production rate of atoms in the metastable states, Γ, does not depend on the RF frequency ν, and that the phase-space distribution of atoms arriving in the MT is identical to the MOT phase-space distribution:

$$n_{ph,MOT}(\overrightarrow{p}, \overrightarrow{r}) = n_{0,MOT}\frac{1}{2(\pi^{3/2})}\exp\left(-\frac{p^2/2m}{k_B T_{MOT}} - \frac{x^2 + y^2 + 4z^2}{2w_{MOT}^2}\right). \qquad (5.23)$$

Here, T_{MOT}, $n_{0,MOT}$ and w_{MOT} are respectively the 'temperature', peak density and 'size' ($e^{-1/2}$ radius) of the MOT. The spatial dependence of $n_{ph,MOT}$, with an aspect ratio of 2 between the vertical and horizontal directions, mostly reproduces the experimental one and allows great mathematical simplifications[3].

---

[2] This kind of arguments can be extended to any trapping potential, by recalculating the mean energy per trapped atom (in the case of an harmonic potential, for example, the 9/2 factor should be replaced by 3).

[3] We checked that the exact aspect ratio of the MOT, which typically ranges between 1.5 and 2 (depending on the day-to-day alignment of the MOT beams), does not modify much the physical parameters that we deduce from this theoretical model.

Let us note that the definition in eq.(5.23) may seem questionable, in the sense that we use the 'MOT temperature' in the conditions where a MOT is not a system at thermal-equilibrium. However the 'widths' of the momentum distribution, characterized by T_{MOT} (as well as that of the spatial distribution, characterized by w_{MOT}) is a physical quantity, which we experimentally measure.

The statistics of the atoms loaded in the $^5D_4$ state is described by the MOT phase-space density distribution $n_{ph,MOT}$. This allows one to calculate both the loading rate and the mean energy per loaded atom. For doing that, let us consider one atom right after its decay from the $^7P_4$ state to the $^5D_4$ state, at the time $t = 0$. If the decay process takes place at a position (x, y, z) and the atom has a velocity v, its total energy at $t = 0_+$ is given by:

$$E_{tot} = \frac{p^2}{2m} + V_0\sqrt{x^2 + y^2 + 4z^2}. \tag{5.24}$$

where p and (x, y, z) follow the distribution given by eq.(5.23). Due to the presence of the RF field, we have an energy filtering of the atoms arriving in the MT, as they can only be trapped in the $^5D_4$ state if their total energy is smaller than the trap depth. We can then deduce that the effective, RF-dependent loading rate of the MT, $\Gamma(\nu)$, is given by the total rate Γ times the probability $P(\nu)$ that an atom has a total energy E_{tot} smaller than the depth U_0 of the truncated MT:

$$\Gamma(\nu) = P(\nu)\Gamma \tag{5.25}$$

The probability $P(\nu)$ can be numerically evaluated by integrating the MOT phase-space density over a restricted domain D, defined by the condition $E_{tot}(p, \overrightarrow{r}) < U_0$ (see eq.(5.20) and eq.(5.24)):

$$P(\nu) = \frac{\int\limits_{D} n_{ph,MOT}(p, \overrightarrow{r})\ d^3p d^3r}{\int\limits_{R^6} n_{ph,MOT}(p, \overrightarrow{r})\ d^3p d^3r}. \tag{5.26}$$

Using the same argument, we can evaluate the average total energy per atom loaded in the truncated MT:

$$E'(\nu) = \frac{\int\limits_{D} E_{tot}(p, \overrightarrow{r}) n_{ph,MOT}(p, \overrightarrow{r}) d^3p d^3r}{\int\limits_{R^4} n_{ph,MOT}(p, \overrightarrow{r}) d^3p d^3r}. \tag{5.27}$$

Collisional losses

In this part we will consider the general case of collisional losses between two clouds, characterized by the density distributions $n_A(\overrightarrow{r})$ and $n_B(\overrightarrow{r})$ and the temperatures T_A and T_B. We will then apply the general expressions for the loss rate and for the mean

energy per lost particle to our magnetically trapped cloud, in the case of collisions with the background, of collisions with the MOT atoms, and in the case of collisions between metastable atoms.

The main assumption we make[4] for describing the mechanism of collisional losses is that the corresponding rates depend only on the local product of the two densities, with a constant coefficient of proportionality β, independent of $\overrightarrow{r}$. The loss rate of cloud A then reads:

$$\Gamma_A = \frac{\beta}{N_A} \int n_A(\overrightarrow{r})n_B(\overrightarrow{r})d^3r \tag{5.28}$$

and the average energy per lost particle is:

$$f_A k_B T_A = \frac{\beta}{N_A \Gamma_A} \int E_A(\overrightarrow{r})n_A(\overrightarrow{r})n_B(\overrightarrow{r})d^3r \tag{5.29}$$

where $E_A(\overrightarrow{r})$ is the total (kinetic plus potential) energy of a particle of the cloud A at the position $\overrightarrow{r}$. Using the two previous equations, and assuming that the mean average kinetic energy per lost particle is $3k_B T_A/2$, independent of the position $\overrightarrow{r}$, we obtain the following expression for the f_A coefficient:

$$f_A = \frac{3}{2} + \frac{1}{k_B T_A}\frac{\int E_{P,A}(\overrightarrow{r})n_A(\overrightarrow{r})n_B(\overrightarrow{r})d^3r}{\int n_A(\overrightarrow{r})n_B(\overrightarrow{r})d^3r} \tag{5.30}$$

where $E_{P,A}(\overrightarrow{r})$ is the trapping potential of the cloud A.

In the following paragraphs I will apply eq.(5.28) and (5.30) to the magnetically trapped atoms (cloud A) – using the expressions (5.6) and (5.5) for the density $n_A(\overrightarrow{r})$ and trapping potential $E_{P,A}(\overrightarrow{r})$ – in three cases:

- *background gas collisions*
  The one body loss rate due to collisions with the background gas can be modeled considering a uniform density distribution for the cloud B. This yields a constant value for the rate coefficient Γ_0, independent of the trap properties, such as number of atoms N and temperature T. This also implies that the average energy per lost atom will be equal to the average energy of atoms in the MT (i.e. $f_0 = 9/2$), and the background gas collisions will not lead to a change in temperature of the trapped cloud.

- *collisions with the MOT atoms*
  The loss rate corresponding to inelastic collisions with the MOT atoms is assumed to be proportional to the product of the MOT and MT local density, with a proportionality coefficient β_{PD} (inelastic loss parameter). This loss rate

---

[4] The same assumption was also made in the case of light-assisted collision in a MOT – see Chapter(4)

can be calculated from (5.28), considering that the density distribution $n_B(\vec{r})$ corresponds to the MOT density:

$$n_{MOT}(\vec{r}) = \int n_{ph,MOT}(\vec{r}, u)\sqrt{u}\,du = n_{0,MOT}\exp\left(-\frac{x^2 + y^2 + 4z^2}{2w_{MOT}^2}\right). \quad (5.31)$$

Using eq.(5.28) we find then:

$$\Gamma_1 = n_{0,MOT}\beta_{PD}F_1\left(\frac{w_{MOT}}{\bar{a}}\right) \quad (5.32)$$

where $F_1(x) \equiv \frac{x^5}{2}\left[-\frac{1}{x} + \sqrt{\frac{\pi}{2}}\left(1 + \frac{1}{x^2}\right)\left(1 - \mathrm{Erf}\left(\frac{x}{\sqrt{2}}\right)\right)\exp\left(\frac{x^2}{2}\right)\right]$ and $\mathrm{Erf}(x)$ is the error function. The $F_1(x)$ function is plotted in fig.(5.10.A). We see that $F_1(x)$ increases with $x = \frac{w_{MOT}}{\bar{a}}$, which can be intuitively understood considering that the overlap between the MT and the MOT increases when the MT size $\bar{a}$ decreases.
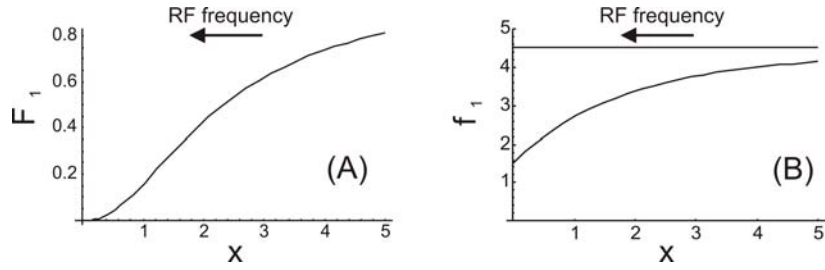

Figure 5.10: F_1 and f_1 as a function of the x parameter (ratio between MOT and MT sizes).

The corresponding f_1 factor is obtained from eq.(5.30):

$$f_1 = \frac{3}{2} + \frac{F_2\left(\frac{w_{MOT}}{\bar{a}}\right)}{F_1\left(\frac{w_{MOT}}{\bar{a}}\right)}, \quad (5.33)$$

where $F_2(x) \equiv \frac{x^7}{4}\left[\frac{4}{x^3} + \frac{2}{x} - \sqrt{2\pi}\left(1 + \frac{3}{x^2}\right)\left(1 - Erf\left(\frac{x}{\sqrt{2}}\right)\right)\exp\left(\frac{x^2}{2}\right)\right]$.

Fig.(5.10) shows the dependence of the f_1 factor on the ratio $w_{MOT}/\bar{a}$. We observe that collisions with the MOT atoms always result in the heating of the MT, as $f_1 < 9/2$; the heating becomes smaller when we decrease the RF frequency (as $\bar{a}$ decreases too, and the ratio x increases).

- *collisions between metastable atoms*
  The loss rate due to collisions between metastable atoms can be calculated making $n_A(\vec{r}) = n_B(\vec{r}) = n_{MT}(\vec{r})$ in eq.(5.28), which gives:

$$\Gamma_2 = \beta_{DD}\frac{n_0}{8}. \quad (5.34)$$

104

where β_{DD} is the inelastic collision parameter between two metastable atoms. For the corresponding mean-energy loss factor f_2 we find:

$$f_2 = 3. \tag{5.35}$$

This means that this process also leads to heating. This result (general, in fact, for any kind of trap) can be explained by the fact that the two-body inelastic losses are mostly localized close to the bottom of the trap, where the density is the highest and the potential energy of atoms is the smallest.

Evaporation

Due to the finite depth of the trap, all atoms having a total energy higher than the trap depth rapidly escape from the trap (in a time on the order of the average oscillation frequency of the trap – ~ 10 ms).

The evaporation process is triggered by an elastic collision between two atoms, which may promote one of them to an energy larger than the trap depth. The more energetic atom can then escape from the trap, leaving the other one with a lower energy than before the collision. The evaporation rate is given by:

$$\Gamma_{ev} = \frac{\sqrt{2}}{8}\Gamma_{el} \times f(\eta) \tag{5.36}$$

where $\Gamma_{el} = n_0\,\sigma_{el}\,\overline{v}$ is the elastic collision rate, with σ_{el} the elastic cross section and $\overline{v} = \sqrt{\frac{8k_BT}{\pi m}}$ the mean thermal velocity. The parameter $f(\eta)$, called the average evaporation fraction is given by (see [77]):

$$f(\eta) = \frac{2\sqrt{2}\left[e^{-\eta}(2\eta - 6) + e^{-2\eta}(\eta^2 + 4\eta + 6)\right]}{1 - (2\eta^2 + 2\eta + 1)e^{-2\eta}} \tag{5.37}$$

which is valid for $\eta \geq 4$, for which the density distribution in the trap is close to the one in an infinite-depth trap. The same reference [77] gives an expression for the average energy per evaporated atom:

$$f_{ev}k_BT = \left(6^{1/3} + \frac{\eta'^2 + 2\eta' + 2}{\eta' + 1}\right)k_BT \tag{5.38}$$

where $\eta' \equiv 1.035(\eta - 6^{1/3})$. In the limit of large η, the parameter f_{ev} tends to $(\eta + 1)$. Evaporation leads to cooling of the sample if $f_{ev} > 9/2$, i.e. if $\eta > 3.01$.

Majorana spin-flips

An important loss factor for magnetic traps with a field minimum close to zero (such as a quadrupole magnetic trap), in the case of cold (or, equivalently, small) clouds, is

the nonadiabatic (Majorana) spin-flip transitions. For cold atoms, this mechanism was demonstrated experimentally in [80], where the authors also provide a simple model for calculating the corresponding loss rates.

We use this model to estimate an order of magnitude for the Majorana loss rate Γ_{maj}. We find that the characteristic time scale Γ_{maj}^{-1} is much longer than the typical trap accumulation times, at any value of the RF frequency (shown in fig.(5.6)). For instance, for a temperature of 40 μK (RF frequency of 3 MHz) we find $\Gamma_{maj}^{-1} \sim 4$ s, whereas the corresponding loading time is only ~ 0.8 s.

5.4.2 Numerical results

Finally, the equations describing the accumulation and evaporation in the truncated MT are:

$$\frac{dN}{dt} = \Gamma(\nu) - (\Gamma_0 + \Gamma_1 + \Gamma_2 + \Gamma_{ev})N \qquad (5.39)$$

$$\frac{d(9Nk_BT/2)}{dt} = E(\nu)\Gamma(\nu) - (f_0\Gamma_0 + f_1\Gamma_1 + f_2\Gamma_2 + f_{ev}\Gamma_{ev})\, Nk_BT \qquad (5.40)$$

and Table(5.1) summarizes the different Γ_i and f_i coefficients.

i	Vacuum coll.	MOT coll.	D-D coll	evaporation
Γ_i	Γ_0	Γ_1	$\frac{\beta_{DD}n_0}{8}$	$\Gamma_{ev}(\nu)$
f_i	9/2	f_1	3	$f_{ev}(\nu)$
heating/cooling	–	heating	heating	cooling

Table 5.1: List of parameters for the rate equations describing the accumulation of the metastable Cr atoms in the RF-truncated magnetic trap.

We will now turn to the interpretation of the experimental results presented in Section(5.3). The experimental parameters of the MOT (peak density $n_{0,MOT} = 7.5 \times 10^{10}$ cm^{-3}, temperature $T_{MOT} = 120$ μK and size $w_{MOT} = 100$ μm) are independently measured and are not affected by the value of the RF frequency. In addition, the inelastic loss parameter β_{DD} (and therefore Γ_2) and Γ_0 were already measured independently, in the experiments discussed in Subsection(5.2.1).

We have therefore only three free parameters (Γ, σ_{ev} and β_{PD}) which we used to fit the numerical results to all experimental results concerning the RF-dependence of the MT density, steady-state total number of atoms and temperature, shown in fig.(5.5) and fig.(5.8).

The approach is the following: we numerically solve eq.(5.39) and (5.40) for different RF frequencies, and we compare the steady-state number of atoms, density and

temperature to the experimental results (see fig.(5.5) and fig.(5.8)). First we consider the regime of large RF frequencies ($\nu > 4$ MHz), for which the trap depth is much larger than the temperature of the atoms (for example for 8 MHz we have $\eta > 10$). In this case, the evaporation time Γ_{ev}^{-1} becomes much smaller than the accumulation time in the truncated MT. We can therefore set $\Gamma_{ev} = 0$, which reduces the number of free parameters to two.

By comparing the simulation results to the data, we then deduce the values of the loading rate $\Gamma = 3.3 \times 10^7$ s^{-1} and the inelastic loss parameter with the MOT $\beta_{PD} = (4.9 \pm 0.3 \pm 0.5) \times 10^{-10}$ cm^3/s (this value being in fairly good agreement with the one measured in reference [43]). The error bars are respectively, the statistic error of the fit, and the systematic error, due mainly to the uncertainty on the number of atoms.

Once the parameters Γ and β_{PD} determined, we tried to interpret the results for RF frequencies lower than 4 MHz, for which the role of evaporation is expected to be non-negligible. However, we find that varying the elastic cross section σ_{el} does not lead to large modifications of the numerical results. We interpret this by the fact that the RF frequency dependence of the loading parameters (eq.(5.24 -5.27)) and of the inelastic loss rates (fig.(5.11)) largely dominate the dynamics of the system, compared to the evaporation terms. This makes it impossible to deduce an experimental value of σ_{el} from the RF-accumulation results.

Conclusions

The main result of this analysis at high RF frequencies is the determination of the inelastic loss parameter between MOT atoms and the metastable atoms β_{PD}.

The analysis also shows what are the dominant inelastic collision processes, which limit the accumulation. For the accumulation without RF (or for large values of the RF frequency, > 8 MHz) we find that $\Gamma_1 \simeq 0.49$ s^{-1} and $\Gamma_2 \simeq 0.33$ s^{-1}. These two values are relatively close, which indicates that both the collisions with the MOT atoms and the D-D collisions limit the accumulation process.

The inelastic collisions with the MOT atoms, as well as the D-D inelastic collisions limit the total number of atoms that can be accumulated in the MT, and produce a strong heating. In absence of inelastic collisions, this temperature could be as low as $T_{MOT}/3 \simeq 40$ μK [81], while we experimentally observe temperatures up to 100 μK for large RF frequencies.

When lowering the RF frequency, we find that the evolutions of Γ_1 and Γ_2 are different. Indeed, as shown in fig.(5.11), the value of Γ_2 is almost independent of the RF frequency. This can be understood from the fact that it is proportional to the MT density (see eq.(5.34)), which remains constant (fig.(5.5)) for a large range of RF
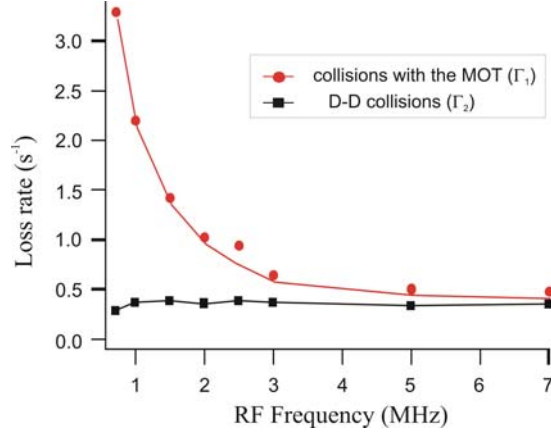
Figure 5.11: MT loss rates due to the collisions with MOT atoms (Γ_1 – circles) and to the D-D collisions (Γ_2 – squares) as a function of the RF frequency. The full lines are guides for the eyes.

frequencies. On the other hand Γ_1 increases rapidly when lowering the RF frequency – as the overlap between the two clouds increases – and the collisions with the MOT atoms become thus the dominant loss process.

As a final remark, let us notice that the theoretical model for evaporation (eq.(5.39-5.40)) allows us to make an additional estimate for the elastic cross section in the $^5D_4$ state. This is presented in the following paragraph, and represents in fact a second interpretation of the previous temperature measurements, presented in Section(5.2.2).

Second determination of the elastic cross section

The results presented in fig.(5.3) show that there is no substantial heating of the magnetically trapped cloud when applying a 3 MHz RF field, just after the MT has been loaded. This indicates that the cooling rate due to evaporation *exactly balances* the heating rate related to two-body inelastic collisions. We checked that for RF frequencies higher than 3 MHz, the cloud does heat, whereas we observe cooling when the RF frequency is lower.

Using eq.(5.40), assuming only one-body losses due to collisions with the background atoms, two-body losses due to D-D collisions and evaporation, and taking into account the experimental observation that $\frac{dT}{dt} \approx 0$, we have:

$$\frac{9}{2}\frac{dN}{dt}T \approx -f_0 NT\Gamma_0 - f_2 NT\Gamma_2 - (\eta + 1)\Gamma_{ev}NT \tag{5.41}$$

from which we deduce, using eq.(5.39):

$$\Gamma_{ev} \approx \frac{(9/2 - f_2)\Gamma_2}{\eta + 1 - 9/2}. \tag{5.42}$$

108

Using the experimentally-measured density n_0 (which, along with β_{DD} gives $\Gamma_2 = 0.27$ s^{-1}) and the evaporation parameter $\eta = 5.5 \pm 1$ (using eq.(5.14)), we deduce the evaporation rate: $\Gamma_{ev} = 0.20 \pm 0.04$ s^{-1}. This value is in reasonable agreement with our first estimate in Section(5.2.2), and confirms thus the first estimate of the elastic cross section $\sigma_{el.}$ of the Cr atoms in the metastable $^5D_4$ state.

5.5 Boltzmann equation and the issue of thermal equilibrium

In this section I present a complementary theoretical approach, based on the Boltzmann equation. The main purpose is to have a second model, which describes the loading dynamics of our finite-depth magnetic trap, and which does not assume that the thermal equilibrium of the magnetically trapped cloud is reached. For this reason, the results shown in this section – which are quite time-demanding – do not represent a fit of the experimental data, which were presented in Section(5.3). They are more a *verification* of the results obtained with the previous model, as we are using no adjustable parameters.

Thermal equilibrium in our experiments

The theoretical model presented in Section(5.4) showed that the continuous accumulation in our trap takes place in a time scale which is mostly fixed by inelastic collisions with the MOT atoms. For low RF frequencies ν, for which the spatial overlap between the MT and the MOT is optimal, the loading time T_{load} is short, between 300 ms and 1 s (see fig.(5.6)).

We now can raise the question of whether thermal equilibrium is indeed reached in the case of the continuous accumulation in the RF-truncated magnetic trap. For that, it would be necessary that there is a 'sufficient' number of elastic collisions taking place during the typical evolution time of the cloud, which is the loading time.

Using the previously-measured elastic cross section σ_{el}, we can have an estimate of the average number of elastic collisions undergone by the atoms before the steady-state is reached in our trap. This quantity is approximatively given by $n_0 \sigma_{el} \overline{v} T_{load}/2$, and we plot it in fig.(5.12). We used the peak density, loading time and mean thermal velocity that have been experimentally determined earlier.

One can see that the number of elastic collisions during the loading time decreases linearly when lowering ν; one can thus expect that thermal equilibrium of the trapped sample is not reached for low values of the RF frequencies. In order to better analyze this issue, we will develop a model based on the Boltzmann equation [82].
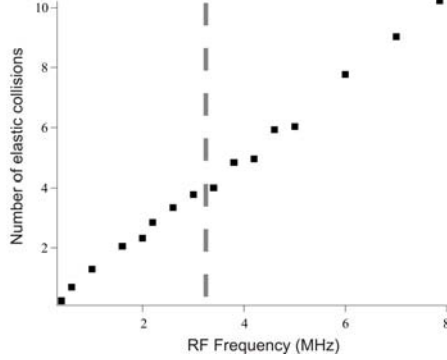
Figure 5.12: Number of elastic collisions within the loading $1/e$ time T_{load} of our trap, as a function of the RF frequency. The dashed line represents the frequency below which there are less than *four* elastic collisions during T_{load}.

Boltzmann and kinetic equation

The evolution of the phase-space distribution function $f(\overrightarrow{r}, \overrightarrow{p})$ of a classical gas in an external potential $U(\overrightarrow{r})$ is described by the Boltzmann equation:

$$\left(\frac{\overrightarrow{p}}{m} \cdot \overrightarrow{\nabla}_{\overrightarrow{r}} - \overrightarrow{\nabla}_{\overrightarrow{r}} U \cdot \overrightarrow{\nabla}_{\overrightarrow{p}} + \frac{\partial}{\partial t} \right) \mathbf{f}(\overrightarrow{r}, \overrightarrow{p}) = \Im_{coll}(\overrightarrow{r}, \overrightarrow{p}) \qquad (5.43)$$

The normalization of $f(\overrightarrow{r}, \overrightarrow{p})$ gives: $N = (2\pi\hbar)^{-3} \int d^3r d^3p f(\overrightarrow{r}, \overrightarrow{p})$. The left-hand side of eq.(5.43) describes the time-evolution of $f(\overrightarrow{r}, \overrightarrow{p})$ in the potential $U(\overrightarrow{r})$, in absence of collisions between particles. The collisional integral $\Im_{coll}(\overrightarrow{r}, \overrightarrow{p})$ in the right-hand side accounts for the elastic collisions between the particles, which modifies $f(\overrightarrow{r}, \overrightarrow{p})$. It depends on the microscopical detail of these collisions and is usually quite difficult to estimate, even in the simple case (which we will consider here) of low-temperature s-wave collisions, where the elastic cross section σ is temperature-independent.

Luiten et al. [79] showed however that this expression is greatly simplified when making the "sufficient ergodicity" assumption, i.e. that the phase-space distribution $f(\overrightarrow{r}, \overrightarrow{p})$ is a function only of the single-particle energy ϵ. This allows one to write:

$$f(\overrightarrow{r}, \overrightarrow{p}) = \int d\epsilon \delta \left(U(\overrightarrow{r}) + \frac{p^2}{2m} - \epsilon \right) f(\epsilon) \qquad (5.44)$$

where the function $f(\epsilon)$ can be interpreted quantum-mechanically as the 'occupation number' for the trap eigenstates with energy ϵ.

Although we will not detail here the demonstration of the kinetic equation, we mention that it is obtained by applying the operation $h^{-3} \int d^3r d^3p \delta(U(\overrightarrow{r}) + p^2/2m - \epsilon)$ to both sides of eq.(5.43); on the left-hand side the gradient terms (which represent

110

simple fluxes of particles) sum to zero, leaving $\rho(\epsilon)\dot{f}(\epsilon)$, where:

$$\rho(\epsilon) = \frac{2\pi(2m)^{3/2}}{(2\pi\hbar)^3} \int\limits_{U(\overrightarrow{r})\leq\epsilon} d^3r\sqrt{\epsilon - U(\overrightarrow{r})} \tag{5.45}$$

is called the trap density of states. As a consequence of the "sufficient ergodicity" assumption, $\rho(\epsilon)$ contains all the characteristics of the trapping potential; $\rho(\epsilon)d\epsilon$ gives the number of single-particle eigenstates in the trapping potential, having energies between ϵ and $\epsilon + d\epsilon$. In the case of a quadrupole magnetic trapping potential – given by eq.(5.5) – we find $\rho_{MT}(\epsilon) = \dfrac{8(2m)^{3/2}}{105\pi V_0^3\hbar^3}$.

Finally, in the case of sufficiently low temperatures (where the interaction between particles reduces only to the s-wave elastic collisions) the authors derive the following 'kinetic equation':

$$\rho(\epsilon_4)\dot{f}(\epsilon_4) = \frac{m\sigma}{\pi^2\hbar^3}\int d\epsilon_1 d\epsilon_2 d\epsilon_3 \delta(\epsilon_1+\epsilon_2-\epsilon_3-\epsilon_4)\rho(\min[\epsilon_1,\epsilon_2,\epsilon_3,\epsilon_4])[f(\epsilon_1)f(\epsilon_2)-f(\epsilon_3)f(\epsilon_4)] \tag{5.46}$$

where ϵ_3 and ϵ_4 (resp. ϵ_1 and ϵ_2) are the energies of the two colliding atoms before (after) the collision.

Thermal equilibrium

The kinetic equation can be used, for example, to study thermalization, i.e. the evolution of a system from an initial, non-equilibrium state towards a thermal equilibrium situation. We can thus find the result of [107], which shows that, in an *infinite trap*, it takes typically about *four elastic collisions* to reach a situation close, within a few %, to thermal equilibrium. Using this criterion in our case – see fig.(5.12), we see that indeed a lack of thermalization is expected at RF frequencies below ~ 3 MHz.

The authors of [79] apply the kinetic equation for describing the time-evolution of a non-equilibrium initial phase-space distribution of a gas in a finite-depth potential. Evaporation in such a case is easy to take into account by introducing an energy cutoff at the trap depth and simply removing, after each collision, the atoms with a total energy higher than the trap depth.

The important conclusion of [79], obtained by using the kinetic equation for a finite-depth trap, is the fact that one can use a distribution (the so-called 'truncated Boltzmann distributions') which is very close to the 'usual', thermal equilibrium Boltzmann distribution, in order to study the evaporative cooling in finite-depth traps.

Continuous loading and thermalization

I will now describe how we take into account the relevant physical mechanisms which influence the continuous loading of the finite-depth magnetic trap. For that,

I will include in the left-hand side of the the Boltzmann equation (5.43) a series of *local* terms, which take into account the physical mechanisms considered in the model described in the previous section (such as the loading and the different loss terms):

$$+ \Gamma f_{MOT}(\overrightarrow{r}, \overrightarrow{p}) - [\Gamma_0 + \beta_{DD} n_{MT}(\overrightarrow{r}) + \beta_{PD} n_{M0T}(\overrightarrow{r})] f(\overrightarrow{r}, \overrightarrow{p}). \qquad (5.47)$$

When applying the operation $h^{-3} \int d^3r d^3p \delta(U(\overrightarrow{r}) + p^2/2m - \epsilon)$ to each of these terms, we will obtain a series of terms which depend only on the energy ϵ and which will be added to the kinetic equation:

- *Loading from the MOT*
  For the loading from the MOT we obtain[5]:

$$\rho(\epsilon) \dot{f}(\epsilon) \mid_{load} = \Gamma f_{MOT}(\epsilon) \rho_{MOT}(\epsilon), \qquad (5.48)$$

  where $f_{MOT}(\epsilon)$ and $\rho_{MOT}(\epsilon)$ are the phase space distribution and density of states in the MOT and Γ is the loading rate. In order to calculate $f_{MOT}(\epsilon)$ and $\rho_{MOT}(\epsilon)$: (*i*) we assume that the kinetic energy distribution of the MOT atoms is that of thermal equilibrium at the temperature T_{MOT} and (*ii*) we neglect the initial potential energy of MOT atoms (which is equivalent to considering a small size of the MOT compared to the MT size), so that the MOT energy density of states is the one in free space. With these two assumptions we find: $\rho_{MOT}(\epsilon) = \frac{4\pi\sqrt{2}m^{3/2}}{h^3}\sqrt{\epsilon}$ and $f_{MOT}(\epsilon) = \exp(-\epsilon/k_B T_{MOT})$.

- *Background gas collisions*
  The background gas collision term gives:

$$\rho(\epsilon) \dot{f}(\epsilon) \mid_{bg} = -\Gamma_0 \rho(\epsilon) f(\epsilon), \qquad (5.49)$$

  where Γ_0 is a constant (energy-independent) rate.

- *Inelastic D-D collisions*
  The density-dependent inelastic collisions (such as the D-D collisions) are technically more difficult to take into account, because the kinetic equation does not directly provide the time-evolution of density distribution $n_{MT}(\overrightarrow{r})$. One can circumvent this problem in the "sufficient ergodicity" approximation. Indeed, by integrating eq.(5.44) over $\overrightarrow{p}$ we obtain:

$$n_{MT}(\overrightarrow{r}) = \frac{2\pi(2m)^{3/2}}{h^3} \int\limits_{\epsilon > U(\overrightarrow{r})} d\epsilon \sqrt{\epsilon - U(\overrightarrow{r})} f(\epsilon). \qquad (5.50)$$

---

[5] For simplicity we will use the notation ϵ instead of ϵ_4 – see eq.(5.46)

We account for the inelastic D-D collisions by adding an additional loss term:

$$\frac{\partial f(\overrightarrow{r}, \overrightarrow{p})}{\partial t}\Big|_{DD} = \beta_{DD} n_{MT}(\overrightarrow{r}) f(\overrightarrow{r}, \overrightarrow{p}) \tag{5.51}$$

in the right-hand side of eq.(5.43). Applying the operation $h^{-3} \int d^3 r d^3 p \delta(U(\overrightarrow{r}) - p^2/2m - \epsilon)$ to this equation gives:

$$\rho(\epsilon)\dot{f}(\epsilon)\Big|_{DD} = -\int d^3 r d^3 p \ \beta_{DD} n_{MT}(\overrightarrow{r}) f(\overrightarrow{r}, \overrightarrow{p}) \delta\left(U(\overrightarrow{r}) + \frac{p^2}{2m} - \epsilon\right) \tag{5.52}$$

The momentum integral in the right-hand side can be easily evaluated[6] and we finally obtain a simplified expression for the inelastic D-D collision loss term:

$$\rho(\epsilon)\dot{f}(\epsilon)\Big|_{DD} = -\left(2\pi \left(\frac{2m}{h^2}\right)^{3/2} \int\limits_{U(\overrightarrow{r}) \leq \epsilon} d^3 r \beta_{DD} n_{MT}(\overrightarrow{r}) \sqrt{\epsilon - U(\overrightarrow{r})}\right) f(\epsilon) \tag{5.53}$$

- *Collisions with the MOT*
  The collisions with the MOT lead to the additional term:

$$\frac{\partial f(\overrightarrow{r}, \overrightarrow{p})}{\partial t}\Big|_{PD} = -\beta_{PD} n_{MOT}(\overrightarrow{r}) f(\overrightarrow{r}, \overrightarrow{p}). \tag{5.54}$$

Following a similar approach as in the case of the D-D collisions, we obtain:

$$\rho(\epsilon)\dot{f}(\epsilon)\Big|_{PD} = -\left(2\pi \left(\frac{2m}{h^2}\right)^{3/2} \int\limits_{U(\overrightarrow{r}) \leq \epsilon} d^3 r \beta_{PD} n_{MOT}(\overrightarrow{r}) \sqrt{\epsilon - U(\overrightarrow{r})}\right) f(\epsilon)$$
$$\tag{5.55}$$

Numerical simulation and results

We now have a model based on the kinetic equation which can describe the dynamics of our system. The numerical method we use for solving the kinetic equation (with additional terms), is similar to the one presented in [79] (see Section **V** therein): we *discretize* both the time and energy scales. In this case evaporation becomes rather simple to take into account numerically, by fixing a RF-dependent energy cut-off at the trap depth U_0 (see eq.(5.43)): after each time-step t_i we 'remove' (by putting $f(\epsilon) = 0$) those particles which acquire an energy $\epsilon > U_0$.

---

[6] Using once more the 'sufficient' ergodicity' assumption we get: $\int d^3 p f(\overrightarrow{r}, \overrightarrow{p}) \delta\left(U(\overrightarrow{r}) + \frac{p^2}{2m} - \epsilon\right) = 4\pi m \sqrt{2m} \sqrt{\epsilon - U(\overrightarrow{r})} f(\epsilon)$.

The calculations are rather time-demanding (the main reason is that the inelastic collision term $\rho(\epsilon)\dot{f}(\epsilon)\mid_{DD}$ requires the knowledge of the density-distribution $n_{MT}(\overrightarrow{r})$ at each moment of time – see eq.(5.50)). As mentioned in the beginning of this section, we did not use the simulations for better fitting the experimental data, but for a confirmation of the results of our previous simple rate-equation model. We thus included the experimental parameters ($\Gamma_0, \Gamma, \beta_{PD}, \beta_{DD}$ and σ_{el}) deduced in Section(5.3).
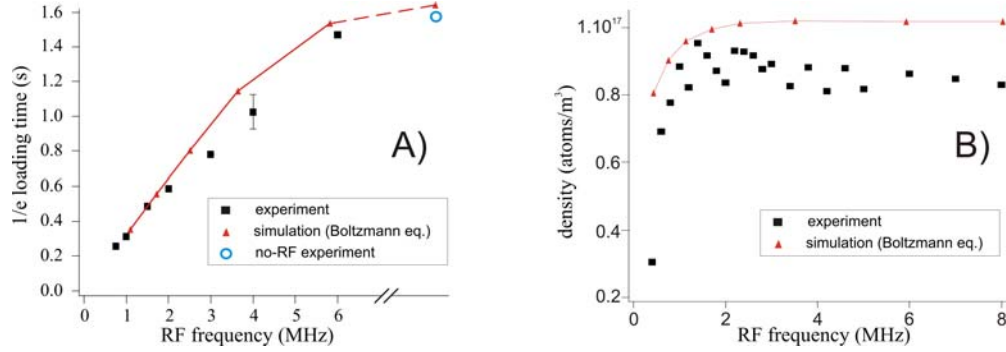

Figure 5.13: A) $1/e$ loading time of the RF-truncated MT, as a function of the value of the RF frequency: comparison between the experimental data (squares) and results of the simulations, using the modified Boltzmann equation (triangles). The circle in the upper-right corner represents the measured loading time, without RF. B) atomic peak density as a function of the value of the RF frequency: experimental data (squares) and simulations (triangles).
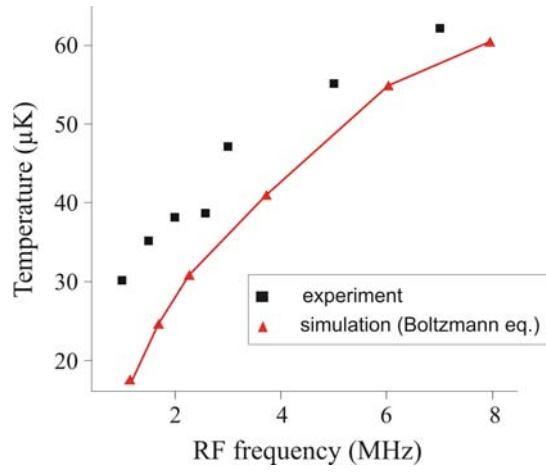

Figure 5.14: 'Effective temperature' of the RF-truncated MT, as a function of the value of the RF frequency: comparison between the experimental data (squares) and results of the simulations, using the modified Boltzmann equation (triangles).

The time-evolution of the number of atoms is found to be approximately exponential, even though the limiting factor comes from the inelastic collisions. A comparison with the experimental $1/e$ loading time is shown in fig.(5.13.A). The steady-state density distribution, calculated using eq.(5.53)), also reproduces roughly the thermal-equilibrium

distribution given by eq.(5.6). We use the latter to fit the simulated cloud shape and deduce the peak density, which is shown in fig.(5.13.B), together with the experimental data. Both for the loading time and for the peak density we find a reasonably good agreement with the experiment.

The final energy distribution $f(\epsilon)$ is not exponential (as it would be expected at thermal equilibrium), even for long loading times. This is an effect due to inelastic collisions, which prevent reaching thermal equilibrium. However, for comparing our results to the experimental data, we can always define, for example, the average kinetic energy of the sample; dividing it by $3k_B/2$, we obtain an 'effective temperature' T_{eff}. In fig.(5.14) we make a comparison between T_{eff} and the experimental 'temperature', and we again see a qualitative agreement between the simulation and the experiment.

Finally, we mention that in both cases (kinetic energy and density distribution), we estimate that the resolution and signal-to-noise ratio of our imaging system are not sufficiently good to detect any deviation from the thermal equilibrium distributions.

Conclusions

As mentioned above, the simulations using the Boltzmann equation show that thermal equilibrium is not fully reached. Because of inelastic collisions, this is observed even for the large values of the RF frequency (or without any RF).

Nevertheless, the results presented in the last paragraphs show that we have a good agreement with the experimental data, for the values of the different parameters that we used. Under these circumstances, the fact that the simple rate-equation model, presented in the previous section, provides good agreement with the experiments may seem fortuitous. We however think that this is explained by the fact that, even though thermal equilibrium is not reached, the physical quantities relevant to this model (density profile and 'effective temperature' – i.e. widths of the velocity distribution) are directly measurable in experiments, and may be used in the model.

5.6   RF-dressed magnetic potentials

5.6.1   Accumulation at low RF frequencies

In the previous sections of this chapter I presented the continuous accumulation of metastable atoms in a finite depth magnetic trap. We found that, at high trap depths, the main limitations for the loading process come from two factors: the inelastic collisions with the MOT (P-D collisions) and the inelastic collisions between metastable atoms (D-D collisions). On the contrary, at trap depths lower than the MOT temperature (which correspond to RF frequencies smaller than ~ 1 MHz) most of the atoms are not trapped. This explains the sudden decrease of the atomic density, which also

dramatically reduces the observed phase-space density.

However for RF frequencies on the order of 800 kHz or below, new interesting features appear in the absorption images. The $1/e$ size of the imaged cloud becomes much larger (see fig.(5.15)), and the atom lifetime is longer than the lifetime measured at 1 MHz.
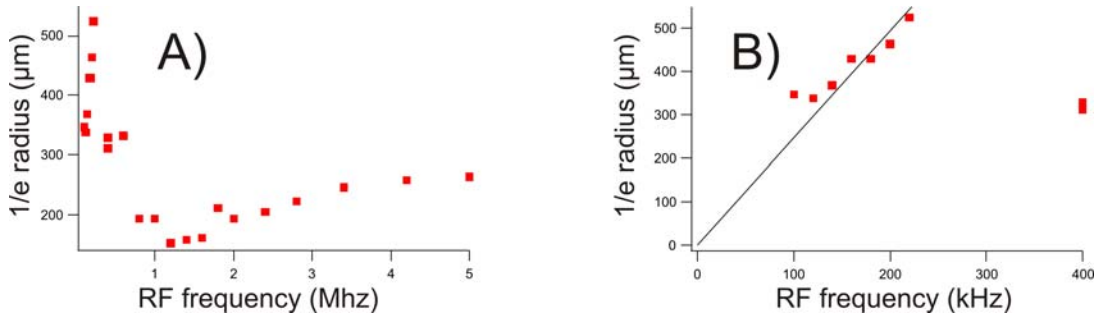

Figure 5.15: A) 1/e radius of the magnetically-trapped cloud (obtained by a Gaussian fit) as a function of the RF frequency. B) zoom for the RF frequencies smaller than 300 kHz, for which most of the atoms are trapped in the W-shaped potential and the cloud presents the shapes shown in fig.(5.19). We see that, for these frequencies the size increases linearly with the RF frequency.

We interpret these observations as the result of accumulation of atoms in the W-shaped, 'RF-dressed' magnetic potential minima, which are presented in fig.(5.16); this trapping technique has been proposed in [83] and experimentally demonstrated in [84]. Let us give an intuitive description of the accumulation mechanism, by considering the high-field seeking atoms, arriving in the $^5D_4$ state after decaying from the MOT. In absence of RF, these atoms are initially expelled form the trap center. When a sufficiently high RF power is applied, the atoms have their spin 'flipped' when passing over the RF-resonance position; they are thus projected into a low-field seeking state, and are then attracted back to the magnetic field minima ($B = 0$ point).

The correct quantum picture – detailed below – can be obtained by considering the interaction hamiltonian between the atoms and the total (static + RF) magnetic field. Diagonalizing this hamiltonian leads to the so-called 'RF-dressed' states schematically shown in fig.(5.16).

Our experimental observations show an interesting possibility of increasing the number of atoms accumulated in the metastable D states, by simultaneously reducing the two main limiting factors presented earlier ('P-D' and 'D-D' collisions). The 'usual' magnetic trap (i.e. without RF) and the MOT are both centered around the $B = 0$ point. From the P-D collision point of view, this configuration is most unfavorable, because it maximizes the overlap integral of the MT with the MOT. The density profile shown in fig.(5.16) is, from this point of view, much more favorable, because the metastable cloud presents a local density minimum at the MOT position (i.e. $B = 0$),
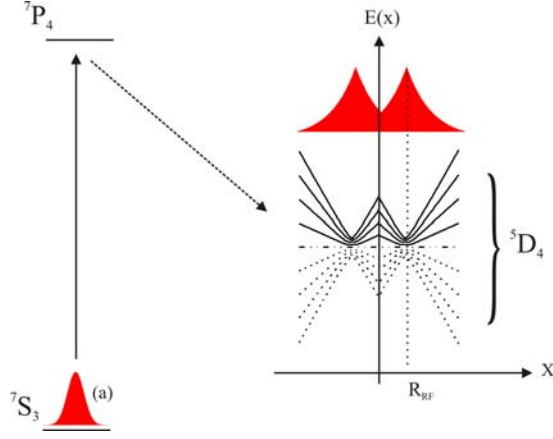
Figure 5.16: Continuous loading in a W-shaped magnetic trap.

thus potentially decreasing the overlap and the inelastic collision term. Additionally, the D-D inelastic collision rate (proportional to the inverse of the trap volume) also decreases, proportionally to the RF frequency.

Another potential advantage of the W-shaped potentials is that their minima are located away from the $B = 0$ region; this could prevent the Majorana spin-flip transitions and increase the lifetime of the trapped clouds, in the 'sufficiently cold' regime where they could be the limitative factor (which is however not the case in our quadrupole magnetic trap). This point will be revisited in Chapter(6).

In the rest of this chapter I study the possibility of efficiently accumulating atoms in such RF-dressed, W-shaped magnetic traps. The ideal scenario would be for the atoms, initially 'created' at the MOT ($B = 0$) position, to accumulate in large numbers and eventually tend towards a thermal equilibrium situation, with density distributions peaked around the avoided crossing positions.

5.6.2   Magnetic+RF adiabatic potentials

Let us now give a brief description of the 'RF-dressed adiabatic potentials'. For the details of these calculations, one can refer, for example, to [85].

The interaction (Zeeman) hamiltonian between the atom and the total magnetic field is: $H(\overrightarrow{r}, t) = g_J \mu_B \overrightarrow{J} \cdot [\overrightarrow{B(r)} + \overrightarrow{B_{RF}} \cos(\omega t)]$, where $\overrightarrow{B(r)}$ is the static magnetic field of trap, $\overrightarrow{B_{RF}}$ is the amplitude of the RF field and $\overrightarrow{J}$ is the total kinetic moment of the atom.

A convenient way to treat this hamiltonian is to consider the rotating frame, at the RF frequency; in this frame a time-independent hamiltonian can be obtained by making

the rotating wave approximation RWA (see for example [85]). By then diagonalizing the hamiltonian[7], one obtains the following eigenenergies ('dressed potentials'):

$$U_{m'_{RF}} = m'_{RF} \hbar \sqrt{\delta^2_{RF}(\overrightarrow{r}) + \Omega^2_{RF}(\theta)} , \qquad (5.56)$$

where m'_{RF} is an integer (going from $-J$ to $+J$), $\delta_{RF}(\overrightarrow{r}) = \omega - \frac{g_J \mu_B B(\overrightarrow{r})}{\hbar}$ is the RF-detuning with respect to the $|m_J\rangle \rightarrow |m_J \pm 1\rangle$ transition between adjacent Zeeman sublevels, and θ is the angle between the direction of the RF and static magnetic fields.

In eq.(5.56), $\Omega_{RF}(\theta) = \frac{g_J \mu_B B_{RF}}{2\hbar} \sin(\theta)$ is the RF coupling constant ('Rabi frequency'), and is proportional to the amplitude of the component of the RF magnetic field $\overrightarrow{B_{RF}}$ perpendicular to the direction of the static field $\overrightarrow{B}(\overrightarrow{r})$. We see that the maximum coupling ($\Omega_{RF,max.} \equiv \frac{g_J \mu_B B_{RF}}{2\hbar}$) occurs for an RF field which is perpendicular to the static field, whereas no coupling is possible if the two fields are parallel.
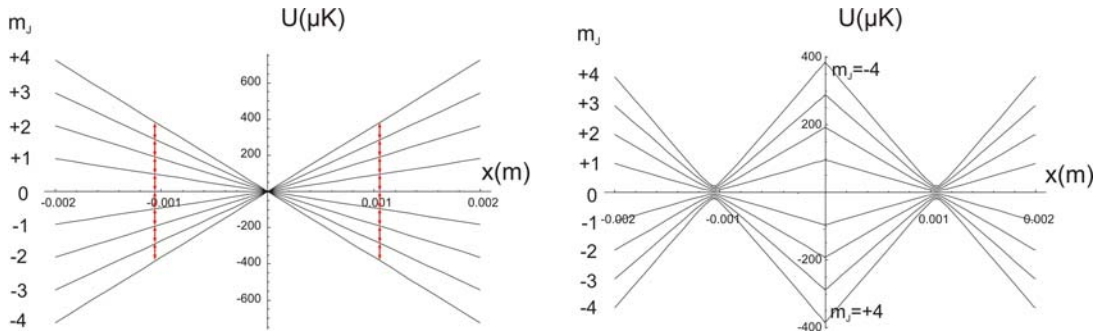

Figure 5.17: Zeeman levels without RF (left) and RF-dressed Zeeman potentials (right), for a RF frequency of 2 MHz.

The corresponding eigenstates ('dressed states'), labeled $|m'_{RF}\rangle$ are space-dependent linear superpositions of the Zeeman magnetic states $|m\rangle$ in absence of the RF field. When $\delta_{RF} \rightarrow -\infty$ a $|m'_{RF}\rangle$ state tends towards a given $|m_J\rangle$ Zeeman state, while when $\delta_{RF} \rightarrow \infty$, $|m'_{RF}\rangle$ tends towards the opposite, i.e. $|-m_J\rangle$ state.

In the case of a quadrupolar magnetic field, like the one in our experiment, the RF-dressed magnetic potentials are shown in fig.(5.17). We see that in the case of ^{52}Cr, because of the absence of the hyperfine structure (and thus of the quadratic Zeeman effect) all the RF resonances take place at the same position.

If $\omega = \delta_{RF}(0) \gg \Omega_{RF}$, the atoms 'produced' in the D-states in a given $|m_J\rangle$, at the position $R \simeq 0$ (far from the RF resonance point), will be virtually in an eigenstate $|m'_{RF}\rangle$ of the 'dressed' hamiltonian. In addition, if the RF-coupling is strong enough

---

[7] We note that the expression (5.56) is valid for ^{52}Cr, in absence of the non-linear Zeeman effect (because of the absence of the hyperfine structure) and all RF resonances between adjacent $|m_J\rangle$ levels are taking place at the same position R_{RF}.

(in the sense discussed in the following paragraph), it will adiabatically follow the corresponding RF-dressed potential.

Depending on their 'initial' m_J state when decaying to the metastable states (close to $R = 0$), atoms can feel two different types of potentials. If $m_J > 0$, which is a low-field seeking state in the 'undressed' picture, we recognize RF-truncated, finite depth potentials we studied in the first part of this chapter. On the other hand if $m_J < 0$, which is an untrapped, high-field seeking state in the 'undressed' case, the atoms will follow the W-shaped potential, which has two minima, as shown in fig.(5.17). In a 3D case the minima are located on the 'evaporation ellipsoid' (defined in Section(5.2.2)). The atoms will then oscillate around the equilibrium position (R_{RF}).

5.6.3 Landau-Zener crossings and lifetime

I will now consider the possibility of accumulating atoms in the W-shaped potentials, by analyzing the probability of an atom to adiabatically follow the 'RF-dressed' potentials.

The magnetic potentials coupled by the RF field can be regarded as several avoided crossings (see fig.(5.17)), all taking place at $R_{RF} = \frac{\hbar\omega}{g_J b'}$, given by the RF resonance condition $\delta_{RF}(\overrightarrow{r}) = 0$. An atom can remain trapped in the W-shaped potentials, as long as it adiabatically follows the initial dressed state at each passage at resonance; if a non-adiabatic transition, which projects the atom to an untrapped state (i.e. adiabatically connected to a $m_J < 0$ state at $R \rightarrow \infty$), occurs, then the atom will be lost from the trap.

For the simplicity of the discussion, let us consider for the moment only the case of a maximum coupling strength $\Omega_{RF,max.}$.

The situation is similar to the quantum-mechanical Landau-Zener problem for an avoided crossing between two intersecting levels. The non-adiabatic transition probability, in this simple case, is given by [86, 87]: $P_{LZ,2} = \exp\left(-\frac{\pi}{2} \frac{\Omega_{RF,max.}^2}{\dot{\delta}_{RF}}\right)$, where $\dot{\delta}_{RF}$ is the time derivative of the RF detuning $\delta_{RF}(\overrightarrow{r}(t))$ at R_{RF}.

In our case, the situation is more complicated, as we have not two, but $N = 9$ potentials which are crossing in the same point. Rather then giving an exact calculation of the diabatic crossing probability (by solving the Schrodinger equation, using the exact hamiltonian [88]) we will give an intuitive solution. For $N - 1$ avoided crossings (between N intersecting levels), the 'survival probability' of remaining in the same initial state is given by $(1 - P_{LZ,2})^{N-1}$.

Finally, the probability of undergoing a diabatic Landau-Zener transition, for one

passage at $r = R_{RF}$, is then given (replacing the value $N - 1 = 8$) by:

$$P_{LZ,9} = 1 - \left[1 - \exp\left(-\frac{\pi}{2} \frac{\Omega_{RF,max.}^2}{\dot{\delta}_{RF}} \right) \right]^8.$$ (5.57)

This expression is in agreement[8] with [88], and allows to estimate the rate γ_{LZ} of such diabatic passages, which fixes the cloud lifetime τ_{LZ}: $\gamma_{LZ} = 1/\tau_{LZ} = P_{LZ,9}/T$, where T is the time interval between two successive passages through the avoided crossing region.

In our case, the atoms are 'created' at the center of the W potential with a certain initial velocity v_0 obeying the thermal distribution at the MOT temperature T_{MOT}. Both the Landau-Zener probability (through the $\dot{\delta}_{RF}$ term) and the oscillation period T_0 depend on v_0. Atoms arriving at the resonance point have a velocity $v(R_{RF}) = \sqrt{v_0^2 + \frac{2m_J\hbar\omega}{m}}$ and the derivative of the detuning reads:

$$\dot{\delta}_{RF}(R_{RF}) = v(R_{RF})\frac{d\delta_{RF}}{dr} \mid_{R_{RF}} = \frac{g_J\mu_B b'}{\hbar}\sqrt{v_0^2 + \frac{2m_J\hbar\omega}{m}}$$ (5.58)

whereas for the oscillation period we find (neglecting the curvature of the potentials at the crossing point):

$$T_0(v_0) = 4\frac{m}{m_J g_J \mu_B B'}\left(2\sqrt{v_0^2 + \frac{2m_J\hbar\omega}{m}} - v_0 \right)$$ (5.59)

Using these two expressions and eq.(5.57) we can finally calculate the loss rate γ, by taking the thermal average over v_0:

$$\gamma = \frac{1}{\tau} = 4\sqrt{\frac{m}{2\pi k_B T_{MOT}}}\int_{-\infty}^{\infty}\frac{1}{T_0(v_0)}P_{LZ}(v_0)\exp\left(-\frac{mv_0^2}{2k_B T_{MOT}} \right)dv_0.$$ (5.60)

The loss rate depends on the RF frequency ω and on the RF coupling Ω_{RF}. In the experiments we want this loss rate to be smaller than all other inelastic collision loss rates, in order to never be limited by the non-adiabatic Landau-Zener transitions.

In fig.(5.18) we plot the dependence of the RF Rabi frequency Ω_τ which is required for obtaining a given Landau-Zener lifetime τ (1 s and 10 s) as a function of the RF frequency ω. We observe that Ω_τ increases with ω, as the atoms arrive at the avoided-crossing position with larger velocities $v(R_{RF})$.

This simple 1D calculation gives an order of magnitude for the RF field, considering an optimal RF coupling, i.e. an RF field orthogonal to the static field direction. In

---

[8] in the case (which applies here) where the adiabatic potentials at the crossing are equidistant.
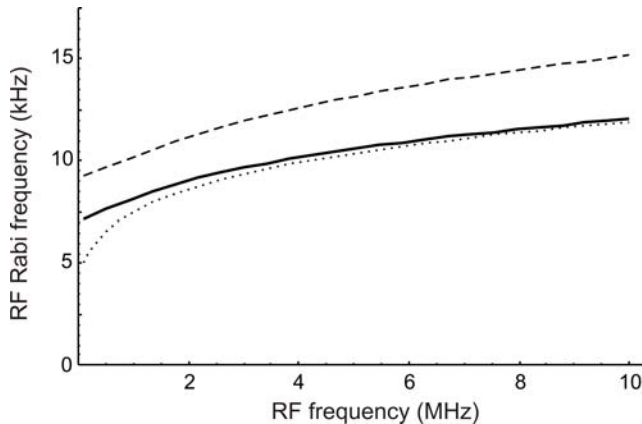
Figure 5.18: Solid, thick curve: RF coupling strength vs. RF frequency for obtaining a trap lifetime of 1s, considering an initial temperature of the atoms of 100 μK. The upper, dashed curve shows the Rabi coupling needed for a 10 s lifetime (for the same initial temperature of 100 μK). The dotted, lower curve shows, for illustration, Rabi coupling for a 1 s lifetime, in the case of lower initial temperature, of 10 μK (we observe, as expected, that at low RF frequency the required RF field is lower than for the $T = 100$ μK case, while at high RF frequency the initial temperature plays no role, and the two curves join together.)

our experiment, we use a 10 W RF amplifier. For an RF coil of 4 turns, having a 7 cm diameter and placed at 5 cm away from the atoms, we estimate that the coupling is ~ 200 kHz, well above the limit shown in fig.(5.18).

Leaks

In our experiment, the RF field (created by a single coil, placed above the upper viewport of the cell) is oriented along the vertical (z) axis; on the other hand, the direction of the static magnetic field (created by the MOT coils) is not spatially uniform.

We mentioned earlier (see eq.(5.56)) that only the projection of the RF field on the local static B-field direction can couple different m_J states; this means that, in our case, the 'effective' Rabi frequency will be space-dependent, given by $\Omega_{RF}(\overrightarrow{r}) = \sin(\theta)\Omega_{RF,max}$, where θ is the azimuthal angle, between the $\overrightarrow{r}$ direction and the z axis. The Landau-Zener transition lifetime will be position-dependent.

In practice, there will always be a region in space, corresponding to small azimuthal angles (i.e. for θ between 0 and a certain θ_{max}), for which the Landau-Zener condition will not be satisfied. The value of θ_{max} will be given by the maximum available RF power.

We estimate that, for $\Omega_{RF,max} \sim 200$ kHz, we have $\theta_{max} \simeq 2.2° \ll 180°$, which should lead to negligible leaks.

We however note that it is possible to completely avoid the 'leaks' problem, by creating a 'fast-rotating' RF field, who 'on average' couples all the direction of the space. Such a field can be easily created, using two RF coils with perpendicular axes,

121

whose currents are 90° out-of-phase: under these conditions the RF field direction rotates at the frequency of the RF field. We experimentally tested this possibility, and observed that the results (exposed in the following paragraphs) are not modified. For this reason we conclude that indeed the RF power is not a limitation in our case.

5.6.4 Experiments

Let us now come back to the experimental realization of the W-shaped potentials. As mentioned earlier (see fig.(5.15.A)), we observe an increase in the size of the magnetically trapped cloud for RF frequencies lower than 800 kHz. For even lower RF frequencies ($\sim$ 200 kHz) the slices through the absorption images clearly present a double-peak structure, shown in fig.(5.19), which is due to the atoms trapped in the W-shaped, RF-dressed adiabatic potential.
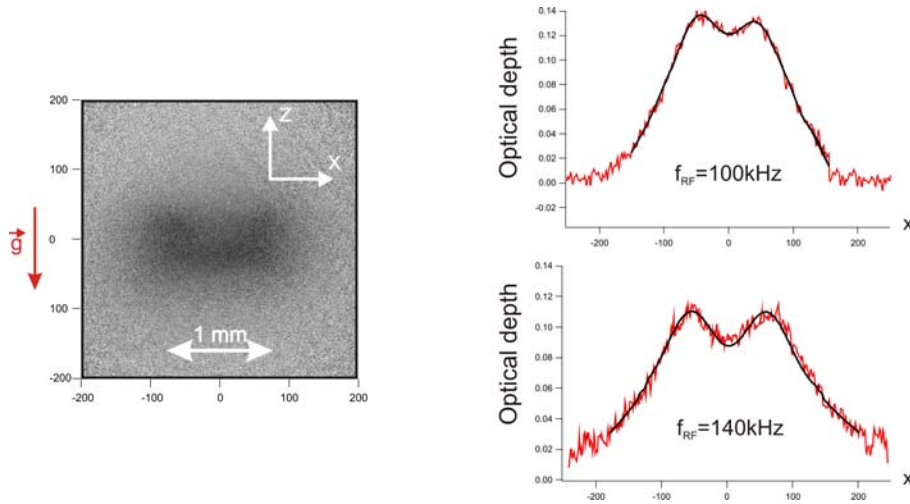

Figure 5.19: Left: image of the atomic cloud in the W-shaped magnetic trap. Right: horizontal slices through the image, passing through the $B = 0$ point, for two different RF frequencies.

We also observe that, because of the gravity, atoms are accumulated towards the bottom of the 'iso-B' ellipsoid. We experimentally checked (see fig.(5.15.B)) that the cloud size increases linearly with the RF frequency, while its vertical position is also linearly shifted downwards.

Another interesting feature is related to the dependence of the number of trapped atoms on the RF power – shown in fig.(5.20), for a value of the RF frequency of 300 kHz. Staring from zero, at low RF powers, we observe a drastic decrease of the number of trapped atoms, which is due to the plain evaporation of the atoms ('low-field-seekers' which were trapped in the absence of the RF).

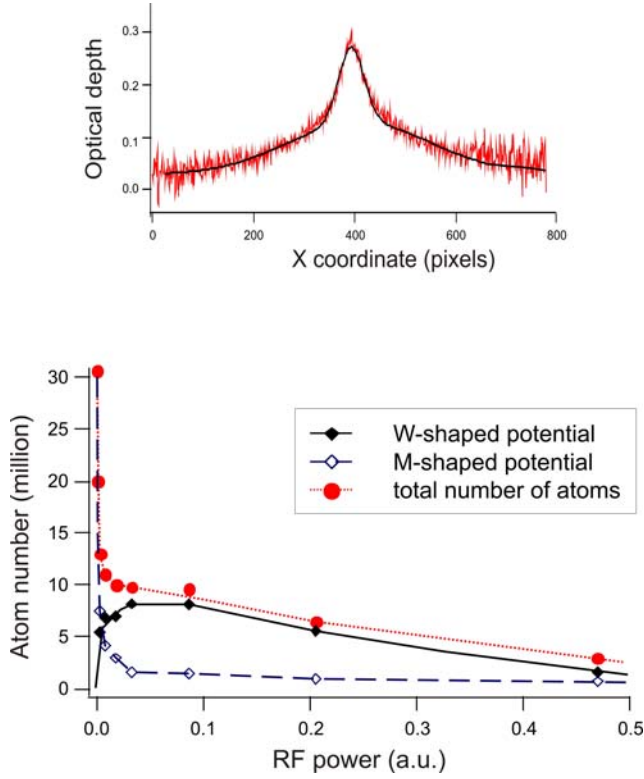When increasing progressively the RF power, we observe a change in the shape of

Figure 5.20: *Above:* horizontal slice through the center of the trapped cloud, for a RF frequency of 300 kHz. At low RF powers we observe a double structure, which is due to the superposition of the clouds trapped in the M-shaped and W-shaped RF-dressed potentials. The line represents a double-gaussian fit, from which we deduce the number of atoms respectively in the M- and W-shaped potentials. *Below:* Atom number in the W-shaped (full diamonds) and in the M-shaped potential (open diamonds), as well as the total number of atoms(dots) as a function od the RF power (for a constant RF frequency of 300 kHz). The lines are guides for the eyes.

the cloud. In fig.(5.20) we observe a double structure, which is the superposition of a central peak (due to the atoms in the M-shaped potential) and a larger structure that is due to the atoms trapped the W-shaped potential. We also plotted the number of atoms in each of the structures, as a function of the RF power, by performing a double-gaussian fit. We see that the atom number in the W-shaped potential (full diamonds in fig.(5.20)) increases with the RF power. This is due to the increase of the Landau-Zener adiabatic transition probability, accompanied with a progressive decrease of the solid angle through which atoms, uncoupled by the RF, escape from the trap.

When increasing further the RF power we unfortunately observe that the atom number in the W-shaped potential decreases back. We attribute this effect to the presence of RF harmonics, at twice the RF frequency, which are resonant with the transition between adjacent m_J-states at $2R_{RF}$. These second harmonics are responsible for unwanted spin-flips, which lead to the evaporation of the atoms which have enough energy to reach $2R_{RF}$. The number of these atoms is relatively high, since they are initially 'produced' at the position where $B = 0$, where they have the same potential energy as

when they reach $2R_{RF}$.

Perspectives

The experiments presented in this section demonstrate the possibility of creating large-volume ('W-shaped') traps in which high-field seekers can be trapped. Unfortunately, there are technical limitations, related to the presence of RF second harmonics (with a frequency 2ν), for efficiently loading metastable ^{52}Cr atoms in the W-shaped potentials.

Filtering these harmonics good enough is somewhat difficult to do. As a perspective, one could however think about the possibility of minimizing the influence of these harmonics, using a second RF field, with a frequency $\nu' > 2\nu$: in this case, the atoms undergoing a spin-flip at the position of the 2ν harmonics could be 'recuperated', by a second spin-flip at the position of the $\nu'-$resonance.

Another possibility is to find a way to prevent the atoms from reaching the second RF-resonance. In this respect, some interesting experiments, using an additional optical confinement, will be presented in the next chapter.

Conclusions

In this chapter I presented a new trapping scheme, which consists of the continuous loading of metastable ^{52}Cr atoms in a RF-truncated quadrupole magnetic trap. We were able to reach phase space densities up to 7×10^{-6}, in less than 1 s, which represents an increase of ~ 7 with respect to the typical value in Cr MOTs.

The theoretical rate-equation model presented in this chapter, provides a convenient tool to describe the loading dynamics of the finite-depth trap. This model shows in particular that heating due to inelastic collisions with the excited MOT atoms greatly limits the phase-space densities which can be reached.

Another important result of the experiments presented here is the measurement of the elastic and inelastic collisional properties of metastable ^{52}Cr atoms.

Finally, we investigated the possibility of accumulating atoms reaching the metastable states in a high-field seeking state, by the use of RF magnetic fields. Although technical problems, related to RF second harmonics, limit the number of atoms accumulated using this method, it opens the way to further experiments presented in the following chapter.

Chapter 6

Accumulation of ^{52}Cr metastable atoms into an optical trap

Why is Bose-Einstein condensation in our magnetic trap not possible for Cr?

Although it provides the means for exploring new interactions in degenerate quantum gases, the large magnetic moment of Chromium ($6\mu_B$ in the stretched state) is also a major experimental obstacle in achieving Bose-Einstein condensation in magnetic traps.

The measurement of a large inelastic collision parameter β_{DD} between metastable Cr atoms shows that it is not possible to use these states for achieving the BEC. Even in the ground state, in our quadrupole magnetic trap configuration, Majorana losses would become a limitation at temperatures close to the condensation threshhold.

Moreover, the works performed in T.Pfau's group in Stuttgart [76, 90] showed that, even in a Ioffe-Pritchard-type trap, with a non-zero magnetic field minimum, there are spin-changing collisional processes – dipolar relaxation and spin-exchange collisions – which are particularly important in Cr, and finally limit the achievable phase-space density. These processes lead to magnetic trap losses, as they can promote atoms in non-trapping, $m_J \leq 0$ states.

For instance, they measured a particularly high spin-exchange collision loss parameter $\beta_{s.e.} \sim 1 \times 10^{-10}$ cm^3/s. Spin-exchange collisions, which are processes where the total spin is conserved, can be suppressed by spin-polarizing the magnetically trapped sample in the $m_J = +3$ stretched state. However dipolar relaxation, which does not conserve the total spin, is still possible in these states ($\beta_{d.r.} \sim 3 \times 10^{-12}$ cm^3/s), and eventually leads to the de-polarization of the sample to lower m_J states; it limited the achievable phase-space density, in their experiment, to values $\sim 10^{-2}$.

Under these conditions, Bose-Einstein condensation in a magnetic trap seems a particularly difficult task in the case of Cr. The solution is the transfer of atoms from

the magnetic trap into an optical dipole trap (ODT). Although they are more difficult to use (mainly because of their limited depth), these traps have a major advantage, which is the fact that they also can be used to trap the high-field seekers. The atoms in these traps can be spin-polarized in the lowest-energy Zeeman state ($m_J = -3$, which is a high-field seeker). In this state, a spin-changing collision becomes energetically unfavorable, as it requires an increase of the Zeeman energy (of $\Delta E_{Zeeman} = g_J \mu_B B$). If ΔE_{Zeeman} is high enough compared to the temperature of the sample, there is not enough kinetic energy in the system to provide this extra energy, and the spin-relaxation processes are suppressed.

We consequently chose for our experiment, as a strategy to achieve Bose-Einstein condensation, to load atoms and perform evaporative cooling inside an optical dipole trap.

6.1 Optical trapping

In this section I will first present a simple classical model for the optical trapping potentials for neutral atoms, which mainly reproduces the description presented in a review paper by Grimm et al. [91], and which has the advantage of well explaining the physics of the problem.

In the last part I will present a theoretical model for multilevel atoms, and use it to evaluate the lightshifts in the case of $^7S_3$ and $^5D_4$ states of ^{52}Cr.

6.1.1 Classical model

Classical light – induced-dipole interaction

Let us consider the classical expression for the oscillating electric field of a laser light beam:

$$\overrightarrow{E}(r, t) = \overrightarrow{\varepsilon} \left[E_0(\overrightarrow{r}) \exp(-i\omega t) + E_0^*(\overrightarrow{r}) \exp(+i\omega t) \right] \tag{6.1}$$

where $\overrightarrow{\varepsilon}$ is the unitary vector of polarization and $E_0(\overrightarrow{r})$ is the fields' (space-dependant) amplitude. $E_0(\overrightarrow{r})$ is related to the local light field intensity by: $I(\overrightarrow{r}) = 2\varepsilon_0 c |E_0(\overrightarrow{r})|^2$, where ε_0 is the vacuum permittivity and c is the vacuum light velocity.

If an atom is placed into the laser light, the oscillating electric field (6.1) induces an atomic dipole moment $\overrightarrow{p}(\overrightarrow{r}, t)$. It oscillates at the field frequency ω and has an amplitude $p_0(\overrightarrow{r})$ proportional to the field amplitude:

$$p_0(\overrightarrow{r}) = \alpha \cdot E_0(\overrightarrow{r}) \tag{6.2}$$

where α is the polarizability of the atom . Usually $\overrightarrow{p}(\overrightarrow{r},t)$ and $\overrightarrow{E}(\overrightarrow{r},t)$ oscillate out-of-phase, which can be taken into account by allowing complex values for α.

The interaction potential between the light field and the induced dipole is $-\frac{1}{2}\overrightarrow{p}(r,t)\cdot\overrightarrow{E}(r,t)$. In the limit where the timescale for atomic motion is much larger than the oscillation period $\frac{1}{2\pi\omega}$, the atoms will only 'feel' the time-average of this interaction potential, which is called the *dipole potential*:

$$U_{dip} = -\frac{1}{2}\langle\overrightarrow{p}(r,t)\cdot\overrightarrow{E}(r,t)\rangle = \frac{1}{2\varepsilon_0 c}Re(\alpha)I(\overrightarrow{r}). \tag{6.3}$$

One can thus see that the dipole potential is proportional to the local laser field intensity $I(\overrightarrow{r})$ and to the real part of the atomic polarizability α (i.e. to the part of the atomic induced-dipole which oscillates in-phase with the light electric field).

The out-of-phase part of the atomic dipole, on the other hand, allows us to calculate the mean power which is absorbed by the atom $P_{abs} = \langle\dot{\overrightarrow{p}}\overrightarrow{E}\rangle$. This power can be expressed in terms of *photon scattering rate* and finally one finds:

$$\Gamma_{sc} = \frac{P_{abs}}{\hbar\omega} = \frac{1}{\hbar\varepsilon_0 c}Im(\alpha)I(\overrightarrow{r}). \tag{6.4}$$

Lorentz classical model

A very convenient way to derive the expression of the atomic polarizability α is the Lorentz (*elastically-bound electron*) model.

The electron, having a mass m_e, is assimilated to a classical, damped harmonic oscillator, characterized by the oscillation eigenfrequency ω_0 and the damping rate Γ. The oscillator is excited at the frequency ω by the Coulomb force of interaction with the external electric field. The time-evolution of the induced dipole $p = e\,x$ can be found by solving the classical equation of motion $\ddot{x} + \Gamma_\omega\dot{x} + \omega_0^2 x = -eE(t)/m_e$. The system is in equilibrium provided that the absorbed energy balances exactly the energy loss due to damping, which gives the expression of the damping coefficient: $\Gamma_\omega = \frac{e^2\omega^2}{6\pi\varepsilon_0 m_e c^3}$. This corresponds to the Larmor formula for an oscillating particle [93].

After some algebra, one finally finds the following expression of the atomic polarizability:

$$\alpha = 6\pi\varepsilon_0 c^3 \frac{\Gamma/\omega_0^2}{\omega_0^2 - \omega^2 - i(\omega^3/\omega_0^2)\Gamma} \tag{6.5}$$

Dipole potential

Finally, using eq.(6.5) for the polarizability of a two-level atom in the general expression of the dipole potential (6.3), we find:

$$U_{dip}(\overrightarrow{r}) = -\frac{3\pi c^2}{2\omega_0^3}\left(\frac{\Gamma}{\omega_0 - \omega} + \frac{\Gamma}{\omega_0 + \omega}\right)I(\overrightarrow{r}). \tag{6.6}$$

127

The scattering rate, useful for estimating the heating due to photon scattering, is given by:

$$\Gamma_{sc}(\overrightarrow{r}) = \frac{3\pi c^2}{2\hbar\omega_0^3} \left(\frac{\omega}{\omega_0}\right)^3 \left(\frac{\Gamma}{\omega_0 - \omega} + \frac{\Gamma}{\omega_0 + \omega}\right)^2 I(\overrightarrow{r}). \tag{6.7}$$

These expressions are valid in the case of *large detunings* and *negligible saturation*; they are not valid near resonance (where they both diverge).

In the case of a red detuning ($\omega < \omega_0$) atoms can be trapped at the local light intensity maxima, such as the focusing point of a laser beam; this is the case we consider in this thesis. For a blue detuning ($\omega > \omega_0$), the atoms are expelled form the intensity maxima (one can nevertheless trap them, for example in more exotic laser modes, like the 'donut modes').

In both cases the scattering rate decreases with the absolute value of the detuning $|\delta|$. This means that Γ_{sc} can be reduced, by detuning further the trapping lasers; the price to pay is, of course, a reduction of the dipole potential depth. An interesting and important feature of the optical traps is the fact that the ratio U_{dip}/Γ_{sc} increases with $|\delta|$, so one can, in principle, make Γ_{sc} arbitrarily small for a given dipole potential, by choosing a laser detuning sufficiently large and increasing accordingly the light power.

There are two types of optical traps, according to the value of ω with respect to ω_0. In most experiments the value of the detuning is much smaller than the optical frequency, so one has: $\Gamma \ll \delta \ll \omega_0$. In this case $1/|\omega + \omega_0| \ll 1/|\omega - \omega_0|$ and one can neglect the 'counter-rotating' term in eq.(6.6), which is the so-called 'rotating wave approximation'. The dipole potential simply becomes $U_{dip} = \frac{3\pi c^2 \Gamma}{2\omega_0^2} \frac{I}{\delta}$, and this type of trap is usually called a far-off-resonance trap (FORT).

Another type of traps are those for which the optical frequency is much smaller than the atomic transition frequency: $\omega \ll \omega_0$ and the two resonance terms in eq.(6.6) are almost equal. The dipole potential becomes: $U_{dip} = -\frac{3\pi c^2 \Gamma}{\omega_0^4} I$, which does not depend any more on ω; this gives the name of these traps: quasi-electrostatic traps (QUEST). Because of the extremely large detuning from resonance, QUESTs are quasi-non-dissipative traps, with optical scattering rates on the order of one photon *per hour*.

In the case of our experiment we use a 1075 nm laser, and we estimate that we are in an *intermediate situation* (as $\frac{\omega_0-\omega}{\omega_0+\omega}$ ranges roughly between 0.3 and 0.7 – see the transitions listed in Table(6.1-6.2)) where one should consider both terms in eq.(6.6).

Semi-classical polarizability for a two-level atom

A semi-classical expression of the polarizability can be obtained, by considering the interaction between a two-level atom (ground state $|g\rangle$ and excited state $|e\rangle$) and a classical laser field in the *low-saturation regime*. The result, in that case, is obtained [91]

128

from eq.(6.5), by simply replacing the oscillation frequency ω_0 by the atomic transition frequency and the damping rate Γ_{ω_0} by the damping rate corresponding to spontaneous emission:

$$\Gamma = \frac{\omega_0^3}{3\pi\varepsilon_0\hbar c^3}|\langle e|\widehat{d}|g\rangle|^2 \tag{6.8}$$

where $|\langle e|\widehat{d}|g\rangle|$ is the dipole matrix element between the ground and the excited state.

Light shifts

A similar result can be obtained in the case of a two level atom, in the 'dressed states' picture [92]. This result is obtained by applying the second order time-independent perturbation theory to the combined system 'atom plus light field' with the electric dipole interaction hamiltonian.

This perturbative treatment shows the interesting fact that the energy of the ground state is shifted by an amount (called 'light shift' or 'AC Stark shift') corresponding exactly to the dipole potential in the classical picture. Moreover, the excited state presents exactly the opposite energy shift.

6.1.2 Theoretical evaluation of the light shifts

We will now discuss the case of real atoms (Cr), where the simple two-level approximation does not apply because of the complex electronic structure, with many atomic levels coupled to each-other by the laser light. In this case one has to consider (the sum of) all the allowed couplings with other levels.

We will make here a theoretical estimate for the Cr light shifts, based on the spectroscopical data from NIST [106]. An interesting conclusion of these calculations is that the light shifts can in fact depend on the magnetic quantum number m_J and on the polarization of the light (as opposed to the case of alkali atoms where the light shifts are almost m_J-independent). In fact complications arise when a given level, or the levels it is coupled to, are not purely spectroscopic terms (i.e. the angular momentum L and the spin S are not good quantum numbers).

As in the case of a two-level atom, when a given atomic level i, of energy $\hbar\omega_i$, is coupled by a laser through dipolar electric transitions to other states n having energies $\hbar\omega_n$, its energy is shifted due to the presence of the AC laser electric field. This light shift depends on $I(\overrightarrow{r})$, the local laser intensity, on $\omega_{ni} = \omega_n - \omega_i$ and on Γ_{ni} (respectively the transition frequency and the cycling rate of the transition between the levels i and n) and on the laser frequency ω. The different Zeeman sublevels, corresponding to the magnetic quantum number m_{J_i}, are coupled differently to the excited states, and the

light shift not only depends on the total angular momentum J_i, but as well on m_{J_i} and on the laser polarization.

In the case where there is no hyperfine splitting of levels (as in the bosonic ^{52}Cr), the coupling rate $\Gamma_{m_{J_i},n}$ between a sublevel (i, J_i, m_{J_i}) and another level (n, J_n, m_{J_n}) is given by:

$$\Gamma_{m_{J_i},n} = \Gamma_{ni}(2J_n + 1) \times C^2_{J_i,m_{J_i},J_n,sign(\omega_{ni})\times q}. \tag{6.9}$$

Here q gives the polarization of the laser ($q = -1, 0, +1$ for σ^-, π or σ^+ light) and the 3J coefficient is $C_{J_i,m_{J_i},J_n,q} = \begin{pmatrix} J_i & 1 & J_n \\ -M_{Ji} & -q & M_{Ji} + q \end{pmatrix}$. We also remind that the selection rules impose that J_i and J_n may only differ by -1,0 or +1.

The light shift can therefore be written [91, 94] as:

$$U_{i,m_{J_i}}(\overrightarrow{r}) = -3\pi c^2 I(\overrightarrow{r}) \sum_n \frac{sign(\omega_{ni})\Gamma_{m_{J_i},n}}{\omega^2_{ni}(\omega^2_{ni} - \omega^2)} \tag{6.10}$$

which is the generalization of (6.6) in the case of multilevel atoms.

An interesting simplification occurs if the state i is a S ground state and if all the states it is coupled to (P states) belong to *true spectroscopic terms*, which means that they are fully characterized by their total orbital momentum L and spin S, in addition to the total momentum J (which is always a good quantum number). Then the cycling rate Γ_{ni} does not depend on the fine structure. Moreover, if the laser frequency is chosen such that *all* the detunings are large compared to the fine structure splitting, we can use the following sum rule over the 3J coefficients to get a great simplification:

$$\sum_{J_n=J_i-1,J_i,J_i+1} (2 \times J_n + 1)C^2_{J_i,m_{J_i},J_n,q} = 1, (\forall q) \tag{6.11}$$

From (6.10) we then see that the light shift is $m_{J_i} - independent$ and can be calculated by completely ignoring the fine structure splitting and the polarization of the light. A generalization of this discussion can be extended, with the same results, in the case of a hyperfine splitting. This conclusion applies, for example, in the case of the alkali species [91].

However this simplification is not valid anymore if either the state i or the levels it is coupled to are not pure spectroscopic terms, or if i is neither a ground state nor a S state; in this case Γ_{ni} depend on J_n. This is indeed the case of the ground state ^{7}S$_3$ of Cr, where the coupling to the excited P states depends on the fine structure of these states (see Table.(6.1)). The effect is even larger for the ^{5}D metastable states (Table.(6.2)), which are themselves not pure spectroscopic terms (as clearly shown by their non zero coupling to the ^7P states).

Level	J_n	λ_{ni} (nm)	Γ_{ni} ($\times 10^7\ s^{-1}$)
z ^7P	2	428.972	3.16
	3	427.480	3.07
	4	425.435	3.15
y ^7P	2	360.533	16.2
	3	359.349	15.0
	4	357.869	14.8
x ^7P	2	236.681	0.69
	3	236.591	0.55
	4	236.471	0.53
w ^7P	2	209.588	0.11
	3	209.539	0.11
	4	209.483	0.12

Table 6.1: Main atomic transitions contributing to the lightshift of the $^7S_3$ level of Cr.

Level	J_n	$\lambda_{ni}(nm)$	$\Gamma_{ni}(\times 10^7 s^{-1})$	Level	J_n	$\lambda_{ni}(nm)$	$\Gamma_{ni}(\times 10^7 s^{-1})$
z ^5P	3	540.979	0.62	x ^5D	3	291.114	2.6
w ^5P	3	278.07	14		4	288.929	6.6
y ^5P	3	464.617	0.87	u ^5P	3	259.185	6.5
z ^5F	4	438.498	0.27	v ^5D	4	252.712	5.3
	5	435.177	1.2	x ^5F	4	270.348	0.63
z ^5D	3	394.149	0.28		5	270.199	2.1
	4	391.916	0.92	w ^5D	3	262.660	0.93
x ^5P	3	305.388	7.97		4	262.286	1.3
y ^5F	4	303.704	5.4	w ^5F	5	260.357	0.62
	5	302.156	29.1	z ^5P	3	240.862	6.7
y ^5D	3	300.506	9.2	s ^5F	4	238.572	1.7
z ^3G	3	258.466	0.61		5	238.333	4.1
v ^5P	3	271.618	1.1	r ^5D	4	199.995	14

Table 6.2: Main atomic transitions participating to the lightshift of the $^5D_4$ level of Cr.

Results

Using eq.(6.10), we can now turn to the estimation of the light shifts of the levels of interest . The laser that we use for optical trapping has a wavelength $\lambda_{IR} = 1075$ nm and its polarization is linear.

In the experiments presented in this chapter, we accumulate atoms in a mixed optical + magnetic quadrupole trap (this configuration will be described in detail in Section(6.3)). This means that the magnetic field direction (which defines the local quatization direction) is changing with $\overrightarrow{r}$, and there is no good choice for q. The polarization seen by the atoms can change between a π polarization ($q = 0$) and an equal mixture – q_{inc} polarization – of $\sigma^+(q = 1)$ and $\sigma^-(q = -1)$ polarizations, corresponding to a local B-field respectively orthogonal and parallel to the laser propagation axis.

The results for these two polarizations, for the $^7S_3$ and $^5D_4$ states, are (in K):

$$
\begin{aligned}
U_{^7S_3,m_{J_i}} &=_{\sigma_{inc}} & I_0 \times (-198.6 - 0.3 \times m_{J_i}^2) \times 10^{-16} \\
&=_{\pi} & I_0 \times (-202.4 + 0.6 \times m_{J_i}^2) \times 10^{-16} \\
U_{^5D_4,m_{J_i}} &=_{\sigma_{inc}} & I_0 \times (-151.4 - 1.2 \times m_{J_i}^2) \times 10^{-16} \\
&=_{\pi} & I_0 \times (-174.6 - 2.4 \times m_{J_i}^2) \times 10^{-16}
\end{aligned}
\tag{6.12}
$$

where I_0 is the laser intensity, measured in W/m^2.

We observe a quadratic dependance in m, which is due to the fact that, for $q = 0$ and q_{inc}, there are no linear terms in m left[1] in the sum (6.10).

In conclusion, we observe that for the $^7S_3$ level there are only small differences, up to $\sim 3\%$, between the optical trap depths for different values of m_J. The situation is quite different for the $^5D_4$ level: up to 21% differences may be expected between the shifts of the $m_J = 0$ and $m_J = 4$ sublevels for a $\pi-$polarization.

6.2   Experimental setup

Optical setup

The optical dipole trap is created, in our experiment, by a CW Ytterbium fiber laser, model YLR-50-LP (IPG). This laser delivers a power of 50 W, at a central wavelength $\lambda_0 = 1075$ nm. The beam is monomode transversally, with a $1/e^2$ diameter of 2.2 mm.

A first optical stage, shown in fig.(6.1), is used for preliminary shaping the beam. The output of the fiber laser is protected against back-reflections by an optical isolator

---

[1] $C^2_{J_i,m_{J_i},J_n,0}$ and $C^2_{J_i,m_{J_i},J_n,+1} + C^2_{J_i,m_{J_i},J_n,-1}$ do not include terms in m for $J_n = J_i - 1, J_i, J_i + 1$

(transmission 93%). A single-passed AOM is used both as a fast switch for the beam and for controlling the laser power during forced evaporation ramps (the utility and the choice of this AOM will be explained in the following paragraphs). The beam diameter is reduced to 1.1 mm, with a 2 : 1 telescope placed before the AOM, in order to adapt its size to the aperture of the AOM and maximize the diffraction efficiency. Finally the diameter is increased back about to its initial size, with a second, 1 : 2 telescope.
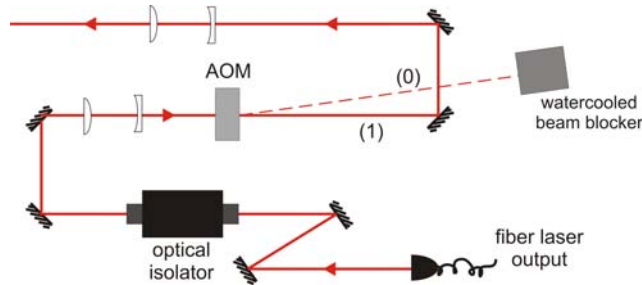

Figure 6.1: Setup for preliminary shaping of the optical dipole trapping beam.

After that, the beam is raised at the height of the experimental chamber (30 cm) with a periscope. A $\lambda/2$ plate and a polarizing beam-splitter (PBS) are used for separating the beam into the two arms of the crossed ODT. The power ratio between the arms can be changed with a motorized, computer-controlled rotation stage for the $\lambda/2$ plate. An alternate solution would be the use of two independent AOMs, one for each arm. Although less flexible, our method has the advantage of allowing the use of the entire available laser power during the single-beam ODT accumulation procedure (see below). A possible limitation comes from the maximum speed $(20°/\text{s})$ of the $\lambda/2$ plate rotation stage.

The two beams are finally focused inside the experimental chamber with plano-convex lenses, mounted on translation stages. In order to double the useful laser power, each arm is retro-reflected and focused back on the atoms. The direction of each IR beam can be finely adjusted using differential screws, which are used for the mirror mounts (M1 and M2 for the horizontal beam and M3 and M4 for the vertical beam – see fig.(6.2)). Finally, the light is sent to a water-cooled beam blocker.

Beam characterization

A weak fraction of the vertical IR laser beam, transmitted through a non-back-side-polished dielectric mirror (M0), is used to measure the transverse profile of the focused beam which is sent to the atoms. A lens, identical to the one producing the ODT, is used for focusing the weak transmitted beam onto a CCD camera, mounted on a micro-controlled translation stage. We can thus measure the size of the beam at different position and deduce the position and the size of the waist of this weak beam.
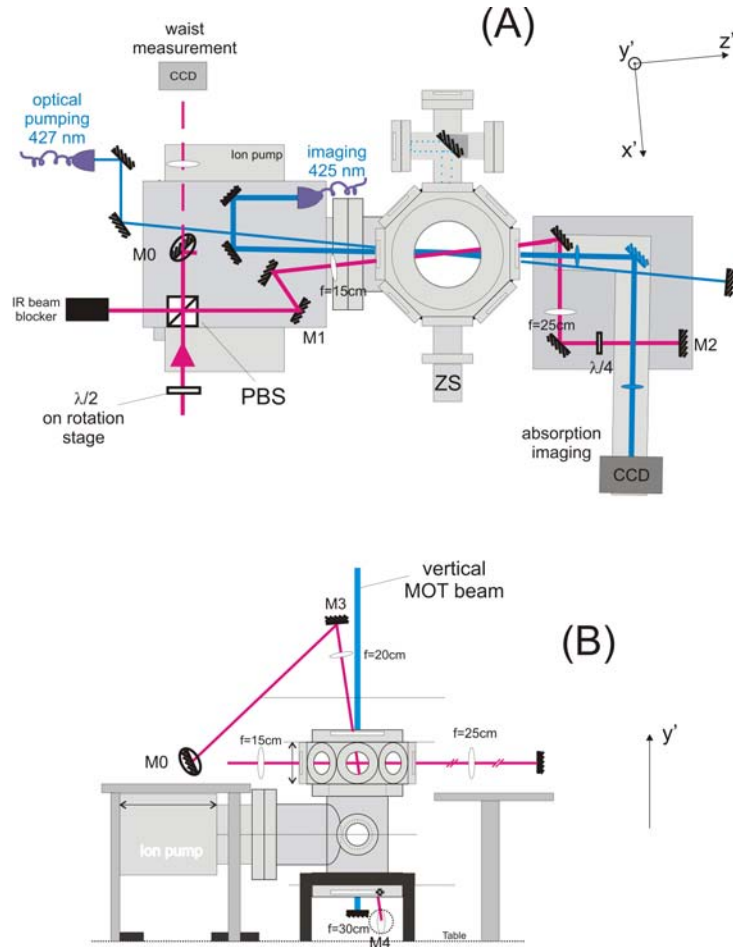
Figure 6.2: Optical setup for the coupling of the horizontal (A) and vertical (B) optical dipole trapping beams. The (x', y', z') reference frame, used throughout this chapter, is adapted for the description of the horizontal trapping beam configuration: z' is the beam propagation axis, while x' (horizontal) and y' (vertical) are orthogonal to the beam direction.

We should note however that this technique does not take into account thermal lens effects, related to the viewports of the vacuum chamber, which can modify the waist of the laser at the position of the atoms.

Beam profile dependence on the fiber laser power

The crossed ODT configuration requires a great deal of pointing stability of the two trapping beams. We tested the possibility of performing evaporative cooling by decreasing the power of the IR beam, by reducing the current of the fiber laser. As shown in fig.(6.3), we observed that the transverse position of the beam changes by up to 10 μm; moreover, the waist of the focused beam increases by almost 40% when
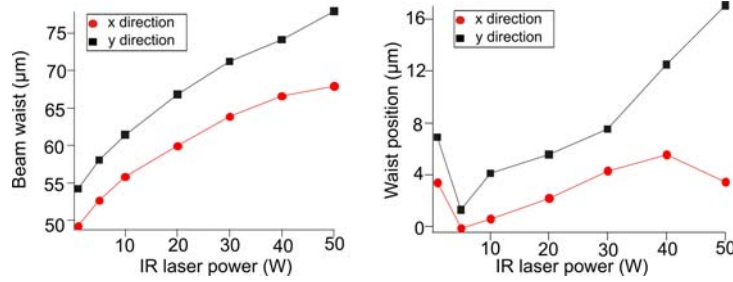
Figure 6.3: Left: size of the focused beam waist (using a 200 mm focal length lens) as a function of the fiber laser power. Right: position of the beam center (along x and y directions) as a function of the fiber laser output power. The measurements were performed with the transmitted beam shown in fig.(6.2).

increasing the power from 0 to 50W. Additional tests also showed that a significant intensity noise (with an amplitude up to 50% at 1 W) appears when the laser power is reduced below 10 W.

Choice of the AOM

The previous observations indicate that it is not possible to perform evaporative cooling in satisfactory conditions, by reducing the current of the fiber laser. An alternate possibility of controlling the ODT beam power is using an AOM (the price to pay being a loss of power, due to the limited diffraction efficiency).

We initially tested a first AOM (Gooch and Housego, model QS080-2G-5N3) working at 80 MHz and dissipating ~ 1 W of RF power for a maximum diffraction efficiency. After suddenly applying the RF modulation at $t = 0$, we observed that the transverse position of the focused beam varies by ~ 25 μm, and reaches a steady position only after a few seconds timescale. We attribute this evolution to slow thermal effects, related to the RF power dissipated in the crystal; this would cause problems during evaporative cooling experiments.
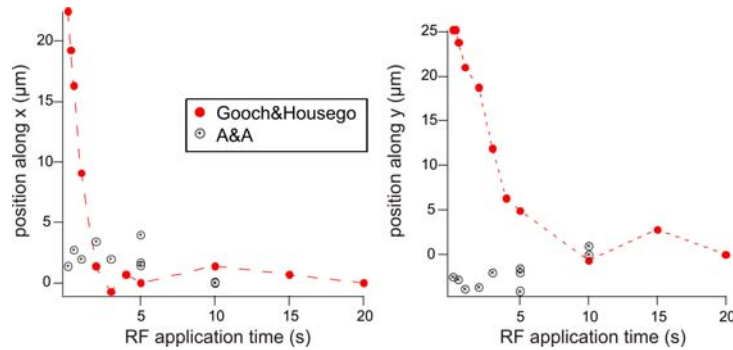
Figure 6.4: Position of the waist in the x (left) and y (right) directions, measured with the CCD 'test' camera, as a function of the application time of the AOM RF modulation.

We tested a second AOM ($A\&A$, model MTS $80-A3-1064$), which uses a different RF coupling technology, allowing a maximum diffraction efficiency for lower values of the RF powers (~ 0.2 W), minimizing thus RF-related thermal effects. The results of the analysis are shown in fig.(6.4) and we indeed observe much smaller displacements of the beam when applying the RF.

The maximum diffraction efficiency achieved with the $A\&A$ AOM is $\sim 77\%$ and the total maximum power available, after the optical setup shown in fig.(6.1), is $\sim 35W$.

Final focused beam characteristics
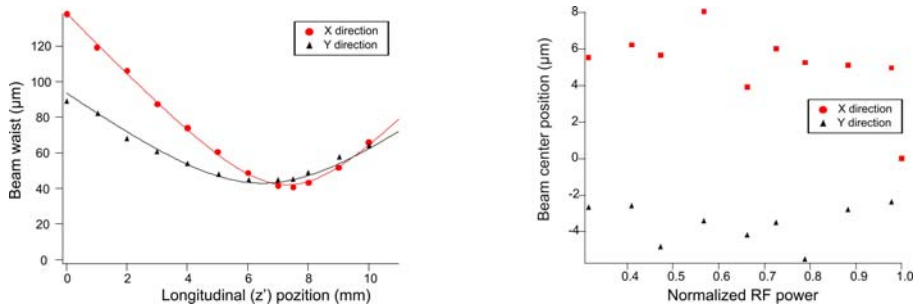
Figure 6.5: Transverse profile of the IR beam, after focusing with a $f_{IR} = 150$ mm lens, as a function of the longitudinal position (i.e. along the beam propagation direction). The measurement was performed at 50W and we observe the difference between the position of the waist in the two directions, due to the astigmatism of the beam.

In our experiments we tested three different values for the focused waists: $w_0 = 42$ μm, 55 μm and 80 μm (corresponding to a focal length of the focusing lens of respectively $f_{IR} = 150$ mm, 200 mm and 300 mm).

In fig.(6.5) we show the focused beam transverse profile (at 50 W laser power, $f_{IR} = 150$ mm and maximum AOM diffraction efficiency), in two transverse orthogonal directions, as a function of the longitudinal position (z'). At maximum diffraction efficiency we observe an astigmatism of the beam of ~ 1 mm, which is reduced at low AOM RF powers. We also observe very small variations of the center of the beam when lowering the RF power ($\simeq \pm 1.5$ μm) which is less than the pixel size of our beam analysis CCD camera.

The observation of the good beam pointing stability is a promising result for achieving evaporative cooling in the crossed ODT configuration.

Preliminary alignment procedure

The geometrical alignment of the horizontal and vertical IR beams onto the center of the experimental cell turned out to be a fairly difficult procedure, because of the fact that the center of the MT does not exactly coincide with the center of the experimental chamber. The method that we use in practice consists in superimposing an additional,

136

low-intensity 425 nm beam on the IR trajectory. This beam, resonant on the $^7S_3 \rightarrow$ $^7P_4$ transition, can be easily aligned onto the center of our magnetic trap.

The experimental procedure is the following: we first form a magnetically trapped cloud in the ground state and then pulse, for a few ms, the additional 425 nm beam. Because of spontaneous emission, the sample can be depolarized, within a few fluorescence cycles, to $m_J < 0$ states, which are expelled from the MT. Using the micro-controlled mirrors we can minimize the fluorescence of the remaining trapped atoms, and thus align the beam precisely on the center of the MT.

6.3   Accumulation of metastable ^{52}Cr in a mixed optical+magnetic trap

Loading an optical dipole trap with Cr atoms is not a straightforward generalization of the methods used for other atomic species. The most common technique is loading an ODT directly from a MOT: this is largely used in the case of the alkalis, where large number of atoms (up to $\sim 10^{10}$) are usually available in the MOTs. But even for alkalis there is no 'standard' technique for yielding the loading process 'efficient' (i.e. transferring up to a few million atoms left in the ODT).

One possibility [95] is to simultaneously operate the MOT and the ODT (this is possible if the cooling transition is only slightly shifted – due to the AC Stark shift –, such that the presence of the ODT beam does not affect much the functioning of the MOT). The MOT atoms traveling inside the ODT beam are accelerated by the optical potential; they can only remain trapped if they are efficiently cooled by the MOT friction force [96].

In other experiments, after fully loading the MOT, atoms are transferred in the ODT by applying additional cooling techniques: one may use optical molasses [97], Raman sideband cooling [98] or change the MOT configuration and forming an effective 'dark SPOT' [99].

These techniques are clearly not relevant in the case of Cr, because of the small number of atoms available in magneto-optical traps and of the large light-assisted collisions parameters, which greatly limit the atom number densities that can be reached in the optical trap, in presence of the MOT beams.

More recent techniques consist in transferring atoms from a previously-loaded reservoir (magnetic or optical trap) into an ODT [78]. This technique has been used, for example, for Cs [100] and Rb atoms [101], but also for ^{52}Cr [26]. In this reference, the authors start from a Ioffe-Pritchard type elongated MT, compress the trap and perform Doppler cooling in it and finally load a single axis ODT from this MT after some RF-evaporative cooling. The advantage of this configuration comes from the good matching between the MT and the elongated geometry of the ODT beam, which

is aligned along the weak axis of the MT.

Our experimental setup provides the possibility (presented earlier) of loading large atom numbers in a quadrupole MT. The trap geometry is however rather poorly adapted for obtaining a good matching between the MT and the ODT beam. We performed preliminary tests of forced RF evaporation in the MT, in presence of the ODT horizontal beam, which showed that this technique does not lead to an efficient loading of the optical trap. The reason for this stands in the large inelastic collision rates – (dipolar relaxation and spin-exchange collisions) which are favored by the tight confinement of the ODT – and in the Majorana spin-flips – which become an important limitation at low temperatures.

6.3.1 Optical trap and mixed trap geometries

Our idea was to test the accumulation of atoms in the optical dipole trap in the metastable states. As mentioned in the previous chapter, the metastable states are shielded from the light-assisted collisions due to the MOT lasers. However, the possibility of optical trapping for metastable Cr atoms has never been previously demonstrated; it was not obvious from the beginning that this strategy would be suitable, because of the high values of the inelastic collision parameters, both with the MOT atoms and amongst the metastable atoms, and of the higher densities which are expected in the ODT, as compared to the typical MT densities.

Optical trapping geometry

The spatial profile of the dipole potential is given by the intensity profile of the laser beam $I(\overrightarrow{r})$. In most of the experiments presented in this chapter we trap Cr atoms at the focus of a single (sometimes retro-reflected) laser beam. We will describe its intensity profile as a gaussian one, given by:

$$I(x', y', z') = \frac{I_0}{1 + (z'/z_R)^2} \exp\left(-\frac{2(x'^2 + y'^2)}{w^2(z')}\right) \tag{6.13}$$

where I_0 is the laser peak intensity at the focus point. The longitudinal variation of the beam $1/e^2$ radius is given by: $w(z') = \frac{w_0}{\sqrt{1+(z'/z_R)^2}}$, where w_0 is the waist of the beam and z_R is the Rayleigh length[2], i.e. the characteristic length-scale along the direction of propagation of the beam (z'). I_0 is related to w_0 and to the total laser power P_0 by:

$$I_0 = \frac{2P_0}{\pi w_0^2}. \tag{6.14}$$

---

[2] For a Gaussian beam $z_R = \frac{\pi w_0^2}{\lambda}$.

Reminding that the optical potential $U_{dip}(x', y', z')$ is proportional to the laser intensity we obtain the following expression:

$$U_{dip}(x', y', z') = U_0 \left[1 - \frac{1}{1 + (z'/z_R)^2} \exp\left(-\frac{2(x'^2 + y'^2)}{w^2(z')} \right) \right] , \qquad (6.15)$$

where we have chosen an offset of the potential such that $U_{dip}(\vec{r} = 0) = 0$. The depth of the optical trap[3] U_0 is proportional to the laser peak intensity I_0; using eq.(6.14) we find thus that U_0 is proportional to the laser power P_0 and inversely-proportional to the waist w_0:

$$U_0 \propto \frac{P_0}{w_0^2}. \qquad (6.16)$$

Oscillation frequencies

The atoms trapped in the optical dipole trap are oscillating around the bottom of the trap. Provided that their energy is small enough compared to the trap depth, they only explore a small region around the trap bottom in which the potential can be approximated to a harmonic potential.

One can in this case use the power series approximation of eq.(6.15) around $\vec{r} = 0$ and find:

$$U_{dip}(x', y', z') \simeq U_0 \left(\frac{2(x'^2 + y'^2)}{w_0^2} + \frac{z'^2}{z_R^2} \right) \equiv \frac{m(\omega_x^2 x'^2 + \omega_y^2 y'^2 + \omega_z^2 z'^2)}{2} \qquad (6.17)$$

which defines the transverse ($\omega_\perp \equiv \omega_{x,y}$) and longitudinal ($\omega_\parallel \equiv \omega_z$) oscillation frequencies:

$$\omega_\perp = \frac{2}{w_0} \sqrt{\frac{U_0}{m}} , \qquad \omega_\parallel = \frac{1}{z_R} \sqrt{\frac{2U_0}{m}}. \qquad (6.18)$$

Using eq.(6.16) we find the following dependence of the oscillation frequencies on the laser parameters:

$$\omega_\perp \propto \frac{\sqrt{P_0}}{w_0^2} , \qquad \omega_\parallel \propto \frac{\sqrt{P_0}}{w_0 z_R}. \qquad (6.19)$$

Mixed, magnetic and optical dipole trapping potential

The magnetic potential in the metastable states, presented in the previous chapter, is modified by the presence of an optical dipole trap. They form together a 'mixed',

---

[3] For sake of simplicity of the notations, we will call $U_{0,X}$, or simply U_0, the trap depth of the atomic level X (which is *always positive*), defined as the *absolute value of the lightshift* at the center of the beam U_X (which is a *negative* quantity for the levels ^{7}S$_3$ and ^{5}D$_4$, which are considered in this chapter): $U_{0,X} \equiv |U_X|$.

magnetic+optical potential which is schematically shown in fig.(6.6). Since the magnetic interaction potential depends on the m_J state of the atoms, there are five possible values with $m_J \geq 0$ for the atoms in the $^5D_4$ state. The optical potential also depends on m_J (as discussed above), but in a less important way – and, for sake of simplicity, we neglect this dependence.
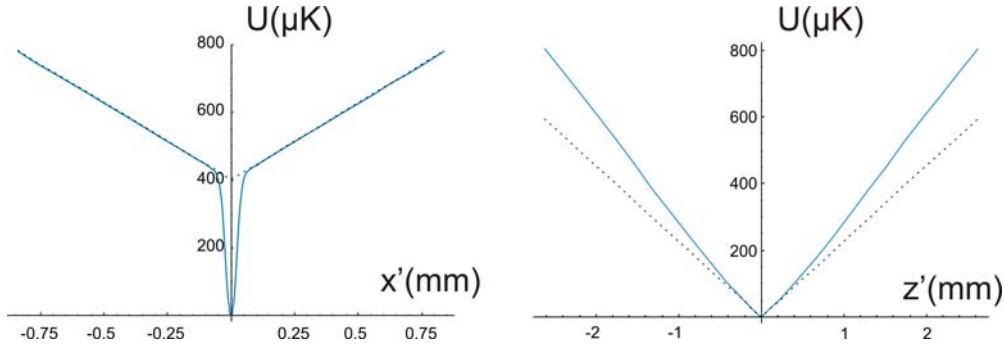

Figure 6.6: Mixed, magnetic+optical dipole potential for the ^{52}Cr atoms in the $^5D_4$ metastable state: in the x' direction (left) and in the z' direction (right). The dashed lines represents the purely magnetic potential. The optical trap parameters considered here are: $U_0 = 400$ μK, $w_0 = 42$ μm and $z_R = 2.5$ mm, and the magnetic potential corresponds to a $m_J = 4$ atom.

The expression of the mixed magnetic + single-beam optical dipole potential reads:

$$U(\overrightarrow{r}) = U_0 \left[1 - \frac{1}{1 + \left(\frac{z'}{z_R} \right)^2} \exp \left(-\frac{2(x'^2 + y'^2)}{w^2(z')} \right) \right] + m_J g_J \mu_B b' \sqrt{x'^2 + 4y'^2 + z'^2} \quad (6.20)$$

where m_J takes integer values, between 0 and 4. As it can be seen in fig.(6.6), for $m_J > 0$, the optical dipole potential is dominant, in the radial directions (x' and y'), near the trap center (i.e. for distances on the order of w_0), while at longer distances it is the magnetic potential which takes over. In the longitudinal beam direction (z') it is always the magnetic potential which dominates, for the typical experimental values of the Rayleigh length (a few mm) and of the magnetic gradient (~ 9 G/cm).

The $m_J = 0$ atoms, on the other hand, do not 'feel' the magnetic potential. They experience only the optical dipole potential of the horizontal beam, which overcomes the gravity and keeps them trapped in all three directions of the space (contrary to the case of a pure MT). Their longitudinal confinement is however much smoother than the one of the $m_J > 0$ states, and, for the same temperature, these atoms will expand over a larger space region in the z' direction, on the order of z_R.

Finally, the $m_J < 0$ atoms cannot be trapped in the mixed trap, as they are expelled from the $|B| = 0$ point along the z' direction by the magnetic force.

6.3.2 Experimental results

Experimental observations about the loading mechanism

During the optimization process of the optically trapped atom number, we found that is is crucial to keep the IR laser on during the whole MOT loading process. We observe that virtually no atoms are loaded into the ODT *directly* from the MOT (in the $^7S_3$ state), after switching off the MOT lasers. We additionally tested the possibility of loading the ODT with ground-state atoms from a (previously loaded) magnetic trap: we observe only little trapping if the ODT beam is turned on after the MOT beams were turned off, and magnetically trapped atoms from the D states were repumped into the $^7S_3$ state.

This indicates that the optical trap loading does not involve a loading mechanism of atoms from the metastable-state magnetic trap. The atoms are in fact directly injected from the MOT into the ODT, by spontaneous decay to the metastable sates. An atom from the MOT, traveling through the ODT experiences both the acceleration due to the optical potential and the friction force of the MOT [96]. If friction is large enough, and if it gets optically pumped in the metastable states while it is in the ODT beam location, an atom will remain trapped in the ODT.

We observed that the functioning of the MOT is not much affected by the presence of the ODT. We however noticed that, when the IR beam is well aligned with respect to the MOT, the central fluorescence of the magneto-optically trapped atoms is slightly decreased – due to the AC Stark shift of the cooling transition. By shifting the frequency of the MOT beams by roughly 3 MHz further to the red of the resonance, the peak fluorescence increases back, to a value $\sim 10\%$ higher than the one in absence of the ODT beam; this proves that the lightshift of the $^7P_4$ state is also negative (as it can be predicted by calculations), and larger than the one of the $^7S_3$ state.

Time sequence

The time-sequence used for accumulation of metastable atoms is the following. At t=0 we simultaneously turn on the MOT beams and the IR laser. After an accumulation time of $\sim 1s$, we switch off the ZS beams, MOT beams and magnetic field gradient. As already mentioned, it takes 20 ms for the eddy currents (and the corresponding induced magnetic fields) to die away and thus a 20 ms waiting time is necessary before taking the image of the atoms in the ODT. Moreover this time is also sufficient for the optically untrapped atoms to fall down under the gravity.

For imaging the remaining atoms we repump them in the ground state, by shining the 663 nm light during the 20 ms waiting time. The atoms are then polarized in the $|m_J = -3\rangle$ magnetic stretched state, in presence of a ~ 2 G quantization magnetic field, using the 427 nm light (according to the procedure described in the next chapter). The absorption image is taken on the $|^7S_3, m_J = -3\rangle \rightarrow |^7P_4, m'_J = -4\rangle$ transition.

The cloud number of atoms, size and density are extracted according to the procedure described thereafter.

The temperature of the atoms can also be measured using the ballistic expansion technique. For that the ODT beam is additionally switched off after a time τ (typically between 0.5 to 3 ms) before an absorption image is taken. The time-evolution of the transverse size is used for determining the 'transverse temperature' of the cloud. This technique cannot be applied to determine the 'longitudinal temperature', because of the much larger initial size of the cloud, which increases insignificantly after $\tau = 3$ ms (for longer expansion times the signal-to-noise ratio becomes too small for a reliable image analysis).

Accumulation results

The experiments presented here were performed using a $f_{IR} = 150$ mm focusing lens (IR beam waist $w_0 = 42$ μm). The IR laser beam is retro-reflected (unless specified otherwise) and a total of ~ 70 W IR laser power is sent to the atoms. Under these conditions the corresponding calculated trap depth, for the $^5D_4$ state, is $U_0 \simeq 420$ μK.

In fig.(6.7) we show the evolution of the trapped atom number as a function of the accumulation time. We observe a very fast loading process of the ODT trap, and the curve is well fitted by an exponential, with a $1/e$ characteristic time of 150 ms. The initial slope yields a loading rate of $\sim 1.1 \times 10^7$ atoms/s. At $t = 500$ ms the cloud has reached the steady-state and we can estimate the asymptotic number of atoms $N_\infty = 1.2 \times 10^6$, and the peak atomic density (20 ms after they are released from the MT) $n_0 = 1.2 \times 10^{11}$ cm^{-3}. The temperature of the cloud is $T = 120$ μK, which corresponds to a value of the evaporation parameter $\eta \equiv U_0/k_B T$ of ~ 3.5.
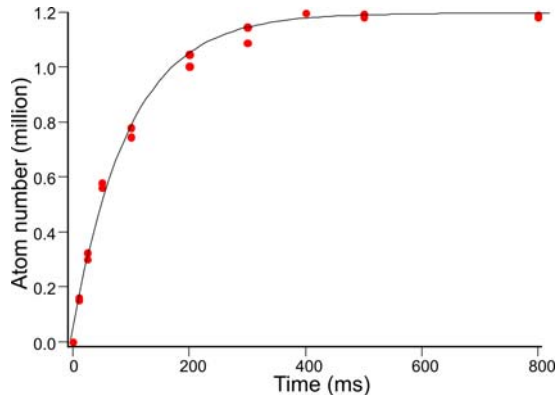

Figure 6.7: Loading curve of the ODT at a maximum laser power and in presence of the retro-reflected beam. The line represents an exponential fit of the data, with a characteristic $1/e$ loading time $\tau = 150$ ms

142

6.3.3 Diagnostic techniques

A closer look of the imaging system orientation, with respect to the optical trapping beam, is shown in fig.(6.8). We find it useful to use two different orthogonal basis: (x,y,z) is used to describe the images and (x',y',z') are the natural coordinates for the ODT. The angle between z (the imaging axis) and z' (the weak axis of the ODT), or between x and x' (one of the strong trapping axis of the ODT) is $\alpha = 7°$; $y \equiv y'$ is the vertical axis.
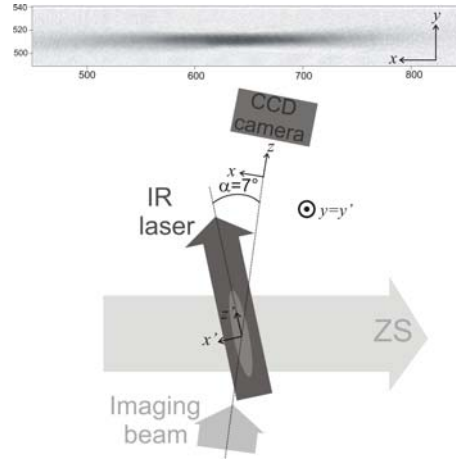
Figure 6.8: Top: image of an optically trapped Cr cloud, taken at $t = 20$ ms (after the extinction of the MOT beams and magnetic gradient at $t = 0$). Bottom: Orientation of the imaging system with respect to the ODT beam.

Single-beam ODT analysis

The optical depth (OD) measured in the plane of the CCD camera is given by:

$$OD(x, y) = \int\limits_{-\infty}^{+\infty} \sigma_{abs} n(x, y, z) dz \qquad (6.21)$$

In this expression, $n(x, y, z)$ is the atomic density of the optically trapped cloud and σ_{abs} is the light absorption cross section. The total number of atoms N_{at} in the trap is proportional to the total integral of $OD(x, y)$: $N_{at} = \frac{1}{\sigma_{abs}} \int\limits_{-\infty}^{+\infty} \int\limits_{-\infty}^{+\infty} OD(x, y) dx dy$.

In practice, to evaluate this integral, we first perform a numerical integration along x of $OD(x, y)$. The function obtained can be well fitted by a Gaussian, and from the fit parameters we deduce the value of the integral.

To obtain the peak density n_0 from the OD measurements, one needs information on the atomic density distribution. The ODT has a cylindrical revolution symmetry

around its weak axis, and the density dependence in y is decoupled from the ones on x and z: $n(x,y,z) = n(y)f(x,z)$ A cut of the $OD(x,y)$ along y gives therefore the shape of $n(y)$ ($\equiv n(y')$): this shape is roughly Gaussian, with a $1/e^2$ radius W_t (equal, for example, to 36 μm for $f_{IR} = 150$ mm and to 50 μm for $f_{IR} = 200$ mm). In addition, if the width of the density along the weak axis z', $\sigma_{z'}$, is much larger than W_t, we have around the trap center: $n(x',y',z') = n_0 \exp\left(\frac{-2(x'^2+y'^2)}{W_t^2}\right)$. Using $x' = x\cos(\alpha) - z\sin(\alpha)$, we thus obtain:

$$n(0,0,z) = n_0 \exp\left(\frac{-2(\sin(\alpha)^2 z^2)}{W_t^2}\right). \tag{6.22}$$

By integrating this equation we can therefore link the maximal value of the OD, OD_{max}, to the peak density:

$$n_0 = \frac{OD_{max}\sin(\alpha)}{\sqrt{\frac{\pi}{2}}\sigma_{abs}W_t} \tag{6.23}$$

This equation is valid as long as the imaging beam path through the atomic cloud (along z') is short compared to $\sigma_{z'}$, which gives: $\frac{W_t}{\tan(\alpha)} \ll \sigma_{z'}$. Introducing the width of $OD(x,y)$ along the x axis, $\sigma_x = \sigma_{z'}\sin(\alpha)$, we finally get the condition $\sigma_x \gg W_t$. Experimentally we measure $\sigma_{z'} \sim 700$ μm for $W_t \sim 50$ μm, which proves that the condition is well satisfied, and we can reliably use eq.(6.23) to deduce n_0.

In-situ images of the mixed trap

In experiments we are mostly interested in the loading optimization and characterization of the optically trapped clouds. It is nevertheless useful to have information on the atomic densities reached during the loading process, i.e. in the mixed magnetic+optical trap.

The analysis of in-situ images of the mixed trap is less straightforward, because of the more complex trapping geometry and because of the angle between the imaging axis and the ODT beam direction. An important part of the absorption signal of the cloud is due to the magnetically trapped atoms which are outside the optical trapping beam. In order to correctly estimate the peak atomic density, in the center of the mixed trap, one needs to distinguish between the signal which is due to the atoms in the ODT region and that of the atoms in the MT (located outside the optical trapping beam).

A useful technique for making this distinction is to consider two different horizontal slices through an absorption image, as shown in fig.(6.9). One of the slices passes through the center of the mixed trap, while the other is slightly off the ODT region. We make the assumption that the density of the large magnetically trapped cloud, which surrounds the ODT beam, varies on length-scales larger than the distance between the two sliced (typically 60 μm). In this case we may consider that the difference between

144
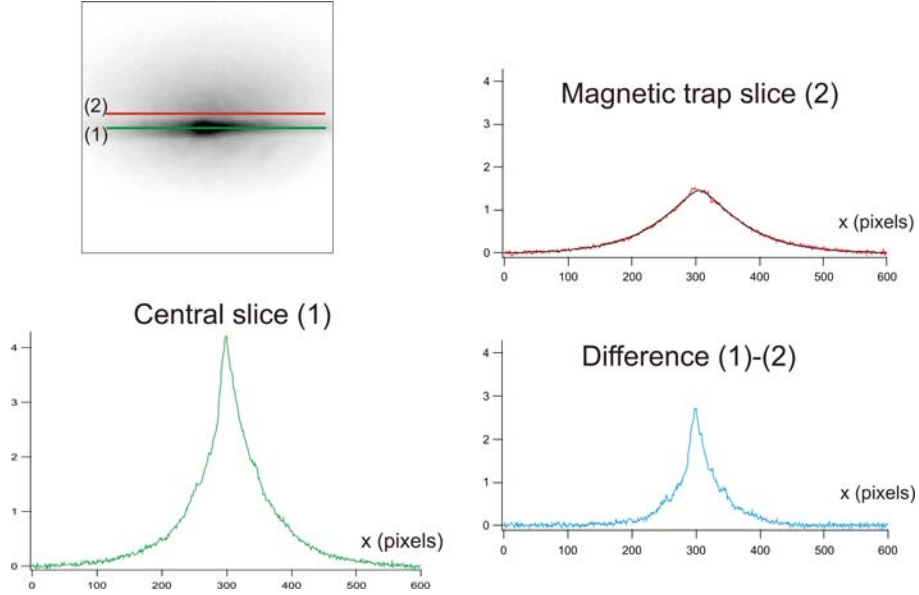
Figure 6.9: In-situ image of the mixed magnetic+optical trap. The image analysis, including two slices (the pixel size is 6.5 μm) of the image and their difference, is described in the text. The MT slice is fitted with the procedure described in Chapter(5), which gives a $1/e$ size $\bar{a} \simeq 300$ μm.

the two slices gives, to a good approximation, the optical depth profile $OD(x, y = 0)$ due only to the atoms located inside the ODT beam.

Analyzing this profile allows us to make estimations of the peak atomic densities reached during the loading process. Typical values, obtained under optimal experimental conditions, are up to 10^{12} atoms/cm^3. It is important to notice that the atomic density for the 'in-situ' mixed magnetic+optical trap (i.e. before the release of the magnetic field gradient and the 20 ms waiting time) is much higher than the value found earlier, for the pure ODT ($n_0 = 1.2 \times 10^{11}$ cm^{-3}). The drop in density we observe after 20 ms is mainly due to the longitudinal expansion of the atoms, in the shallow optical potential (along the z' direction), after being released from the tightly-confining magnetic trap.

We also notice that the profile in fig.(6.9.D) presents a double-structure, consisting of a narrow central peak and a larger profile (which is however narrower than the MT profile shown in fig.(6.9.C)). We interpret the narrow peak as coming from the atoms in $m_J > 0$ states, which are confined in the longitudinal direction mostly by the magnetic potential. The larger profile is a signature of the $m_J = 0$ atoms, which are insensitive to the magnetic potential, but can still be trapped by the optical dipole trap. We will come back to this point later, in Section(6.5).

6.3.4 Experimental issues

Waist position alignment

The preliminary alignment procedure, using a resonant beam (discussed earlier) is accurate enough for obtaining an initial starting signal of optically trapped atoms. A more precise alignment is however needed for matching the MOT and the beam waist position.

The transverse alignment of the beam, using the mirror mounts with differential screws, for maximizing the number of trapped atoms is quite straightforward. The longitudinal alignment of the waist, on the other hand, is more difficult, because of the lack of precision in pointing accurately the center of the elongated cloud (which is even more difficult because of the imaging geometry).

A more suitable alignment technique, that we use in practice, involves the parametric excitation of the atoms in the optical region of the mixed trap. This technique, which will be detailed later, provides a measurement of the parametric resonance frequency, which is proportional to the transverse oscillation frequency $\omega_\perp$ of the ODT.

The longitudinal position of the cloud center (for the $m_J > 0$ atoms) is fixed at the same position as the MT center (B=0), because the MT confinement along z' largely dominates the ODT confinement. Moving the beam focus with respect to the MT center will then change the beam $1/e^2$ diameter $w(z')$ at the position of the atoms. The local transverse oscillation frequency $\omega_\perp(z')$, proportional to $w(z')^{-2}$, will then change consequently, and will have a maximum value when $w(z')$ is at its minimum (i.e. when $w(z') \equiv w_0$).

We performed a series of experiments, varying each time the position of the beam focus (using the micrometric translation stage of the IR focusing lens) and measuring the parametric excitation resonance frequency. The results are shown in fig.(6.10.A), and the observed maximum corresponds to the position where the beam focus matches precisely the position of the MT center.
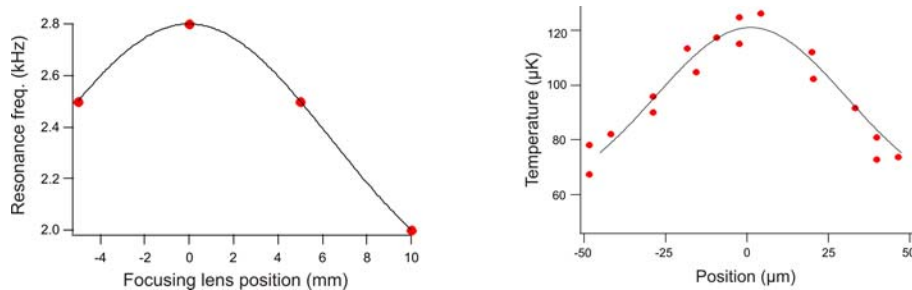

Figure 6.10: A): experimental dependence of the parametric excitation resonance frequency on the position of the focusing lens. The solid line is a lorenzian fit indicating the optimal position. B): Temperature of the cloud as a function of the transverse position (x') of the retro-reflected beam.

This procedure cannot be performed separately for the retro-reflected beam. A different method was used for adjusting the focus of this beam, by slightly missaligning it with respect to the 'main' beam; in this way, an atomic cloud could be trapped in each of the two beams. We then superposed the center of the two atomic clouds in the z' direction, by varying the focusing lens position.

Finally, a precise alignment of the retro-reflection of the trapping beam is possible by maximizing the trap depth. This was done by maximizing the temperature of the trapped cloud. The results of this technique are shown in fig.(6.10.B), where we plot the cloud temperature as a function of the transverse displacement between the two laser beams.

Choice of the optimal waist

We performed additional experiments, in search of the optimal waist of the optical trapping beam. For that, we changed the focal length of the lens used for focusing the IR beam onto the MOT. We repeated the alignment procedures described earlier (parametric excitation for different lens position, and temperature maximization for the retro-reflection of the beam).

We found that for $w_0 = 55$ μm (corresponding to $f_{IR} = 200$ mm) we obtain roughly the same number of trapped atoms as for $w_0 = 42$ μm ($f_{IR} = 150$ mm), whereas for $w_0 = 82$ μm ($f_{IR} = 300$ mm) the atom number is reduced by a factor ~ 0.8. The transverse temperature we measure ($T = 70$ μK for $f_{IR} = 200$ mm and $T = 32$ μK for $f_{IR} = 300$ mm) is in each case consistent with a value of the evaporation parameter η of $\simeq 3.5$. Since the $f_{IR} = 300$ mm value seems clearly less favorable than the other two, let us make a simple comparison between the two other cases ($f_{IR} = 150$ mm and $f_{IR} = 200$ mm).

For that, let us write the scaling of the peak density n_0 and the phase-space density $D_{ph.}$ with the laser geometric parameters w_0 and z_R. Assuming initial thermal equilibrium of the cloud in a 3D harmonic potential (with oscillation frequencies $\omega_\perp$ in two directions and $\omega_\parallel$ in the other), one can show that the peak density scales like: $n_0 \propto \frac{N\omega_\perp^2 \omega_\parallel}{T^{3/2}}$. Using eq.(6.18 - 6.19), as well as the experimental observation that $\eta = 3.5$ remains constant (which sets the temperature scaling: $T = \frac{U_0}{\eta k_B} \propto U_0$), we find that: $n_0 \propto \frac{1}{w_0^4}$. Finally, the phase-space density $D_{ph.} = n_0 \Lambda_{dB}^3 \propto \frac{n_0}{T^{3/2}}$ scales as: $D_{ph.} \propto \frac{1}{w_0}$.

We observe that both n_0 and $D_{ph.}$ increase when decreasing the waist w_0 of the laser. We thus conclude that the $f_{IR} = 150$ mm lens is the optimal choice: it provides the highest phase-space density, but also the highest density, i.e. the highest initial elastic collision rate, favorable for future evaporative cooling experiments.

As the best starting point (both in terms of phase space density and elastic collision rate) seems to correspond to the smallest experimentally-tested value of the waist, it would be interesting to extend our study to even smaller waist sizes. However we are limited, in the current setup, by the radius of the experimental chamber (12 cm) which prevents us from using lenses with shorter focal lengths.

Another possibility would be to increase the initial size of the IR beam, which would also reduce the waist after the focusing lens. This can however not be done in out current setup, because of limitations in the size of the optics used.

6.4   Measurement of the trap properties

In this section I present an experimental determination of the properties (depth and transverse frequency) of the optical dipole trap. This provides a direct measurement of the light-shift and polarizability of the $^5D_4$ metastable state.

6.4.1   Parametric excitation spectra

The parametric excitation is a commonly-used method for measuring the oscillation frequencies of optical dipole traps [105]. The method can be understood by considering an atom in a harmonic potential whose frequency ω_0 is modulated at a frequency ω_m. The equation of motion of the atom reads then: $\ddot{x} + \omega_0^2(1 + \varepsilon \sin(\omega_m t))x = 0$. Considering the modulation as a small perturbation one can solve this equation (see [102]) and show that the energy of the atom increases exponentially at the so-called parametric excitation resonance, when $\omega_m = 2\omega_0$.

Experimentally, the modulation of ω_0 can easily be performed with the AOM which adjusts the power of the trapping beam; one can see that this also translates into a modulation of the trap frequency. The measurement of a parametric resonance frequency can be done by either monitoring the heating of the cloud [103] or the reduction in the trapped atom number [104]. The first technique is well adapted for high values of η, where the cooling due to evaporation is negligible and the cloud heats without major losses in atom number. The measurements are quite straightforward, by monitoring the temperature increase using the time-of-flight technique. The advantage of this method is to keep the atoms at a sufficiently low temperature (i.e. close to the trap bottom) so that they experience an almost purely harmonic potential. In the second technique one takes advantage of the fact that, in a finite-depth ODT, heating translates into an increase of the evaporation rate, and thus of the number of atoms lost from the trap. In this case, effects related to the anharmonicity of the trap need to be taken into account (as discussed in the following paragraphs).

The parametric excitation spectra in the case of a single-beam optical dipole trap can be affected by systematic effects, because of the shallow confinement of the atoms in the longitudinal direction. In this case the beam waist, and hence the transverse oscillation frequency vary throughout the atomic sample, leading both to a broadening and a shift of the resonance. A solution to circumvent this problem is to form a crossed optical dipole trap, where the atoms are tightly confined in all three directions and explore a much smaller region of space.

In the case of our experiment, because of the high inelastic D-D collisional losses, it is impossible to obtain a sufficiently long-lived sample of metastable atoms in the crossed ODT and perform parametric excitation experiments. We chose to reduce the beam inhomogeneity effects by performing parametric excitation directly in the mixed magnetic+optical trap; in this configuration the longitudinal size of the cloud is greatly reduced (for the $m_J > 0$ states), by the magnetic confinement. As the cloud has a rather small initial value of η ($\simeq 3.5$), we use the second technique described above: we monitor the atom losses as a function of the modulation frequency.
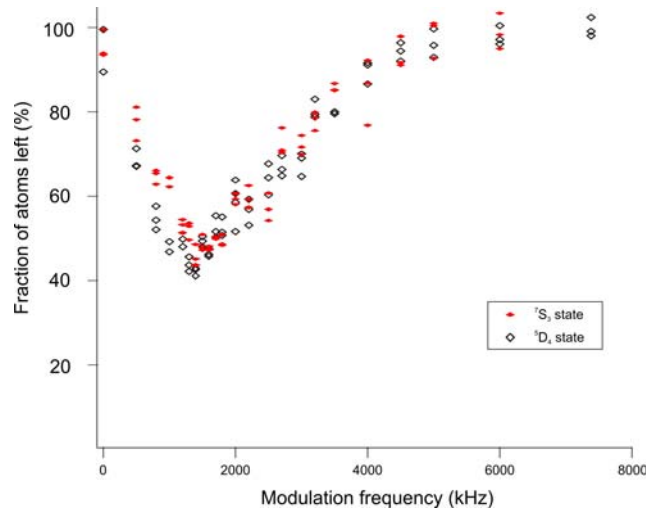

Figure 6.11: Experimental parametric excitation spectra for the $^5D_4$ state (open diamonds) and for the $^7S_3$ state (full diamonds). We plot the number of atoms left in the ODT (in %) versus the trap modulation frequency, after an excitation duration of 40 ms.

For modulating the power of the trapping beam we apply a sinusoidal modulation to the voltage controlling the amount of RF power sent to the AOM. We modulate this voltage around a value corresponding to 29 W of power in the diffracted beam ($\sim 80\%$ of the maximal value), in order to obtain an almost linear intensity modulation. The laser power is modulated with a 20% peak-to-peak amplitude. These experiments were performed for a IR beam waist $w_0 = 55$ μm ($f_{IR} = 200$ mm), for which the cloud temperature is $\simeq 60$ μK. To reduce additional errors related to the retro-reflected beam waist position and size, the excitation spectra was acquired using only the incident

trapping beam.

The time-sequence we use is the following: we first load the mixed trap for 1 s. After switching-off the MOT and ZS beams we apply the modulation of the optical trap power for 40 ms. Finally we monitor the losses in the optical trap by switching-off the magnetic field and imaging, 20 ms later, the remaining cloud. We repeat the sequence, for different values of ω_m, and the results are shown in fig.(6.11). For comparison, we also measured the excitation spectra in the $^7S_3$ state, by first repumping the atoms, before applying the 40 ms trap depth modulation.

We observe that the lineshapes obtained are rather broad, with relatively well-defined minima, the one corresponding to the $^5D_4$ state being slightly shifted to lower frequencies. A detailed interpretation of these spectra, yielding an estimate of the induced lightshifts, is presented in the following section.

6.4.2 Simulation of the parametric excitation spectra

Eq.(6.17) shows that a gaussian optical dipole potential can be approximated to a harmonic potential near the trap bottom, where the quantized energy levels are almost equidistant. This is no longer true for higher energies, as it may be seen in fig.(6.12). We plotted the oscillation frequency (difference between two adjacent energy levels) as a function of the energy, and we observe indeed that this frequency decreases with the energy.

As the oscillation amplitude of an atom depends on its energy, only the least energetic atoms, oscillating near the trap bottom, feel a 'purely' harmonic potential. We note that, for an initial temperature of the cloud of 120 μK (which is only ~ 3.5 smaller than the trap depth) there are already many atoms oscillating at $\sim 85\%$ of the trap bottom oscillation frequency (see fig.(6.12)). The atoms are heated further during the parametric excitation, and they eventually explore the anharmonic regions of the optical potential before leaving the trap.
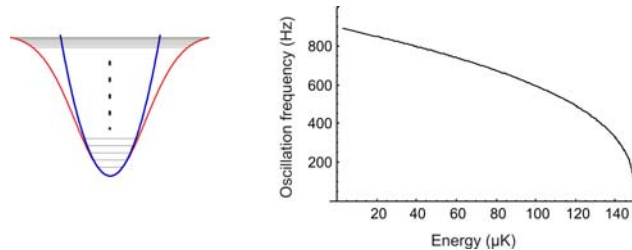

Figure 6.12: Oscillation frequency (i.e. the energy difference between two adjacent levels) as a function of the quantum number in a 1D gaussian-shaped potential.

As a consequence, the parametric excitation spectra that we measured are expected to be both broadened and shifted compared to the ones which would be obtained in a

150

purely harmonic trap, as noticed previously, for example, in [104]. Calculations providing analytical expressions for describing the spectra are rather complicated; instead we chose to perform classical Monte Carlo simulations, which also permit to take into account the 3D profile (6.20) of the mixed trap. The effect of both elastic and inelastic collisions are not taken into account in this analysis.

To perform the Monte Carlo simulation we start by making an initial draw of the radial coordinate $r = \sqrt{x'^2 + y'^2}$, the longitudinal coordinate z' and the velocity v_i. We assume that all three quantities have gaussian distributions, characterized by the (experimentally-determined) respective $1/e^2$ widths: $W_t = 50$ μm, $\Delta_{z'} = 280$ μm (deduced with the in-situ measurement technique – see Section(6.3) and fig.(6.9) therein) and $2\sqrt{k_B T/m}$ (where $T = 120$ μK is the cloud temperature). We then solve the equation of motion in the mixed potential given by eq.(6.20), where we replace the constant depth U_0 of the ODT by the time-depending expression: $U_0(1 + f(t))$, where $f(t)$ is a function which accounts for the experimental time-dependence of the IR laser power during the modulation.

The final (after 40 ms of application of the modulation) total energy of atoms in the ODT is given by $E_f = \frac{1}{2}mv_f^2 + U_0 \left[1 - \exp\left(\frac{-2r_f^2}{w_0^2}\right) \right]$, where v_f and r_f are the final velocity and radial position of the atoms. The proportion of atoms remaining in the ODT, which correspond to the condition $E_f < U_0$, gives the trap losses.

Numerical results

We computed various spectra, for different values of our only adjustable parameter, which is the optical trap depth U_0. An example of a simulated spectra is shown in fig.(6.13), along with the corresponding experimental one. The simulated spectra are always narrower and we chose the one which reproduces the best the position of the minimum of the experimental spectra; this sets the value of U_0.

Using this value and eq.(6.18) we can deduce the trap bottom radial oscillation frequency. We then observe that the minimum of the experimental spectra is indeed considerably shifted, by about 25%, with respect to twice the trap bottom oscillation frequency, represented by the vertical solid line in fig.(6.13). This confirms the importance of trap anharmonicity effects in the excitation spectra.

The results for the optical trap depth in the ^{5}D$_4$ state is: $U_{0,^5D_4} = (3.2 \pm 0.6 \pm 0.6)$ MHz. The first uncertainty of 20% is a result of the estimated 10% accuracy on the waist measurement; the second is an estimate of the fit uncertainty. The same procedure, in the case of the optical potential depth in the ^{7}S$_3$ state gives: $U_{0,^7S_3} = (3.8 \pm 0.7 \pm 0.7)$ MHz.
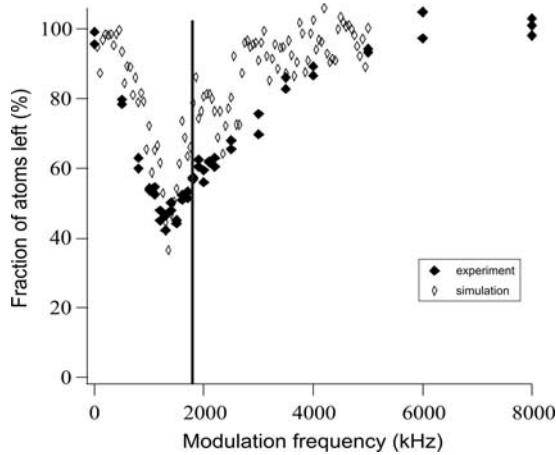
Figure 6.13: Comparison between the experimental excitation spectra (full diamonds) and the best adjusted simulated excitation spectra for the $^5D_4$ state. The full line corresponds to twice the optical trap-bottom frequency (for $^5D_4$), which would be the position of the resonance for the harmonic approximation of the optical potential.

Comparison with the theoretical values

In Section(6.1) we theoretically derived the expressions (6.13) of the lightshifts $U_{^7S_3}$ and $U_{^7D_4}$ of the $^7S_3$ and $^5D_4$ levels, as a function of the laser intensity I_0. We also showed that these lightshifts are expected to depend on the Zeeman sublevel m_J.

Because the parametric excitation is performed in the 'mixed' trap, where the magnetic field direction is changing with $\overrightarrow{r}$, we remind that there is no good choice for the light polarization q which is seen by the atoms. However, for a majority of atoms, the local B-field is almost orthogonal to linear polarization axis of the IR trapping laser (except for a small region, near the $B = 0$ point). Therefore, we can chose the σ_{inc} polarization to evaluate the lightshifts.

Moreover, the atomic sample in the 'mixed' trap is not spin-polarized, and the exact m_J distribution is unknown. For all these reasons, giving an exact value of the lightshift is not obvious. However, for having a comparison with the experimental values determined earlier, let us give the 'average' values of the lightshifts, considering that the atomic sample is equally-distributed in all the $m_J > 0$ substates:

$$U_{^7S_3, m_{J_i}} =_{\sigma_{inc}} -2.54 \, {}^{-2.53}_{-2.56} \text{ MHz}$$
$$U_{^5D_4, m_{J_i}} =_{\sigma_{inc}} -2.02 \, {}^{-1.93}_{-2.17} \text{ MHz} \tag{6.24}$$

We additionally gave the minimum (i.e. for $m_J = 0$) and maximum (i.e. for $m_J = +3$ and $m_J = +4$, respectively for the $^7S_3$ and $^5D_4$ levels) values of the lightshifts. These values correspond to the experimental laser parameters ($P = 29$ W and $w_0 = 55$ μm) used for obtaining the parametric excitation spectra.

152

When comparing the theoretical results to our experimental measurements, we observe differences which are slightly off the experimental error bars. One possibility to explain them is that the laser mode is modified by the passage through the viewport of the experimental chamber (we remind that the measurement of the experimental waist is done with a beam which does not cross the viewport). This hypothesis is confirmed by the fairly good agreement between the theoretical (1.25) and experimental (1.19) ratios between the lightshifts of the $^7S_3$ and $^5D_4$ levels.

Finally, let us mention that one could consider, for future experiments, more precise measurements of the trap oscillation frequencies, for example by using colder atomic samples in a crossed optical trap. These measurements could be done directly in the $^7S_3$ state (in which evaporative cooling is possible), but also in the $^5D_4$ state. For that, one could think of an experimental procedure which consists in optically pumping, in the $^5D_4$ state (using for example a Raman transition), a sample previously cooled in the ground state crossed ODT.

6.5 ODT loading dynamics

In Section(6.2) we qualitatively presented the loading mechanism of the 'mixed' magnetic+optical trap with metastable atoms. We will now study in detail the loading dynamics of this trap, in order to find (and eventually reduce) the main limiting factors.

6.5.1 Experimental results

We obtained interesting experimental information about the loading dynamics of the ODT by studying the influence of the horizontal IR beams' pointing (transverse position) on the stationary number of atoms in the trap, N_∞. For this experiment we changed the direction of the beam using the horizontal adjusting screw of the $M1$ mirror in fig.(6.2), while the retro-reflection was blocked (in order to simplify the analysis). The results are shown in fig.(6.14.A) and we observe that there are two positions which maximize N_∞, as well as a local minima, located between them.

We additionally recorded the ODT loading curves, corresponding to the positions of the two maxima and to that of the local minima; the results are shown in fig.(6.14.B). The characteristic $1/e$ time, obtained by exponential fitting, is $\tau_{opt} = 240$ ms for the optimal position ($x' = \pm 50 \mu$m), whereas for $x' = 0$ we measure $\tau_0 = 110$ ms.

As the loading time is set by the dominant loss rate(s), and as the inelastic loss rate between metastable states should be higher for a larger number of atoms (and consequently a larger density), this rules out the inelastic collision between metastable states as the single dominant limiting factor.

In addition we verified that the $1/e$ lifetime of the mixed trap (when the MOT beams
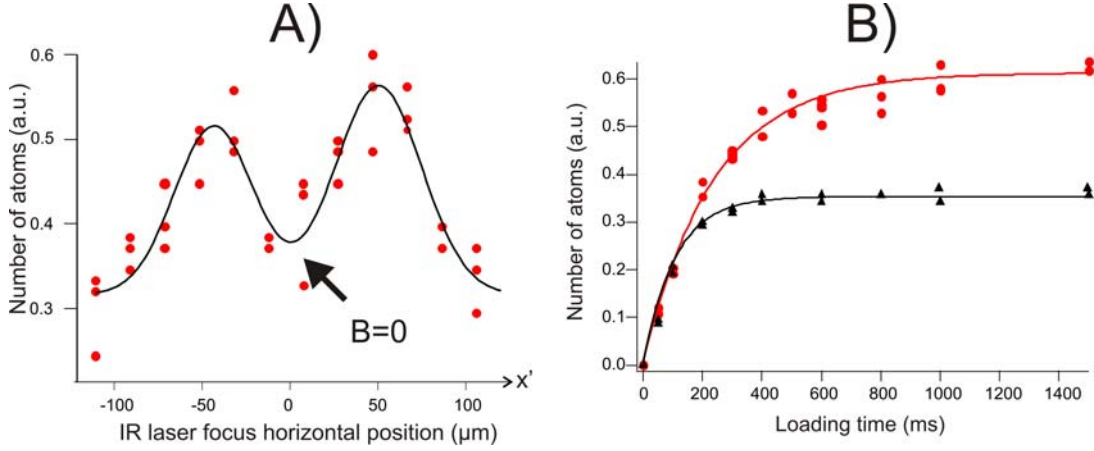
153

Figure 6.14: A) Dependence of the steady-state number of atoms N_∞ with the IR laser focus position on the horizontal plane, in absence of the retro-reflected beam. If the IR beam crosses the MOT center ($x' = 0$), the atom number reaches a local minimum. We fitted the data by the sum of two gaussians and the result is shown in the black line. The centers of the two peaks are separated by 100μm. B) Loading curves, for $x' = 0$ – triangles – and $x' = \pm 50\mu$m – dots. The solid lines represent exponential fits of the data.

are turned off after the accumulation), in each position ($x' = 0$ and $x' = \pm 50\mu$m), is equal to the corresponding loading times. This rules out the inelastic collisions with the MOT atoms as the limiting factor.

Finally, the slopes at $t = 0$ of the two loading curves shown in fig.(6.14B) are almost identical, indicating an unchanged ODT loading rate which corresponds to the local minima and maxima in fig.(6.14B).

In conclusion, we interpret the dependence in fig.(6.14A) as a consequence of the influence of one-body losses on the loading dynamics. As the collisions with the MOT or with the background gas (which corresponds to much longer time-scale, of 9 s) are ruled out, we conclude that the Majorana losses are in fact an important limiting factor of the loading. This possibility is analyzed in the following section.

6.5.2 Majorana and two-body inelastic collision loss rates

Non-adiabatic spin-flips may be an important loss factor for magnetic traps with a zero magnetic field position near the potential minima. This can indeed be the case in our trapping configuration if the optical dipole trapping beam is well aligned with the center of the magnetic trap.

If the atoms initially in a $m_J \geq 0$ state endure a spin-flip towards a $m_J < 0$ state, they are expelled from the mixed trap along the longitudinal (z') axis, as the weak confinement of the optical potential is dominated by the repulsive magnetic potential. When the IR beam is slightly off-centered from the $B = 0$ point, the Majorana losses decrease, as their source is cast out of the ODT volume. This also accounts for the larger loading time observed. On the other hand we note that for IR beam displacements

larger than 50 μm the loading rate Γ_{load}, proportional to the overlap with the MOT, decreases too, which leads to the experimental trade-off observed in fig.(6.14).

Majorana loss rate

In Section(5.1) we mentioned that, if the modulus of the magnetic field is 'strong enough', the magnetic moment μ of a moving atom adiabatically follows the direction of the magnetic field. In a quantum picture, an atom initially in a $|m_J\rangle$ state (with respect to the quantization axis defined by the direction of an initial field $\overrightarrow{B_i}$) will remain in the same $|m_J\rangle$ state, with respect to the direction of the local field at any time later.

The condition for the adiabatic passage to happen is that the rate of change of the magnetic field direction is slow compared to the Larmor frequency $\omega_L = \mu B/\hbar$. On the contrary, if this condition is not satisfied, the atom will remain in the same initial state with respect to $\overrightarrow{B_i}$, which is a superposition of many states $|m'_J\rangle$ with respect to the magnetic field at a later time.

In order to estimate the Majorana loss rate Γ_{maj}, we adapted the model presented in [80] in the case of our mixed trap. Let us consider one atom traveling with a velocity v at a distance x from the $B = 0$ point. The direction of the magnetic field changes at a rate $\Gamma_B = 1/B(dB/dt) = v/b'$, where b' is the magnetic field gradient. Spin-flips will occur inside a *'death-sphere'* of radius d, defined by the condition $\omega_L \simeq \Gamma_B$ which gives: $d = \sqrt{\frac{hv}{\mu b'}}$.

Compared to the case of a quadrupole magnetic trap [80], the Majorana loss rate is strongly modified by the geometry of the mixed trap. Indeed, the motion of the atoms is constrained in two directions by the strong confinement of the ODT. If the $B = 0$ point is well aligned with the IR beam, the loss rate will be given by twice the oscillation frequency of the MT along the z' axis[4] times the probability of passing through the *'death sphere'*, which is roughly given by the ratio between the transverse surface of the *'death sphere'* and the transverse surface of the cloud trapped inside the ODT beam. We find thus:

$$\Gamma_{maj} = a\frac{2}{\tau_{MT}}\left(\frac{d}{W_t}\right)^2 \tag{6.25}$$

where a is a numerical factor on the order of one (for example, a was measured $\simeq 3$ in [80]).

Using the value $b' = 10$ G/cm and the experimentally measured $W_t \simeq 35$ μm and $T \simeq 100$ μK, we obtain a radius of the *'death sphere'* $d = 4$ μm and an oscillation period $\tau_{MT} \simeq 20$ ms. Finally the Majorana loss characteristic time is $\Gamma_{maj}^{-1} = \frac{800}{a}$ ms.

---

[4] as there are two passages through the MT center per oscillation period

The difference between the loading times ($\tau_{opt} = 240$ ms and $\tau_0 = 110$ ms) observed in fig.(6.14.B) corresponds to an additional loss process with a time scale ~ 200 ms. We thus see that Γ_{maj}^{-1} gives the correct order of magnitude for explaining this additional loss process (for example, for $a = 3$, as in [80], we obtain $\Gamma_{maj}^{-1} = 266$ ms).

This estimate shows indeed the important difference – at comparable temperatures – between the Majorana loss rates in a purely 3D magnetic trap (~ 0.25 s^{-1}), as mentioned in Section(5.4) and in our mixed, optical+magnetic trap.

Second limiting factor

The Majorana losses decrease rapidly with the distance to the $B = 0$ position. We estimate thus that the Majorana losses should be almost completely suppressed when the IR beam waist is shifted by 50μm from the central position. On the other hand, we mentioned before that the lifetime τ_{opt} at the optimal position in fig.(6.14) becomes only a factor of two larger than τ_0, which means that other loss processes must come into play.

Let us now estimate the influence of two body collisions. The characteristic life-time in this case[5] is given by Γ_{inel}^{-1}, where $\Gamma_{inel} = \beta_{DD}n_0/4$ is the initial loss rate of the trap. The geometrical factor 4 comes from the shape of our mixed trap, which is roughly harmonic in two directions and linear in the third[6]. With the value $\beta_{DD} \simeq 3 \times 10^{-11}$ cm^3/s, measured previously, and with $n_0 = 10^{12}$ cm^{-3} (as discussed above), we obtain $\Gamma_{inel}^{-1} \simeq 280$ ms, which is close to τ_{opt}.

Conclusion

In conclusion, we demonstrated that there are two limiting factors playing a role in the accumulation of metastable Cr atoms in the ODT. These factors are the *Majorana spin-flips* and the *inelastic D-D collisions*, and both have about the same loss rates ($\sim 1/200$ s^{-1}).

The Majorana loss rate can be dramatically reduced, by shifting the position of the ODT beam with respect to the MT center; this leads to an increase of ~ 2 of the number of optically trapped atoms.

For this alignment (which was chosen for further experiments) the main limitation comes from the inelastic D-D collisions. Decreasing the inelastic collision rate in the metastable states can only be achieved by decreasing the atomic densities, which implies

---

[5] We remind that, for a system dominated by the inelastic collisions, the characteristic $1/e$ loading time and lifetime are roughly equal – within a numerical factor close to 1 – and given by $0.7\sqrt{\frac{V}{\beta\Gamma}}$ (see Section(3.2) and the notations therein).

[6] In this case the 'collisional volume' V_{coll}, defined in Section(4.1), is equal to $4V_{trap}$, where the trap volume is defined by $n_0 = N/V_{trap}$.

a modification of the trapping geometry. Some ideas will be analyzed in the last section of this chapter.

6.5.3 RF-deformation of the mixed trap

In the previous chapter we presented an idea for increasing the number of atoms magnetically-trapped in the metastable states with the use of RF magnetic fields. The advantage was the possibility of accumulating atoms in a W-shaped magnetic trap, having a large volume, which is favorable for reducing the role of the limiting inelastic (both D-P and D-D) collisions. However we found that the accumulation in the RF-dressed potentials was limited by the unwanted evaporation produced by second harmonics of the RF.

The experimental observations presented previously showed that in the 'mixed' optical+magnetic trap, Majorana losses are an important limitation of the accumulation, when the ODT beam is centered on the $B = 0$ point; shifting the position of the beam can significantly reduce these losses.

Another possibility for reducing Majorana losses, that we will study here, is the use of the RF-dressed magnetic potentials, presented in Chapter(5). In fig.(6.15.A) we explain this idea: the atoms in the low-field seeking states are trapped near the $B = 0$ point. They can thus undergo Majorana transitions to high-field seeking states and, in absence of the RF field, be expelled from the trapping region. In presence of the RF field, in the RF-dressed picture, they can however be 'recuperated' and remain trapped in the W-shaped potential; the Majorana transitions would thus no longer lead to trap losses.

The RF field can, in fact, provide a means to accumulate not only atoms in $m_J < 0$ states (which see a W-shaped potential, discussed up to now), but also atoms initially in $m_J > 0$ states. These atoms can be trapped in the z' direction by the M-shaped (RF-truncated) magnetic potential, provided that this potential is deep enough (i.e. the RF frequency is high enough with respect to the MOT temperature).

In the previous chapter, we found that the accumulation in the magnetic quadrupole RF-dressed potentials was limited by the unwanted evaporation produced by second harmonics of the RF. The situation is slightly different and more favorable in the case of the mixed magnetic+optical trap. In fig.(6.15.B) we compare the profile of a 'simple' W-shaped magnetic+RF trap (dashed line) and the same trap, modified by the optical trapping potential in the z' direction (full line). In this case the ODT confinement, even though shallower than the magnetic potential, can nevertheless partially prevent the atoms from reaching the second harmonic resonance point. Indeed, for reaching the $2R_{RF}$ point, the atoms oscillating along the $\widehat{z'}$ axis need to overcome an extra (optical) potential energy given by $\Delta U = U_{dip}(2R_{RF})$.
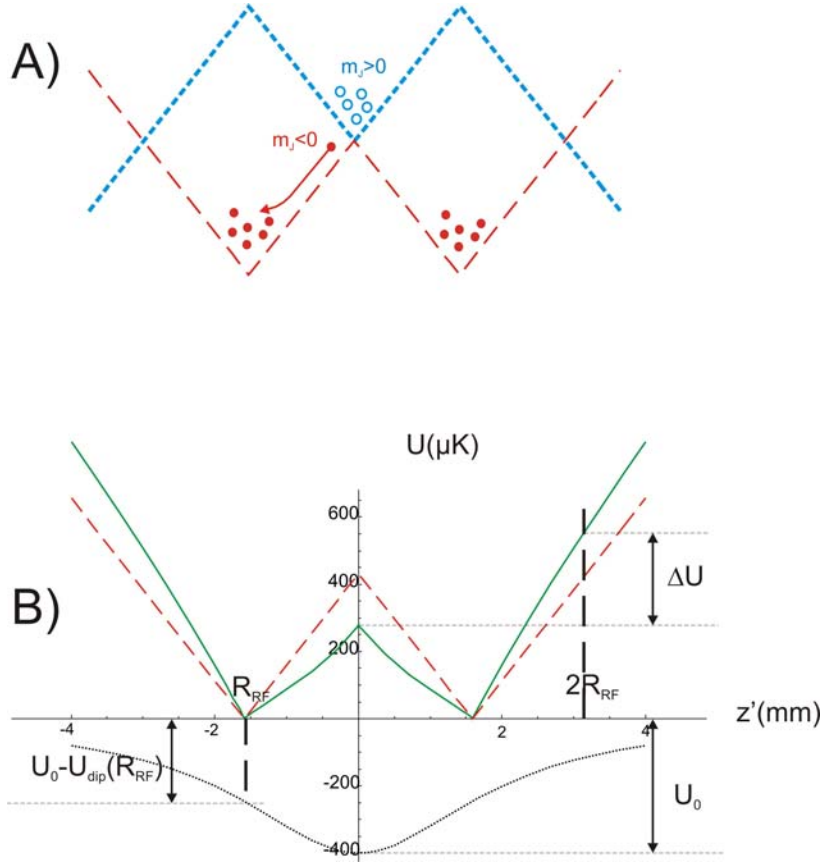
Figure 6.15: A) Schematic demonstration of the reduction of Majorana losses using an RF field: a $m_J > 0$ atom undergoing a spin-flip is 'saved' and remains trapped in the W-shaped magnetic potential. B) Solid line: profile of the mixed, magnetic+RF+OD trap in the longitudinal direction of the ODT beam; dashed line: magnetic+RF trap; dotted line: optical dipole potential. We observe that the MT+RF trap is modified by the presence of the ODT beam, which introduces an additional confinement. Even though it is relatively shallow, the ODT can nevertheless prevent the atoms from reaching the second, unwanted RF resonance, as they have to beat the extra optical potential energy ΔU.

We finally note that the geometry of our mixed magnetic+optical trap gives the possibility to benefit of the maximum RF coupling strength $\Omega_{0,max}$. Indeed, as mentioned before, only the RF field component which is perpendicular to the local static B field can couple the different m_J−states; even if we thought that this was not a limitation in the case of a pure magnetic trap, the situation is even more favorable for the atoms in the ODT; by placing RF coils on top of the experimental chamber, the RF field will then always be almost perpendicular to the ODT beam direction.

We performed experiments for studying the accumulation of metastable atoms in a mixed, magnetic+RF+optical trap and the results are shown in fig.(6.16). We observe that the number of atoms trapped in the ODT (after switching off the MT gradient) increases with the RF frequency and reaches a maximal value for $f_{RF} \simeq 3$ MHz. We also

observe in the absorption images a different, more elongated structure of the optically trapped cloud, with two lobes corresponding to the two potential minima shown in fig.(6.15); the distance between the two lobes increases linearly with the RF frequency. At $f_{RF} > 3$ MHz the signal starts to decrease and reaches the initial value (i.e. the one without RF) for frequencies above ~ 10 MHz.
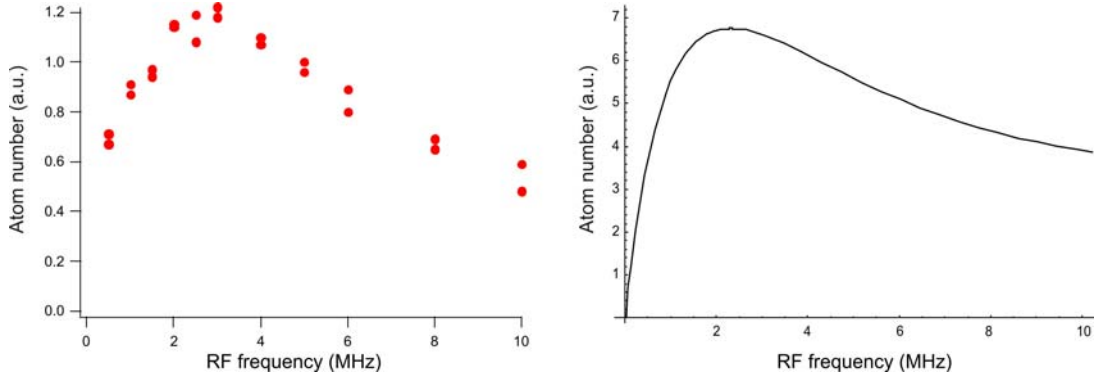

Figure 6.16: Left: experimental data of the dependence of the atom number on the RF frequency, in the magnetic+RF+OD trap. Right: results of our simple theoretical model (see text).

Simple theoretical model

The shape of the number of atoms dependence on the RF frequency can be reproduced with a simple model which takes into account two opposite effects. One is the benefic effect of the ODT, which prevents atoms from reaching the RF second harmonic resonance; this effect increases with the RF frequency, because R_{RF} (and thus ΔU) increases with f_{RF}. The second effect, which tends to decrease the number of trapped atoms, comes form the fact that the trap depth at the equilibrium point R_{RF}, given by $U_0 - U_{dip}(R_{RF})$, decreases with f_{RF}.

A very simple calculation can be performed, by considering that the atoms are 'created' in the ${}^5D_4$ state at the position of the MOT $(R = 0)$, with a thermal velocity distribution at $T_{MOT} \simeq 100$ μK. The atoms which are not evaporated by the RF second harmonic are those having a longitudinal kinetic energy $E_{c,\parallel} = mv_\parallel^2/2$ (where $v_\parallel$ is the initial longitudinal velocity) smaller than ΔU (as they cannot reach $2R_{RF}$). The same atoms will remain trapped in the mixed, magnetic+RF+ODT only if they have a transverse kinetic energy $E_{c,\perp} = mv_\perp^2/2$ (where $v_\perp$ is the initial longitudinal velocity) smaller than the ODT depth at R_{RF} (as only they can remain trapped in the ODT). Finally we perform a thermal average over the transverse and longitudinal initial (MOT) velocity distributions and obtain the dependence of the trapped number of atoms on the RF frequency, which is shown in fig.(6.16.B). We observe that our model is in qualitatively good agreement with the experimental data.

159

Conclusions

In conclusion, we interpret our results as a demonstration of the possibility of simultaneously accumulating low- and high-field seeking atoms in the 'mixed', trap where the magnetic potential is modified using RF fields. In such a configuration, we think that Majorana no longer leads to trap losses.

This experiment is another demonstration of trapping of atoms in a RF-dressed magnetic (plus optical) trap.

The results presented in fig.(6.16), which show an enhancement of ~ 2 of the trapped atom number, were obtained in the configuration where the ODT beam was perfectly aligned on the center of the MT. When the beam is off-centered (i.e. is in the optimal position shown in fig.(6.14).A) we observe almost no enhancement of the ODT signal with the RF.
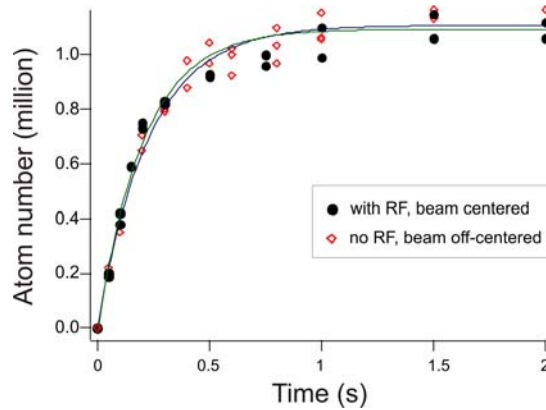
Figure 6.17: Comparison between two ODT loading curves: one (dots) in presence of the RF field, when the beam is centered on the $B = 0$ point and the other (diamonds) where the beam was shifted to the optimal position, shown in fig.(6.14), in absence of the RF.

We also compared the loading of the ODT, in presence of the RF, when the beam is centered onto the $B = 0$ position to the loading in absence of the RF, when the optimal situation, in absence of the RF and when the beam is shifted to the optimal position (see fig.(6.14)). The results are shown in fig.(6.17): we observe that the loading rates (given by the slopes at $t = 0$) are identical, which may be surprising, as the RF should make possible the accumulation of all m_J states. The observation could be explained by the fact that, although the RF allows the trapping of high-field seeking states, it also reduces the depth of the M-shaped potential (experienced by the high-field seekers).

Unfortunately, we observe that the maximum number of atoms, obtained in the presence of the 3 MHz RF field, is very close to the one in the case when the ODT beam (without RF) is only shifted from the MT center.

A possibility of increasing the number of atoms would be to increase the value of the

optimal RF frequency, and thus increase the depth of the M-shaped potential. This would however require higher ODT laser powers.

6.5.4 Trap characteristics dependence on IR laser power

We studied the dependence of the steady-state number of optically trapped atoms N_∞, and of their temperature T_{OT}, as a function of the trapping laser power P_0.
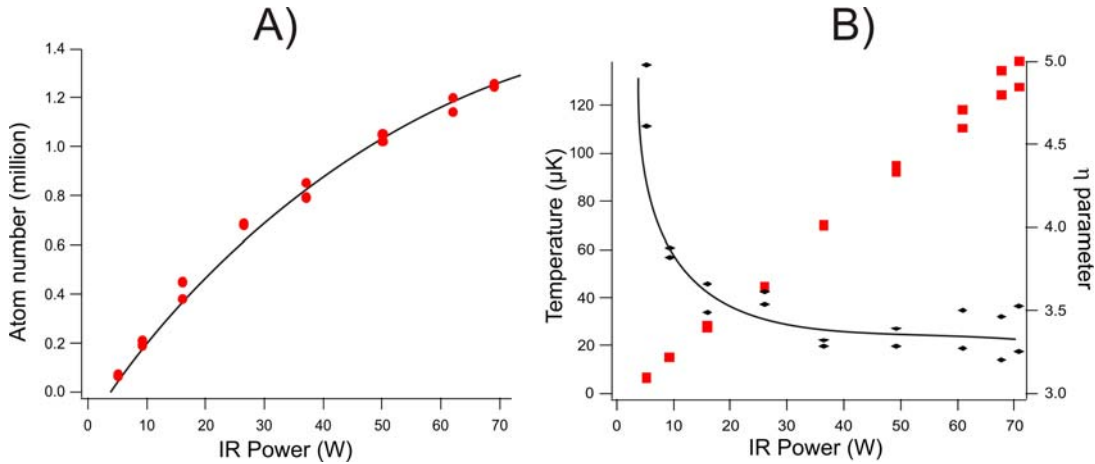

Figure 6.18: A) dependence of the number of optically trapped atoms on the total IR laser power (in presence of the retro-reflected beam). B) same dependence of the temperature (rectangles) and of the evaporation parameter η (diamonds). On both graphs, the solid line represents a guide for the eyes.

In fig.(6.18.B) we observe that the temperature of the cloud (rectangles) increases almost linearly with P_0. At full power ($P_0 = 70$ W) we obtain $T_{OT} = 120 \pm 10\mu$K. We additionally plot, in the same figure, the dependance of the evaporation parameter $\eta = \frac{U_0(P_0)}{k_B T}$, estimated using the theoretical value of the trap depth $U_0(P_0)$, on the total power P_0. Interestingly, we observe that the value of the evaporation parameter remains almost constant ($\eta \simeq 3.5$) for large IR power.

The number of atoms trapped in the ODT, as a function of the trapping laser power, is shown in fig.(6.18.A). Although the slope of this dependence decreases with the IR power, it still remains positive and we do not observe a complete saturation, even at full power.

To interpret this lack of saturation we analyzed in-situ images of the hybrid magnetic+optical trap, taken just after the accumulation and repumping in the ground state, for different laser powers. Using the technique described earlier, we are able to extract from these images the density profile which corresponds only to the atoms inside the optical trapping beam. In fig.(6.19) we compare these profiles, corresponding to different IR laser powers.
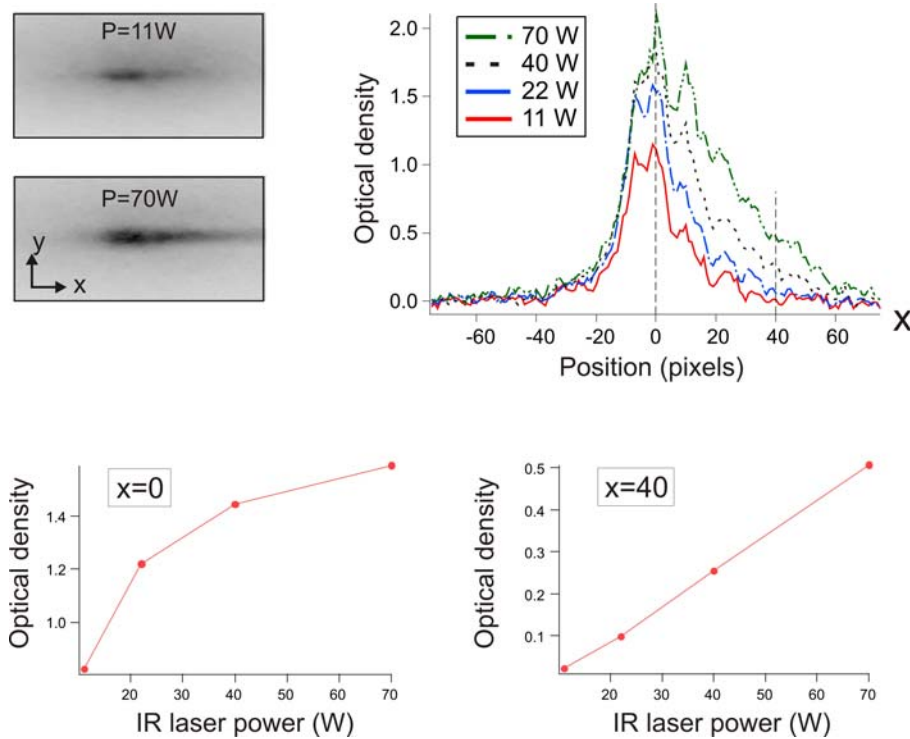
Figure 6.19: *Above:* In-situ images (left hand side) of the optically trapped cloud. On the right hand side there is a comparison of four longitudinal profiles of the atoms in the ODT region, for four different IR laser powers. *Below:* Optical depth, averaged over 20 pixels, around the $x = 0$ position (right) and $x = 40$ pixels position (left) as a function of the IR laser power.

For this experiment, the imaging laser was deliberately detuned by $+2.5$ MHz to the blue of the atomic resonance in zero magnetic field. This translates into a dissymmetry in the profiles shown in fig.(6.19): because of the Zeeman effect, the atoms to the right are more resonant than those in the center, themselves 'more resonant' with the imaging beam than the atoms to the right. We checked that the dissymmetry is inverted when changing the sign of the laser detuning (to -2.5 MHz).

An interesting feature appears in the observed profiles as a function of the trapping laser power. While the amplitude of the signal (proportional to the local atomic density) in the center of the trap (where B=0) saturates for IR powers ~ 25 W, the signal to the right does not show the same saturation, as it continues to increase even when approaching the maximum laser power.

We interpret the signal observed to the right as a signature of the presence of the atoms in the $m_J = 0$ state. As already mentioned, these atoms do not feel the magnetic confinement in the IR beam longitudinal direction, and are thus trapped in this direction only by the optical dipole potential. They can thus expand over a larger space region (fixed by the Rayleigh length, of ~ 2.5 mm, of the beam) than the atoms in the $m_J > 0$ states, which are confined closer to the magnetic trap center.

162

The density saturation near the $B = 0$ region is interpreted as a consequence of the inelastic collisions and comes as a confirmation of our previous conclusions. The signal due to $m_J = 0$ atoms on the other hand is expected to saturate less rapidly with the laser power. These atoms oscillate along the z' direction with a smaller longitudinal frequency; they are thus spending less time in the high-density region (around B=0) and are less exposed to inelastic collisions.

6.6   Other experiments and perspectives

The experiments presented in the previous section demonstrated that the accumulation of atoms in the metastable states is ultimately limited by the inelastic D-D collisions. The mixed magnetic+optical trap configuration is not optimal from this point of view, because of the *strong* and *unnecessary* magnetic confinement of atoms with $m_J > 0$ along the longitudinal direction of the ODT beam.

Under these conditions one could increase the number of metastable atoms that are trapped in the ODT by decreasing the atomic density or, equivalently, by increasing the trap volume in the ODT longitudinal direction. For example, one can imagine that an elongated Ioffe-Pritchard trap would provide a better matching between the MT and ODT shapes. Of course this would imply major changes in the design of out experimental setup.

Another solution would be to try deform the quadrupole magnetic trap, at least in the z' direction, of course without altering significantly the performances of the MOT. The experiments I will shortly present in this section did not lead to better accumulation results; they nevertheless opened some promising perspectives for future improvements.

6.6.1   Accumulation in two separate horizontal ODT beams

The alignment procedure of the retro-reflected ODT beam, presented earlier, consisted in maximizing the temperature of the optically trapped cloud by maximizing the trap depth. On the other hand, having two misaligned trapping beams can be regarded as an increase in the optical trapping volume, which could eventually increase the overlap with the MOT and decrease the inelastic collision rate during loading time (by decreasing the density of the optically-confined atoms).

In practice we can easily misalign (and subsequently recombine) the incident and retro-reflected ODT beams using the AOM shown in fig.(6.1), by taking advantage of the fact that the Bragg angle depends on the modulation frequency of the AOM[7]. We demonstrated this technique by accumulating atoms at different values of the AOM

---

[7] Using simple geometrical optics arguments one can see that the incident and retro-reflected beams are actually shifted in opposite directions along the z' axis.
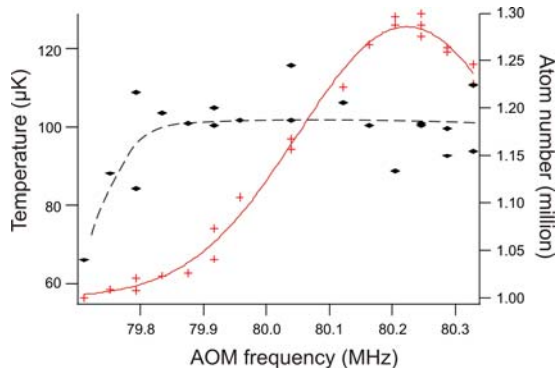
Figure 6.20: Cloud temperature (crosses) and number of atoms (lozenges) as a function of the AOM RF modulation frequency. The full line is a gaussian fit and the dashed line is a guide for the eye. When the two beams are perfectly aligned (for a AOM frequency $\simeq$ 80.2 MHz) the temperature has a maximum value of 120 μK, which drops down to about 60 μK when the beams are completely separated and the trap depth is reduced by a factor of two.

RF frequency and monitoring the temperature of the cloud. The experimental results are shown in fig.(6.20). The maximum value of the temperature ($\sim 120\,\mu$K) is reached when the two beams are perfectly aligned; the temperature drops down to about 60 μK when the beams are completely separated and the trap depth is reduced by a factor of two. The atom number remains almost constant over the entire RF frequency range.

After reaching the steady-state number of atoms we recombine back the two beams, by applying a linear RF frequency ramp back to 80.2 MHz. For ramping times shorter than the optical trap oscillation period (< 1 ms) an important number of atoms was spilled out of the trapping volume. For longer ramps, the two beams adiabatically recombined and we were able in the end to keep the initial number of atoms. Unfortunately the final temperature of the cloud, after recombination, always returned to 120 μK. We attribute this effect to the adiabatic heating of the cloud during the recombination.

6.6.2 Other experiments for loading a single beam ODT

Time-averaged optical trap

An idea that we tested is to modulate the transverse position of ODT beam. This experiment does not modify the longitudinal magnetic confinement; it nevertheless can be useful by allowing to accumulate colder atoms.

The modulation, along x', of the beam waist position can easily be performed, using the same idea as in the previous paragraphs, by applying a modulation to the AOM RF frequency. If this modulation is fast enough, the atoms will feel a time-averaged optic potential, shown in fig.(6.21.A). One can see that this technique effectively changes the size of the waist – and thus the confinement – in one direction.

We performed some preliminary experiments; we found that, after accumulation in the modulated trap – at frequencies up to 40 kHz – and recombination (in $\sim$ 50 ms) the temperature of the trap was slightly reduced by about 15%; unfortunately the number of atoms was also reduced, by more than 30%.
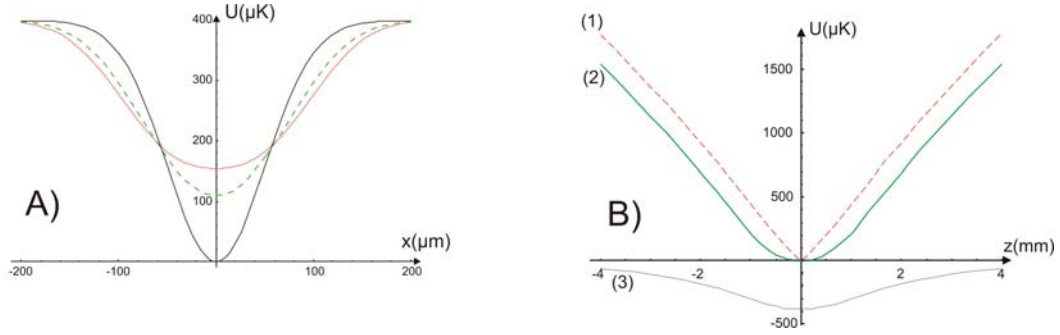

Figure 6.21: A) Effective optical dipole potential in the case of modulation of the beam direction: dashed line corresponds to a linear modulation, while the dotted line to a sinusoidal modulation. The solid curve is the transverse profile of the non-modulated optical dipole potential. B) Modulation of the MT trap along the center (1) – mixed magnetic+optical trap; (2) – mixed trap in presence of a sinusoidal modulation of $0.5z_R$; (3) pure ODT.

We do not fully understand this reduction of the number of atoms. A possible limitation would come from the bandwidth of the AOM; we measured the 'response time', when applying a 1 μs linear ramp: in this case, the beam moves in $\sim$ 8 μs in one direction, and in $\sim$ 40 μs in the other. This important dissymmetry limits our ability to modulate the optical trap at frequencies on the order of the kHz.

Time-averaged magnetic trap

Another idea that we tested was to decrease the longitudinal confinement of the magnetic trap by introducing a fast modulation of the MT center along the direction of the ODT beam. This idea uses similar arguments to the ones demonstrated in [80] by Cornell et al. for creating a time-orbiting potential (TOP) which prevents Majorana losses in a in a quadrupole magnetic trap.

To illustrate this ides, let us consider a constant, uniform bias magnetic field B_0 applied along the z' axis, in addition to the MT quadrupole magnetic field. The bias field shifts the position of the MT center ($B = 0$ point) by B_0/b', where b' is the magnetic gradient along z'.

If the bias field is rapidly modulated in time with a periodic function (for example a sinus function, with a frequency ω_{mod} and an amplitude B_0) the magnetic potential along the z' axis will be given by:

$$U_{MT}(z,t) = \overline{m_J} g_J \mu_B b' \left| z + \frac{B_0}{b'} \sin(\omega_{mod} t) \right| \tag{6.26}$$

165

Provided that the modulation frequency ω_{mod} is sufficiently high with respect to the MT oscillation frequency ω_{MT}, the atoms will not be able to respond to the fast changes of the magnetic potential and will only feel an effective, time-averaged potential given by:

$$U_{av}(z) = U_{dip}(z) + \frac{\omega_{mod}}{2\pi} \int\limits_{t=0}^{2\pi/\omega_{mod}} U_{MT}(z,t)dt \tag{6.27}$$

The corresponding time-averaged potential is shown in fig.(6.21.B), in the case of a modulation amplitude $\sim z_R$. We observe that the shape of the mixed trap is strongly modified near the position of the ODT beam waist and the magnetic confinement is strongly reduced.

We performed such experiments by using a modulated bias magnetic field, created by an additional magnetic coil whose axis is aligned with the ODT beam. We observed that at low modulation amplitudes there was no effect on the ODT signal, but when increasing the amplitude (up to a few mm) there was a negative effect of the modulation. For the same large amplitudes we also observed a decrease of the MOT fluorescence, which may explain the negative effect on the ODT signal. The effect on the MOT is due to the fact that the zero B field is no longer correctly aligned with respect to the MOT beams.

6.6.3 Direct loading of metastable atoms in a crossed ODT

Our strategy for Bose-Einstein condensation implies using a crossed optical dipole trap. After having demonstrated the possibility of loading $^5D_4$ Cr atoms in the single-beam ODT, we experimentally investigated the perspective of loading of metastable atoms directly in the crossed ODT.

The alignment procedure, used in this experiment for the vertical ODT beam with the MOT was similar to the one for the horizontal beam (i.e. by superposing a resonant blue laser beam and aligning it onto the MT center). The longitudinal confinement of the vertical ODT beam is not sufficient to overcome gravity, and atoms cannot accumulate all along this beam (except for the small crossing region). For this reason parametric oscillation procedure could not be applied for positioning the waist with the MT center, as in the case of the horizontal beam. We performed only a geometrical alignment of the focusing lens.

Results of this accumulation technique are shown in fig.(6.22); the corresponding IR powers were 30 W for the horizontal and 40 W for the vertical beam. The interesting feature of these loading curves are the different $1/e$ loading times. We measure a loading time $\tau_1 = 90$ ms for the wings and a much shorter time $\tau_2 = 20$ ms for the crossing region.
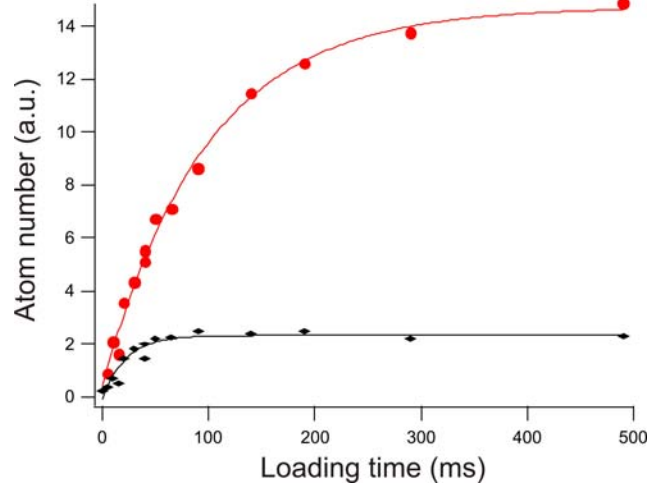
Figure 6.22: Loading curves of the crossed optical dipole trap with metastable atoms: atoms in the crossing region (diamonds) and in the wings (dots). The solid lines are exponential fits of the data.

We think that both time scales are fixed by the inelastic D-D collisions, and the difference comes from the fact that much higher densities are reached inside the crossing region. On the other hand we observe that the time scale τ_2, although longer than τ_1, is shorter than in the case of the loading of a single-beam ODT. This indicates that the presence of the vertical beam induces additional inelastic collisional losses for the horizontal trap.

Finally, we observe that the steady-state number of atoms is 5×10^5 (about 12% being in the crossing region). This atom number represent a reduction by ~ 2.4, compared to 1.2×10^6 at 70 W, and by ~ 1.3, compared to 6×10^6 at 30 W (see fig.(6.18)). These reductions are due to the following facts: (i) the power in the horizontal beam is smaller (only 30 W compared to 70 W), while no atoms are trapped solely in the vertical beam, because of gravity, and (ii) the presence of the vertical beam increases the inelastic losses for the atoms in the horizontal wings.

In conclusion, because the overall number of atoms is significantly reduced, we estimate that the situation is less favorable then when loading a single-beam ODT.

However, there is a possibility for increasing, in future experiments, the number of atoms accumulated in the crossed ODT. The idea is to build a configuration where both of the arms would be *horizontal*; in this way, losses due to gravity would be prevented and atoms could be trapped in both arms.

Conclusion and perspectives

In this chapter we demonstrated a new loading scheme for metastable Cr atoms, using a 'mixed' trap created by the superposition of a quadrupole magnetic trap and a single-beam ODT. When releasing the magnetic field gradient, we observe up to 1.2×10^6 atoms at a temperature $T \sim 120$ μK. Parametric excitation of the ODT allowed to measure the trap characteristics and deduce the polarizability of the $^5D_4$ metastable state.

Studying the loading dynamics of the ODT we found that Majorana losses and inelastic collisions are the two main limitations, which set the loading time-scale (~ 200 ms) and limit the number of atoms. Increasing the number of atoms can be done by reducing the loss processes. We demonstrated that Majorana losses may be reduced using two different methods: one is to shift the position of the ODT beam away from the $B = 0$ field. The other involves using an RF magnetic field; in its presence the atoms undergoing a spin-flip to a $m_J < 0$ state are recuperated in the W-shaped 'RF-dressed' potential.

Inelastic collisions on the other hand can be reduced by decreasing the density (almost 10^{12} atoms/cm^3) during the accumulation procedure. This might be achieved by changing the shape of the confining potential. A recent and most promising improvement in this direction was investigated during the writing of this manuscript. The idea consists in 'erasing' the magnetic potential felt by the metastable atoms, by using rapid RF sweeps. Indeed, if the sweeps are fast enough with respect to the longitudinal oscillation frequency in the magnetic trap, the atoms will spend in average half of the time in a given m_J state and the rest in the opposite, $-m_J$ state. Under certain conditions applying the sweeps will not lead to heating of the atoms and the result is a magnetic potential which averages to 0.

Preliminary results demonstrate a substantial increase in the number of optically trapped atoms by a factor of ~ 2.

Chapter 7

Evaporation experiments in the ODT

7.1 Optical pumping

7.1.1 Introduction

Dipolar relaxation is ultimately the limiting factor in reaching the Bose-Einstein condensation of Cr in a magnetic trap. In this section, I will present some experimental results which show the influence of the polarization of atoms in the stretched spin states ($m_J = \pm 3$) on the lifetime of the optically trapped cloud.

As shown in the previous chapter, optical dipole traps provide the possibility of trapping all Zeeman sub-states; transitions to low-field seeking states, due to spin-changing collisions do not 'directly' expel the atoms out of the trap, as it is the case for a magnetic trap. However, because of the Zeeman energy released during a spin-changing collision, the cloud heats up; this heating translates into atom losses, due to the evaporation in the finite-depth ODT.

Dipolar relaxation does not raise a problem in the $B = 0$ limit; in this case, the Zeeman energy released by a spin-changing collision can be arbitrarily small, so that no heating occurs. In this case, at thermal equilibrium, the sample is an evenly-distributed spin-mixture, where different spin components are discernable and Bose-Einstein condensation is harder to achieve, since it would necessitate[1] an increased number of trapped atoms. Furthermore, this requires controlling the magnetic fields extremely well, which may be an important experimental challenge.

Another possibility to avoid problems due to dipolar-relaxation is to simply cancel it, using the idea (proposed in [109] and successfully used in the case of Cs [100], and also for Cr [26]) which consists in transferring all the atoms in the lowest Zeeman substate. In this case, spin-flip collisions become energetically unfavorable, since they

---

[1] The saturation of the excited state populations would be required for each spin component.

would imply an increase in the Zeeman energy. If the Zeeman energy difference between adjacent levels is much larger than the temperature of the sample, the kinetic energy of the two colliding atoms is not large enough to provide the extra magnetic energy required for a spin-flip. This situation can be realized by applying a sufficiently-strong magnetic field, i.e. having a value B_0 which fulfils the condition: $g_J \mu_B B_0 \gg k_B T$.

7.1.2 Optical pumping in presence of a magnetic field

Spin-polarization of the optically-trapped ground state Cr atoms in the lowest Zeeman-energy state, i.e. $|m_J = -3\rangle$, can be realized by optical pumping. For that, we use a σ^-−polarized laser beam[2], resonant with the $^7\mathrm{S}_3 \to{}^7\mathrm{P}_3$ transition, at 427 nm. It drives $\Delta m_J = -1$ transitions between $|^7S_3, m_J\rangle$ and $|^7P_3, m_J - 1\rangle$ states. Atoms in $|^7P_3, m_J-1\rangle$ can decay, through spontaneous emission, towards $|^7S_3, m_J\rangle$, $|^7S_3, m_J-1\rangle$ and $|^7S_3, m_J-2\rangle$ states. An absorption+spontaneous emission cycle can thus decrease the value of m_J. After several cycles, the atoms are eventually driven to the $m_J = -3$ stretched state.

The advantage of using the $^7\mathrm{S}_3 \to{}^7\mathrm{P}_3$ transition for optical pumping (rather than the $^7\mathrm{S}_3 \to{}^7\mathrm{P}_4$ cycling transition) consists in the fact that the $|^7S_3, m_J = -3\rangle$ state is a 'dark state' (with respect to the optical pumping transition). This means that an atom in $|^7S_3, m_J = -3\rangle$ no longer absorbs any resonant σ^- light, and the heating due to photon scattering ($T_{rec.} = 1.02~\mu$K for Cr) stops as soon as the atom reaches this state.
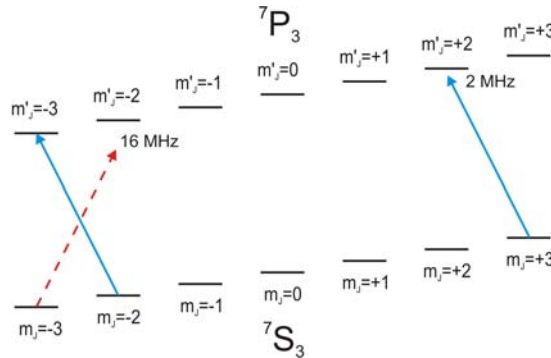

Figure 7.1: Optical pumping scheme, using the $^7\mathrm{S}_3 \to{}^7\mathrm{P}_3$ transition.

In presence of a uniform magnetic field B, aligned along the axis of the optical pumping beam, the detuning to resonance for different σ^+ transition ($|m_J\rangle \to |m_J+1\rangle$) reads: $\delta_{m_J} = \delta_0 - \left[m_J g_{^7S_3} - (m_J - 1)g_{^7P_3}\right]\mu_B B$, where δ_0 is the laser detuning to the $B = 0$ resonance. For a non-zero magnetic field, δ_{m_J} depends on the value of m_J;

[2] The corresponding experimental setup was previously described, in Section(2.3), and in fig.(6.2).

however, because of the fact that the Landé g-factors of the $^7\mathrm{S}_3$ and $^7\mathrm{P}_3$ levels are relatively close ($g_{^7S_3} = 2.01$ and $g_{^7P_3} = 1.92$), these differences are small. For example, for a typical magnetic field of $B = 3$ G (as mentioned below) there is only a ~ 2 MHz difference between the extreme values of the δ_m detunings (i.e. δ_3 for the $|m_J = 3\rangle \to |m'_J = 2\rangle$ and δ_{-2} for the $|m_J = -2\rangle \to |m'_J = -3\rangle$ transitions). This is why the presence of a magnetic field does not affect the efficiency of optical pumping.

Using a non-zero magnetic field has however the advantage of yielding the stretched state $|m_J = 3\rangle$ more robust with respect to the heating due to additional photon scattering, in the eventuality of the presence of some unwanted σ^+-component of the pumping light. The magnetic field shifts in opposite directions the resonances for σ^- and σ^+ polarizations. For a $B = 3$ G magnetic field, the frequency difference between the $|m_J = -2\rangle \to |m'_J = -3\rangle$ (σ^-) and $|m_J = -3\rangle \to |m'_J = -2\rangle$ (σ^+) transition resonances equals ~ 16 MHz, about three times the natural line-width. For such a difference, the unwanted σ^+ component induces a negligible heating during the optical pumping light pulse (duration $\sim 10\,\mu$s, corresponding to a saturation parameter $s_0 = I/I_{sat} \simeq 6$ – see below).

7.1.3 Polarization experiments

Polarization of atoms in the magnetic stretched states

The precise alignment of the optical pumping beam can be done by shining it onto the MOT. The presence of this beam translates in a decrease of the MOT number of atoms, because the atoms excited in the $^7\mathrm{P}_3$ state can decay to the $^5\mathrm{S}_2$ state with a rate of 2.9×10^4 s^{-1} [106].

A first adjustment of the frequency of the pumping beam on resonance with the atomic transition was performed, via a spectroscopy experiment. We used the 427 nm light for absorption-imaging an optically-trapped atomic cloud, in the $^7\mathrm{S}_3$ state, in presence of a 3 G magnetic field. The spectrum shown in fig.(7.2.A) represents the atomic signal (cloud absorption) as a function of the AOM frequency; a lorenzian fit provides the exact position of the resonance.

A measurement of the timescale for optical pumping is shown in fig.(7.2.B); we used a short σ^+, 427 nm laser pulse, with a variable duration τ, shone to the atoms just before the absorption image was taken. For this image we used the usual σ^+, 425 nm light, attenuated to an intensity of ~ 0.2 mW/cm^2 (saturation parameter $s_0 \sim 0.02$). Under these circumstances, one can neglect the optical pumping due to the 425 nm light during the imaging pulse (50 μs), and it is mostly the 427 nm pulse which optically pumps the atoms in the stretched $m_J = +3$ state.

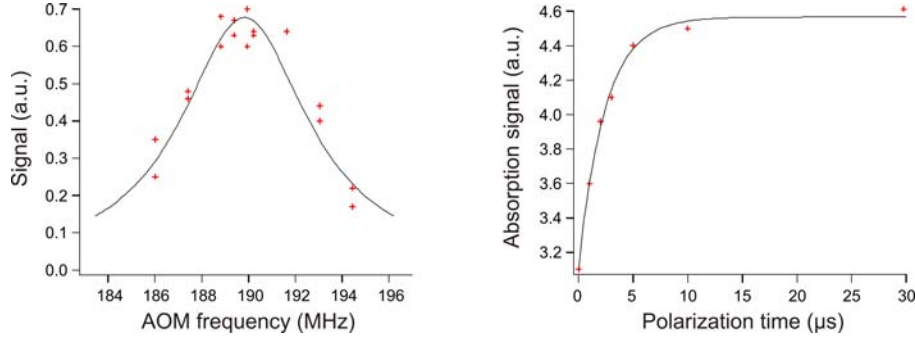The increase in the absorption signal with the polarization pulse duration, observed

Figure 7.2: A): spectroscopy of the $^7S_3 \rightarrow ^7P_3$, 427 nm transition, performed using a magnetically-trapped ^{52}Cr cloud. The solid line represents a lorenzian fit of the spectra, providing the position of the resonance. B): Determination of the optical pumping time scale: we plot the absorption signal as a function of the duration of the polarization pulse. The line represents an exponential fit, with a $1/e$ time constant of 2.5 μs.

in fig.(7.2.B), is due to the fact that atoms which have reached the $m_J = +3$ state, due to the polarization pulse, absorb more 425 nm photons than the $m_J < 3$ atoms (as they have the largest Clebsch-Gordan coefficient). The saturation corresponds to the situation where a maximum of atoms have been polarized in the $m_J = +3$ state. The characteristic polarization time-scale, given by the $1/e$ time of an exponential fit, is of ~ 2.5 μs, at an intensity of ~ 50 mW/cm^2 (saturation parameter $s_0 = 6$). In practice we chose a 10 μs duration for the optical pumping pulse.

A similar experiment was performed using the σ^- polarization, both for the polarization and imaging light. We measured a slightly longer time-scale, of ~ 5 μs, indicating that the atoms accumulated in the horizontal ODT are initially mostly in $m_J \geq 0$ states, and the optical pumping time to $m_J = -3$ is thus longer that the one to $m_J = +3$. We finally chose for further experiments a $\tau = 20$ μs optical pumping pulse duration.

RF sweep spin-inversion

When polarizing the atoms in the $m_J = -3$ state, we observed the occurrence of oscillations of the center of the cloud, trapped in the horizontal beam ODT, along the longitudinal direction (see fig.(7.3)). These oscillations have a smaller amplitude when the atoms are polarized to the $m_J = +3$ state (not shown), and disappear when no polarization pulse is applied.

We attribute these oscillations to the 'kicks' received by the atoms during the polarization in the $m_J = -3$ state. Indeed, each photon-absorption event results in a recoil of the atom, in the direction of the polarization beam, corresponding to the recoil velocity $v_{rec} = 1.8$ cm/s. An atom initially with $m_J = +3$ absorbs about six photons, and thus a momentum corresponding to 6 v_{rec} in the longitudinal direction, before reaching the $m_J = -3$ dark state. This kick produces the observed oscillations in the ODT beam longitudinal direction; the oscillations are damped within a few 100

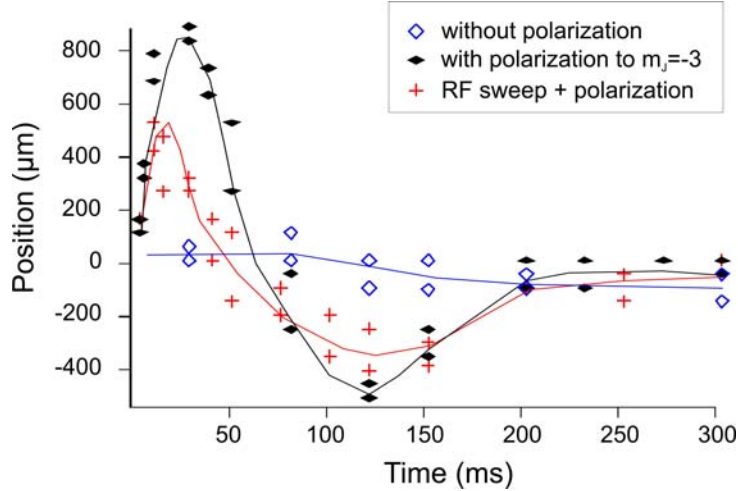ms, because of the anharmonicity of the optical trap.

Figure 7.3: Cloud oscillations due to optical pumping to the $m_J = -3$ state: without polarization (diamonds), with polarization beam only (triangles) and with an RF sweep applied just before the polarization pulse.

A solution to reduce the amplitude of these oscillations is to apply an RF sweep, which inverts the sign of the initial m_J-distribution, bringing the atoms in the $m_J \leq 0$ states. The atoms are not yet fully polarized to the $m_J = -3$, and the 427 nm pulse is still needed; however the atoms will absorb less photons before reaching the $m_J = -3$ stretched state and the momentum kick is reduced.

The corresponding experiment is shown in fig.(7.3) (crosses), where a 20 ms linear sweep, from 5 to 9 MHz was applied before the optical pumping pulse, in the presence of the 3 G polarization magnetic field. We observe that the oscillation amplitude is reduced by a factor of ~ 2.

Heating due to optical pumping

Although reduced, the oscillations are not completely eliminated when using the RF m_J-inversion before the polarization pulse. To completely eliminate the unidirectional momentum kick, we then retro-reflected the optical pumping beam. In this case, the atoms absorb photons with equal probabilities from each beam, and the average momentum kick is zero.

A weak heating is however expected, coming from the momentum diffusion, associated with spontaneous emission on the one hand (3D heating), and to the random absorption on the other hand (1D heating, along the beam direction). Both heatings are expected to be small compared to the atoms' temperature, and we were not able to measure it.

7.1.4 Transfer to the lowest energy state

Density-dependent losses in the ODT

In this subsection I study the influence of the polarization of the atomic sample on the inelastic collision losses in the optical trap.

Because of the limited lifetime due to background gas collisions (30 s), we found experimentally that the influence of the atomic spin-polarization on the inelastic collisions (dipolar relaxation) is rather hard to demonstrate in a single-beam ODT configuration, with typical densities limited to about 10^{11} atoms/cm^3.

The experiments presented here were performed in a crossed optical dipole trap configuration. This configuration is used as a way of locally increasing the atomic density, and thus the inelastic collision rates, for better experimentally highlighting the presence and the consequences of spin-changing collisions (such as dipolar relaxation).

In order to demonstrate the presence of such losses, we performed the following experiment. We first loaded the single-beam (horizontal) ODT, following the procedure described in the previous chapter. After a 2 s loading time, the MOT beams and magnetic gradient are switched off and the quantization magnetic field is turned on. The atoms are then optically pumped to the $|m_J = +3\rangle$ state.

About 3 s after the loading of the single-beam ODT, we start rotating the $\lambda/2$ plate by $\sim 25°$ in 2.5 s. During this rotation the vertical beam was blocked, using a mechanical shutter.
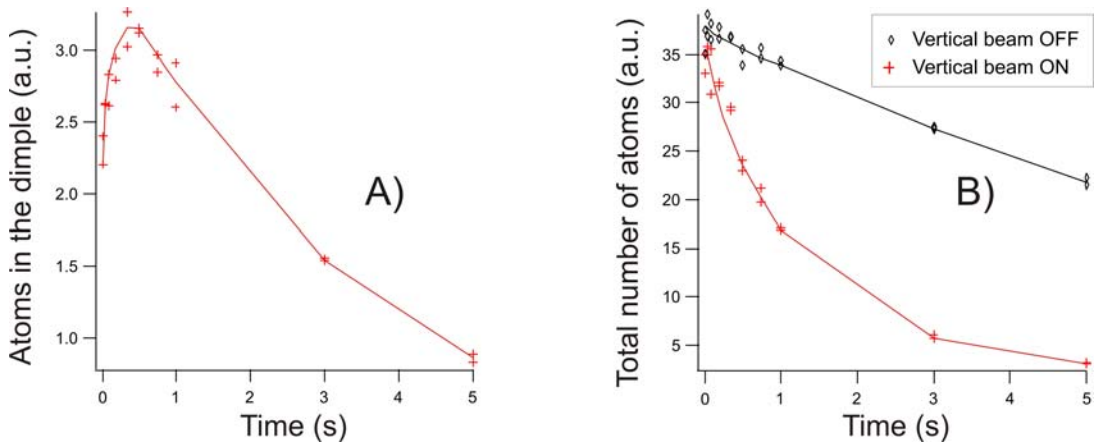

Figure 7.4: Demonstration of the influence of the vertical beam on the lifetime of the ODT: A) when the vertical beam is turned on, we observe the fast accumulation (within a few 100 ms) of atoms in the crossing region. B) comparison between the lifetime of the ODT, in presence and in absence of the vertical beam.

When the rotation is complete (time $t = 0$), the 45 W vertical beam is suddenly unblocked and sent to the atoms. We observe (see fig.(7.4.A)) the formation of a dimple,

within about 500 ms, containing up to 10% of the atoms (5×10^4) at a maximum peak density of $\sim 10^{12}$ atoms/cm^3, which is a factor of about 10 higher than in the horizontal ODT.

In fig.(7.4.B) (crosses) we show the *total* number of atoms in the ODT as a function of time. For comparison, we also plotted (diamonds) the time-evolution of the number of atoms, obtained with the same experimental sequence, except that we keep the vertical beam blocked all along the experiment.

We observe that the presence of the vertical beam creates important losses of atoms. As spin-changing collisions are not suppressed in the $|m_J = +3\rangle$ state, this observation can be explained by the fact that the atoms in the horizontal ODT pass through a region of high density, during their oscillations in the beam longitudinal direction, which increases the inelastic loss rates.

Polarization to the $|m_J = -3\rangle$ state

Finally, we checked the effect of polarization of atoms in the lowest-energy state, $|m_J = -3\rangle$, where dipolar relaxation can be suppressed, as discussed earlier. The experimental time-sequence is similar to the one previously presented, for the polarization in the $|m_J = +3\rangle$ state: after accumulating the atoms in the horizontal ODT – at only half the power, the rest being in the vertical beam, blocked with a shutter during the loading sequence – we polarize the atoms in the lowest energy state and, after some 1 s of additional waiting time, we suddenly unblock the vertical beam and form a crossed ODT. The results, representing the number of atoms as a function of time, are shown in fig.(7.5) (full diamonds), together with the case where the vertical beam was kept off all the time (crosses).

We observe that the situation is different than in the previous case (polarization to the $|m_J = +3\rangle$ state). For the same local increase of the density (10^{12} atoms/cm^3 in the dimple), this time there is no longer any influence of the presence of the vertical beam on the lifetime of the ODT. We conclude that, indeed, the polarization of atoms in the lowest energy state dramatically reduces the collisional loss of our trap, and provides the best starting point for future evaporative cooling experiments.

7.2 Single-beam lifetime experiments

7.2.1 Compensation of the residual magnetic field gradient

The elongated geometry of the single-beam (horizontal) ODT is very sensitive to any residual magnetic field gradients along the z' direction. In fig.(7.6) we show,
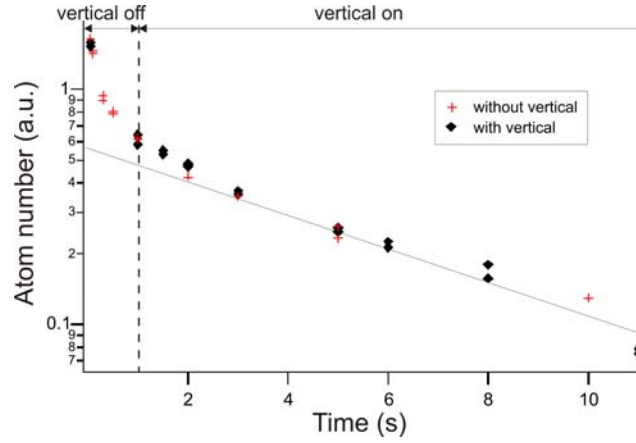
Figure 7.5: Effect of polarization in the $|m_J = -3\rangle$ state: the presence of the vertical beam (applied at $t = 1$ s for the full diamonds) is no longer a source for atom losses in the ODT.

for illustration, the longitudinal confinement of the ODT in presence of a 0.6 G/cm gradient. The trap depth is significantly lowered, from 500 μK (without the gradient) down to ~ 250 μK.
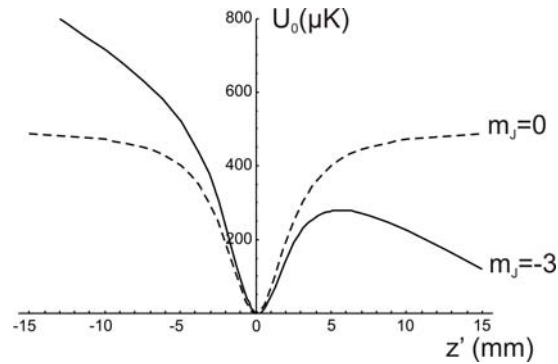

Figure 7.6: Solid line: sum of the optical potential + magnetic potential, due to the residual uniform gradient (0.6 G/cm). Dashed line: optical dipole potential.

Experimental measurement of the 'residual' magnetic gradient

While performing the RF-sweep experiments – described in Section(7.1.3) – we observed that, if the RF is kept on after the 427 nm laser pulse, at the final value of the RF sweep, the shape of the cloud changes. We observe two components of the cloud, one being centered on the ODT beam and the other being shifted by a distance which linearly depends on the value of the RF frequency, as shown in fig.(7.7).

This observation can be explained by the presence of a residual magnetic field gradient, which, together with the RF, deforms the trapping potential along its weak
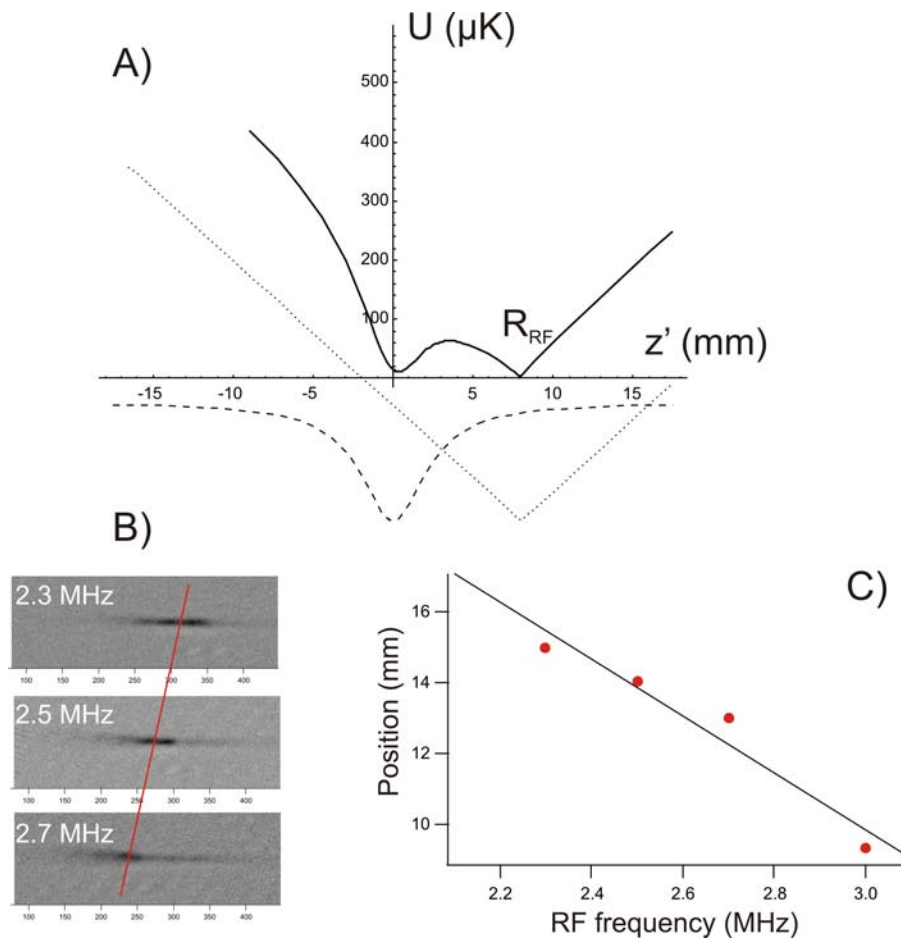
176

Figure 7.7: A) Full line: total potential, sum of the optical (dashed line) and magnetic potential modified by the RF (dotted line). B) Absorption images of the trapped cloud, for three different values of the RF frequency. C) position of the cloud component which depends on the RF frequency.

(longitudinal) direction. The situation is illustrated in fig.(7.7), where we plot the total potential, sum of the optical dipole potential and the magnetic+RF potential, in the z direction. The position of the RF resonance, R_{RF}, corresponds to a second potential minima in which atoms can accumulate, which explains the shapes observed experimentally.

From the slope of the plot shown in fig.(7.7.C) we can deduce a value of the residual magnetic field gradient of 0.5 G/cm. The origin of this gradient can be explained as coming from two sources. The most important is the last coil of the Zeeman slower, which produces a magnetic field gradient of ~ 0.45 G/cm at the position of the MOT. The second source is the ion pump, which produces a gradient of 0.1 G/cm at the position of the MOT (this value has been measured, with a Hall effect gaussmeter, before the installation of the vacuum system).

177

Compensation of the magnetic field gradient

We decided to compensate for the residual field gradient by replacing the symmetric pair of coils, previously used for the optical pumping, by a single coil, which has the roles of both creating the polarization magnetic field and compensating for the residual gradient. This rather handy solution cannot offer the possibility of changing at will the magnetic field; for an optimal gradient compensation it provides a B-field value of ~ 3 G at the position of the atoms, which is still high enough to ensure the robustness of the polarization and also prevent dipolar relaxation in the lowest energy state (as it gives a 400 μK Zeeman level separation, which is almost by a factor 4 larger then the initial temperature of the atoms accumulated in ODT)[3].

7.2.2 Compensation of the longitudinal magnetic field curvature

After compensating the residual magnetic field gradient, we performed a lifetime experiment of the atoms in the horizontal optical trap, using different atomic polarizations. The results are shown in fig.(7.8), where we plot the time-evolution of the number of atoms as a function of time, after having polarized the atoms in the $|m_J = -3\rangle$ state (circles) and $|m_J = +3\rangle$ state (triangles). For comparison, we also plot the evolution of a non-polarized sample. The 3G magnetic field, used for optical pumping, was kept on all along these experiments.

In a previous subsection we showed that inelastic collisions can be suppressed in the $|m_J = -3\rangle$ state, whereas they are still present in the $|m_J = +3\rangle$ state. However, fig.(7.8) shows the intriguing feature that the lifetime of the atoms in the $|m_J = -3\rangle$ state, in the horizontal ODT, is shorter then the lifetime of the non-polarized sample, which is itself shorter than that of $|m_J = +3\rangle$ atoms.

This effect can be attributed to the fact that the polarization coil does not produce a constant magnetic field gradient, on the longitudinal length-scale of the optical trap (i.e. the Rayleigh length). The situation is explained in fig.(7.9.A), where we plot the total potential (optical and magnetic, due to the polarization coil) along the ODT beam axis. The atoms in the $|m_J = +3\rangle$ state see, in this direction, a trap depth which is higher than the ODT depth, and their evaporation is somewhat slower than for the atoms in lower m_J−states (such as the atoms of a non-polarized sample; see for example the case of $|m_J = 0\rangle$ atoms, which only feel the optical potential).

The situation is inverted for $|m_J = -3\rangle$ atoms: the trap depth in the longitudinal direction is lowered by the presence of the magnetic field curvature (typically of

---

[3] Another solution would be to switch off the last ZS coil after the loading of the ODT and to magnetically shield the ion pump.
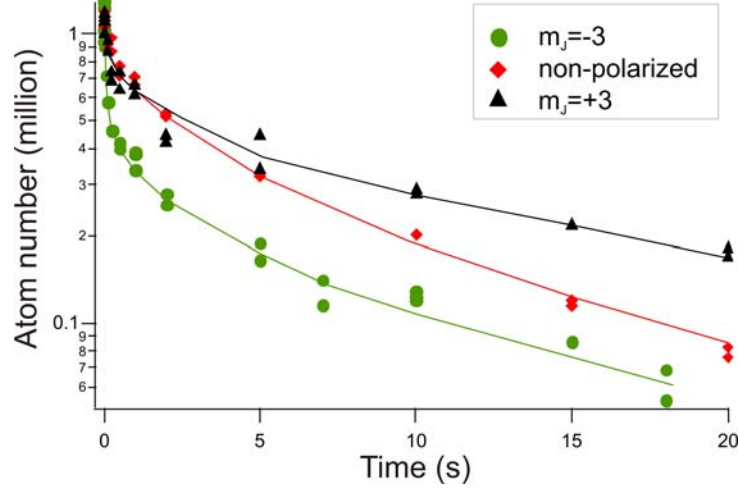
Figure 7.8: Lifetime experiment for atoms in different spin states. We plot the time-evolution of the number of atoms in the horizontal ODT, for the $|m_J = -3\rangle$ state (circles), for the $|m_J = +3\rangle$ state (triangles) and for a non-polarized sample. The solid lines are guidelines for the eye.
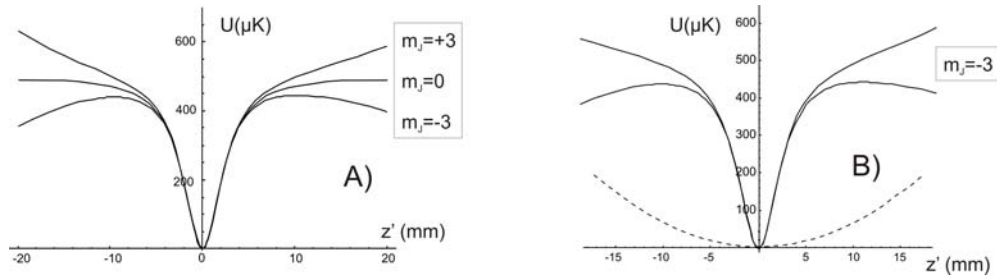

Figure 7.9: A) Optical + magnetic potential, for three different atomic spin states, in the ODT beam longitudinal direction. B) Optical + magnetic potential, for the atoms in the $|m_J = -3\rangle$ state, with and without the curvature-compensating coil. The dashed line is the magnetic potential due to the curvature-compensation coil.

$\sim 60 \ \mu$K, in our experimental conditions). Evaporation removes more atoms in this case, which explains the curves in fig.(7.8).

In order to compensate for the magnetic field curvature, we used a 'transverse' magnetic coil, having a radius of ~ 4.5 cm and placed at 9 cm above the upper viewport of the experimental chamber. Its axis is thus perpendicular to the horizontal ODT beam direction. This coil produces a magnetic field maximum in the ODT weak-confining direction, and the corresponding Zeeman potential for $m_J = -3$ atoms (high field seekers) is illustrated in fig.(7.9.B) – dashed line[4].

---

[4] A well-known result says that the 3D magnetic trapping of high-field seekers is not possible; the magnetic field of this coil has however a maxima along two directions of space. An interesting idea would be to use a 'transverse' coil for increasing the longitudinal confinement of the ODT. However, calculations showed that relatively small distances to the atoms are required (a few cm), and this

On the other hand, the 'transverse' coil also creates a magnetic field gradient in the ODT beam direction (which changes thus the 'optimal' value of the current for the 'polarization coil'). However, one can show that the combination of these two coils can be used for compensating the residual magnetic field gradient along z', while providing a 'good' magnetic field curvature (i.e. confining for the $m_J = -3$ atoms along the ODT beam direction – see fig.(7.9.B)).
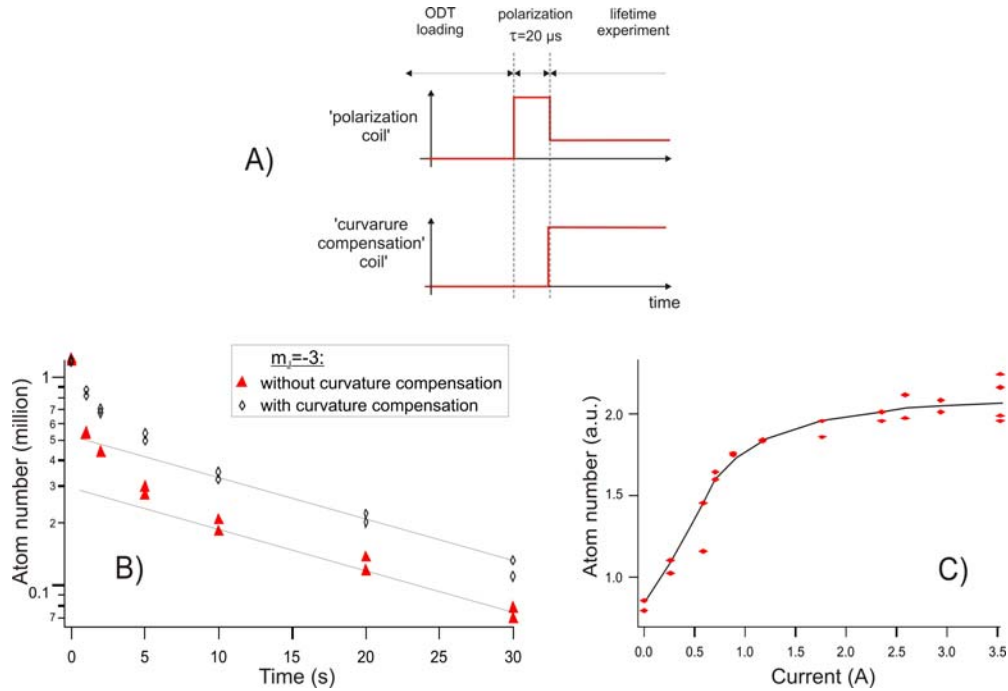

Figure 7.10: A) Time-sequence for polarization of atoms ($m_J = +3$), and for the subsequent compensation of the magnetic field curvature. B) Horizontal ODT lifetime, in presence (diamonds) and in absence (triangles) of the 'curvature compensation' coil (3 A current). C) Atomic signal, at $t = 5$ s during the 'lifetime experiment', as a function of the current applied to the coil.

To test the influence of the magnetic field curvature compensation, we performed the following experiment: after loading the horizontal ODT, we optically pumped the atoms in the $|m_J = -3\rangle$ state, in presence of the 'usual' 3 G polarization magnetic field, created by the 'polarization coil'. After atomic polarization, we switched on the current in the 'transverse' coil, and also changed the value of the 'polarization coil' current. The switch-on time of both coils are relatively long – about 2.5 ms –, and we expect that the atoms adiabatically follow the direction of the magnetic field, remaining thus in the $|m_J = -3\rangle$ state.

From this point, we repeated the lifetime experiment, by recording the time-evolution of the atom number. The results are shown in fig.(7.10.B), and we observe that the

cannot be implemented in the current configuration of our experiment.

atom number, at 'long times', is improved by a factor of ~ 2. For optimization, we also plotted the dependence of the atom number, at $t = 5$ s, as a function of the current in the 'transverse' coil, as shown in fig.(7.10.C).

7.2.3 Plain evaporation and lifetime

We studied the time evolution of the atomic cloud trapped in the single beam (horizontal) ODT, after the beams and magnetic field gradient of the MOT are switched off, and after polarization in the lowest energy state. Fig.(7.11.A) shows the decay of the number of atoms, with a fast non-exponential evolution in the first few seconds.

We attribute this evolution to the plain evaporation, which occurs after the sudden release of the magnetic field gradient, when the depth of the trap is lowered, from an 'almost infinite' value (a few K) – mixed magnetic+ODT trap – to a finite value of ~ 400 μK in the pure ODT. We checked this hypothesis by analyzing the evolution of the temperature. We observe, in the plot shown in fig.(7.11.B), that indeed the loss of atoms is accompanied by a $\sim 40\%$ temperature decrease, from the initial value of 120 μK to about 80 μK.

The temperature evolution stops almost completely after about 5 seconds; this can be also seen in fig.(7.11.A), as the atom loss also decreases and the atom number time-dependence becomes (almost) exponential, with a time constant of 25 s. At low time-scales, when the evaporation is expected to be almost completely reduced (as the density has dropped down to about a few 10^9 atoms/cm^3) we could not detect any increase of the temperature.

Finally, in fig.(7.11.C) we plot the evolution of the phase-space density as a function of time. We observe a fast increase of a factor of 2, in about 500 ms, before reaching a plateau at a value of $\sim 4 \times 10^{-6}$. After 5 s, we observe a decrease, which is explained by the fact that the cooling has almost completely stopped, whereas there is still a loss in the number of atoms.

The situation in our experiment is rather different that what has been observed in the group in Stuttgart [110, 103]: in their experiment, they observe an important increase, of more than one order of magnitude in the phase-space density in the first 5 seconds of plain evaporation, while losing only a factor of two in the number of atoms. Although we do not have yet a final explanation for this difference, we think that the initial conditions in the ODT, after releasing the magnetic trap, are rather different in the two experiments. In their case, we think that the initial situation is closer to thermal equilibrium, as the optical trap has been loaded in a relatively long time – i.e. several seconds of RF evaporation in the MT, in presence of a horizontal ODT beam –, sufficient to ensure thermal equilibrium. In our case, after releasing the MT, thermal equilibrium in the ODT is probably not reached, because of the strong inelastic
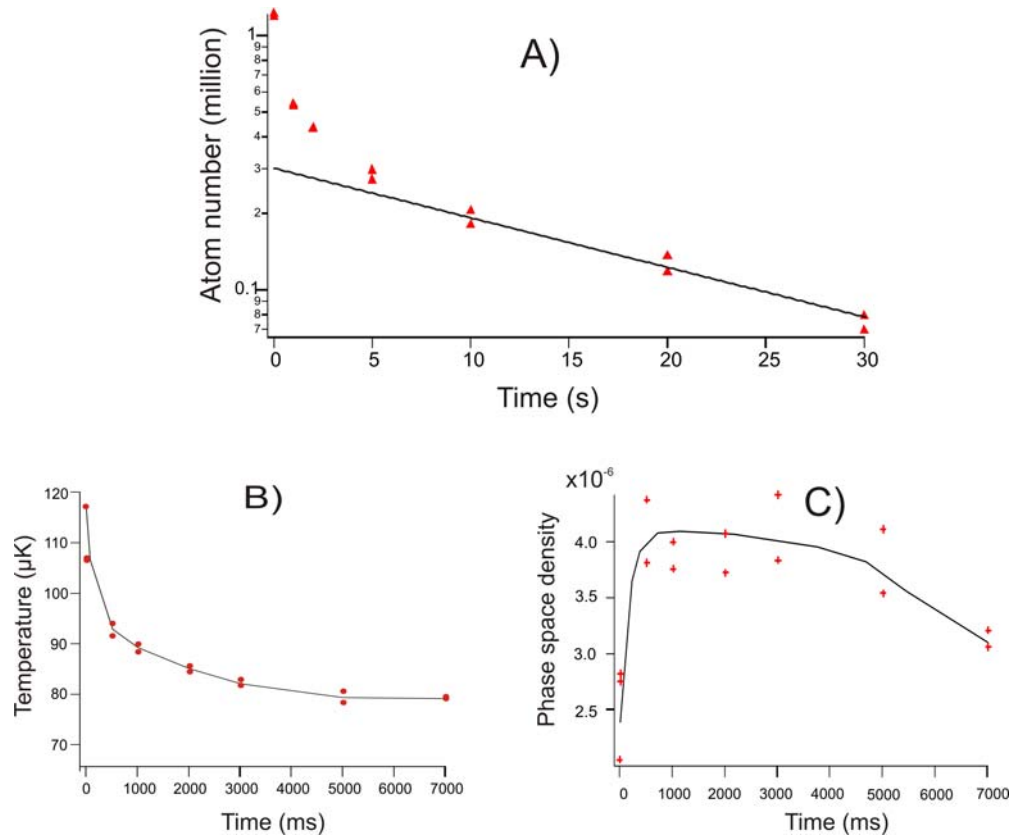
Figure 7.11: Plain evaporation in the horizontal optical dipole trap. A) time-evolution of the atom number (semi-log scale), showing a non-exponential decay at short times. B) temperature evolution during the first 7 seconds of the decay. C) phase-space density evolution.

collision rates in the metastable states[5].

Simulations using the Boltzmann equation (not detailed here) confirmed that the initial conditions play indeed a crucial role and may lead to very different time-evolutions for the atom number and temperature. An exact simulation of our system is however not possible, because the exact phase-space distribution cannot be measured precisely. For example, deviations from the equilibrium velocity distribution could not be observed using the ballistic expansion of the cloud (it provides only the widths of the velocity distribution).

---

[5] We remind that this was already the case in the magnetic trap – see Chapter(5). During the loading of the 'mixed' magnetic + horizontal-beam ODT, the peak densities are even higher; this increases the inelastic collision rates, which prevents thermal equilibrium to be reached.

7.2.4 Adiabatic recompression of the ODT

We performed additional experiments, by changing the initial conditions and testing their influence on the 'plain evaporation' in the horizontal ODT. For that, we accumulated atoms using smaller laser powers (and thus at lower temperatures) before adiabatically ramping up the laser power to the maximum value and performing a 'usual' lifetime experiment.

The situation is rather complicated, in our experimental conditions: first, thermal equilibrium is not fulfilled at $t = 0$; second, the initial density and 'temperature', before compression, both depend on the laser power used during the loading of the trap. Let us however give an intuitive idea of how the evaporation rates can be modified, by adiabatically compressing an optical trap, in the case of a thermalized sample.

Increasing the laser power, by a factor α, leads to an increase of α of the ODT depth and of $\sqrt{\alpha}$ of the trap bottom oscillation frequency (see eq.(6.19)). If the power ramp is adiabatic (i.e. slow compared to the trap oscillation frequency), it leads to an increase of the temperature by a factor $\sqrt{\alpha}$; the evaporation parameter $\eta = U_0/k_B T$ is thus also increased, by a factor $\sqrt{\alpha}$. On the other hand, the peak density increases[6] by a factor $\alpha^{3/4}$.

We can see that the initial evaporation rate, given by $\Gamma_{ev,i} \propto n_0 \sigma_{el} v_{th} f(\eta)$ (see eq.(5.36)) will be thus decreased, to a final value $\Gamma_{ev,f} = \Gamma_{ev,i} \frac{\alpha f(\sqrt{\alpha}\eta)}{f(\eta)}$. In fig.(7.12) we plot $\Gamma_{ev,i}$ and $\Gamma_{ev,f}$, before and after a recompression by a factor two ($\alpha = 2$) as a function of the η parameter before the recompression.
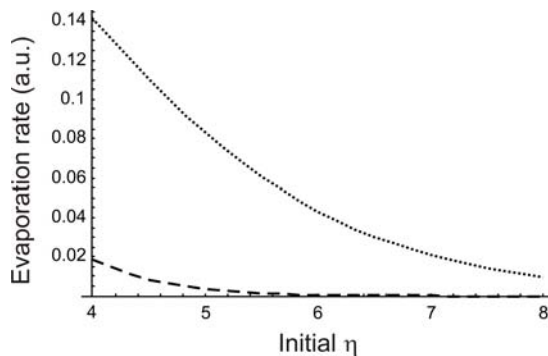

Figure 7.12: Evaporation rate before (dashed line) and after (dotted line) recompression by a factor of two of the ODT ($\alpha = 2$).

We performed the following experiment: we loaded the horizontal ODT at a fraction α of the maximum power (using the AOM of the fiber laser). After a 2 s accumulation, we ramped up the laser power to the maximum value, in ~ 40 ms, and performed the usual lifetime experiment, after polarization in the $|m_J = -3\rangle$ state. The results are

---

[6] One sees that the compression does not lead to an increase of the phase space density.

shown in fig.(7.13.A), where we plot the number of atoms at $t = 5$ s (when plain evaporation has stopped) as a function of the ODT laser power during the accumulation.
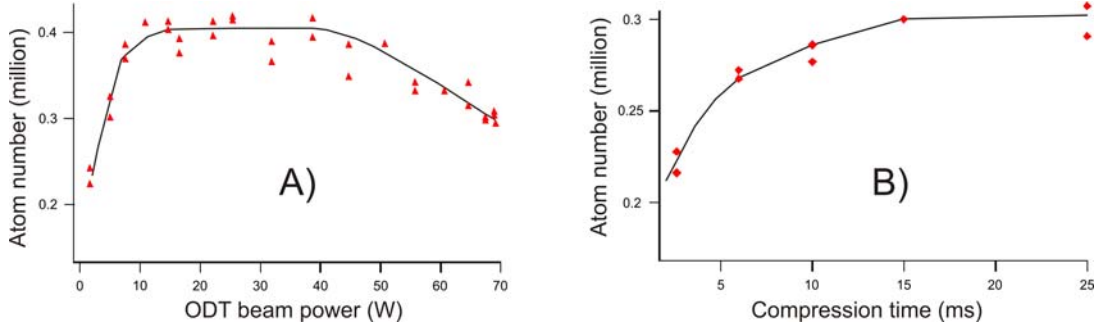

Figure 7.13: A) Number of atoms at 5 s after the recompression of the ODT, as a function of the IR laser power during the accumulation. B) Atom number as a function of the compression ramp duration, for an optimal accumulation, at ~ 20 W.

Although the initial atom number is lower when we accumulate using a smaller laser power (see fig.(6.18)), we observe that the number of atoms which remain in the ODT, at $t = 5$ s after the recompression, can be increased up to $\sim 35\%$, with respect to the accumulation at full power. The final temperature is observed to be constant after recompression, independently of the ODT beam power during the accumulation. The optimum is rather smooth, and is reached when accumulating between 20 to 40 W.

We additionally checked (see fig.(7.13.B)) that the adiabaticity of the compression is satisfied, by varying the time used to ramp up the power: for low compression times atoms are lost in the process, whereas for times longer than 25 ms the signal reaches a plateau. This timescale is set by the oscillation time along the axis of the laser beam, which, in our experimental conditions, is ~ 10 ms.

As reaching a BEC usually requires at least a few 10 s, and as the number of atoms at $t = 5$ s is higher (than when accumulating at full power), we included the recompression sequence in our ODT loading procedure.

7.3 Preliminary optimization procedures for evaporative cooling

The previous experiments showed that we are able to polarize the optically-trapped atoms in the lowest energy state, and thus suppress the inelastic collisions due to dipolar relaxation. In the current stage of our experiment, we are trying to find a route to Bose-Einstein condensation. For that, we need to optimize the transfer of the atoms from a single-beam ODT into a crossed ODT and then perform evaporative cooling,

by decreasing the trapping laser power.

Experiments are currently in progress, and the results reported in this section are preliminary. They may however provide some useful guidelines for the optimization procedure of the evaporative cooling in a crossed ODT.

Dynamic formation of a crossed ODT

In the previous chapter we presented the loading procedure of a single-beam ODT; as shown in fig.(6.18), the number of atoms which are accumulated does not saturate with the trapping laser power. This means that the maximum is obtained when using all the available power during the ODT loading sequence.

From this point, the following step in our experiment would be to dynamically create a crossed ODT, i.e. by rotating the $\lambda/2-$wave plate which controls the power ratio between the horizontal and vertical ODT beams. In fact, this step combines two sequences: the formation and loading of the crossed ODT, and the first stage of evaporative cooling, due to the decrease of the power in the horizontal beam.

We mention that the optimization procedure is not obvious, as there are several important parameters: the final temperature (after the $\lambda/2-$wave plate rotation), the number of atoms in the dimple (which is important, as it increases the elastic collision rate, and the evaporation speed), the number of atoms left in the 'wings' (as they represent a 'reservoir' of atoms to join the 'dimple' in future stage of the evaporation) or the final phase-space density.

Our experimental procedure consists in first loading (using the 'usual procedure' described in the previous chapter) the horizontal ODT with metastable atoms, followed by turning-off the MOT and the MT gradient, repumping the atoms in the ground state. Additionally, we included in the sequence the 'ODT recompression' technique, described in the previous section, and the polarization to the lowest-energetic Zeeman state. After that, we start the $\lambda/2-$wave plate rotation sequence. Experimentally, there are two parameters that can be tuned: the final rotation angle θ_f and the duration of the rotation (or, equivalently, the rotation velocity, which is limited to 20 degrees/s).

For a given final angle θ_f of the $\lambda/2-$wave plate, we analyze the number of atoms which are loaded inside the dimple, as a function of the time used for turning the plate. In fig.(7.14) we show the results, for three different values of θ_f: 25°, 27° and 30°. In each case, we additionally measure the total number of atoms left in the trap (dimple+wings) and the final temperature.

For each value of θ_f, we observe different optima for the number of atoms in the dimple region; the best optimum from this point of view corresponds to $\theta_f = 27°$. For $\theta_f = 25°$, the total number of atom is equivalent, but there are less atoms in the dimple and the temperature is higher. For $\theta_f = 30°$, although the temperature is lower, both N_{dimple} and N_{total} are reduced by a factor of ~ 2, which is probably not promising for
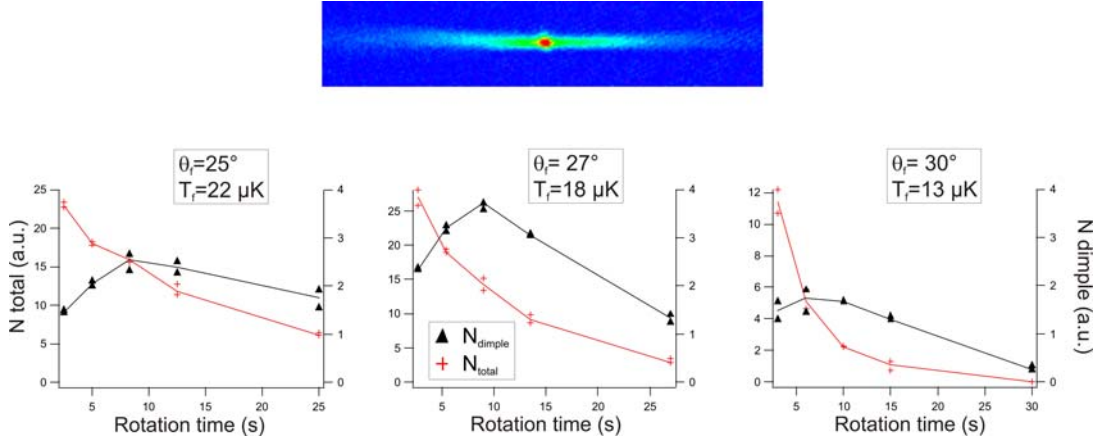
Figure 7.14: Optimization of the $\lambda/2-$wave plate rotation: for three different values of θ_f, we plot the final number of atoms in the dimple region N_{dimple} (triangles) and the total number of atoms left N_{total} (crosses), as a function of the duration of the rotation.

future evaporation.

We conclude that the best rotation sequence is to turn the $\lambda/2-$wave plate by $27°$ in 8 seconds. This sequence correspond to a final total number of atoms $N_{total} = 1.5 \times 10^5$ and to a temperature of 18 μK. The dimple contains $\sim 3 \times 10^4$ atoms at a density of 1.1×10^{11} atoms/cm^3. We note that these values correspond to a phase-space density of 2×10^{-5}, which represents a 20-fold increase of the initial phase space density (obtained at $t = 0$ after the loading of the single-beam ODT).

Of course, more complicated sequences, such as turning the $\lambda/2-$wave plate in several steps (with different durations and θ_f values) can be considered, and will make the object of future optimization procedures. Such a possibility may include a different optimization criterion; for example, after each rotation step, one may search to maximize the 'evaporation efficiency' (defined in the next paragraph).

Evaporative cooling optimization procedure

The following step, after the $\lambda/2-$wave plate rotation, consists of performing evaporative cooling in the crossed ODT, by progressively lowering the power of the laser (using the RF power-control of the fiber laser's AOM). The optimization criterion we chose is to maximize the quantity defined by:

$$\xi_{ev.} = -\frac{\log(D_{ph,f}/D_{ph,i})}{\log(N_f/N_i)} \tag{7.1}$$

where $D_{ph,f}$ ($D_{ph,i}$) and N_f (N_i) are respectively the final (initial) phase-space density and number of atoms. $\xi_{ev.}$ is usually named 'evaporation efficiency', and represents

the 'number of orders of magnitude gained in phase-space density for one order of magnitude lost in the number of atoms'.
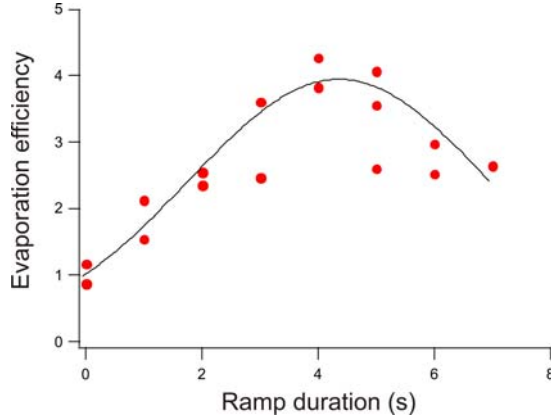

Figure 7.15: Evaporation efficiency as a function of the duration of the evaporation ramp.

In fig.(7.15), we show an experimental example of the optimization procedure. We used a linear ramp, in which the IR laser power was lowered by $\sim 30\%$. We plotted the dependance of the 'evaporation efficiency' on the duration of the ramp. We observe that we obtain a well-defined maximum, corresponding to an optimal ramp duration of ~ 4 seconds. The gain in phase-space density is $\sim \times 5$, whereas the atom number is reduced by only a factor 1.46. This corresponds to a high value of the 'evaporation efficiency' ($\xi_{ev.} = 4$).

Following the optimization procedures, we achieved a final phase space density up to $\sim 5 \times 10^{-4}$, for a final temperature of $8\ \mu K$. Unfortunately, when further decreasing the laser power, we observe a decrease of the density in the dimple region, which, despite the temperature decrease, leads to a constant value of the phase-space density. The evaporation efficiency becomes lower than unity.

Perspectives

The previous observation, of the decrease of the density in the dimple region, may be a consequence of the complicated evaporation dynamics in the crossed optical dipole trap. Indeed, the peak density is fixed mainly by the number of atoms which are loaded in the dimple region. In the ideal case, when performing evaporative cooling, atoms are loaded from the wings ('reservoir') in the dimple region, and the peak density increases.

In our experiments this is not the case: N_{dimple} remains always small compared to the number of atoms in the 'wings' ($\sim 15\%$), and we observe a decrease of N_{dimple} at a certain point of the evaporation. In fact, as we perform the evaporation ramps, using

the AOM, the power decreases both in the horizontal and in the vertical beam (the ratio of the two being constant, fixed by the angle of the $\lambda/2-$wave plate). This may lead to a situation where the atoms actually leave the dimple region into the wings (i.e. the dimple evaporation rate exceeds the loading rate, due to the atoms in the wings).

A possibility for canceling this effect is, for example, to maintain a constant power in the vertical beam while decreasing the power of the horizontal trap. Although more difficult in our current setup, this is possible by compensating the power decrease (due to the forced evaporation of the wings) by a rotation of the $\lambda/2$ plate. Some preliminary tests showed that this allows, for the same final temperature and total number of atoms, to obtain more atoms in the dimple region. Similar techniques, consisting in evaporating the atom reservoir in the 'wings' for lowering the temperature of the dimple, is currently used in other BEC experiments [100, 26].

Another perspective, which would allow to use longer evaporation ramps, is to increase the lifetime related to background gas collisions (currently limited to 30 s). There are several possibilities: either baking the cell or cooling it, with an external chiller.

Other perspectives, currently under development in our group, consist in increasing the initial number of atoms in the single-beam ODT. Increasing the initial number of atoms (and density) could mean higher elastic collision rates, which would increase the evaporation speed; under these circumstances the limitation related to background gas collisions would be less important.

Yet another perspective would be to implement a cooling scheme, which is efficient for Cr: demagnetization cooling. This scheme, proposed and demonstrated in the group of T.Pfau [111], is particularly appealing as is permits to decrease the temperature without loosing atoms. The authors found a very high evaporation efficiency, of about 15, and the final limitation (when the temperature approaches 10 μK) was due to the difficulty to control the magnetic fields 'accurately enough'.

In our case, the possibility is particularly appealing, as the initial number of atoms in the ODT is equivalent, but the temperature is considerably higher.

Conclusions

During my thesis, a new cold atom experiment for Cr atoms was designed and built. The technical solutions, which have been detailed in this dissertation, are quite different from the ones used in other similar experiments, mostly performed with alkalis. The realization of a hot Cr oven, functioning around 1500°C, as well as different tests of materials were presented; the lasers system – providing ~ 300 mW of 425 nm laser light (a wavelength which is not available with diode lasers) was built and stabilized on an atomic transition. The experiment which was built during my thesis is a Zeeman-slower-fed MOT. Both ^{52}Cr and ^{53}Cr MOTs were obtained and studied, either separately or simultaneously.

The experiments presented in this dissertation improved the knowledge about the properties of Cr atoms. Some of them have already been studied elsewhere: for example, our experiments confirmed a large inelastic collision parameter $\beta_{MOT} \sim 6.3 \times 10^{-10}$ cm^3/s in a ^{52}Cr MOT, but they also allowed us to measure it in the case of the fermionic MOT, which has values almost one order of magnitude higher. A large inter-isotope inelastic collision parameter $\beta_{MOT} \sim 2 \times 10^{-9}$ cm^3/s was also measured. A theoretical model was developed to understand better these results, and to account for the difference with the alkali atoms – for which light-assisted collision parameters are much smaller, and the loss mechanisms are well understood. This model indicates that, in the case of Cr, (almost) all pair of atoms, excited by the MOT beams and reaching a typical interparticle distance $\sim \lambda/2\pi$, are mysteriously expelled from the trap.

Due to the high inelastic collision parameters, the number of atoms in Cr steady-state MOTs are limited to a few 10^6. To reach BEC, our strategy is to first accumulate atoms in the metastable ^{5}D states, which are shielded from the MOT light-assisted collisions. For this reason, the measurement of the elastic and inelastic collisional properties of the metastable Cr atoms had a major importance for us, and led to a better understanding of the accumulation results.

Experiments performed in a quadrupole magnetic trap led to the measurement of the inelastic collision parameter $\beta_{DD} = 3.3 \times 10^{-11}$ cm^3/s between metastable atoms. Further experiments, involving RF magnetic field which truncate the magnetic trap, provided a measurement of the elastic collision cross section between metastable atoms

Cr isotope	Value	Error bar	Unit
^{53}**Cr**	$\beta_{MOT}= \mathbf{4 \times 10^{-9}}$	± 40 %	**cm^3/s**
^{53}**Cr**	$\gamma_{PD}= \mathbf{250}$	± 30 %	**s^{-1}**
^{52}**Cr** $-$ ^{53}**Cr**	$\beta_{MOT}= \mathbf{1.8 \times 10^{-9}}$	± 40 %	**cm^3/s**
^{52}Cr	$\beta_{MOT} = 6.3 \times 10^{-10}$	± 35 %	cm^3/s
^{52}Cr	$\beta_{DD} = 3.3 \times 10^{-11}$	± 20 %	cm^3/s
^{52}**Cr**	$\sigma_{el,DD}= \mathbf{7 \times 10^{-12}}$	± 50 %	**cm^2**
^{52}Cr	$\beta_{PD} = 4.9 \times 10^{-10}$	± 15 %	cm^3/s

Table 7.1: Properties of the Cr which have been measured in this work.

$\sigma_{el} = 7 \times 10^{-12}$ cm^2, close to the unitary limit, as well as the inelastic collision parameter with the excited atoms from the MOT $\beta_{PD} = 4.9 \times 10^{-10}$ cm^3/s. Finally, parametric excitation experiments in an optical dipole trap (ODT) loaded with metastable atoms yielded a measurement of the AC Stark shift of these states.

The work presented here explored new trapping methods for metastable Cr atoms. For example, I demonstrated the continuous loading of metastable ^{52}Cr atoms in a RF-truncated magnetic: in this scheme, accumulation and evaporation are simultaneous. This leads to the fast production, within less than 1 s, of a cold, magnetically trapped sample, having a phase-space density as high as 7×10^{-6} (see fig.(7.16)), which represents an increase by almost one order of magnitude compared to the MOT phase-space density. A theoretical model, using rate equation for the mean energy and number of atoms, showed that this value is limited by inelastic collisions, mostly with the excited MOT atoms.
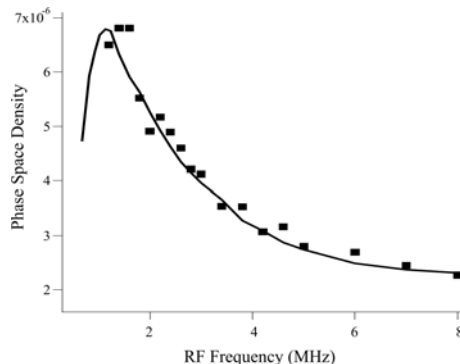

Figure 7.16: Increase of the phase-space density of the cloud of ^{52}Cr metastable atoms, accumulated in a RF-truncated magnetic state.

Even though the inelastic collision properties of Cr do not allow to reach condensation in the metastable states, our experiments may be interesting in the perspective of continuously loading a magnetic waveguide – for BEC or atom optics experiments.

Because dipolar relaxation is ultimately the major obstacle for condensing Cr in a magnetic trap, our experiments aiming towards condensation will be performed in an optical trap. The very same inelastic collisional processes, as well as Majorana losses, make difficult the transfer of a Cr cloud from a quadrupole magnetic trap to an ODT. We developed a new accumulation technique to trap metastable atoms into a mixed magnetic+optical trap. This is an original method, which allows us to load up to 1.2×10^6 atoms (see fig.(7.17)) at 100 μK in a very short time ($\sim$ 200 ms). Studies of the loading dynamics of the mixed trap showed that the accumulation is limited by Majorana spin-flips and inelastic collisions between metastable atoms.
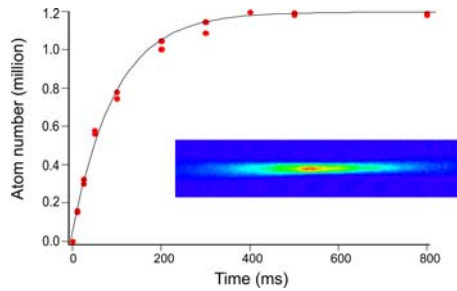

Figure 7.17: Loading of a single-beam optical dipole trap with metastable ^{52}Cr atoms.

Using RF fields to modify magnetic potentials is a very interesting idea, opening new ways for original trapping mechanisms. In this respect, we demonstrated that a magnetic quadrupole potential, modified by the RF, is able to capture not only the low-field seekers, but also the high-field seeking MOT atoms which decay to the metastable states. Low-field seekers are trapped close to the $B = 0$ point, while high-field seekers are first expelled from the center of the quadrupole trap. However, once they reach the point where the RF field is resonant, their spin is flipped, and magnetic forces bring them back to the center of the trap. An interesting application in the context of Cr would be to create large-volume, magnetically trapped metastable samples, with lower densities, which presumably would allow to trap a higher number of atoms. Furthermore, as atoms are trapped in the minima which are away from the $B = 0$ point, Majorana spin-flips are expected to induce negligible losses in such a configuration.

There is a technical difficulty for this method, residing in the existence of RF second harmonics, and which turned out difficult to overcome. In the case of a purely quadrupole trap, high-field seekers, produced around $B = 0$, always reach the position of the second RF harmonics resonance. There, their spin may be flipped again, which projects them back into a state which is expelled. We proved that, in presence of an additional optical dipole confinement, the atoms are prevented from reaching $2R_{RF}$, and are no longer expelled.

The use of the RF fields allows one to remove the influence of Majorana spin-flips (which is otherwise one of the limiting factors in the ODT) and to increase the number
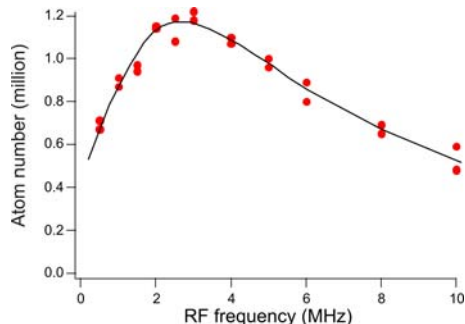
191

Figure 7.18: Reduction of the Majorana losses in a mixed, optical+quadrupole magnetic trap, which leads to an increase of the number of atoms accumulated in the ODT.

of atoms trapped in the optical dipole trap, as it is shown in fig.(7.18). Finally, current studies which are under development in our group, demonstrated the possibility of using RF sweeps for periodically reversing the spins of atoms at a fast rate, for 'erasing' (i.e. averaging to zero) the strongly-confining magnetic potential of the mixed trap. These experiments (not presented in this manuscript) allowed us to further increase, by a factor of two, the number of atoms in the ODT.

The work performed during my Ph.D. opens perspectives for finding an original route towards Bose-Einstein condensation of Cr. Future experiments will study the optimization of evaporative cooling in a crossed optical dipole trap; preliminary experimental procedures in this direction were presented here.

The results obtained for magneto-optical trapping of the fermionic isotope show that sympathetic cooling by the boson will probably be the way towards obtaining the first Fermi sea, as well as the first degenerate Bose-Fermi mixture with strong dipole-dipole interactions. The path is still long, and experiments will be very exciting...

With Cr, the perspectives for fundamental studies in the quantum regimes are numerous. From the experimental point of view, our setup gives the possibility of transferring the atoms into optical lattices. There, the anisotropic character of the dipole-dipole interactions is expected to lead to many interesting effects, related to the reduced geometries. In a 2D geometry of pancake-shaped planes, repulsions due to the dipole-dipole interactions – when the spins are perpendicular to the planes – may lead to a strong reduction of the three-body recombination rate; in a 1D geometry, in presence of attractive interactions, one may observe the formation of solitons. In a spin-polarized sample of dipolar fermionic atoms, where contact interaction is suppressed at low temperature, dipole-dipole interactions may lead to the observation of thermalization.

These are only three ideas developed by our group, which, I hope, give a flavor about the richness of the physics of dipole-dipole interactions in the degenerate regime, which can be performed with Cr.

192

Appendix

Appendix A

Hyperfine splitting and nonlinear Zeeman effect

In this appendix we briefly summarize the physics of the hyperfine coupling, which is responsible for the hyperfine splitting of the atomic levels, but also for the non-linear Zeeman effect.

A.1 Hyperfine splitting

The hyperfine coupling interaction hamiltonian $\mathbf{H}_{Hyp}$ is given by:

$$\mathbf{H}_{Hyp} = A\mathbf{I} \cdot \mathbf{J} \tag{A.1}$$

where A is the coupling constant. $\mathbf{H}_{Hyp}$ couples the nuclear spin $\mathbf{I}$ to the electronic momentum $\mathbf{J}$. This means that, in presence of the hyperfine interaction, the so-called 'decoupled basis' $|I, J, m_I, m_J\rangle$ (or simply $|m_I, m_J\rangle$ – defined by a set of common eigenvectors of $\mathbf{I}$, $\mathbf{J}$, $\mathbf{I}_z$, $\mathbf{J}_z$), does no longer diagonalize the total atomic hamiltonian. $\mathbf{H}_{Hyp}$ can however be written as:

$$\mathbf{H}_{Hyp} = \frac{A}{2}\left[\mathbf{F}^2 - \mathbf{J}^2 - \mathbf{I}^2\right] \tag{A.2}$$

where $\mathbf{F} = \mathbf{I} + \mathbf{J}$. The hyperfine interaction hamiltonian (and the total atomic hamiltonian) are thus diagonal in the so-called 'coupled basis' $|I, J, F, m_F\rangle$ (or simply $|F, m_F\rangle$ – defined by a set of common eigenvectors of $\mathbf{I}$, $\mathbf{J}$, $\mathbf{F}$, $\mathbf{F}_z$).

Using this basis, we calculate the eigenenergies of the hyperfine hamiltonian, which are given by:

$$H_{Hyp} = \frac{A}{2}\hbar^2\left[F(F+1) - I(I+1) - J(J+1)\right] \tag{A.3}$$

This formula is used for finding the hyperfine structure of the atomic levels (see Chapter(1)).

A.2 Non-linear Zeeman effect

In presence of a magnetic field, we add the Zeeman interaction hamiltonian:

$$\mathbf{H}_Z = B\frac{g_J\mu_B}{\hbar}\mathbf{J}_z \ . \tag{A.4}$$

where $\mathbf{J}_z$ is the projection of $\mathbf{J}$ on the quantization axis given by the direction of the magnetic field[1] (with the corresponding eigenvalues $\hbar m_J$).

In order to diagonalize the hamiltonian $\mathbf{H}_{Hyp} + \mathbf{H}_Z$, and find the eigenenergies as a function of the external magnetic field, we may write it in the $|F, m_F\rangle$ basis:

$$
\begin{aligned}
\langle F', m'_F|\mathbf{H}|F, m_F\rangle &= B \cdot g_J\mu_B \sum_{m_I, m_J} m_J\langle F', m'_F|m_I, m_J\rangle\langle m_J, m_I|F, m_F\rangle \\
&+ \frac{A}{2}\hbar^2\left[F(F+1) - I(I+1) - J(J+1)\right]
\end{aligned} \tag{A.5}
$$

In practice, for example to calculate the Zeeman effect for the ^{53}Cr transitions in the ZS, we use a mathematica program *Mathematica* to numerically diagonalize the hamiltonian given by eq.(A.5). For the ground-state of ^{53}Cr, it is a 28×28 matrix, and a 36×36 for the ^{7}P$_4$ excited state.

The scalar products in the sum are nothing else than the 'common' Clebsch-Gordan coefficients, which can be found using the 'ClebschGordan' *Mathematica* function: $\langle m_J, m_I|F, m_F\rangle \equiv \text{ClebschGordan}[\{J, m_J\}, \{I, m_I\}, \{F, m_F\}]$.

---

[1] Due to the fact that the nuclear magneton much smaller then the Bohr magneton ($\mu_N \ll \mu_B$) we neglected the nuclear magnetic moment, which is much smaller than the electronic one

Appendix B

Chromium light assisted collisions

B.1   Survival probability

I detail here the calculation of the survival probability which implies some subtleties. I consider the case where the lifetime of the excited molecular state, Γ_M^{-1}, does not depend on the interatomic distance. Since losses are expected to take place mostly at distances $R' \ll R$, I will also consider that $S(R, R') \simeq S(R, 0)$. In this case the eq.(4.18) becomes:

$$S(R, R') \simeq \exp\left(-\Gamma_M \int_{t(R)}^{t(0)} dt'\right) = \exp\left(-\Gamma_M \int_0^R \frac{dr}{v(r)}\right),$$

(B.1)

where $v(r)$ is the velocity acquired by the atom (which is traveling on the excited state potential) when arriving at a distance r. To evaluate $v(r)$, we can use the energy conservation for the evolution from the excitation point R and r:

$$\frac{\mu v(r)^2}{2} + \frac{\hbar^2 l(l+1)}{2\mu r^2} - \frac{C_3}{r^3} = \frac{\mu v(R, E, l)^2}{2} + \frac{\hbar^2 l(l+1)}{2\mu R^2} - \frac{C_3}{R^3}.$$

(B.2)

Using the previous expression (4.15) for $v(R, E, l)$ we find:

$$v(r) = \sqrt{\frac{2}{\mu}\left(E - \frac{C_3}{R^3} + \frac{C_3}{r^3} - \frac{\hbar^2 l(l+1)}{2\mu r^2}\right)}$$

(B.3)

and the survival probability becomes:

$$S(R, 0) = \exp\left(-\Gamma_M \int_0^R \frac{dr}{\sqrt{\frac{2}{\mu}\left(E - \frac{C_3}{R^3} + \frac{C_3}{r^3} - \frac{\hbar^2 l(l+1)}{2\mu r^2}\right)}}\right).$$
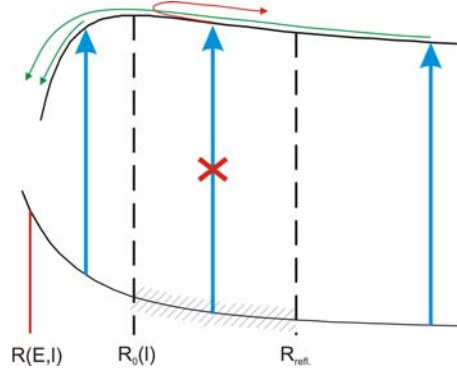
(B.4)

Figure B.1: Evolution on the excited effective potential.

It is important to notice that there are certain values for the $(R_{E,l}$ parameters that might give negative values for $v(r)$ in eq.(B.3). The situation is explained in fig.(B.1), considering the case where the classical turning point in the ground state, $R_{E,l}$, is on the left-hand-side of the excited state barrier $R_0(l)$.

If the atom-pair is excited in R_{exc} between $R_0(l)$ and $R_{E,l}$, it may always reach $R = 0$, as it is created on the attractive part of the effective potential.

On the other hand, if the excitation occurs at $R_{exc} > R_0(l)$, the situation becomes slightly more complicated, as the pair is 'created' on the repulsive part of the effective excited potential. It can thus be 'reflected', if its energy at the excitation point is lower than the excited state barrier, i.e. if:

$$E - \frac{C_3}{R_{exc}^3} < V(R_0) \tag{B.5}$$

When calculating the survival probability we impose thus an additional restriction on the $R-$integration domain in eq.(4.19), which eliminates the excitation radius between R_0 and $R_{refl.} = \left(\frac{C_3}{E-V(R_0)}\right)^{1/3}$.

B.2 Excitation rate

Julienne and Vigué use the following expression for the excitation rate:

$$\Omega_{exc}(R) = \frac{\lambda^2}{2\pi} \frac{(\Gamma/2)^2}{\Gamma^2/4 + (\delta_0 - C_3/R^3)^2} I_0. \tag{B.6}$$

This expression, valid in the low excitation regime ($I_0 \ll I_{sat}$), shows a linear dependence of the excitation rate on the laser intensity.

198

The JV model often considered as a 'quasi-static' model, because the excitation rate in eq.B.6 supposes that the optical pumping is very fast and the stationary population of the excited state is reached for every R. The low excitation also implies that the excited stationary population always remains very small compared to the ground state population.

In the experimental conditions that we used when measuring the light assisted collision parameters, the low intensity condition was not fulfilled (we typically used total MOT laser intensities of 10 to 20 I_{sat}). We must thus take into account the saturation effects which come to play. For that, we replaced the JV excitation rate by an expression which is proportional to the product of the stationary populations in the ground- and excited-state:

$$\Omega_{exc}(R) = \Gamma \left(\frac{\Omega^2/4}{\Omega^2/2 + \Gamma^2/4 + (\delta_0 - C_3/\hbar R^3)^2} \right) \left(1 - \frac{\Omega^2/4}{\Omega^2/2 + \Gamma^2/4 + (\delta_0 - C_3/\hbar R^3)^2} \right),$$
(B.7)

where $\Omega = \Gamma\sqrt{I_0/2I_{sat}}$ is the Rabi frequency. (B.7) expresses thus the fact that the collision parameter β is proportional to the probability of exciting a pair. We considered in our model that this probability is equal to the probability of having an atom in the ground state, times the probability of having a second atom in the excited state.

We can easily see that (B.7) becomes identical to the JV rate (B.6) in the low intensity regime, while for high intensity it saturates to $\Gamma/4$ (equal populations of $1/2$ in the ground and excited state).

B.3   Partial waves

An interesting result can be seen by plotting – see fig.(B.2) – the dependance of the terms in the sum given by eq.(4.19) as a function of the partial wave l. We observe that at high temperature, the cutoff is given qualitatively by l_{max} (see eq.(4.13)), i.e. the rotational barriers in the excited state.

At low temperature, the cutoff naturally occurs at l−values considerably smaller than at high temperatures. This fact is explained as the effect of the centrifugal barriers in the ground state, which gives another cutoff $l_{max,g} < l_{max}$ [58], smaller than the one in the excited state (as the ground-state potential $-C_6/r^6$ is flatter than the $-C_3/r^3$ potential).

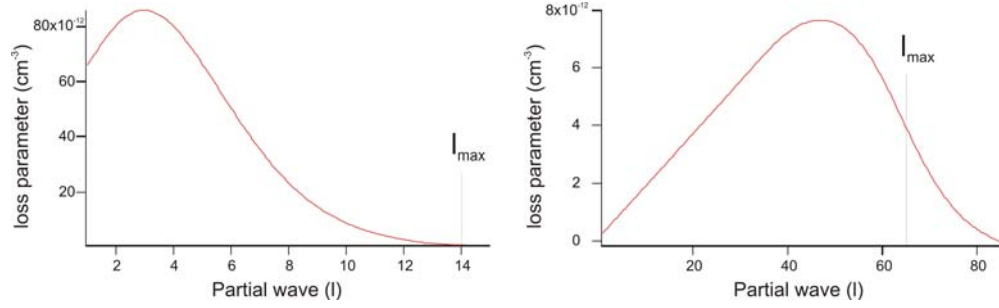Figure B.2: Dependance of the terms in the sum (4.19) on the partial wave number l: at $T = 100 \; \mu$K (left) and $T = 1$ K (right). The corresponding cutoffs, due to excited potential rotation barriers, are $l_{max} = 14$ and respectively $l_{max} = 65$.

Bibliography

[1] M. Anderson, J. Ensher, M. Matthews, C. Wieman, and E. Cornell, *Observation of Bose-Einstein Condensation in a Dilute Atomic Vapor* – Science, **269**, 198 (1995)

[2] K. Davis, M.-O. Mewes, M. Andrews, N. van Druten, D. Durfee, D. Kurn, and W. Ketterle, *Bose-Einstein Condensation in a Gas of Sodium Atoms* – Phys. Rev. Lett., **75**, 3969 (1995)

[3] B. DeMarco and D.S. Jin, *Onset of Fermi degeneracy in a trapped atomic gas* – Science., **285**, 1703 (1999)

[4] J. M. Gerton, D. Strekalov, I. Prodan, and R. G. Hulet, *BDirect observation of growth and collapse of a Bose-Einstein condensate with attractive interactions* – Nature, **408**, 692 (2000)

[5] J. R. Ensher, D. S. Jin, M. R. Matthews, C. E. Wieman, and E. A. Cornell, *Bose-Einstein Condensation in a Dilute Gas: Measurement of Energy and Ground-State Occupation* – Phys. Rev. Lett., **77**, 4984 (1996) L. V. Hau, B. D. Busch, C.

[6] Liu, Z. Dutton, M. M. Burns, and J. A. Golovchenko *Near-resonant spatial images of confined Bose-Einstein condensates in a 4-Dee magnetic bottle* – Phys. Rev. A, **58**, R54 (1998)

[7] F. Dalfovo, S. Giorgini, L. P. Pitaevskii, and S. Stringari *Theory of Bose-Einstein condensation in trapped gases* – Rev. Mod. Phys., **71**, 463 (1999)

[8] M. R. Andrews, C. G. Townsend, H.-J. Miesner, D. S. Durfee, D. M. Kurn, and W. Ketterle, *Observation of interference between two Bose condensates* – Science, **275**, 637 (1997)

[9] M.-O. Mewes, M. R. Andrews, D. M. Kurn, D. S. Durfee, C. G. Townsend, and W. Ketterle, *Output Coupler for Bose-Einstein Condensed Atoms* – Phys. Rev. Lett., **78**, 582 (1997)

[10] Immanuel Bloch, Theodor W. Hänsch, and Tilman Esslinger, *Atom Laser with a cw Output Coupler* – Phys. Rev. Lett., **82**, 3008 (1999)

[11] K. W. Madison, F. Chevy, W. Wohlleben, and J. Dalibard, *Vortex Formation in a Stirred Bose-Einstein Condensate* – Phys. Rev. Lett., **84**, 806-809 (2000)

[12] M. R. Matthews, B. P. Anderson, P. C. Haljan, D. S. Hall, C. E. Wieman, and E. A. Cornell, *Vortices in a Bose-Einstein Condensate* – Phys. Rev. Lett., **83**, 2498 (1999)

[13] M. Greiner, O. Mandel, T. Esslinger, T. H¨ansch, and I. Bloch, *Quantum Phase Transition from a Superfluid to a Mott Insulator in a Gas of Ultracold Atoms* – Nature, **415**, 39 (2002)

[14] T. Stoferle, H. Moritz, C. Schori, M. Kohl, and T. Esslinger, *Transition from a Strongly Interacting 1D Superfluid to a Mott Insulator* – Phys. Rev. Lett., **92**, 130403 (2004)

[15] B. Paredes, A. Widera, V. Murg, O. Mandel, S. Fölling, I. Cirac, G. V. Shlyapnikov, T. W. Hänsch, and I. Bloch, *Tonks-Girardeau gas of ultracold atoms in an optical lattice* – Nature, **429**, 277 (2004)

[16] S. Jochim, M. Bartenstein, A. Altmeyer, G. Hendl, S. Riedl, C. Chin, J. Hecker Denschlag, and R. Grimm, *Bose-Einstein Condensation of Molecules* – Science, **302**, 2101 (2003)

[17] M. W. Zwierlein, C. A. Stan, C. H. Schunck, S. M. F. Raupach, S. Gupta, Z. Hadzibabic, and W. Ketterle, *Observation of Bose-Einstein Condensation of Molecules* – Phys. Rev. Lett., **91**, 250401 (2003)

[18] C. A. Regal, M. Greiner, and D. S. Jin, *Observation of Resonance Condensation of Fermionic Atom Pairs* – Phys. Rev. Lett., **92**, 040403 (2004)

[19] T. Bourdel, L. Khaykovich, J. Cubizolles, J. Zhang, F. Chevy, M. Teichmann, L. Tarruell, S. J. J. M. F. Kokkelmans, and C. Salomon, *Experimental Study of the BEC-BCS Crossover Region in Lithium 6* – Phys. Rev. Lett., **93**, 050401 (2004)

[20] C. Chin, M. Bartenstein, A. Altmeyer, S. Riedl, S. Jochim, J. H. Denschlag, and R. Grimm, *Observation of the Pairing Gap in a Strongly Interacting Fermi Gas* – Science, **305**, 1128 (2004)

[21] M. W. Zwierlein, C. A. Stan, C. H. Schunck, S. M. F. Raupach, A. J. Kerman, and W. Ketterle, *Condensation of Pairs of Fermionic Atoms near a Feshbach Resonance* – Phys. Rev. Lett., **92**, 120403 (2004)

[22] L. Santos, G. V. Shlyapnikov, P. Zoller, and M. Lewenstein, *Bose-Einstein Condensation in Trapped Dipolar Gases* – Phys. Rev. Lett., **85**, 1791 (2000)

[23] K. Goral, K. Rzazewski, and T. Pfau, *Bose-Einstein condensation with magnetic dipole-dipole forces* – Phys. Rev. A, **61**, 051601 (2000)

[24] K. Goral, L. Santos, and M. Lewenstein, *Quantum Phases of Dipolar Bosons in Optical Lattices* – Phys. Rev. Lett., **88**, 170406 (2002)

[25] L. Santos, G. V. Shlyapnikov, and M. Lewenstein, *Roton-Maxon Spectrum and Stability of Trapped Dipolar Bose-Einstein Condensates* – Phys. Rev. Lett., **90**, 250403 (2003)

[26] A. Griesmaier, J. Werner, S. Hensler, J. Stuhler and T. Pfau, *Bose-Einstein condensation of chromium* – Phys. Rev. Lett, **94**, 160401 (2005)

[27] J. Stuhler, A. Griesmaier, T. Koch, M. Fattori, S. Giovanazzi, P. Pedri, L. Santos and T. Pfau, *Observation of Dipole-Dipole Interaction in a Degenerate Quantum Gas* – Phys. Rev. Lett., **95**, 150406 (2005)

[28] Th. Lahaye, T. Koch, B. Fröhlich, M. Fattori, J. Metz, A. Griesmaier, S. Giovanazzi, T. Pfau, *Strong dipolar effects in a quantum ferrofluid* – Nature, **448**, 672 (2007)

[29] A.S. Bell, J. Stuhler, S. Locher, S. Hensler, J. Mlynek and T. Pfau – *A magneto-optical trap for chromium with population repumping via intercombination lines* – Europhys. Lett., **45**, 156 (1999)

[30] C. C. Bradley, J. J. McClelland, W. R. Anderson and R. J. Celotta, *Magneto-optical trapping of chromium atoms* – Phys. Rev. A, **61**, 053407 (2000)

[31] Jürgen Stuhler, Ph.D. thesis, *Kontinuierliches Laden einer Magnetfalle mit lasergekühlten Chromatomen* – Universität Konstanz –(2001)

[32] Jonathan David Weinstein, Ph.D. thesis, *Magnetic Trapping of Atomic Chromium and Molecular Calcium Monohydride* – Harvard University – (2001)

[33] *Handbook of Physics and Chemistry* (2000)

[34] Arnaud Pouderous, Ph.D. thesis, *Refroidissement et piegeage d'atomes de Chrome* – Université Paris Nord – (2007)

[35] T.W. Hänsch and B. Couillaud *Laser frequency stabilization by polarization spectroscopy of a reflecting reference cavity* – Optics. Comm., **35**, 441 (1980)

[36] R.W.P. Drever, J.L. Hall, F.V. Kowalski, J. Hough, G.M. Ford, A.J. Munley, and H. Ward, *Laser phase and frequency stabilization using an optical resonator* – Appl. Phys. B., **31**, 97 (1983)

[37] Antoine Browaeys, Ph.D. thesis,   *Piegeage magnetique d'un gaz d'helium metastable : vers la condensation de Bose-Einstein* – Université Paris Sud –(2000)

[38] W. D. Phillips and H. Metcalf –   *Laser Deceleration of an Atomic Beam* – Phys. Rev. Lett., **48**, 596 (1982)

[39] P. A. Molenaar, P. van der Straten, H. G. M. Heideman, and H. Metcalf –   *Diagnostic technique for Zeeman-compensated atomic beam slowing: Technique and results* – Phys. Rev. A, **55**, 605 (1997)

[40] F. Reif, *Fundamentals of Statistical and Thermal Physics* (McGraw-Hill, New York, 1965)

[41] K. M. O'Hara, S. R. Granade, M. E. Gehm, and J. E. Thomas – *Loading dynamics of CO_2 laser traps* – Phys. Rev. A, **63**, 043403 (2001)

[42] J. D. Weinstein, R. deCarvalho, C. I. Hancox, and J. M. Doyle – *Evaporative cooling of atomic chromium* – Phys. Rev. A, **65**, 021604 (2002)

[43] P. O. Schmidt, S. Hensler, J. Werner, T. Binhammer, A. Gorlitz and T. Pfau –   *Continuous loading of cold atoms into a Ioffe-Pritchard magnetic trap* – J. Opt.B.:Quantum Semiclass. Opt., **5**, S170-S177 (2003)

[44] H. C. Mastwijk, J. W. Thomsen, P. van der Straten, and A. Niehaus – *Optical Collisions of Cold, Metastable Helium Atoms* – Phys. Rev. Lett., **80**, 5516 (1998)

[45] Paul J. J. Tol, Norbert Herschbach, Eric A. Hessels, Wim Hogervorst, and Wim Vassen – *Large numbers of cold metastable helium atoms in a magneto-optical trap* – Phys. Rev. A., **60**, 5516 (1998)

[46] F. Bardou, O. Emile, J.M. Courty, C.I. Westbrook and A. Aspect, –   *Magneto-optical Trapping of Metastable Helium: Collisions in the Presence of Resonant Light.* – Europhys. Lett., **20**, 681 (1992)

[47] F. Pereira Dos Santos, F. Perales, J. Léonard, A. Sinatra, J. Wang, F. S. Pavone,E. Rasel, C. S. Unnikrishnan, and M. Leduc, – *Efficient magneto-optical trapping of a metastable helium gas.* – Eur. Phys. J. AP, **14**, 68-76 (2001)

[48] Kalle-Antti Suominen, –   *Theories for cold atomic collisions in light fields.* – J. Phys. B.: At. Mol. Opt. Phys., **29**, 5981-6007 (1996)

[49] M. J. Holland, K.-A. Suominen, and K. Burnett, –   *Cold collisions in a laser field: Quantum Monte Carlo treatment of radiative heating.* – Phys. Rev. A., **50**, 1513 (1994)

[50] Band Y. B., Tuvi I., Suominen K.-A., Burnett K. and Julienne P. S., – *Loss from magneto-optical traps in strong laser fields.* – Phys. Rev. A., **50**, R2826 (1994)

[51] R. Chicireanu, A. Pouderous, R. Barbé, B. Laburthe-Tolra, E. Maréchal, L. Vernac, J.-C. Keller and O. Gorceix, – *Simultaneous magneto-optical trapping of bosonic and fermionic chromium atoms* – Phys. Rev. A, **73**, 053406 (2006)

[52] F. Pereira Dos Santos, F. Perales, J. Léonard, A. Sinatra, Junmin Wang, F.S. Savone, E. Rasel, C.S. Unnikrishnan, M. Leduc, – *Penning collisions of laser-cooled metastable helium atoms* – Eur. Phys. J. D, **14**, 15-27 (2001)

[53] L. G. Marcassa, G. D. Telles, S. R. Muniz, and V. S. Bagnato, – *Collisional losses in a K-Rb cold mixture* – Phys. Rev. A., **63**, 013413 (2000)

[54] M. Marinescu, and A. Dalgarno, – *Dispersion forces and long-range electronic transition dipole moments of alkali-metal dimer excited states* – Phys. Rev. A, **52**, 331 (1995)

[55] E. I. Dashevskaya, A. I. Voronin, and E. E. Nikitin, – *Theory of excitation transfer in collisions between alkali atoms. I. Identical partners* – Can. J. Phys., **47**, 1237 (1969)

[56] W. J. Meath, – *Retarded Interaction Energies between Like Atoms in Different Energy States* – J. Chem. Phys., **48**, 227 (1968)

[57] J. Léonard, A. P. Mosk, M. Walhout, P. van der Straten, M. Leduc, and C. Cohen-Tannoudji, – *Analysis of photoassociation spectra for giant helium dimers* – Phys. Rev. A, **69**, 032702 (2004)

[58] P. S. Julienne, J. Vigué, *Cold collisions of ground- and excited-state alkali-metal atoms* – Phys. Rev. A., **44**, 4464 (1991)

[59] P. L. Gould, P. D. Lett, P. S. Julienne, W. D. Phillips, H. R. Thorsheim and J. Weiner – *Observation of associative ionization of ultracold laser-trapped sodium atoms* – Opt. Lett., **60**, 788 (1988)

[60] M. G. Prentiss, A. Cable, J. E. Bjorkholm, S. Chu, E. L. Raab, and D. E. Pritchard – *Atomic-density-dependent losses in an optical trap* – Phys. Rev. A., **13**, 452 (1988)

[61] A. Gallager, D. E. Pritchard– *Exoergic Collisions of Cold Na*-Na* – Phys. Rev. Lett., **63**, 957 (1989)

[62] D. Sesko, T. Walker, C. Monroe, A. Gallagher, and C. Wieman – *Collisional losses from a light-force atom trap* – Phys. Rev. A., **63**, 961 (1989)

[63] P. D. Lett, W. D. Phillips, S. L. Rolston, C. E. Tanner, R. N. Watts and C. I. Westbrook, – *Optical Molasses* – J. Opt. Soc. Am. B., **6**, 2084 (1989)

[64] Thad Walker, David Sesko, and Carl Wieman, – *Collective Behavior of Optically Trapped Neutral Atoms* – Phys. Rev. lett., **64**, 408 (1990)

[65] David Sesko, Thad Walker, and Carl Wieman, – *Behavior of neutral atoms in a spontaneous force trap* – J. Opt.Soc. Am. B., **8**, 946 (1991)

[66] G. Modugno, G. Ferrari, G. Roati, R. J. Brecha, A. Simoni, M. Inguscio , – *Bose-Einstein Condensation of Potassium Atoms by Sympathetic Cooling* – Science, **294**, 1320 (2001)

[67] C. Silber, S. Günther, C. Marzok, B. Deh, Ph. W. Courteille, and C. Zimmermann, – *Quantum-Degenerate Mixture of Fermionic Lithium and Bosonic Rubidium Gases* – Phys. Rev. Lett, **95**, 170408 (2005)

[68] F. Schreck, L. Khaykovich, K. L. Corwin, G. Ferrari, T. Bourdel, J. Cubizolles, and C. Salomon, – *Quasipure Bose-Einstein Condensate Immersed in a Fermi Sea* – Phys. Rev. Lett, **87**, 080403 (2001)

[69] J. M. McNamara, T. Jeltes, A. S. Tychkov, W. Hogervorst, and W. Vassen, – *Degenerate Bose-Fermi Mixture of Metastable Atoms* – Phys. Rev. Lett, **97**, 080404 (2006)

[70] H. C. Mastwijk, J. W. Thomsen, P. van der Straten, and A. Niehaus, – *Optical Collisions of Cold, Metastable Helium Atoms* – Phys. Rev. Lett., **80**, 5516 (1998)

[71] T. P. Dinneen, K. R. Vogel, E. Arimondo, J. L. Hall, A. Gallager, – *Cold collisons of Sr*-Sr in a mgneto-optical trap* – Phys. Rev. A., **59**, 1216 (1999)

[72] M.W. Müller, A. Merz, M.-W. Ruf, H. Hotop, W. Meyer, and M Movre, – *Experimental and theoretical studies of He Bi-excited collision systems He*(2 ^3S)+He*(2 ^3S, 2 ^1S) at thermal and subthermal kinetic energies* – Z. Phys. D., Atoms, Molecules and Clusters **21**, 89 (1991)

[73] P. O. Fedichev, M. W. Reynolds, U. M. Rahmanov, and G. V. Shlyapnikov – *Inelastic decay processes in a gas of spin-polarized triplet helium* – Phys. Rev. A. **53**, 1447 (1996)

[74] M. Walhout, U. Sterr, C. Orzel , M. Hoogerland, and S. L. Rolston, – *Optical Control of Ultracold Collisions in Metastable Xenon* – Phys. Rev. Lett., **74**, 506 (1995)

[75] Stephan Ritter, Anton Öttl, Tobias Donner, Thomas Bourdel, Michael Köhl, and Tilman Esslinger, – *Observing the Formation of Long-Range Order during Bose-Einstein Condensation* – Phys. Rev. Lett., **98**, 090402 (2007)

[76] S. Hensler, J. Werner, A. Griesmaier, P.O. Schmidt, A. Görlitz, T. Pfau, S. Giovanazzi and K. Rzazewski, – *Dipolar Relaxation in an ultra-cold Gas of magnetically trapped chromium atoms* – Appl. Phys. B., **77**, 765 (2003)

[77] Robert deCarvalho and John Doyle, – *Evaporative cooling at low trap depth* – Phys. Rev. A., **70**, 053709 (2004)

[78] D. Comparat, A. Fioretti, G. Stern, E. Dimova, B. Laburthe Tolra, and P. Pillet, – *Optimized production of large Bose-Einstein condensates* – Phys. Rev. A., **73**, 043410 (2006)

[79] O. J. Luiten, M. W. Reynolds, and J. T. M. Walraven, – *Kinetic theory of the evaporative cooling of a trapped gas* – Phys. Rev. A., **53**, 381 (1996)

[80] Wolfgang Petrich, Michael H. Anderson, Jason R. Ensher, and Eric A. Cornell, – *Stable, Tightly Confining Magnetic Trap for Evaporative Cooling of Neutral Atoms* – Phys. Rev. A., **74**, 3352 (1995)

[81] J. Stuhler, P. O. Schmidt, S. Hensler, J. Werner, J. Mlynek, and T. Pfau, – *Continuous loading of a magnetic trap* – Phys. Rev. A., **64**, 031405(R) (2001)

[82] K. Huang, – *Statistical Mechanics* – Wiley, New York (1987)

[83] O. Zobay et B.M. Garraway, – *Two-dimensional atom trapping in field-induced adiabatic potentials* – Phys. Rev. Lett., **86**, 1195 (2001)

[84] Y. Colombe, E. Knyazchyan, O. Morizot, B. Mercier, V. Lorent and H. Perrin, – *Ultracold atoms confined in rf-induced two-dimensional trapping potentials* – Europhys. Lett., **67**, 593 (2004)

[85] Yves Colombe, Ph.D. thesis, *Condensat de Bose-Einstein, champs evanescents et piegeage bidimensionel* – Université Paris Nord – (2004)

[86] L. Landau, – *Zur Theorie der Energieübertragung - II* – Phys. Z. Sowjetunion, **2**, 46 (1932)

[87] C. Zener, – *Non-adiabatic crossing of energy levels* – Proc. R. Soc. London Ser. A, **137**, 696 (1932)

[88] N. V. Vitanov and K.-A. Suominen, – *Time-dependent control of ultracold atoms in magnetic traps* – Phys. Rev. A, **56**, R4377 (1997)

[89] J.R. Rubbmark, M.M. Kash, M.G. Littman et D. Kleppner, – *Dynamical effects at avoided level crossings: a study of the Landau-Zener effect using Rydberd atoms* – Phys. Rev. A, **23**, 3107 (1981)

[90] Piet O. Schmidt, Ph.D. thesis, *Scattering properties of ultra-cold chromium atoms* – Universität Stuttgart – (2003)

[91] R. Grimm, M. Weidemüller, and Y. B. Ovchinnikov, – *Optical dipole traps for neutral atoms* – Advances in Atomic, Molecular, and Optical Physics, **42**, 95 (2000)

[92] C. Cohen-Tannoudji, J. Dupont-Roc, and G. Grynberg, – *Processus d'interaction entre photons et atomes* – EDP Sciences (1996)

[93] J. D. Jackson, – *Classical electrodynamics* – Wiley, New York (1962)

[94] Claude Cohen-Tannoudji, Bernard Diu, Franck Laloë, – *Mécanique quantique* – Hermann (1997)

[95] K. M. O'Hara, S. R. Granade, M. E. Gehm, T. A. Savard, S. Bali, and J. E. Thomas, – *Ultrastable CO_2 Laser Trapping of Lithium Fermions* – Phys. Rev. Lett., **82**, 4204 (1999)

[96] K. M. O'Hara, S. R. Granade, M. E. Gehm, and J. E. Thomas, – *Loading dynamics of CO_2 laser traps* – Phys. Rev. A, **63**, 043403 (2001)

[97] D. L. Haycock, S. E. Hamman, G. Klose, and P. S. Jessen, – *Atom trapping in deeply bound states of a far-off-resonance optical lattice* – Phys. Rev. A, **55**, R3991 (1997)

[98] T. Weber, *Bose-Einstein Condensation of Optically Trapped Cesium* – Universität Stuttgart – (2003)

[99] M. D. Barrett, J. A. Sauer, and M. S. Chapman, – *All-Optical Formation of an Atomic Bose-Einstein Condensate* – Phys. Rev. Lett., **87**, 010404 (2001)

[100] T. Weber, J. Herbig, M. Mark, H.-C. Nägerl, and R. Grimm, – *Bose-Einstein Condensation of Cesium* – Science, **299**, 232 (2003)

[101] J. V. Porto, – *Private communications*

[102] L. D. Landau and E. Lifshitz, – *Mecanique* – Moscou (1960)

[103] Axel Griesmaier, Ph.D. thesis, *Dipole-dipole interaction in a degenerate quantum gas* – Universität Stuttgart – (2006)

[104] Kenneth O'Hara, Ph.D. thesis, *Optical Trapping and Evaporative Cooling of Fermionic Atoms* – Duke University – (2000)

[105] S. Friebel, C. D'Andrea, J. Walz, M. Weitz, and T. W. Hänsch, – *CO_2-laser optical lattice with cold rubidium atoms* – Phys. Rev. A, **57**, R20 (1998)

208

[106]   NIST Atomic Spectra Database – http://physics.nist.gov/PhysRefData/ASD

[107] D. W. Snoke, and J. P. Wolfe, – *Population dynamics of a Bose gas near saturation* – Phys. Rev. B, **39**, 4030 (1989)

[108] A. Robert, O. Sirjean, A. Browaeys, J. Poupard,dagger S. Nowak,ddagger D. Boiron, C. I. Westbrook, and A. Aspect, – *A Bose-Einstein Condensate of Metastable Atoms* – Science, **292**, 461 (2001)

[109] D. Guéry-Odelin, J. Söding, P. Desbiolles, and J. Dalibard, – *Is Bose-Einstein condensation of atomic Cesium possible?* – Europhys. Lett., **44**, 25 (1998)

[110] A. Griesmaier, J. Stuhler, and T. Pfau, – *Production of a chromium Bose-Einstein condensate* – Appl. Phys. B., **82**, 190404 (2006)

[111] M. Fattori, T. Koch, S. Goetz, A. Griesmaier, S. Hensler, J. Stuhler, and T. Pfau, – *Demagnetization cooling of a gas* – Nature Physics, **2**, 765 (2006)

STUDIES OF COLD CHROMIUM ATOMS IN MAGNETIC AND OPTICAL TRAPS: steps towards Bose-Einstein Condensation

Abstract: In the perspective of studying dipole-dipole interactions in quantum degenerate Bose and Fermi gases, we have built an experimental setup for cooling and trapping Chromium (Cr) atoms. In this respect, one needs to use appropriate technological solution, such as a high-temperature oven ($\sim 1500°$C) and a laser system providing high laser power at 425nm. Our experiments allow us to obtain magneto-optical traps for the two main isotopes of Cr (i.e. the bosonic ^{52}Cr and the fermionic ^{53}Cr). These traps are characterized by large light-assisted collisional loss rates, which have been studied both experimentally and theoretically. The existence of radiative decay channels towards two long-lived metastable states allows the magnetic trapping and accumulation of fairly large atom numbers of cold Cr atoms. We have studied the possibility of modifying the shape of these traps with the use of RF magnetic fields, which allowed the study of collisional properties of Cr atoms in the metastable states. Finally, we have demonstrated a new continuous loading technique of an optical dipole trap with more than one million metastable ^{52}Cr atoms, at 100μK. The transfer into the ground state and the polarization in the lowest-energy Zeeman sublevel opens the perspective for reaching the Bose-Einstein condensation of Cr through evaporative cooling.
Keywords: chromium, magneto-optical trapping, cold collisions, magnetic trapping, optical trapping, evaporative cooling

ATOMES FROIDS DE CHROME PIEGES MAGNETIQUEMENT ET OPTIQUEMENT: premières étapes vers la condensation

Résumé: Dans la perspective d'étudier les interactions dipolaires dans des gaz de bosons et de fermions dégénérés, nous avons mis en place un dispositif expérimental pour refroidir et piéger les atomes de chrome (Cr). Il faut pour cela recourir à des solutions technologiques particulières, comme l'utilisation d'un four à haute température ($\sim 1500°$C) et d'un dispositif laser délivrant une puissance lumineuse élevée à 425nm. Nos expériences permettent d'obtenir des pièges magnéto-optiques pour les deux isotopes majoritaires du Cr (le ^{52}Cr bosonique et le ^{53}Cr fermionique). Ces pièges sont caractérisés par des forts taux de collisions inélastiques assistées par la lumière, que nous avons étudié expérimentalement et théoriquement. La présence de fuites vers des états métastables permet l'accumulation dans des pièges magnétiques d'un nombre conséquent d'atomes. Nous avons aussi étudié la possibilité de modifier la forme de ces pièges, à l'aide de champs RF. Les propriétés collisionelles des états métastables sont étudiées en détail. Finalement, nous avons mis en œuvre une nouvelle méthode de chargement en continu d'un piège optique avec plus d'un million d'atomes métastables de ^{52}Cr, à 100μK. La polarisation des atomes de Cr dans l'état minimal en énergie du niveau fondamental ouvre des perspectives pour atteindre la condensation de Bose-Einstein du chrome par refroidissement évaporatif.
Mots clés: chrome, piégeage magnéto-optique, collisions froides, piégeage magnétique, piégeage optique, refroidissement évaporatif